Manufacturing and Characterization of Textile Fabricated Lattice Materials

by

Stephen Ryan

A thesis submitted to Johns Hopkins University in conformity with the requirements for the degree of Doctor of Philosophy

Baltimore, Maryland

October, 2015

© 2015 Stephen Ryan

All Rights Reserved

Abstract

Traditional materials science looks to uncover the relationship between processing, microstructure, and properties. Frequently, processing is tailored to achieve a desired microstructure that will yield specific properties. Recently, the ability to model, make and characterize materials at the micron length scale has allowed for the design and fabrication of materials with specific architectures and tailorable properties. This thesis examines the validity of controlling the exact microarchitecture of a material in order to dramatically change and decouple the material properties.

In this project, metallic microlattice materials were made by weaving metallic wires with a non-crimp 3D weaving process. The architectures of these materials were specified by a constrained topology optimization to maximize the permeability and shear stiffness. After weaving, the material structure was preferentially bonded (through brazing, soldering, vapor phase processing, and transient liquid phase bonding) in order to increase the mechanical properties of these materials, and to expand the available architectures and geometries.

The microscale internal architecture of these materials was characterized by traditional metallographic techniques and 3D reconstruction of x-ray tomography and serial sectioning. The shear stiffness and permeability were measured in order to evaluate the validity of the architectural optimization and to evaluate the quality of bonding. Two specific areas where I took the lead, brazing and damping, received the greatest effort and make up the make up the majority of this dissertation. This thesis

shows how brazing can be used to selectively bond wire junctions and turn a 3D weave into a lattice material. The damping properties of unbonded metallic lattices were measured using a DMA at both room temperature and after exposures to temperatures as high as 1200°C, and they have been shown to possess high damping properties. The decrease in the damping with temperature was examined by sectioning the material and measuring the changes in residual stress within the individual wires with temperature exposure. The thermal transport properties of these materials were also. FE modeling was also performed and compared with experimental results in order to evaluate the mechanisms that were responsible for these unique properties.

Advisor: Professor Kevin J. Hemker

Readers: Professors Kevin J. Hemker, Timothy P. Weihs, and James K. Guest

Acknowledgments

I would like to take a moment to thank all of those who have helped me along the way on this path to my Ph.D. I would like to thank my advisor Dr. Kevin Hemker for his help and guidance in carrying out the research that forms the topic of this dissertation. I would also like to extend my thanks as well for his help and support in editing this thesis. I would like to thank Dr. Timothy Weihs and Dr. James Guest as well for their guidance as well on this research project and their help in reading and editing this thesis. I would like to thank Dr. Kevin Hemker, Dr. Tim Weihs, Dr. James Guest, Dr. Jonah Erlebacher, Dr. Richard Fonda, Dr. Bob Cammarata, and Dr. Somonath Ghosh for participating in my thesis defense committee. I would also like to thank the Hemker research group and the members of the DARPA MCMA team, particularly Dr. Yong Zhang, Longyu Zhao, Dr. Seunghyun Ha, and Dr. Stefan Szyniszewski, Sen Lin, Rui Xiao and Josephine Carstensen. Thank you to Jeanine Majewski, Marge Weaver, Dorothy Reagle, Paula Davis, Ada Simari, Brooke Mesta, Paula Davis, Kevin Adams, Cindy Larichiuta, Marty Devaney, Melissa Andrews, and Deana Santoni for their help in handling all of the administrative work that keeps the departments running so well. I would like to thank my mother, father, and brother. Without my family I believe it would have been impossible to be where I am today. Last but not least, I would also like to thank Katie for her continuing support and encouragement.

Table of Contents

List of Figures

List of Tables

Chapter 1: Introduction

In civil engineering, the application of efficient structural design has yielded significant improvements and greater efficiency. Compare the ancient pyramids in Egypt to the Eiffel Tower in Paris. The pyramids reach only half the height of the Eiffel Tower, yet they have a weight that is 600 times greater. This substantial improvement in height with a drastic reduction in mass was made possible through the development and use of efficient iron lattice structures.

In the field of materials science, traditional materials such as iron and steel are considered inexpensive, whereas the traditional shaping and processing of materials (machining, forging, etc.) are costly. Recently, however, there has been a major shift. Making materials in complex shapes has become increasingly less expensive through the use of advanced manufacturing techniques such as 3D printing [1]. As a result, there has been greater interest in the shape of materials and components because intricate designs are not only possible but are increasingly less expensive to produce. This design freedom has been augmented further by a rise in computational modeling, which gives designers greater freedom to properly analyze these complicated designs.

Inspired by the proliferation of advanced manufacturing techniques, a new direction in material science is emerging: developing different processing techniques to control the internal architecture of a material in addition to its microstructure. Traditionally, material science has focused on uncovering the relationship among processing, microstructure, and properties so that more efficient and reliable materials

can be realized through the variation of processing, which improves the microstructures and resulting properties. By controlling the microarchitecture, materials with even more efficient designs with greater specific properties (such as impact resistance [2–4]) and in some cases unique combinations of multifunctional properties [5] (such as low CTE and high stiffness [6], stiffness and permeability [7], and density, strength, and thermal transport [8]) can be developed. This shift in focus to looking at the interplay of processing, properties, and microarchitecture (as opposed to microstructure) might open the door to new demanding applications that have not been possible with traditional materials.

This traditional material science approach searched for methodology to control the average microstructure of metallic materials through the use of chemistry, processing, and heat treatments in order to control grain size, precipitate size and spacing, and other microstructural features. Microstructure frequently is used to increase the strength of materials by providing barriers to the movement of dislocations within a material.

Strengthening of metallic materials as a result of average grain size control is frequently thought of in terms of the famous Hall-Petch relations [9,10]. This relationship states that the yield strength of a material increases as the average grain size decreases with the form,

$$\sigma_y = \sigma_o + kd^{-1/2} \quad (1)$$

where, σ_y is the yield stress of a polycrystalline material, σ_o is the yield stress of a single crystal oriented for multiple slip, k is a constant that is material specific, and d is the average grain size. This equation highlights that materials with small average grain sizes have a higher yield stress than larger grain materials.

Precipitates also are commonly controlled to increase the strength of a material. The role of precipitates in materials, specifically the spacing between multiple precipitates, is captured in the Orowan bowing relationship. This relationship examines the stress required to bow a dislocation past a pair of precipitate particles within a grain [11]. The shear stress required to bow a dislocation past a pair of precipitates is,

$$\tau_o = \frac{Gb}{\lambda} \tag{2}$$

where, τ_o is the shear stress required to bow the dislocation between the precipitates, G is the shear modulus of the matrix, b is the magnitude of the burgers vector, and λ is the spacing between the precipitate particles. To increase the strength of a material, it is best to have many closely spaced precipitates, which will prevent the movement of dislocations.

Grain size and precipitate strengthening operate to increase the strength of materials by modifying the motion of dislocations in a material. Precipitates and grain boundaries act as barriers to dislocation motion, so increasing the amount of grain boundary area or decreasing the spacing of precipitates can serve to disrupt the

movements of dislocations and increase the strength of a material. The movement of dislocations facilitates plasticity, so limiting the motion of dislocations can increase the yield strength in a material.

Classic processing techniques are, however, limited by the manufacturer's lack of control in defining the exact size and location of these features. It is possible to control the average size and distribution of features (grain size, precipitate size, number of precipitates, etc.) in a material but not their exact location. If the microscale architecture of the material (the exact placement of matter in a material) could be controlled instead of just the average size, shape, and distribution of microstructural features, could the properties of the material be improved, in the same way that civil engineering was greatly improved through the use of more efficient truss designs? The purpose of this work is to examine if improved or new properties are possible through the control of microscale architecture within a material.

This is not the full story, however, because a final product is a combination of both materials and shape. With the advent of better and cheaper manufacturing and shaping processes, shape is more easily and inexpensively controlled. Precise control of shape has allowed for the development of new materials in which the material itself has a microscale architecture that can be tuned to provide these materials with properties that are tailored for a specific purpose. In fact the internal "shape" of these materials might even be optimized rigorously for particular properties. The desired architecture will be determined by the properties that are desired, and the desired shape will in turn control the process and the obtainable property space that can be manufactured by that process.

This new materials science paradigm now includes the architecture of the material with the microstructure, and it is shown in Figure 1. [12]

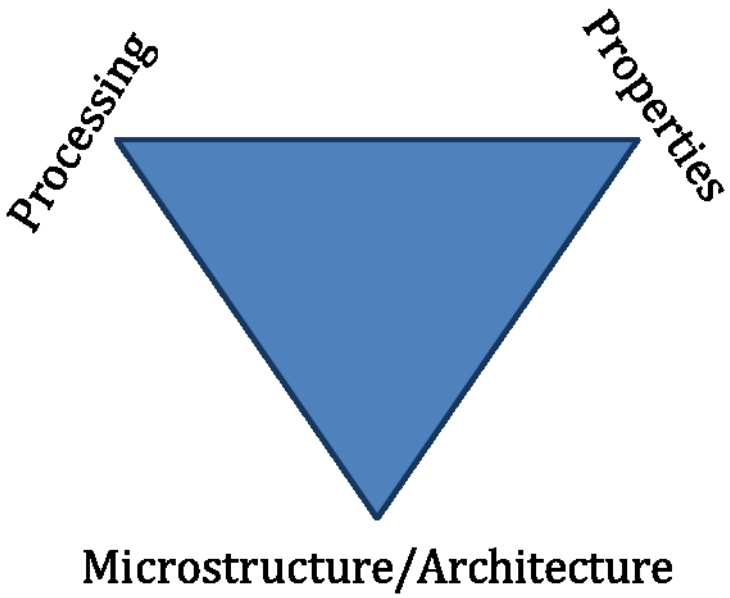

Figure 1: The "new" materials science paradigm. This figure highlights the interplay among microstructure and architecture, processing, and the material's properties. The traditional paradigm's design refers to the average microstructure of a material, but the new paradigm presented here suggests that the design of the architecture of the material is also important.

This paradigm traditionally examines the interplay among processing methods, material properties, and the average microstructure. The shift from focusing on only controlling the average microstructure of a material to controlling the exact architecture of a material as well has led to a change in the traditional paradigm. These new approaches have the potential to increase the available design space through the use of materials that are specifically tuned to a particular application. Furthermore, through the use of architectural design, material properties that are coupled in traditional

materials, such as stiffness and permeability, might be able to be decoupled and varied independently of each other [7,8].

This thesis addresses the possibility of combining 3D weaving of metallic wires (in designs that are informed through topology optimization) with post-weaving alloying and bonding techniques in order to develop a new class of multifunctional materials with a controlled microarchitecture. The 3D weaving process allows for easy scalability of the production process so that the technology can proceed from the lab to the real world. Additionally, this work not only confirms the ability of the process to manufacture microlattice materials, but it also presents some of the unique multifunctional properties of the new class of materials.

Chapter 2: Background

The 3D woven metallic microlattice materials that are the focus of this work are part of a larger category of metallic cellular materials. These materials are a field of material science that has received a substantial amount of attention over the past two decades [5,13–18], although the field has been in existence since the middle of the last century with the commercialization of metallic foams [19,20]. Metallic cellular materials are subdivided further into two major sub-categories: stochastic cellular materials and periodic cellular materials. Stochastic materials, such as metallic foams, have a random distribution of pores and ligaments within their architecture with no long range order, whereas periodic cellular materials have well-defined unit cell architectures with long range order [21].

2.1: Stochastic Cellular Materials - Metallic Foams

Metallic foams, which represent the major type of stochastic cellular metallic materials, possess unique properties (such as high specific strength and stiffness, high specific energy absorption, and high thermal transport [19,20]) that are a result of its microarchitecture. Within the category of metallic foams, there are two further subdivisions of open cell and closed cell foams, the latter of which is analogous to polymeric foams. Open cell foams have interconnected pores throughout the bulk of the material, whereas closed cell foams do not possess an interconnected pore structure.

Limits to the density and average pore size of the foams are controlled by the process that is used to manufacture them, and the density of these materials tends to be quite low (usually with relative densities under 20% for open cell foams). Foams are made through a variety of processes (as many as nine, although fewer have been commercialized) [19,20], and each has its own candidate materials, benefits, and limitations. The most common processes are: 1.) releasing or forming a gas in a liquid metal; 2.) compacting a metal powder with a secondary material, which can be removed after sintering; 3.) electro- or vapor phase deposition of metal onto a polymer foam substrate; 4.) creation of a foam substrate from a polymer host, which is filled with metal before removal of the host structure; and 5.) sintering of hollow spheres. Usually, the process chosen is the one that best balances the chemistry, cost, purity, and properties of the chosen foam.

The properties of metallic foams frequently are reported in terms of their relative density. Relationships for properties have been derived empirically in terms of the relative density of the material [19,20,22,23]. The properties usually are dependent on not only the relative density but also on whether the foam is open or closed cell. For instance, the stiffness of closed cell foams scale linearly with the relative density as [20],

$$\frac{E}{E_s} = \alpha_1 \rho \tag{3}$$

where, E is the modulus of the foam, E_s is the modulus of the material from which the foam is made, α_1 is a scaling factor that depends on the geometry of the cells in the foam

and is usually a value of ~0.3-0.4, and ρ is the relative density of the foam. In contrast, the stiffness of open cell foams scales non-linearly with the relative density as,

$$\frac{E}{E_s} = \alpha_2 \rho^2 \tag{4}$$

where α_2 is also a scaling factor that describes the geometry of the foams, but it is usually equal to 1. Metallic foams tend to exhibit a lower stiffness than periodic cellular structures; however, foams possess more isotropic properties, they have the ability to easily accommodate complex shape requirements, and they have a relatively low cost, which makes them attractive candidates for certain applications. The isotropic properties also make metallic foams attractive candidates for impact protection. Although honeycomb materials are highly anisotropic and can be highly efficient energy absorbers when the direction of impact is well defined [24,25], foams are much more attractive when the direction of impact may vary [19]. Additionally, open cell foams have been highlighted as possible candidates for use in high performance compact heat exchangers [19,20,26,27]. The high surface area to volume ratio, combined with the relatively high thermal conductivity of the open cell foams gives them unique and advantageous convective thermal properties [20]. The limiting factor of foams for thermal devices is the stochastic nature of the pores, which leads to greater pumping losses than are found in periodic structures of the same scale [28]. The unique combination of properties of metallic foams makes them attractive for use as materials in a wide variety of multifunctional applications.

Modeling of metallic foams, where the ligaments in the foam are treated as a series of beams that are connected by a series of fixed joints, has given us a greater understanding of their properties and how they are related to the underlying pore structure, [15]. Two main configurations are considered. The first is a diamond shape, and the second is a modified diamond shape with a connecting member that joins two opposing corners.

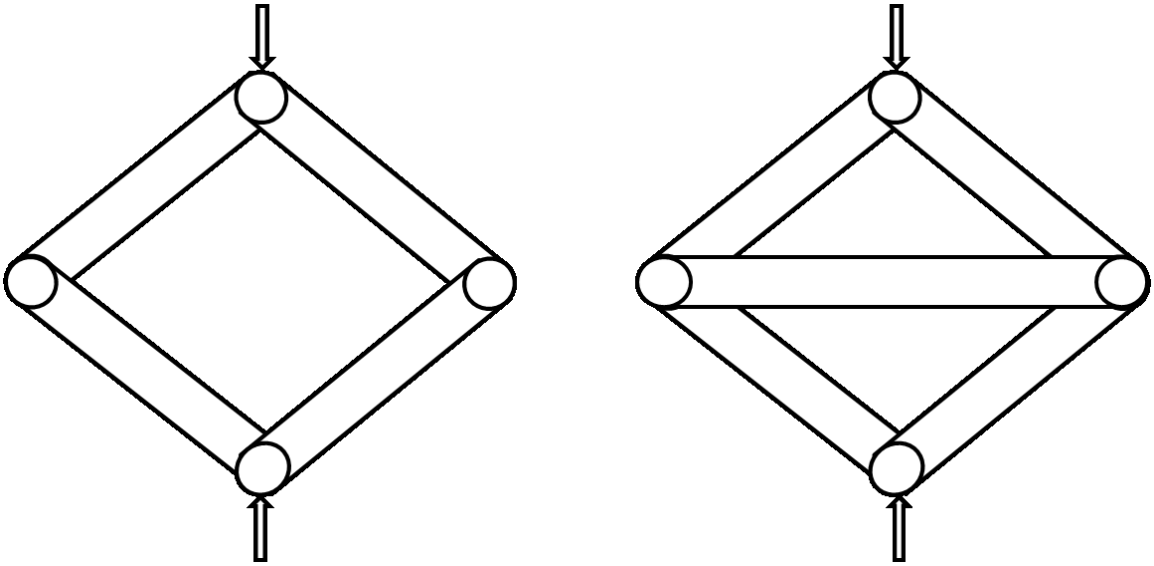

Figure 2: Diamond-shaped truss structures that are joined with fixed connections as a simplified model for the cell structure of metallic foams. The truss on the left does not possess the additional bracing of the truss on the right, and therefore applied loads at a pair of opposite nodes will cause the truss to "bend" as opposed to the braced truss, which will exhibit higher strength due to the "stretching" mechanism of the extra link.

A substantial enhancement in the mechanical properties can be realized in the second case because of the way the load is transferred through the structure. The unbraced structure exhibits lower strength because the fixed joints induce bending in the struts as a load is applied. In this case, the struts in the structure deform by "bending." In the

second truss structure, the additional brace prevents the bending of the members around the fixed joints, therefore, for deformation to occur, the bracing member must either be pulled or compressed (depending on the nature of the applied load), which results in superior strength and stiffness [15]. The deformation mode in the braced structure is "stretch" dominated. These models [15] originally were developed to explain the differences in the observed properties of metallic foams; however, metallic foams do not possess structures with the regularity that is found in the theoretical trusses. In fact, the properties and architecture of foam are stochastic in nature. This is merely an approximation of the average effective structure of the foams and not the true architecture of the foam. In reality, this model shows an upper limit on the obtainable properties of foams, if they were regular structures. It implies that a way to enhance the properties of materials would be to manufacture a material with the microscale feature size of metallic foams (due to the benefits discussed above and elsewhere in the literature) with regular "stretch"-dominated, unit cell architectures.

2.2: Periodic Cellular Materials

2.2.1: Honeycomb and Corrugated Materials

Periodic cellular materials (PCM) possess a well-defined architecture that allows them to serve as lightweight, multifunctional materials [5]. There are two distinct categories of PCMs: 1.) honeycomb and corrugated core structures, which possess a 2.5D

architecture (a 2-D planar geometry that is extruded into a 3rd dimension) and 2.) lattice materials that possess a more complex 3D architecture. Honeycomb structures are aligned in a manner such that the openings in the structure are perpendicular to the face sheets to which they are bonded, and they can have a variety of geometries, such as triangular, square, and hexagonal unit cells. Corrugated structures are oriented with their large openings parallel to the face sheets. This orientation allows the structures to be permeable in one direction as opposed to honeycombs, which are not permeable. The corrugated structures and honeycombs can be fabricated through bending, rolling, or slotted sheet metal processes, which all require subsequent joining of the material. In a manner that is analogous to closed cell metallic foams, the elastic modulus of PCMs scales linearly with the relative density of the material. The design and constrained use of these materials give them unique properties that are in most cases superior to metallic foams [5,21]. Specifically, they might have higher stiffness and strength then foams while also exhibiting other multifunctional properties. Honeycombs have been shown to excel as thermal barriers, whereas corrugated structures, because of their high permeability, can be used as high strength heat exchangers [29]. Researchers also have highlighted both for applications in which thermal shock and impact protection are required [24,25].

2.2.2: Lattice Structures

Although the properties of honeycomb and corrugated structures are interesting and novel, a greater array of properties can be realized through the use of more complex

lattice structure geometries [2,5,21,25,30]. Traditionally, these materials were formed through labor-intensive processing. This processing included techniques such as sheet metal punching/forming, hand laying in premade alignment jigs, and casting. Usually, a final bonding step is required to join the ligaments together to form a lattice. The most common geometries are pyramidal, tetrahedral, and kagome architectures. The kagome architectures also can be manufactured through a twisted wire insertion process that is semi-automated but is still labor intensive [18,31–35]. As a result of their more intricate geometry, the properties of these materials are also often more complex. In most cases, these structures possess more efficient geometries, for instance equal or greater strength for the same relative density. Additionally, properties such as heat transfer, blast protection, and penetration protection can be tuned more appropriately for a particular application with the greater design space that is available with these types of materials. Many of these real lattice structures unfortunately exhibit lower than predicted properties because their failure is often mediated by defects, particularly at the nodes [5,18,30–32].

The previous work on periodic structures indicates the potential benefits of using lattice geometries for designing multifunctional materials, but several barriers must be overcome to make periodic structures more viable. Manufacturing defects must be diminished. The manufacturing process must be made less labor intensive (through automation or selection of a different process) to allow for it to be scaled to larger, commercial quantities of material. To fully take advantage of the benefits of these lattice structures, the feature size of these materials must be made smaller (particularly for heat transfer applications in which the surface area to volume ratio is important). Finally,

small repeatable features sizes are necessary to turn these macro structures into architected materials that can be used and integrated into other systems.

It is worth noting that small-scale lattice materials have been fabricated by HRL using a novel rapid polymerization technique [17]. In this process, an array of UV lasers polymerize a solution of monomers to form a truss material with a well-defined geometry. This truss then is plated with nickel (through an electroless plating process), and then the plastic is chemically etched away to make a hollow microarchitectured truss system [17]. These materials have a range of obtainable geometries, which is limited by the current range of the incident light beam angles that induce polymerization. The material also is limited mechanically by localization of deformation at the nodes of struts [36]. The structures, however, exhibit extremely low density and promising mechanical and damping properties [37]. Additionally, the heat transfer of these structures for extended surface, cross flow, and heat pipe applications has been shown to be promising [8,38,39]. Overall, these metallic microlattice materials show that one can develop new and unique materials by combining the architectures of lattice structures with the feature size of foams.

Further expansion of the available design space for microlattice materials requires consideration of the limitations of the processing method used to make the material. The next generation of lattice materials must use a processing method that provides the ability to make small-scale features in regular unit cell architectures, and it should be scalable to manufacture large amounts of material quickly. Additive manufacturing techniques provide great flexibility, but the fabrication of large quantities of high strength metallic materials is often an indirect process in which a wax mold is 3D printed and the resulting

parts are formed through a traditional investment casting procedures [40]. Direct manufacturing of 3D metallic parts is still in its infancy although recently there have been some promising advances [41].

2.2.3: 3D Woven Metallic Microlattice Materials

In this thesis, the non-crimp 3D weaving with a patented process known as 3WEAVE® was used to manufacture metallic lattice material [42–44]. The process is capable of weaving wires and filaments in a wide variety of patterns. This and other 3D weaving processes initially were developed to provide interlaminar strength without the added processing steps and losses in the mechanical strength that are frequently associated with through thickness stitching of composite materials [45–47]. In 3D weaving, the interlaminar strength is generated by through-thickness z-wires that are woven as part of the design of the fabric. The 3WEAVE® process used in this work uses every third warp wire, which is pulled through the thickness of the weave on alternating cycles to create the through-thickness z-wires. This process decreases the number of aligned in-plane fibers, which might lead to lower overall strength in plane, but the 3D woven material exhibits increased interlaminar strength and superior isotropic properties when compared to stitched composites. The process is also highly scalable, and it has the potential to quickly and easily change the wire/filament material, internal architecture, and overall shape.

The 3D weaving process is capable of making a large number of geometries and architectures in an assortment of materials that can be easily changed, so there is a wide

design space in which to select an internal architecture. More complex designs are made possible through the use of non-uniform architectures, graded, composite (multiple types of wires), and fugitive wire-based designs (in which wires are removed after the fabric is woven). To determine the optimal weaving geometry, our collaborative effort used a unique type of topological optimization that accounts for the limitations of the weaving process [7,48,49].

Topological optimization defines the optimal shape or architecture of a material or structure for a well-defined set of boundary conditions and optimization parameters. The various geometries that are derived computationally then are examined and compared to define the available property space. The limit of the maximum obtainable property space is known as the Pareto front. The optimization also is capable of providing the geometries associated with the edge of the design space. Unfortunately, the solutions for topology optimization often result in structures that are difficult or prohibitively expensive to manufacture. Advanced topology optimization methods incorporate the manufacturing constraints through explicit constraints or implicit methods such as projection methods [7,8,48,49]. In short, the method penalizes a solution that falls outside the range of architectures that can be manufactured with a particular process. In this project, the 3D woven metallic lattices were successfully topologically optimized for stiffness and permeability, and the results can be found in the literature [50,51].

In this project, the established 3WEAVE® process was used to generate porous microarchitectured materials. The weaving process is not what makes this research novel; it is the way we use the process that is novel. First, we used metallic wires instead of traditional carbon, glass, or ceramic fibers. Second, the designs of the weaving

patterns were informed with topology optimization that accounted for the limitations of the manufacturing process. Third, the woven material then was combined with a series of post-processing options to bond the structures and to modify their composition and microstructure. Finally, the properties of these materials were characterized and shown to have interesting multifunctionality. The details of the textile manufacturing, post-processing, and characterization of these unique materials can be found in the chapters that follow.

Chapter 3: Manufacturing by Weaving and Bonding of Lattice Materials

The 3D woven metallic microlattice materials that are the subject of this thesis allow the architecture to be optimized in order to tailor the properties of the material for multifunctional applications. The 3D weaving process that was used in this work is unique in that it couples 3D weaving of metallic wires with architectures that are informed by topology optimization. In order to more accurately optimize the material, it is important to bound the optimization problem with the limitations of the 3D weaving process, but also to take into account the manufacturing defects that are present (which are different than usual 3D woven materials as a result of the switch to metallic wires). Additionally, the experimental and modeling work highlighted the fact that in order to realize the mechanical properties that make the material competitive with currently existing materials, while simultaneously maintaining the unique permeability of this material, selective bonding of the nodes had to be performed.

This chapter will explain the unique 3D weaving process that was used to generate the metallic 3D weaves and the post-weaving processes that were used to preferentially bond the nodes of the woven structures together. Efforts to expand beyond the limitations of the current weaving process through fugitive wire and multilayer bonding techniques and to modify the chemistry and microstructure of the wire (through vapor phase processing) will also be explained.

3.1: 3D Weaving, Design, and Analysis of Woven Product

3.1.1: Design by Topology Optimization

Topology optimization, performed by Dr. James Guest and Dr. Seunghyun Ha, was employed to design two architectures within the confines of the weaving process. The in-plane (warp/fill plane) shear stiffness and permeability were the objective properties of the optimization problem. The 'standard' pattern has all possible wire positions occupied with wires, while the optimized patterns has alternating pairs of warp and fill wires removed in order to open large flow channels within the weave without drastically compromising the shear stiffness of the material. The optimized pattern still retained completely filled top and bottom fill layers in order to provide stability during the weaving process and to aid in maintaining a high shear stiffness. The removal of selective warp and fill wires opens up large flow channels that are oriented 45° to the warp-fill plane. These large channels are predicted to increase the in-plane permeability by 380% while decreasing the in-plane shear stiffness by only 30%. The modeling predictions were confirmed through the manufacturing and testing of samples as described in Chapter 4 and in the literature [50,51]. An image of the two architectural patterns that were utilized in this work are shown in Figure 3.

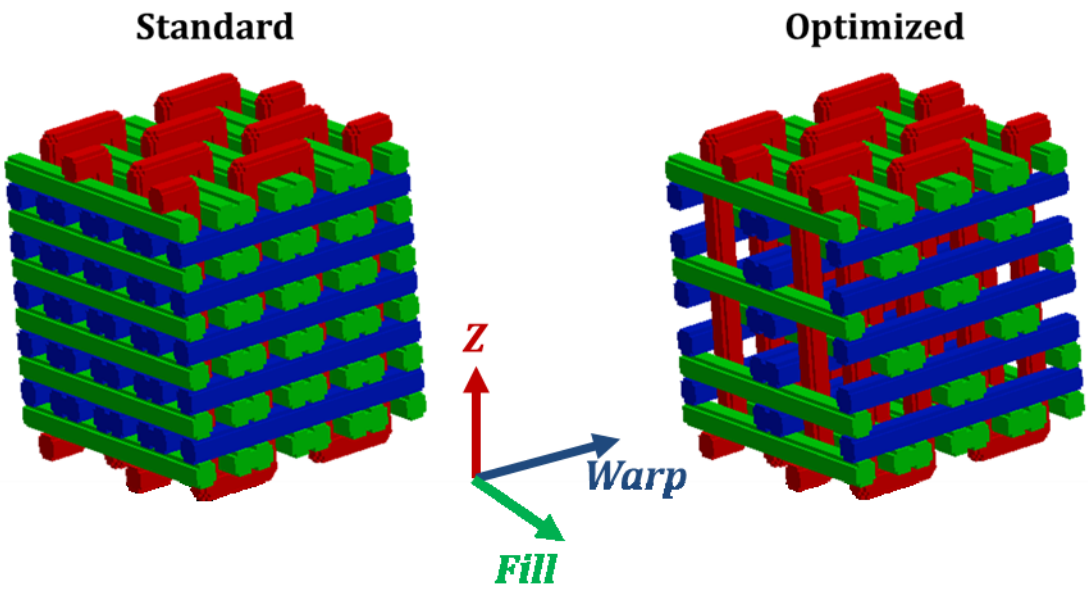

Figure 3: Models of the standard and optimized structures with warp wires illustrated in blue, fill wires in green, and z-wires in red. The standard pattern has wires filling all positions in the 11-layer weave. The optimized pattern has warp and fill wire pairs removed from the middle layers of the weave in order to open large channels in the weave that do not drastically reduce the shear stiffness (the top and bottom fill layers must have wires occupying all positions).

3.1.2: Manufacturing of 3D Weaves

Dr. Keith Sharp at SAERTEX fabricated 15 m of 3D woven material in both the optimized and standard patterns from oxygen free high conductivity (OFHC) copper wire (sourced from Arcor electronics (www.arcorelectronics.com)), and 3 m of Chromel-A (an 80% Ni and 20% Cr alloy) (also from Arcor electronics) wire, all with a nominal diameter of 202 μm (32 guage). This constituted most of the material that was manufactured and studied in this work. Other homogeneous optimized pattern weaves (2 m long) were made with shape memory NiTi wire. Additionally, non-homogeneous

optimized pattern weaves were made with 160 μm OFHC copper wire occupying all of the z-wire positions and the usual 202 μm OFHC copper wires in the warp and fill positions (4 m). A fugitive wire weave was also 3D woven where braze wires (Lucas-Milhaupt 721-VTG alloy wires with a 255 μm diameter) were inserted in all of the middle fill wire positions in the architecture. An example of an optimized pattern OFHC copper weave with 202 μm wires is shown Figure 4. At the writing of this thesis, more weaves were currently being manufactured, so the stated values are lower estimates of the final production amounts at the conclusion of this project.

All of the 3D woven materials employed in this thesis were made at from orthogonally stacked pairs of warp and fill wires. These wires are held together with a single z-wire for every pair of warp wires (e.g. every third warp wire is pulled through the thickness of the weave in order to form a z-wire). During the weaving process, a pair of fill wires are inserted between the warp layers in the weave. After the fill wires are inserted, the 1st reed pushes the fill wires back against the previous layer of z-wires (that originates from the middle of the creel and shed), which serves to bend the z-wires around the previous layer of fill wires. At this point, the harnesses that hold the z-wires in individual rapiers switch positions from top to bottom and bottom to top. At this point the fabric is then moved back in order to accommodate the increase in length and to keep the end of the fabric in the same position in relationship to the weaving machine. An image of the weaving machine is shown in Figure 5.

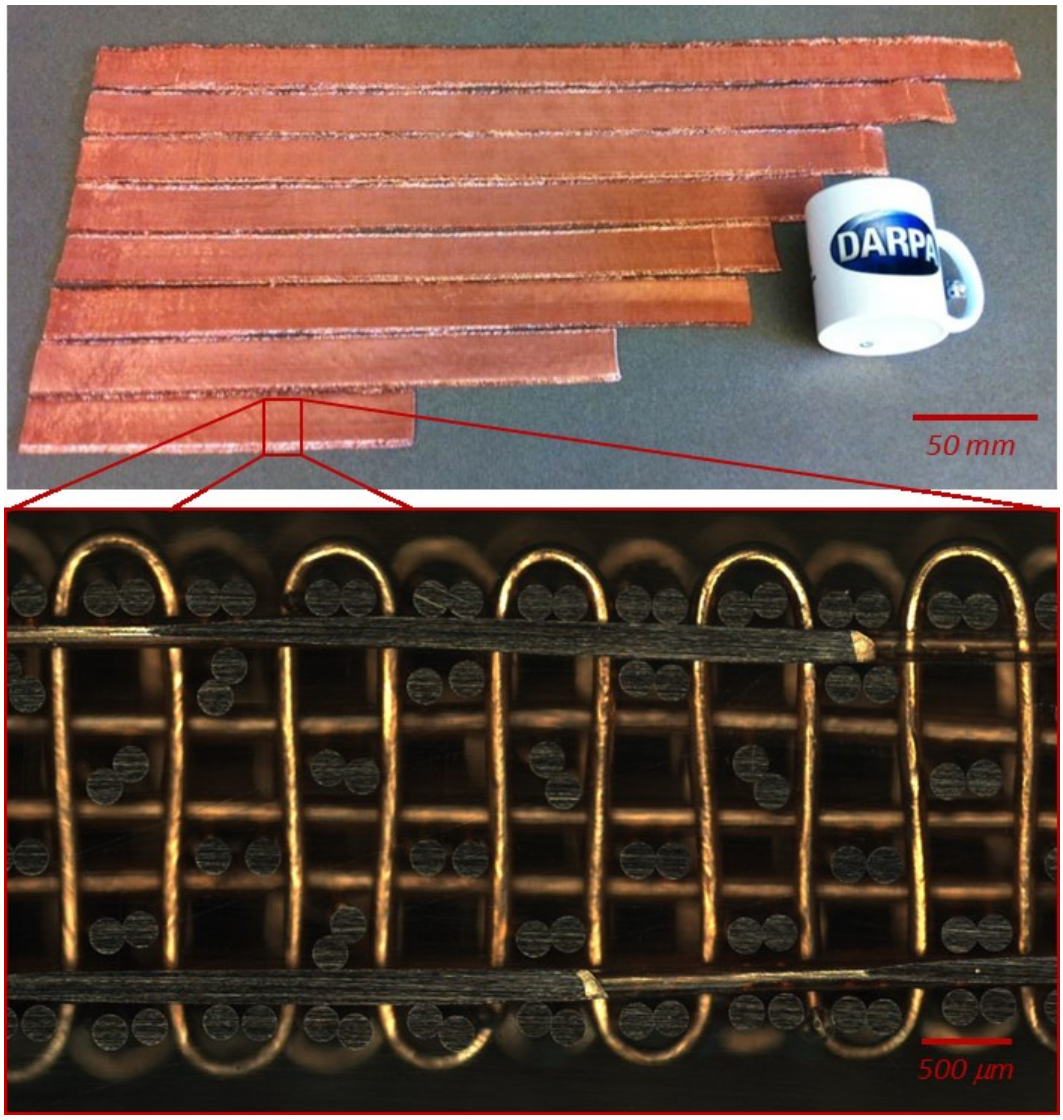

Figure 4: An example of some of the optimized pattern copper weave that was produced by 3TEX. The top image shows 1.2 kg of as-woven material totaling 4.25 m long. The bottom image shows a cross section of the material exposing the warp/z plane. Gaps and twisting of some fill wires can be seen in this cross-section of the material which are some of the differences between the real and modeled materials.

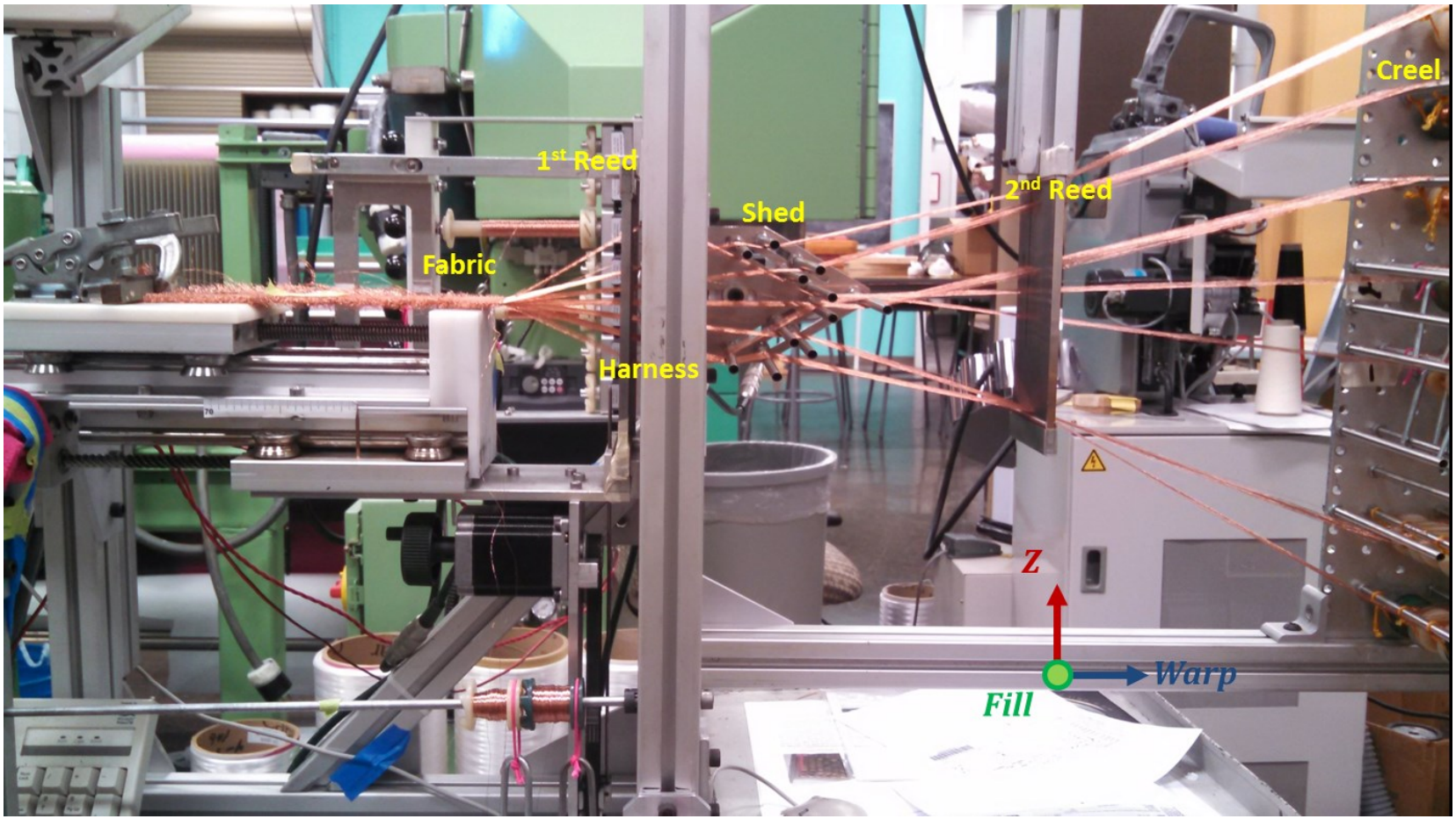

Figure 5: The 3D weaving machine at SAERTEX that is used to making the non-crimp 3D woven metallic lattice materials shown in this work. The already woven optimized pattern copper material (fabric) is shown on the left. The fill is inserted from the spools of copper wire that are seen behind the weaving machine just to the left of the harness. The creel (a portion of which is shown on the right side of the image) is where the rest of the wire for the weave is held and the counterweights which tension the wires.

The final woven product differed from the original modeled design in several ways. The most obvious difference is in the fact that there are gaps between the wires in the weave in all three directions that were not initially specified in the topology optimized designs (shown in Figure 3). Also, the wires in the real material were not perfectly straight and sometimes were observed to twist and bend. Adjustments to the weaving process were successfully performed to control and minimize the twisting and additional spacing in the weaves, but the wire to wire gaps in the weave were never fully removed. In order to examine the spacing in the weave, a series of samples were sectioned from large strips of weaves by cutting with shears. These samples were then mounted in Allied High Tech EpoxySet 2 part epoxy and allowed to cure for 24 hours. An Allied High Tech Powercut 10 abrasive cut-off saw was then used to cut sections that exposed the warp/z and fill/z planes, and removed the areas damaged by cutting with shears. The samples were then polished by hand with wet abrasive papers progressively from 120 – 1200 grit to flatten, remove damage from cutting with the high speed saw, and to polish the wires and epoxy for proper imaging. Images were captured using a Zeiss upright optical microscope and a 5x objective with a 0.63x reducing objective on the imaging camera. The images were then analyzed using Image Pro Plus and measurements of the unintended gaps between the wires were calculated by measuring the distance between the polished wire ends in the weaves. An example of the cross sectional images is shown in Figures 6-7.

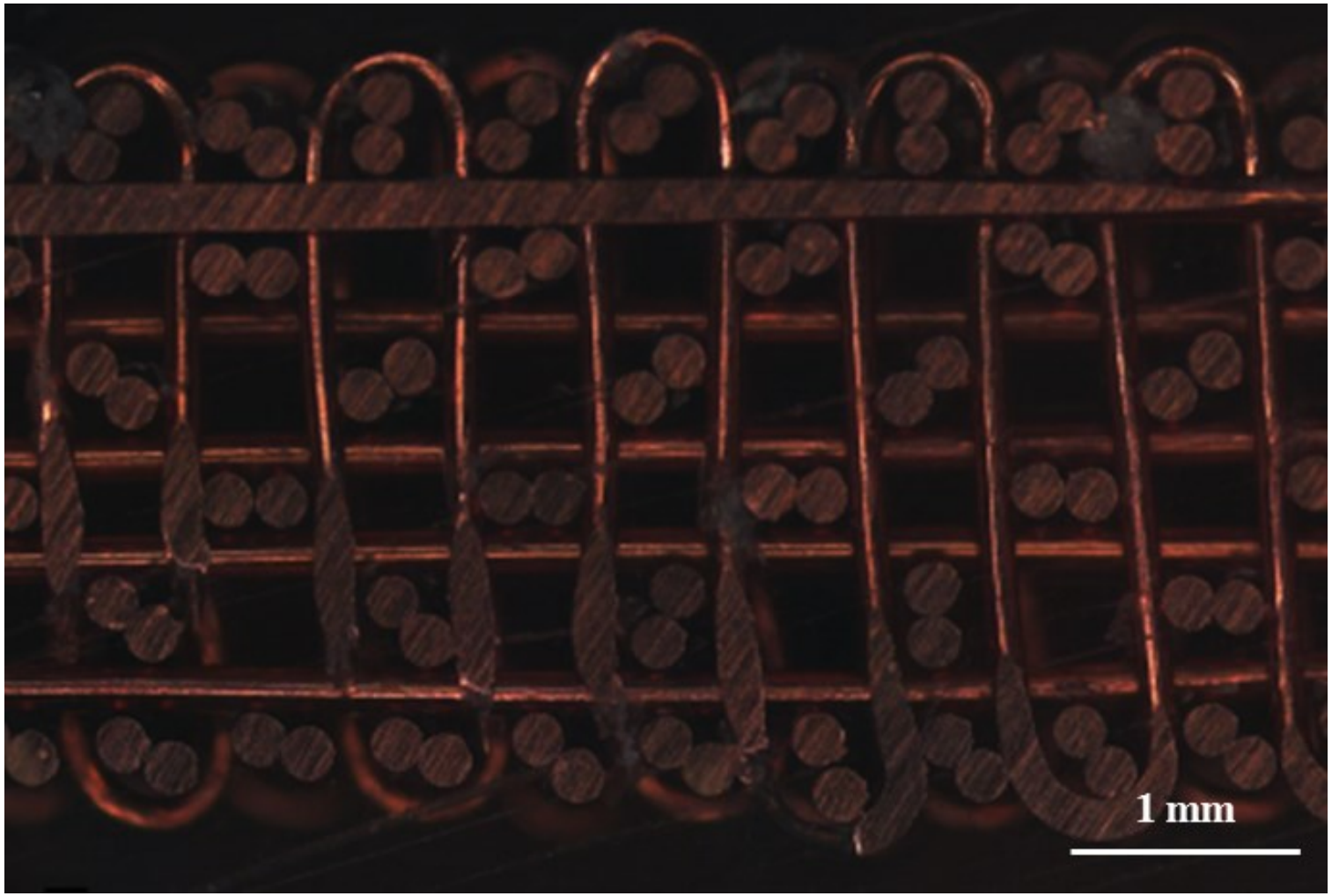

Figure 6: Representative cross-section of the warp/z plane of a copper weave. The sample was mounted in epoxy and polished to expose the weave for optical spacing measurements. This is a composite of ~50 images that were stitched using Microsoft ICE.

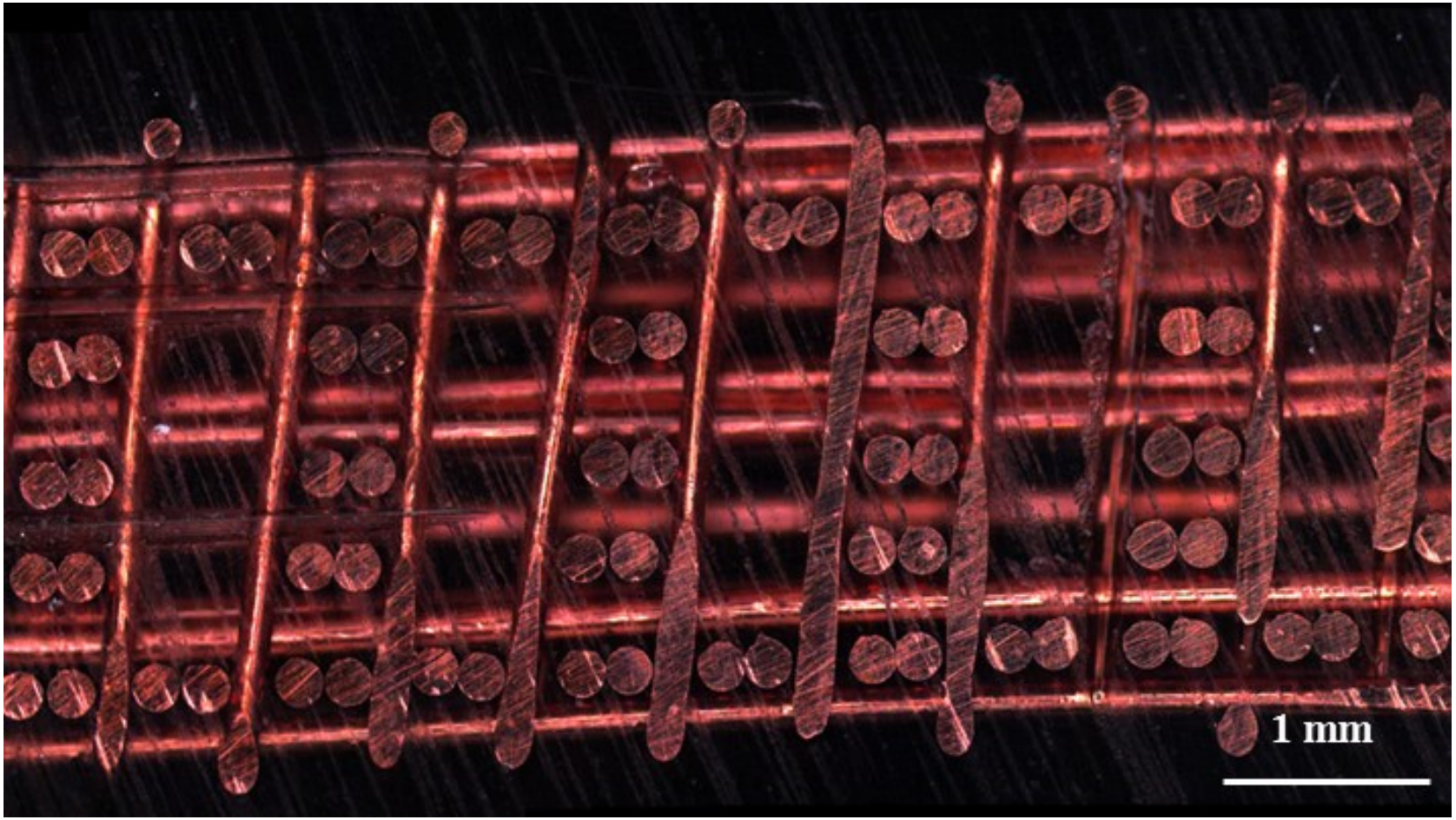

Figure 7: Representative cross-section of the fill/z plane of a copper weave. The sample was mounted in epoxy and polished to expose the weave for optical spacing measurements. This is a composite of ~50 images that were stitched using Microsoft ICE.

Examination of the gap sizes in the different architecture weaves for the different combinations of wires (summarized in Table 1) revealed that the gap size was not uniform throughout the weaves and differed on average from architecture to architecture. Additionally, the fill/z gaps were on average larger than the warp/z gaps. This is a likely the result of spring back (elastic recovery) of the z-wires after they are bent to form the z-loops when the fill layer is pushed against them by the reed. In order to minimize this spacing, we manufactured and characterized some lattice structures with a smaller diameter z-wire (160 μm instead of the usual 202 μm). This wire would exert a lower force on the fill during the elastic recovery (since the stress would decrease with the cross-sectional area of the wire), and would also require less force to bend into the same configuration. The majority of this work, however, was performed with weaves compromised of 202μm wires throughout the architecture. The summary of the unintended wire gap measurements (which includes at least 100 individual measurements for each case) of the copper weaves is shown in Table 1.

Table 1: Summary of the wire gap measurements of the as-woven 3D copper weaves

	Ideal (μm)	Standard Cu (μm)	Optimized Cu (μm)	Optimized Cu (Small-Z) (μm)
Warp-Z	0 ± 0	16 ± 17	10 ± 9	63 ± 15
Warp-Warp	0 ± 0	10 ± 9	21 ± 20	18 ± 16
Fill-Z	0 ± 0	61 ± 41	68 ± 14	32 ± 18
Fill-Fill	0 ± 0	21 ± 34	16 ± 26	40 ± 15
Warp-Fill	0 ± 0	40 ± 40	42 ± 36	77 ± 76

Examination of the gap size measurements confirms the hypothesis that decreasing the diameter of the z-wire makes the z-wire easier to bend into the desired radius, since the fill/z gaps decreased by approximately half of the other two patterns which employed a uniform wire size. We do note, that the warp/z and the warp/fill gaps of this pattern are on average noticeably larger than in previous samples. This is attributed to the fact that the reed spacing (which sets the warp and z-wire positions) was not changed when this pattern was made, so spacing between the warp and z-wires was artificially large (since the reed was set to accommodate z-wires that were 202 μm). Additionally, as a result of the extra space in the weave, there was significant amounts of twisting in the fill wires. These twists can lead to artificially larger average gaps due to their inefficient packing of wires in the weave. Changing the reed spacing to accommodate this change in wire diameter would likely eliminate the issues with twisting and decrease the wire spacing.

Another difference between the modeled weaves and the actual woven material is that there is a non-uniform residual stress in the z-wires. Elastic recovery (spring back) is inhibited when the z-wires are confined by the fill wires after being bent into a z-loop during weaving. After careful examination of the z-wires (the details of which are discussed in section 5.2), it was found that there is a residual stress in the z-wires that is a result of an asymmetry in the weaving process. The residual stress causes a noticeable curvature in the z-wires about the fill direction. This curvature relaxes upon exposure to temperature, which is manifested as a temperature dependence in the damping properties of the weaves. The details of the effect of the relaxation on the damping properties are discussed in Chapter 5, but the reasons for the asymmetry are best addressed here.

In order to understand this asymmetry in the final woven product, we need to examine the geometry of the weaving process in detail. The asymmetry in the final product, that is manifested as a curvature in the z-wires (when they are removed from the weave), is the result of asymmetric positioning of the z-wires during weaving. The points where the wires change direction were measured with the help of Dr. Keith Sharp. The plot of the positions of each wire as it converges to form the fabric are shown in Figure 8. The plot shows the measured wire positions that correspond to the image of the weaving machine in Figure 5. From the plot of the wire positions one can see that z-wires originate from the middle of the creel (the peg board that supports the wire spools). Since we use an odd number of warp wires in our weave, we end up with a different number of warp wires above the center line of the weave, than below. After the z-wires leave the shed, where they are located in the middle, they are separated into the top and bottom harness. The harness is made up of a series of rapiers, which are small eyelets that supports the individual wires. Every other z-wire goes into the rapiers in either the top or the bottom harness. In order for the harnesses to switch, they are not aligned horizontally. We surmise that the combination of the odd number of warp wires (which puts more warp wires above the z as they go through the shed), and the fact that the top and bottom z-wires are not aligned (which is necessary in order for them to switch between top and bottom positions) leads to an asymmetry in the residual stresses that are present in the z-wire after weaving. Additionally, it was found that the positions of the rapiers which support the z-wires were not the same above and below the fabric; in fact, the position of the z-wire in the upper harness is located 2 cm higher above the centerline of the weave than z-wires in the lower harness. A quantitative summary of the relative

vertical positions of the points where each wire changes direction in the weaving machine (corresponding to Figures 5 and 8) is shown in Table 2.

The measurements of the wire pickup positions reveals that the vertical positions of the z-wires in the rapiers of the harnesses are not uniform. These values can be seen in the measurements of the positions of 'Z1' and 'Z2" in the harness. The z-wires are pulled 2 cm higher above the weave than below the weave. This changes the angle of the z-wire in relation to the weave. The difference in harness position correlates to the 'Z2' wire positioned (the upper harness in this case) 32° above the weave and the 'Z1' wire (the lower harness in this case) 23° below the weave. This 9° difference is one possible source of the difference in residual stress between the top and bottom of the z-wire which leads to the global curvature of the z-wire. The curvature is also further explained by the fact that the z-wire harnesses are also horizontally offset from one another which will lead to further asymmetries in the z-wires.

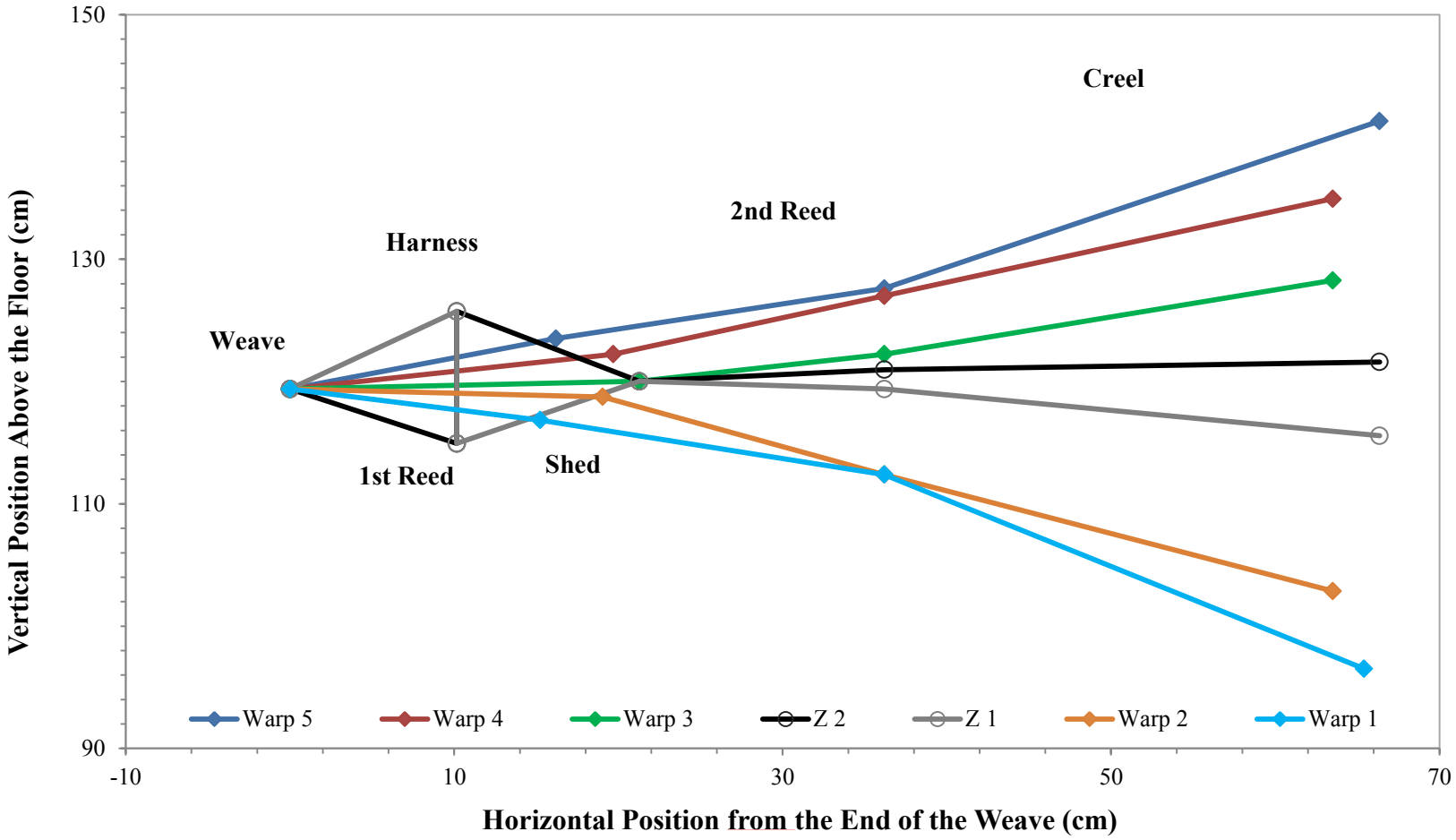

Figure 8: A plot of the positions of the fabric, 1st reed, harness, shed, 2nd reed, and where the copper wires leave the creel. The height was measured in relationship to the floor and the horizontal position was calculated in relationship to the end of the completed weave. Note that the position of the z-wires (Z1 and Z2) switch in the harness. This diagram shows the Z1 wire in the upper position and the Z2 wire in the lower position.

Table 2: Summary of the positions of all of the wires in the weaving machine

	Distance Above Fabric (cm)				
Wire	**Fabric**	**Harness**	**Shed**	**2nd Reed**	**Creel**
Warp 5	0.0	-	4.1	8.2	21.9
Warp 4	0.0	-	2.9	7.6	15.6
Warp 3	0.0	-	0.6	2.9	8.9
Z 2	0.0	6.4	-	1.6	2.2
Z 1	0.0	-4.4	-	0.0	-3.8
Warp 2	0.0	-	-0.6	-7.0	-16.5
Warp 1	0.0	-	-2.5	-7.0	-22.9

In summary, these measurements reveal that there are differences that are seen in the weaves from the ideally designed architectures. One major difference is the unintended wire twists and gaps between wires. The magnitudes of the gaps are relatively small and on average vary from 10 – 70 μm, which is significantly smaller than the diameter of the smallest wires used in these weaves (160 μm). Additionally, it was found, and will be discussed in further detail in later chapters, that the z-wires store elastic energy when they are bent and held between columns of fill wires. Examination of the process that is used to produce these materials reveals that the z-wires are neither horizontally aligned, which is necessary for the z-wires to switch positions, nor are they positioned symmetrically above and below the weave. This, when combined an odd number of warp layers, is believed to generate an asymmetric curvature in the z-wires. The details and measurements of the curvature and its effects on the damping properties of the weave are the subject of Chapter 5.

Despite these unintended differences between the modeled architectures and the real materials, these differences are, on a whole, rather small and it does not detract from the fact that this 3D weaving technique can be used in order to make metallic materials with a well-defined microarchitecture. That being said, these differences from the ideal designed architecture (primarily the small spacing between the wires) are especially important when attempting to selectively bond the woven materials, which directly affects the mechanical properties of the weaves. The increased spacing between wires increases the difficulty of successfully bonding the wires together without filling in the larger channels in the weaves, which would negatively affect the permeability. Therefore, control of the spacing in the weave is important for selective bonding. A discussion of how bonding of the weaves was performed is discussed in the next section in addition to the role of these unintended gaps in the weave on that process.

3.2: Brazing

One of the primary considerations for multifunctional materials are their mechanical properties. The in-plane (warp/fill plane) shear stiffness of this material was optimized assuming that all of the nodes between wires were fully bonded. Without bonding, the in-plane shear stiffness of these materials is orders of magnitude lower than their bonded counterpart. The shear stiffness of the as-woven materials is on the order of 10 of MPa, while the brazed materials possess a shear stiffness of 2-6 GPa depending on

the architecture. The specific details of the mechanical properties of the weaves will be discussed in the following chapters (Chapter 4 will discuss the quasi-static in-plane shear stiffness and Chapter 5 will discuss the dynamic mechanical properties). The concentration of section 3.2 will be to discuss the various bonding processes that have been used in this work to improve the mechanical properties and to expand the possible geometries and applications of 3D woven metallic lattice materials through multilayer and fugitive wire bonding techniques.

3.2.1: Brazing of Single Layers Weaves

In order to preferentially bond the woven materials together, brazing was selected as a result of initial successful soldering studies that were performed with these materials by Dr. Yong Zhang [51]. Solder, has limitations that were undesirable in the final microlattice material such as, low stiffness and strength, low service temperature, and higher density (which negatively affects the specific properties of a material). As a result of these limitations, I elected to use a silver-copper eutectic braze in order to preferentially bond the material. Braze and solder are by definition metals that melt at a lower temperature than the material being bonded, however, a braze has a melting temperature of at least 450°C [52], which allows for a much higher use temperature for the final product, and the strength of brazed materials are usually higher than that of solders.

In this work the selective bonding of the wire contacts was performed by brazing with a silver-copper eutectic alloy braze from Lucas-Milhaupt (alloy 721-VTG). This alloy was chosen among a large number of available brazing alloys for a number of reasons. First, this alloy has one of the highest melting temperatures (T_m = 780°C) that could be reasonably processed with the OFHC copper base metal (T_m = 1050°C). Second, this alloy has excellent wettability of clean (not oxidized) copper surfaces, and it alloys with the copper wire easily providing a solid bond between the wires. Third, since the alloy used is a copper eutectic alloy, as brazing occurs and it alloys with the base metal, the melting temperature of the brazed junction increases. This allows the same alloy to be used for a secondary brazing processing without reflowing braze from the initial bonding step. Fourth, the thermal conductivity of this alloy (371 W/mK) is almost as high as the copper wire (398 W/mK) that forms the woven materials. Finally, the yield and tensile strength (272/372 MPa respectively) and elastic modulus (83 GPa) of the braze are relatively high compared to many solders [53].

Surface oxidation must be removed from the surface of the wire in order to properly braze the materials together. If the surface oxide is not removed, it is energetically unfavorable for the liquid braze to wet the surface of the oxidized wire and form a new interface. Instead, if the oxide is not removed, it is energetically more favorable for braze to minimize its surface area and to form a spherical ball on the surface of the weave. Two common methods to remove surface oxidation from OFHC Cu wire are through the use of a vacuum or reducing environment. A vacuum environment could be used to reduce the Cu wire, but the Ag in the brazing alloy has a tendency to evaporate due to its high vapor pressure when exposed to high temperatures in a vacuum

environment. The option I employed was to use a reducing environment, a 95% nitrogen / 5% hydrogen (forming gas) environment, to reduce the wire and brazing materials. This technique works quickly at the elevated temperatures we are using, and is highly conformal. Proper wetting of the surface is important for brazing, because it allows braze to not only wet the surface of the wire, but it also allows for capillary action to draw molten braze preferentially to the areas with the greatest capillarity, which in the case of the weaves are the tangential junctions between the wires.

Samples were brazed by placing foils of the 50μm thick brazing alloy above and below sections of 3D woven copper material. The brazing alloy and the weave were both cut with shears. Cutting the weave with shears leaves a small crimped region around the cut junction. This region was found to be on the order of ~3 mm. As a result, the samples were cut oversized in order to be able to remove the damaged region after brazing. The sample and foils were supported on an alumina substrate. Alumina was chosen as the substrate material, because it is able to support the weave during brazing without issues of contamination. Additionally, the alumina is not negatively affected by the temperature or hydrogen environment. Finally, since alumina is an oxide that is not reduced by hydrogen, braze will not wet the surface of the substrate, so it will not take braze away from the weave during processing. An image of a Cu weave sample prepared for brazing is shown in Figure 9.

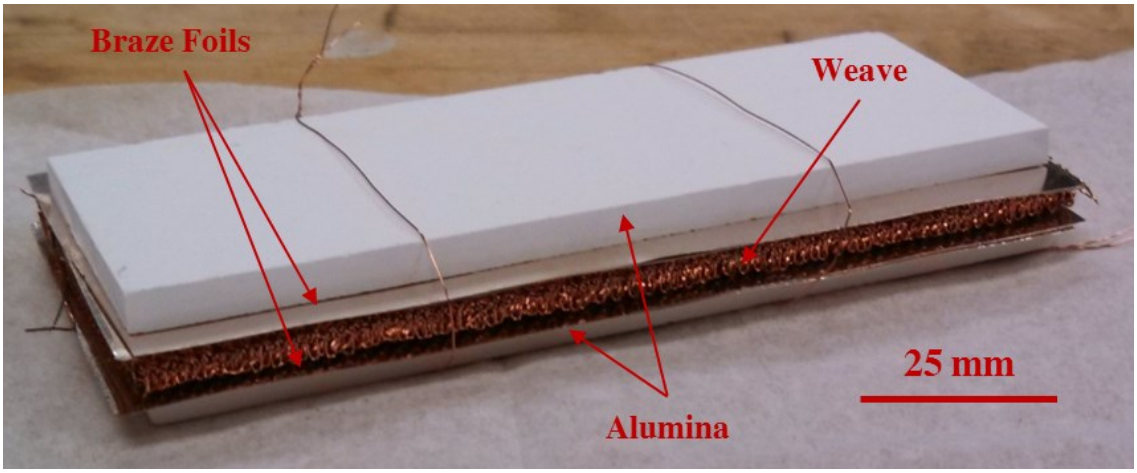

Figure 9: A 3D woven copper section before furnace brazing. The section of weave is sandwiched between 45μm thick foils of Lucas-Milhaupt 721-VTG braze and alumina plates. The whole sample is wrapped in nickel-chromium wire since the braze will not wet the surface of that material.

Samples were placed inside a quartz tube that was evacuated to $1x10^{-3}$ Torr with a roughing pump and backfilled with forming gas to 1 psig at least three times to ensure adequate purity of the environment. Once the tube was backfilled the last time, the tube was placed inside a Lindberg Blue tube furnace that was preheated to 900°C. This temperature was chosen to ensure that there was adequate fluidity of the braze so that it could penetrate the interior of the weaves. Once the sample temperature reached 900°C (8-12 minutes depending on the mass of the sample), the sample temperature was then held at that temperature for 5 minutes in order to ensure that the sample had sufficient time to reach thermal equilibrium, which is necessary for uniform penetration of braze into the woven lattice. The furnace was then rolled off the quartz tube and the sample cooled through natural convection to room temperature in 10-15 minutes, before the sample was returned to a room environment and the sample was removed from the quartz tube.

In order to maintain the appropriate environment for brazing, and to achieve rapid heating and cooling of the samples, I designed and constructed a custom made rapid heating and cooling furnace. It used to perform the majority of the brazing in this work. An image of the custom furnace is shown in Figure 10. The design of this furnace is based off a similar type of furnace at the Army Research Lab (ARL) at Aberdeen Proving Grounds that was initially used in this work. Dr. Kristopher Darling and Anthony Roberts helped me in the initial designs of this furnace.

This furnace system is unique in that it allows the user to independently set the environment in the quartz sample tube and vary the temperature of the furnace. The furnace is a Lindberg Blue tube furnace that is controlled with a custom made Eurotherm Nanodac PID controller and data logger. The furnace and the controller can be found on the left side of Figure 10. On the right side of the figure the quartz tube, that supports the sample during processing, and the environmental systems and controls can be seen. The quartz tube is connected into the rest of the system by a viton o-ring sealed compression fitting. The environment used for brazing in this furnace is the 95% N_2/5% H_2 forming gas, however, a wide variety of atmospheres including inert,

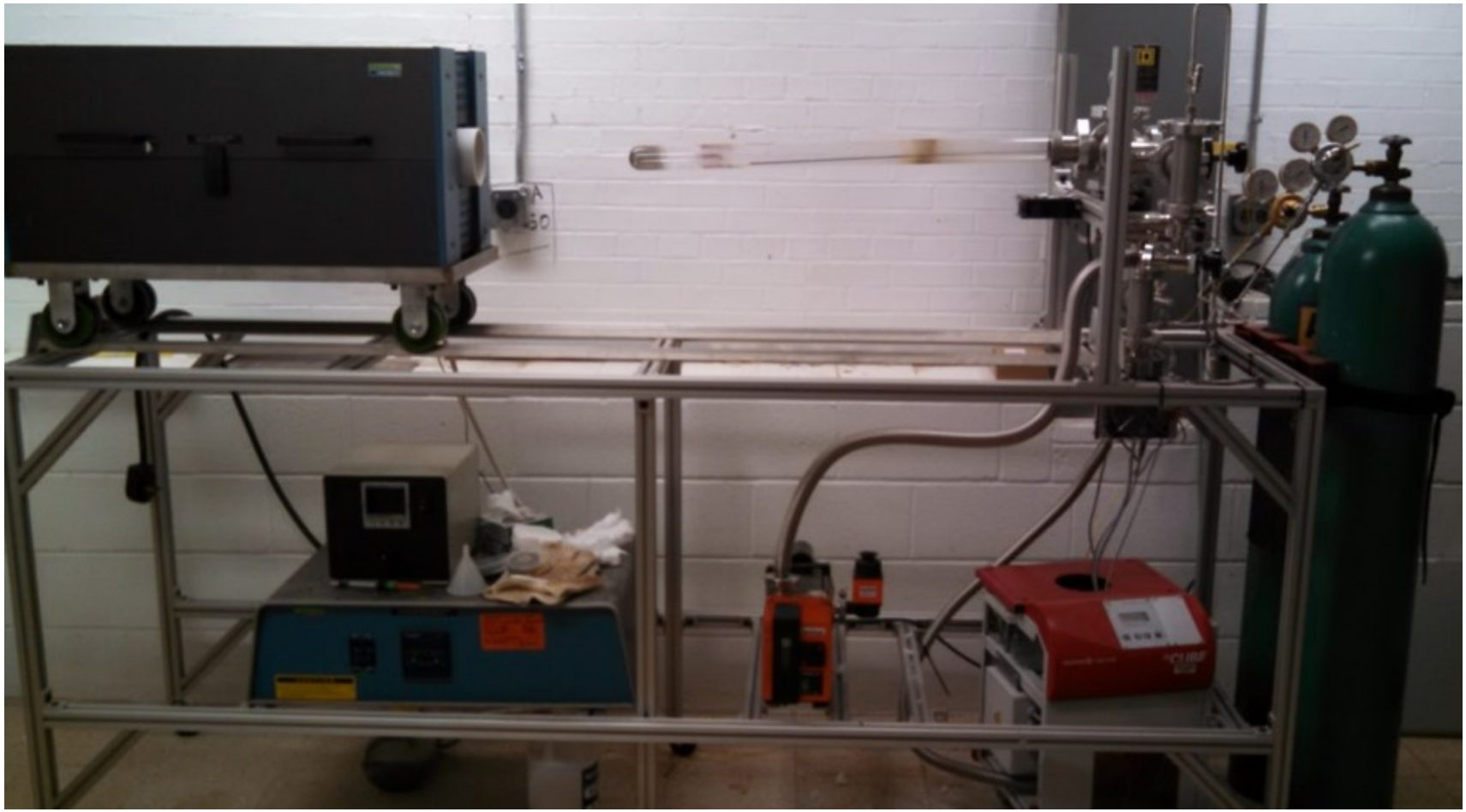

Figure 10: An image of custom built furnace that was used for the majority of the brazing work for this project. The tube furnace shown in the upper left portion of the image is mounted on a sliding frame which allows it to slide over top of the environmentally controlled 4 foot long quartz tube that is shown in the upper right of the image. This allows for rapid heating and cooling of samples inside the quartz tube without having to wait for the large tube furnace to heat up and cool down.

such as nitrogen or argon, or high vacuum with the use of the attached Pfieffer HighCube 80 diaphragm backed turbo molecular pump can be used. The high vacuum side of the system is separated by a series of high vacuum rated diaphragm valves which serve to maintain a clean environment for high vacuum heat treatments and to minimize the pumping path length for the turbo molecular pump. The high vacuum side of the system has been shown to be capable of vacuum levels of $1x10^{-6}$ Torr. Once the sample was mounted in the quartz tube and the appropriate atmosphere was obtained, the preheated furnace was then moved over top of the quartz tube by rolling the v-groove wheels that are attached to the furnace on the complimentary v-shaped tracks that are supported by the frame. These rails provide consistent alignment of the furnace over the tube. All as-woven materials were initially cut oversized, using either wire electrical discharge machining (EDM) or sheet metal shears, in order to allow for the removal of damaged areas on the outer edges of the samples, which are the result of handling during the brazing process.

After brazing, the samples were then cut to their final dimensions using wire EDM and all cut faces were then hand polished to 1200 grit to remove the recast layer. The brazing of woven materials is a function of many factors which include but are not limited to: the atmosphere in which the brazing process takes place, the maximum brazing temperature, the profile of the temperature cycle, the amount of braze used, the brazing alloy, and the wire material that is being brazed. These are some of the parameters that are not only important, but they are parameters that we also have the ability to control when brazing these lattice materials.

The brazing process as described above assumes that the base metal wires are free of oxide. Surface oxide would inhibit the wetting of the surface by the liquid braze. The two primary methods employed to braze materials that have a surface oxide are to either reduce the oxide from the surface or to use a brazing material that actively reduces the surface oxide. For the copper weaves we chose to remove the surface oxide during brazing with a reducing atmosphere, as discussed previously. Due to the small pores and nodes in the material, it would have been prohibitive to use a chemical flux because removal of the flux after brazing would have been difficult. Also, due to the complex bond geometry, flux may have been trapped in the joints after brazing leading to reduced bond strength. Instead, a reducing atmosphere composed of 5% hydrogen / 95 % nitrogen was used to strip the weakly bound oxide from the surface of the copper. Since high purity OFHC copper was used in these experiments, the hydrogen environment should not embrittle the copper wires [54,55]. It is important to note that this method does not work for the woven NiCr structures, due to the stable gas tight Cr_2O_3 layer on the surface of the Chromel-A wires that is not reduced by hydrogen [56,57]. The lack of oxide removal does not allow braze to wet the wires in the weaves, and instead, the braze balls up on the surface in order to minimize its surface to volume ratio. A ball of braze is seen on the surface of a NiCr weave in Figure 11.

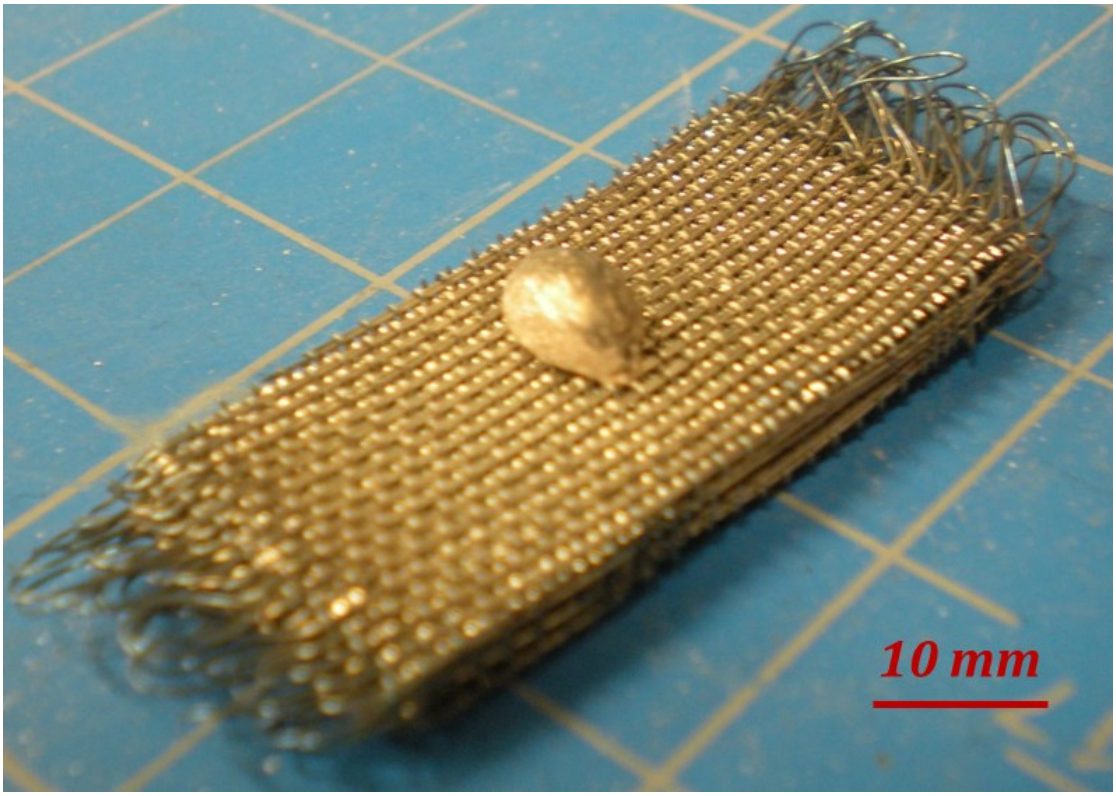

Figure 11: Optimized architecture NiCr sample that was brazed with the silver-copper eutectic alloy at 900°C for 5 minutes in a 95%N_2/5% H_2 atmosphere. The atmosphere was unable to strip the Cr_2O_3 from the surface of the wire and that oxide prevented braze from wetting the wire. Instead, the wire balled up on the surface of the weave in order to minimize its surface area to volume ratio.

The maximum brazing temperature is another important parameter for our processing since temperature can be used to directly control the viscosity of the braze and the interdiffusion of the different species. An example of two woven samples that were brazed at too low and too high of a temperature are shown in Figure 12.

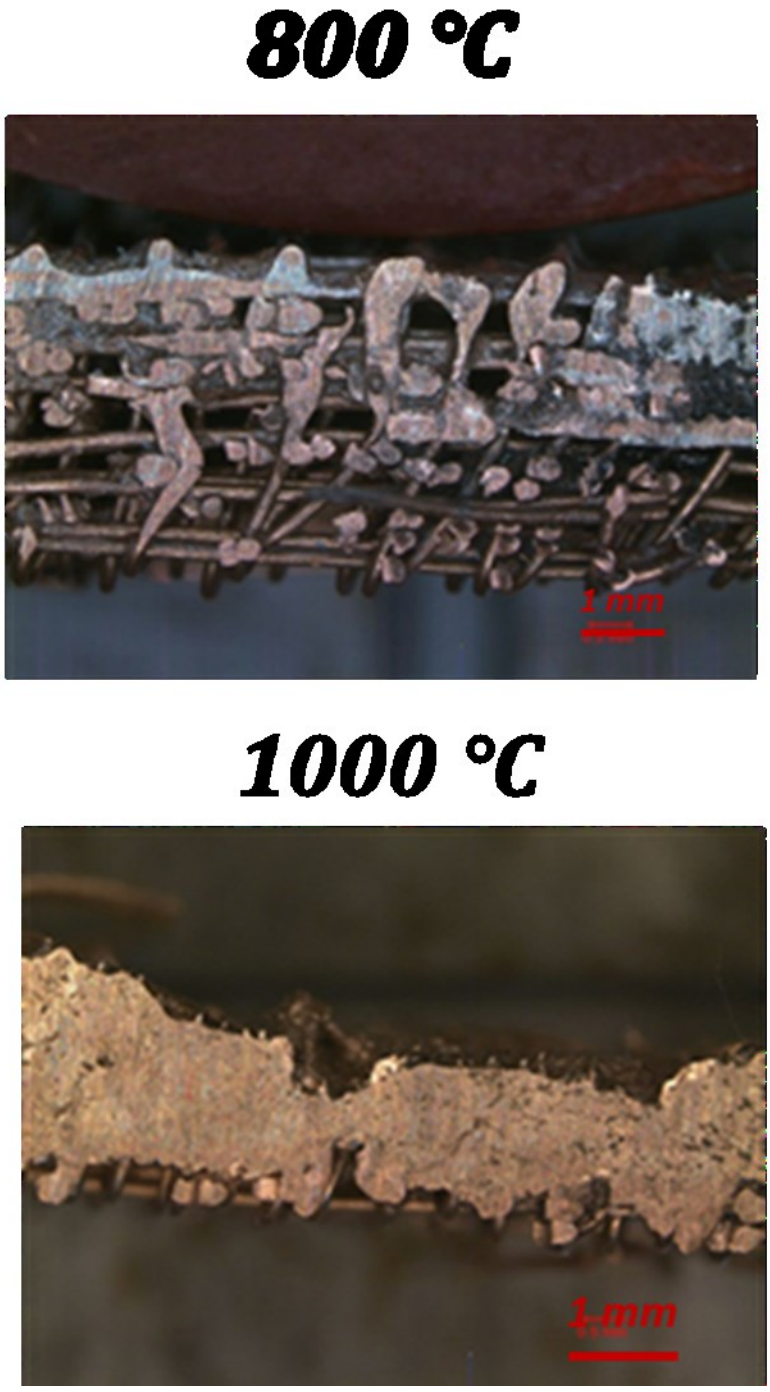

Figure 12: Two examples of optimized architecture copper weaves that were brazed at the wrong temperature with a silver-copper eutectic braze. The fill/z plane is shown in each example. In the sample that was brazed at 800°C the viscosity of the brazing material was too high and it failed to adequately penetrate the weave. In the sample that was brazed at 1000°C braze penetrated the weave, but diffusion of braze into the wires decreased the melting temperature of the weave leading to melting of the wires in the structure. Both of these samples were held at their processing temperatures for 5 minutes.

As the temperature increases above the melting temperature, the viscosity of the braze drops. When the braze is viscous, surface tension forces prevent the penetration of the braze into the structure. In Figure 12, the 800°C temperature was too low and the viscosity of the braze was too high. As a result we see inadequate penetration of the braze into the weave. If the viscosity of the braze is lowered by going to higher temperatures, the capillary forces will dominate over the surface tension forces allowing braze to wick into the nodes of the structure. In the figure at the right, the temperature was too high. Although there is good penetration of the braze into the weave, the alloying of the braze with the wire results in localized melting of the weave. The brazing temperature is a directly related to the brazing alloy that is used since each alloy has a specific melting temperature and temperature dependent viscosity. In order for us to maintain a high service temperature in our final brazed lattice, we choose a brazing alloy with as high of a melting temperature as possible. This high melting temperature, however, is at odds with the fact that the brazing alloy must melt at a temperature that is sufficiently low enough such that we can heat the liquid above its melting temperature (decreasing the viscosity) to obtain adequate penetrate into the weave without melting the base metal. It is important to note that, even though the wires in our structure are solid during brazing, braze will also diffuse into the wire and locally modify the composition. This change in composition can modify the local melting temperature of the material. An example of the diffusion of the Ag from the braze into the solid wires that make up the weave can be seen in Figure 13.

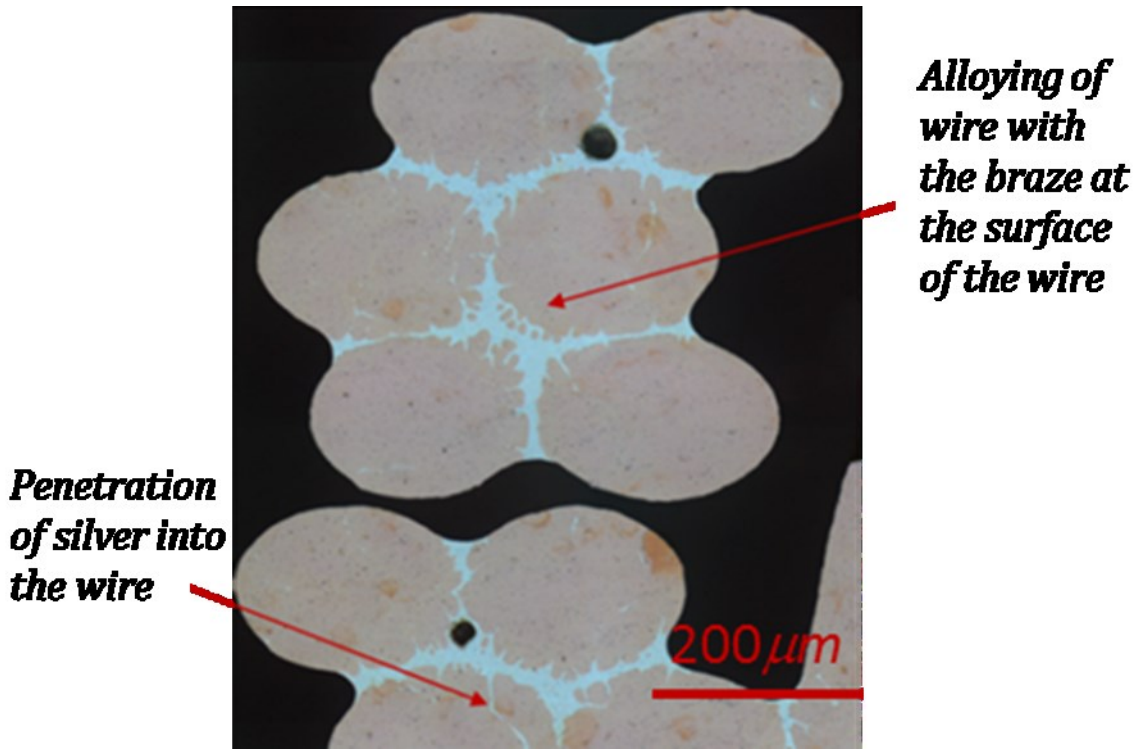

Figure 13: A polished cross section at 45° to the warp direction (in-plane) of the optimized pattern weave in copper after brazing at 900°C for 5 minutes with a silver-copper eutectic braze. Image courtesy of Dr. Dick Fonda and Dr. Amanda Levinson (NRL).

From the polished cross section of the weave, diffusion of silver into the surface of the copper wire and within the bulk of the wire can be observed. The cumulative amount of time that the material spends at elevated temperatures (either in a single or multiple brazing cycles) is important since it affects the amount of Ag that diffuses into the Cu wire. This process can be described by Fick's second law, which for one dimension can be written as [58],

$$\frac{\partial C}{\partial t} = D\frac{\partial^2 C}{\partial x^2} \tag{5}$$

where C is the concentration as a function of the distance x, t is time, and D is the diffusivity of the species. This equation can be integrated with time to estimate the concentration of the diffusing species at a distance, x, and at time, t [58].

$$n(x,t) = n_0 erf\left(\frac{x}{2\sqrt{Dt}}\right) \tag{6}$$

where, n is the concentration of the diffusing species at a distance x from the initial interface and time t and n_o is the initial concentration of the diffusing species.

The denominator of the error function ($2\sqrt{Dt}$), is known as the diffusion length and it indicates how far the diffusing species has diffused with time. The diffusivity, D, is a function of the materials, the diffusion mechanism (bulk, grain boundary, surface, etc.), and the temperature and it usually increases with temperature. In order to minimize the diffusion length, we must either minimize the temperature or the time. In order to achieve the proper viscosity with this alloy, we cannot change the temperature, so therefore we must minimize the time for brazing in order to minimize the diffusion length.

Although there does appear to be diffusion at the surface of the wire, there is also diffusion into the bulk of the wire which appears to be along grain boundaries. The diffusion of silver into OFHC Cu has been studied extensively and is well published in the literature. The diffusivity of Ag at 900°C within a grain of pure Cu has been shown

to be 9.5×10^{-10} cm^3/s as measured from single crystal experiments with a Ag radioisotope tracer and 6.6×10^{-11} cm^3/s at 780°C [59–61]. The diffusivity of the Ag along a grain boundary in pure Cu at 900°C has been shown to be 4.5×10^{-4} cm^3/s as measured with a Ag radioisotope as well and 5.4×10^{-5} cm^3/s at 780°C assuming a grain boundary width of 7.6×10^{-8} cm [59,62,63]. These values of the diffusivity were used to calculate the diffusion length of Ag into Cu for both bulk and grain boundary (GB) diffusion at 780°C (the melting temperature of the braze) and 900°C (the brazing temperature for our process) for a range of times up to 10,000 s (2.8 hours) and the results are shown in Figure 14.

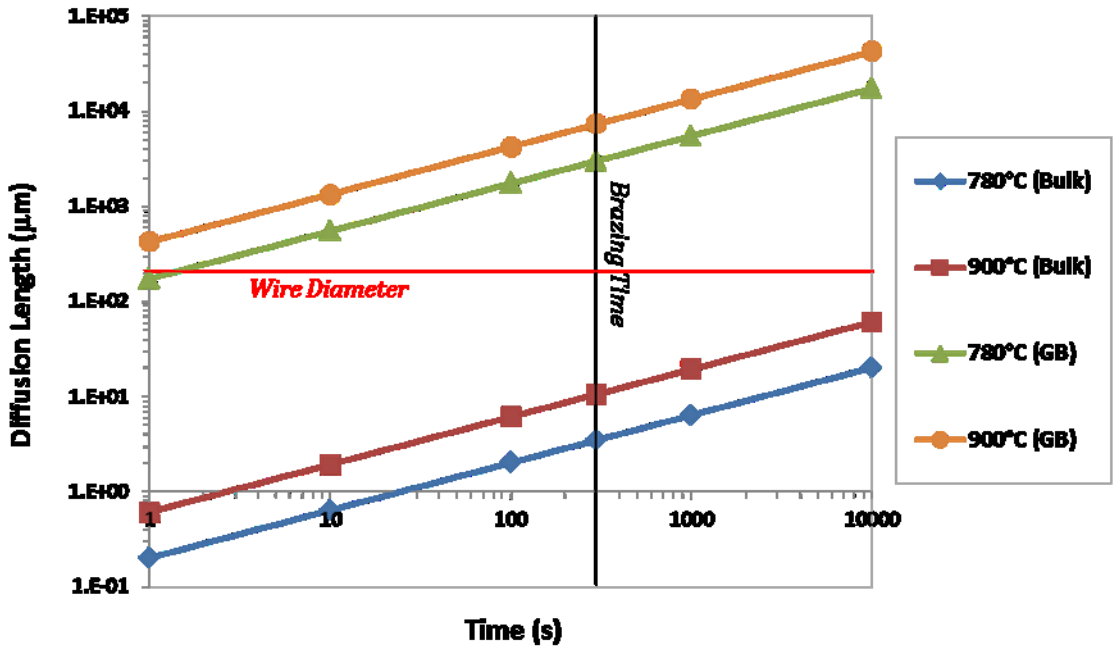

Figure 14: A plot of the calculated diffusion length of Ag diffusion into Cu at both 780°C and 900°C for bulk and grain boundary (GB) diffusion. Lines indicating the wire diameter and the brazing time used in the actual processing cycle used in this study are shown on the plot as reference lines for the reader.

The calculation of the diffusion length performed at the melting temperature of the braze and at the usual brazing temperature provides an upper and lower bound for the diffusion across the range of temperatures that the braze is liquid during the brazing process. From the calculation of the diffusion length for the two cases, it becomes obvious that the Ag in the braze will quickly penetrate the interior of the wire along grain boundaries and we are not able to braze the material quickly enough to prevent this diffusion mechanism. Our 5 minute processing time, however, appears to be fast enough to limit diffusion of the silver into the bulk of the wire. In order to minimize the size of the diffusion zone, the lattice should only remain at temperature long enough for a uniform temperature to be reached and for braze to wick into the weave (which happens on the order of seconds). Therefore, in order to minimize the diffusion of Ag into the Cu wires and to minimize the heating and cooling times (in order to process more samples), our custom high heating and cooling rate furnace was used for brazing (Figure 10).

A silver-copper eutectic (72% Ag /28% Cu by mass) braze was chosen, in order to maintain high thermal and electrical conductivity, high strength, as well as to penetrate and properly bond the weave. In addition to these reasons for choosing this brazing alloy, as the braze alloys with the wire (as is shown in Figure 15), the local composition of the brazed junction becomes more rich with Cu (as Ag diffuses into the wire) and the melting temperature of the brazed region increases. Therefore, the brazed junction always possess a higher melting temperature than the brazing alloy and a lower melting temperature than the pure wire. Unfortunately, this also means that the melting temperature of the alloyed region of the wire is suppressed with the addition of braze, although the melting temperature of the alloyed region of the wire is always higher than

the brazed junction. This alloying and melting temperature suppression of the wires can be seen in the samples processed at 1000°C for 5 minutes (Figure 12) where the wires melted during processing at 1000°C as a result of wire composition change. The silver-copper phase diagram [64] is shown in Figure 15 with arrows indicating how the composition of the wire and the brazing alloy changes during brazing.

When needed, this local alloying process also allows us to use the same brazing alloy to attach face sheets to the exterior of the weave during a second brazing process. Since the melting temperature of the bonds within the material increases after the first brazing process, due to alloying with the wire, we can heat the material to the melting temperature of the pure braze without reflowing the braze that is already in the structure. At this temperature, we can attach a face sheet to the surface of the material without reflowing the initial braze that was used to bond the wires together. The attachment of a face sheet does not require great fluidity of the braze since the braze does not need to wick into the weave, but instead it only needs to bond the junction where the braze is located at the start of the processing.

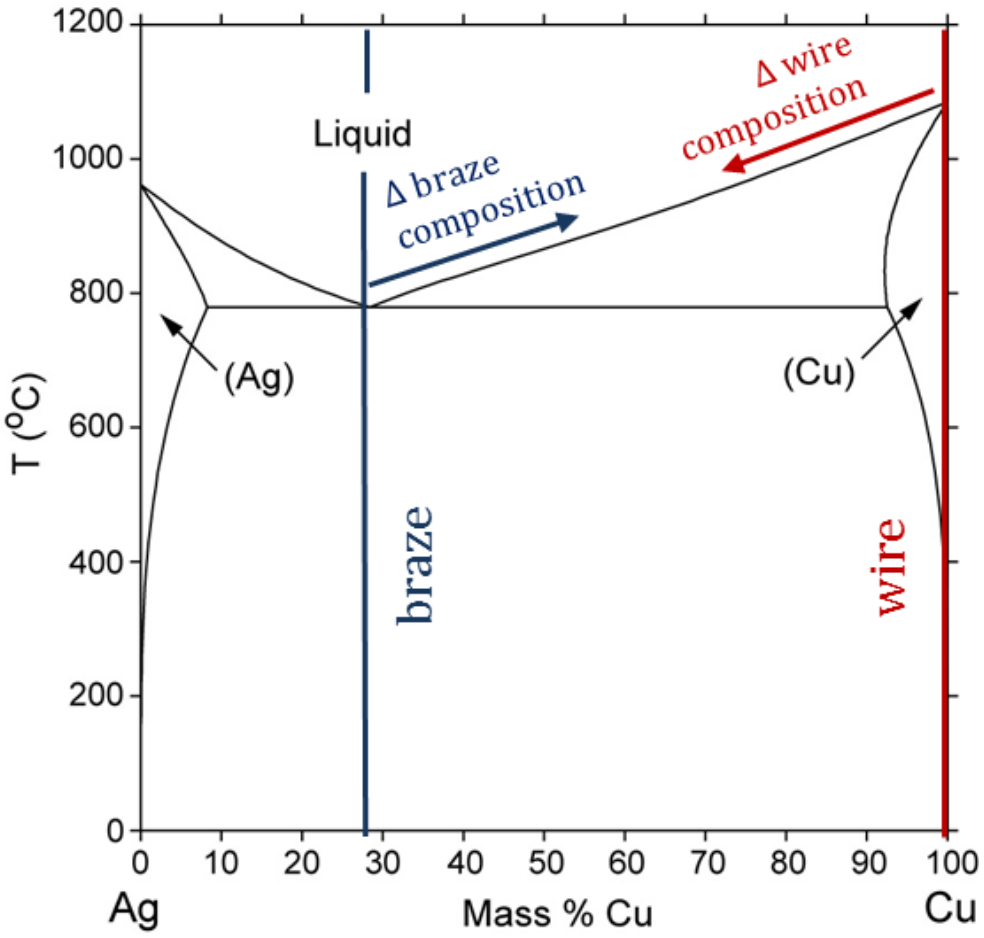

Figure 15: Binary silver-copper eutectic phase diagram showing the composition of the copper wire and the brazing alloy in our system. The red and blue arrows indicate how the local composition of the wire and brazed bond changes respectively. Note how the local composition change lowers the melting temperature of the wire and raises the melting temperature of the liquid braze [64].

In this study the amount of braze was varied in order to determine the optimal amount of brazing material. If too little braze is used, there will be an insufficient amount of brazing material present in order to bond all of the tangential wire contacts together, which will negatively affect the shear stiffness of the material. If too much braze is used, it will start to fill in the larger pores within the material's architecture, which will negatively affect the permeability of the material. The amount of braze was therefore varied in a series of samples for each of the woven architectures. As a result of

the different densities of the architectures, the amount of braze is denoted in this study as the mass gain of the weave as a result of brazing. The number of tangential wire pairs in the material increased from the optimized to the standard architecture, and a normalized way of describing the amount of braze that was added to the structure was employed to account for the change in density. The mass gain during brazing is defined as,

$$MG = \frac{M_b}{M_w} \times 100 \tag{7}$$

where, MG is the percent mass gain of the weave as a result of brazing, M_b is the dry mass of the brazing material used in that sample, and M_w is the dry mass of the 3D woven copper weave.

In order to evaluate the role of capillary forces in the weaves, a study was performed to evaluate the distance over which the liquid braze can travel. The brazing material used was a 50μm thick foil that was cut to the same dimensions as the specific woven sample. Initially equal amounts of foil were placed above and below the samples to limit the distance that brazing material had to propagate into the woven material, however, in the course of this work it became clear that the braze has the ability to wick over relatively large distances (up to 25 mm has been observed) and against gravity in this material due to the high capillary forces. In order to quantify the effects of capillarity during this process, an optimized architecture woven sample was prepared and braze was distributed non-uniformly across the sample. A 50 mm long sample was cut and placed on an alumina substrate and a single foil of braze was prepared to the same dimensions as

the woven sample. The braze material was then folded in half and placed on one side of the weave on the top surface as shown in Figure 16.

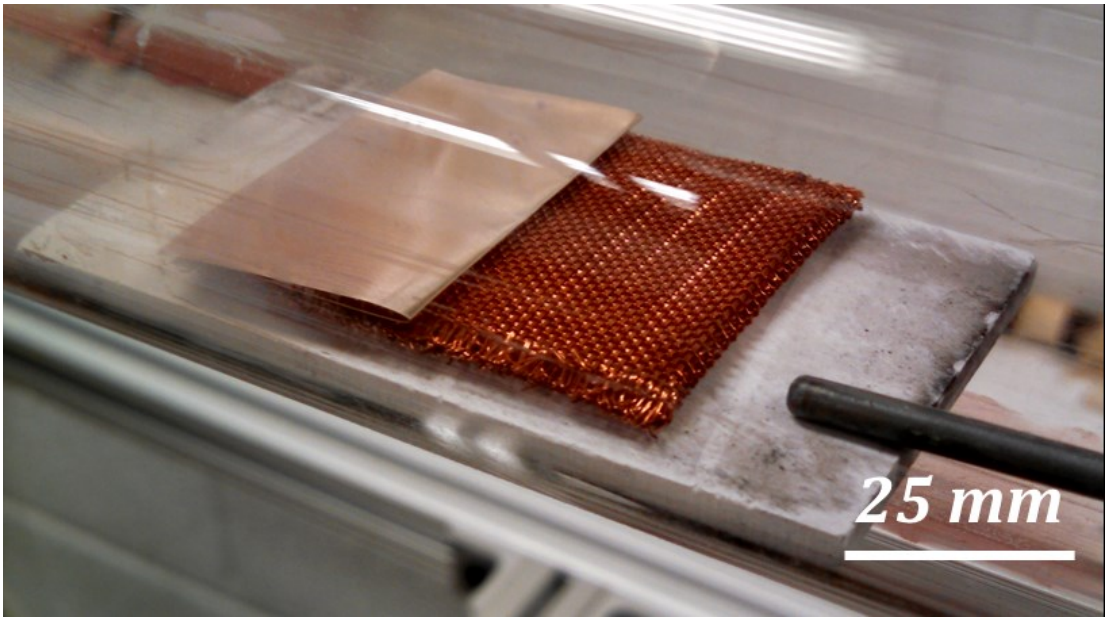

Figure 16: As-woven 'modified' pattern copper weave supported on an alumina substrate inside a quartz tube. The foil on top is alloy 721-VTG brazing alloy that was cut to the same size as the woven sample before being folded in half and placed on top of the sample and aligned to the left edge.

The sample was then brazed in a forming gas atmosphere at 900°C for 5 minutes similar to the way that other copper weaves were brazed. After bonding, the sample was then cut using wire-EDM and hand polished to a 1200 grit finish using successively finer polishing papers. The polished cross section of the resulting lattice material is shown in Figure 17.

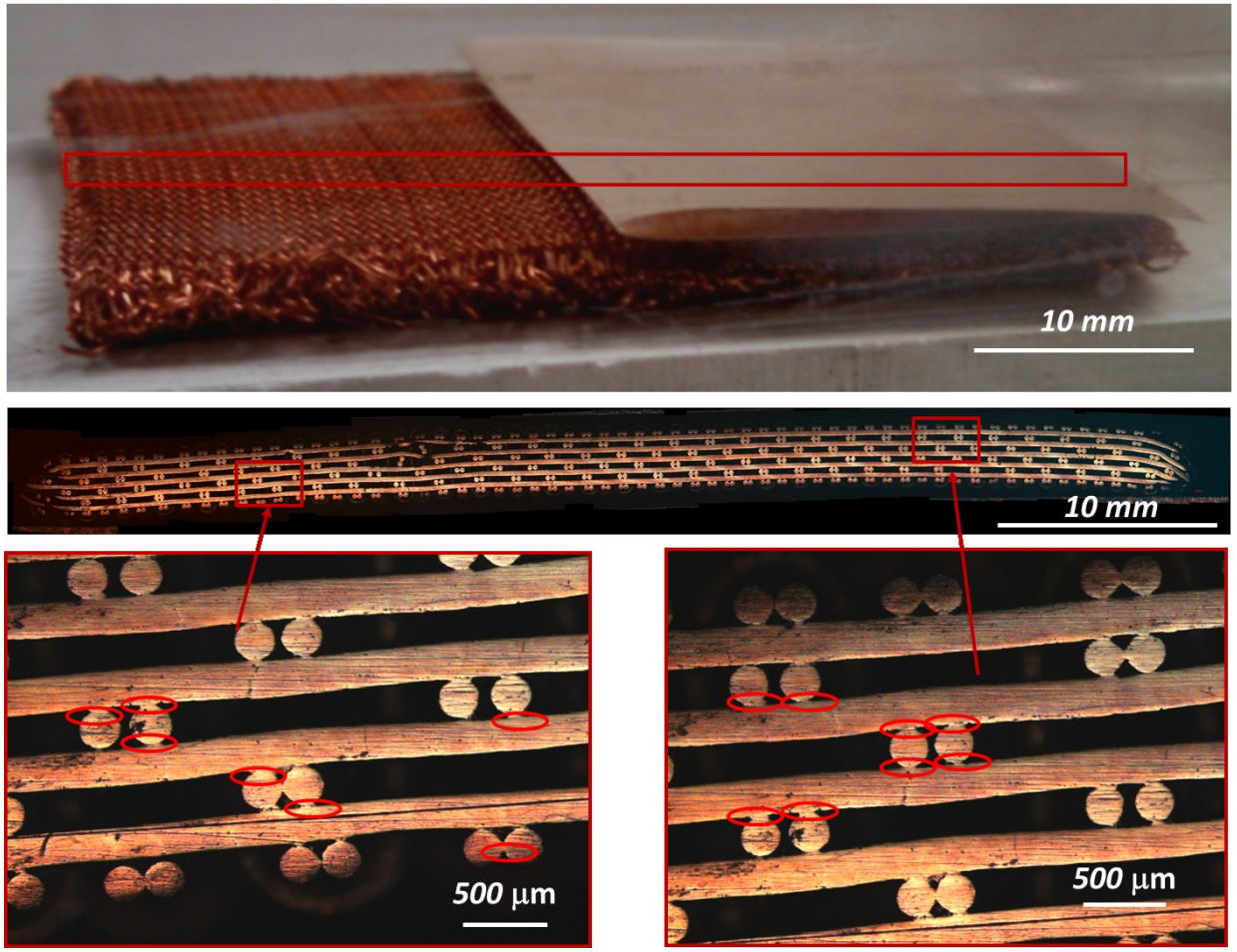

Figure 17: An image of the woven material both before and after brazing. The image at the top shows the copper weave with the single foil of braze on the top left corner before being inserted into the furnace. The image on the middle show a cross-section and the remaining two images show close up views of the weave where you can see evidence of braze localizing between the tangential contact points of the wires. Some of the many successfully bonded brazed junctions are circled.

Examination of the cross-sections reveal that the braze is able to wick over distances of at least 25 mm and is selectively aggregated at the junctions between tangential wires. This shows direct evidence that capillarity provides a self-organized bonding method, and that the braze will localize at the small tangential wire junctions in the material under these bonding conditions. Preferential bonding of wire junctions without filling in the larger pores in the material provides the greatest increase in stiffness and strength with the smallest decrease in permeability. This process is made possible because of the strong capillary action that is present as a result of the many wire to wire contact points. This also emphasizes the importance of controlling the spacing in the weaves that are a result of the weaving process. Large gaps in the structure will have lower capillary forces and are therefore less likely to form a successful bond.

The simple case of capillary force in a column can be used to gain an understanding of the capillary forces between two wires in the weave. The relationship between the height of a liquid in a column (which indicates the magnitude of the capillary action) and the size of the column (which is analogous to the spacing between wires in the weave) is described as [65,66],

$$h = \frac{4\gamma \cos\theta}{\rho g d} \tag{8}$$

where, h is the height of the liquid in the column, γ is the surface tension between the liquid and the air, θ is the contact angle between the minicsus and the tube, ρ is the

density of the liquid, g is the gravitational constant, and d is the diameter of the tube. This relationship shows that the diameter of the tube is inversely proportional to the height of the liquid in the tube (i.e. the capillary forces). Therefore, the extension of this theory to our woven structure shows that as the spacing between wires decreases, capillary action can better draw the braze into these junctions. Changing the wire diameter will also change the curvature of the interface, which will also affect the capillary action in the material (smaller wire leads to greater capillary action)

It is also important to determine the proper amount of braze that is needed to bond the nodes. The correct amount of braze will bond the warp-warp, warp-fill, warp-z, and fill-z junctions, but will minimize the filling in of the pores in the structure. The amount of braze then depends on the number of wire to wire junctions in the system (which is a result of the design geometry) and the spacing between the wires (which is a result of manufacturing).

The order in which wires are preferentially joined depends on the capillary forces that are present in the material and therefore they are directly related to spacing of the wires within the structure and the fact that smaller spaces within the material have higher capillary forces. In the current 3D woven lattice materials, joining can be separated into four phases based on the spacing of the structure. In the first phase of bonding warp-warp and fill-fill wire pairs are bonded. This arises from the fact that these parallel wires have the greatest amount of contact surface area within the structure. Bonding of these junctions is also relatively insensitive to weaving defects, because even pairs of twisted warp or fill wires tend to twist together such that there is a small gap between the wires for bonding. In the second phase of bonding, the warp-fill junctions are bonded together.

In an ideal architecture, these should have the same bonding priority as the wires bonded in the first phase, but these junctions are negatively affected by the defects in the weaving process. Twisted pairs of warp or fill wires increase the average wire spacing in the z-direction between warp and fill wires. The increase in distance therefore decreases the capillary forces in those junctions and lowers the bonding priority of these junctions. The third phase of bonding involves the bonding of the z-wires to the warp or fill wires. Since we are weaving metallic wires, the z-wires cannot make perfectly tight 180° bends at the top and bottom of the weave. This leads to extra z-fill wire spacing, which is randomly distributed through the thickness. This tends to increase the average spacing of the weave in the warp direction and not in the fill, which causes initially more fill-z connections than warp-z connections. The fourth phase of brazing occurs when too much braze is added to the structure which results in the filling of the pores within the lattice. Once all of the other junctions within the material have been filled with braze, the capillary forces decrease and braze will fill in the larger pores within the structure. This is highly undesirable, because this type of bonding increases the shear stiffness slightly while drastically decreasing the permeability.

In order to determine the amount of braze that was required to fully bond all of the wire nodes in the different architectures, I developed a simple analytical model of the weaves and examined a representative repeat unit where the volume of wire and braze that is required to bond every node is determined. The volumes of wire and braze in the repeat unit was then calculated and multiplied by their corresponding densities in order determine the mass of the wire and braze. Eq. 7 was then used to calculate the mass gain, *MG*, of braze for each of the architectures.

The representative repeat unit was chosen in order to capture all of the features of both the standard and optimized architectures, but to do so in a small volume which made accounting for the numbers of wires and bonds easier. The representative repeat unit is shown in Figure 18.

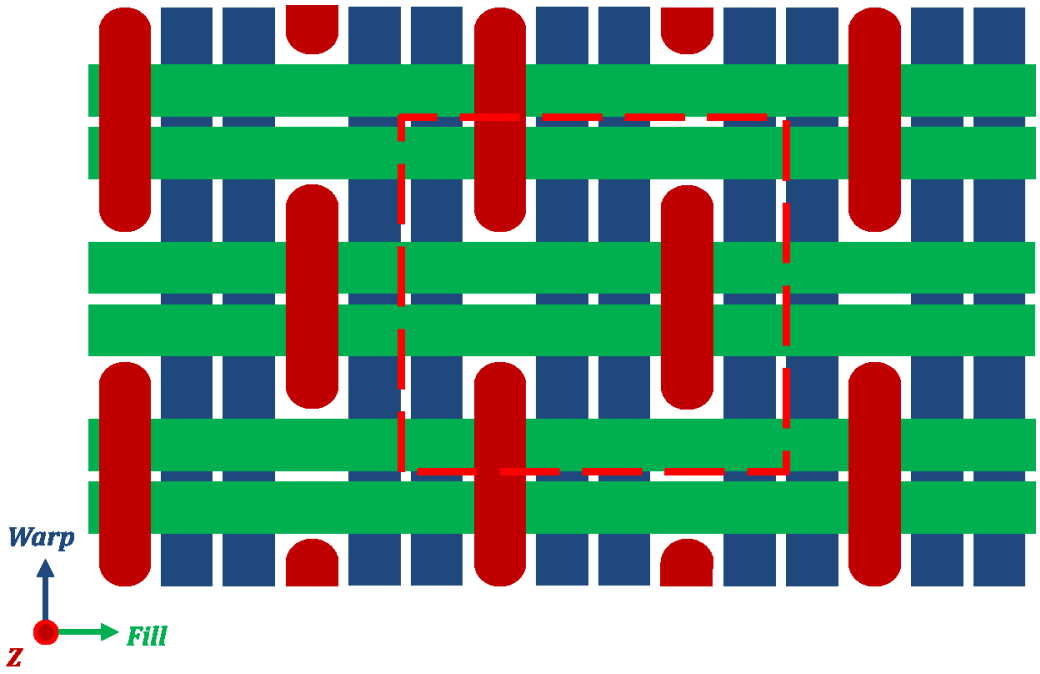

Figure 18: Representative model of the warp-fill plane of the weave with the representative repeat unit denoted by a dashed line.

In the repeat unit, if all of the wires are perfectly tangent to one another and there are no unintended gaps, than the length of the unit cell in the warp and fill directions is simply six wire diameters. The z-wires were assumed to have rounded loops at the top and bottom, but that the tops and bottoms of the loops were tangent to the top and bottom

fill-layers. This correlates to a thickness in the z-direction of the perfect modeled weave is thirteen wire diameters.

It is important, however, to account for the unintended gaps in the materials that are a result of the weaving process, since this gap between the wires will require more braze in order to bond the wires together. When gaps are included, the length of the repeat unit in the warp direction becomes,

$$W = 12r + 2g_{w-w} + 4g_{w-z} \tag{9}$$

where, W is the length of the repeat unit in warp direction, r is the radius of the wire, $g_{w\text{-}w}$ is the size of the gap between pairs of warp wires, and , $g_{w\text{-}z}$ is the size of the gap between neighboring warp and z-wires. In the fill direction, the length of the representative unit cell with the inclusion of gaps between wires becomes,

$$F = 12r + 2g_{f-f} + 4g_{f-z} \tag{10}$$

where, F is the length of the repeat unit in warp direction, $g_{f\text{-}f}$ is the size of the gap between pairs of fill wires, and , $g_{f\text{-}z}$ is the size of the gap between neighboring fill and z-wires. In the z-direction, the length of the representative unit cell with the wire gaps included becomes,

$$Z = [20r + 10g_{w-f}] + [6r + 2g_{f-z} + g_{f-f}] \quad (11)$$

where, Z is the length of the repeat unit in warp direction and $g_{w\text{-}f}$ is the size of the gap between pairs of fill and warp wires in the z-direction. The size of the unintended gaps as a result of weaving for each architecture are summarized above in Table 1.

With the size and geometry of the repeat unit defined, the volume and subsequent mass of the wires within the repeat unit can be calculated. There are three types of wires (warp, fill, and z) and the number of warp and fill wires are different depending on the architecture of the material. In this model, a z-wire was defined as the section of wire that propagates vertically through the thickness of the weave from the center of one z-crown to the center of the next z-crown (on the opposite side of the weave). An illustration of the z-wire used in the model is shown in Figure 19.

The volume of the wires in the repeat unit is a summation of the volume of an individual wire multiplied by the total number of wires in the repeat unit, since the volume of all wires of the same type (warp, fill or z) are equal within the repeat unit. The volume of an individual warp wire in the repeat unit is simply the volume of a cylinder which in terms of the geometry of the repeat unit is,

$$V_w = \pi r^2 W \quad (12)$$

The volume of an individual fill wire in the repeat unit is,

$$V_f = \pi r^2 F \tag{13}$$

The volume of an individual z-wire is a combination of a cylindrical section and two quarter sections of a torus on the top and the bottom. The volume of the z-wire with the geometry that is shown above in Figure 19 is,

$$V_z = \left[\pi r^2 \left(20r + 10g_{w-f}\right)\right] + \left[\pi^2 r^2 \left(3r + g_{f-z} + {}^{g_{f-f}}/_{2}\right)\right] \tag{14}$$

The volume of each individual wire within the repeat unit was calculated using Eqs. 12-13. The volumes were tabulated for the standard and optimized architectures for models with no gaps and for model with the measured gap sizes that were measured from cross-sections of the actual weaves (shown in Table 1).

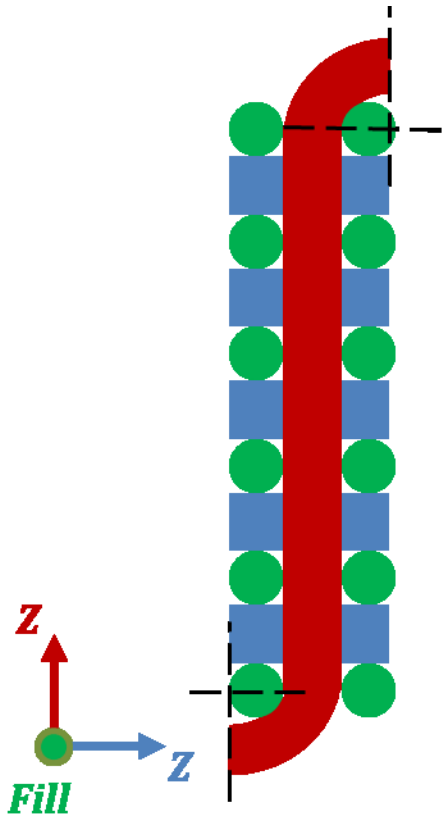

Figure 19: A model of the z-wire in the weave used to calculate the volume of the z-wire in the weave. The z-wire extends from the center of one z-wire crown to the next and the base of the z-wire crown is aligned with the top and bottom outermost fill wire centers.

Table 3: Volume of individual warp, fill, and z-wires in the repeat unit for the standard and optimized architectures

Bond Type	Individual Wire Volume (mm^3)			
	No Gaps		Measured Gaps	
	Standard	Optimized	Standard	Optimized
Warp	3.88E-02	3.88E-02	4.80E-02	4.86E-02
Fill	3.88E-02	3.88E-02	4.15E-02	4.15E-02
Z	9.52E+03	9.52E-02	1.15E-01	1.16E-01

In order to determine the total amount of Cu wire in the repeat unit, the volume of the individual wires in the weaves must be multiplied by the number of each type of wire in the repeat unit. The number of individual wires within the repeat unit are shown in Table 4 and the total volume of each type of wire in the weave for both architectures and gap sizes are shown in Table 5.

From the estimates of the amount of Cu wire in the repeat unit, we can see that the standard architecture contains 26% more Cu wire than the optimized architecture. When the average measured gaps are incorporated into the model, the length of the warp, fill, and z-wires must also increase in order to accommodate the increased dimensions in the repeat unit. Even with the incorporation of the average gaps, the increase in the amount of Cu from the optimized to the standard remains the same at 26% even though the gaps are different in different directions.

Table 4: Number of individual warp, fill, and z-wires in the repeat unit for the standard and optimized architectures

Number of Each Type of Wire in a Repeat Unit		
Wire Type	Standard	Optimized
Warp	20	14
Fill	24	16
Z	4	4

Table 5: Total volume of individual type of warp, fill, and z-wires in the repeat unit for the standard and optimized architectures for the models with no gaps and for the models with measured gaps

Bond Type	Total Wire Volume in a Repeat Unit (mm^3)			
	No Gaps		Measured Gaps	
	Standard	Optimized	Standard	Optimized
Warp	7.77E-01	5.44E-01	9.60E-01	6.80E-01
Fill	9.32E-01	6.21E-01	9.97E-01	6.64E-01
Z	3.81E-01	3.81E-01	4.61E-01	4.65E-01
Total	2.09E+00	1.55E+00	2.42E+00	1.81E+00

The volume of braze within a repeat unit was also calculated by first calculating the volume of an individual bond and then multiplying it by the number of each type of bond in the repeat unit. There are five types of bonds in the woven materials (warp/warp, fill/fill, warp/fill, warp/z, and fill/z) and each type of bond has its own individual volume, but the geometry of the bonds between parallel wire pairs (warp/warp and fill/fill), and the z-wire bonds (warp/z and fill/z) are of a similar geometry.

The bond between parallel pair of wires was assumed to fill in the space between the pair of wires completely with an hour glass shape to the centerline of each wire. An illustration of the assumed cross section of the bond geometry next to images of real wire pair bonds are shown in Figure 20.

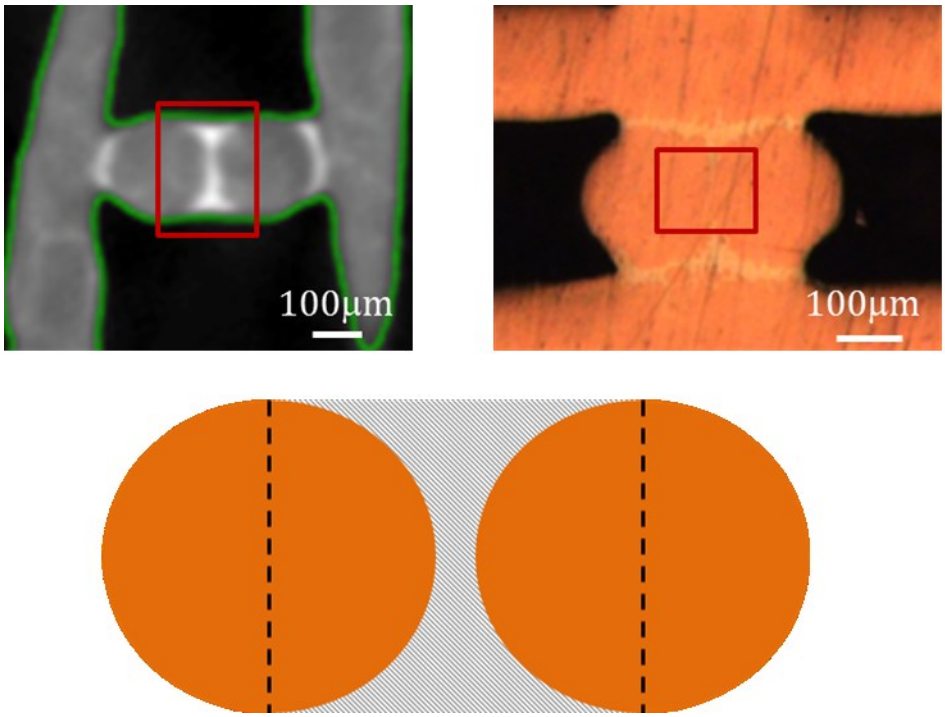

Figure 20: An x-ray microtomography image (courtesy of NRL) and an optical image of a cross section which shows the geometry of a parallel wire pair in the copper weaves after brazing at 900°C for 5 minutes in a forming gas atmosphere. The bond of interest is outlined in both images by a red box. Below is an illustration of the model of a parallel wire pair with the hour glass cross-section of the braze junction, which extends to the centerline of each of the wires in the pair.

This bond geometry was used in the model for both warp/warp and fill/fill wire pair bonds in the weave model. The geometry of this bond is a long rectangular box, with two half cylinders removed from each side. The volume of the warp/warp bond including the unintentional gap between the wires is therefore,

$$V_{w-w} = [(4-\pi)r^2 + 2g_{w-w}r]W \tag{15}$$

and analogously the volume of a fill/fill parallel wire bond is,

$$V_{f-f} = \left[(4-\pi)r^2 + 2g_{f-f}r\right]F \tag{16}$$

The geometry of the z-wire bonds were defined as a rectangular box that once again extended to the center of the two bonded wires, which necessitates the removal of a half cylinder from each side of the rectangular box. Unlike the warp/warp and fill/fill bonds, the bond does not extend the length of the repeat unit, and the half cylinder cutouts are oriented 90° apart due to the orthogonal orientation of the bonded wires. An image of the z-wire bond and an illustration of the modeled bond are shown in Figure 21.

In order to calculate the size of the z-wire bond, the volume of the rectangular box must be calculated from the geometry of the lattice, and then the two half cylindical areas can be calculated and removed from the bond volume. In the case of a warp/z bond, the volume of an individual bond including gaps between warp and z-wires is,

$$V_{w-z} = (8-2\pi)r^3 + 4g_{w-z}r^2 \tag{17}$$

and analogously the volume of an individual fill/z wire bond is,

$$V_{f-z} = (8 - 2\pi)r^3 + 4g_{f-z}r^2 \quad (18)$$

The warp/fill bond is found between two orthogonally oriented pairs of warp and fill wires that are stacked in the z-direction. For the purposes of this model, the warp/fill bond is assumed to have the shape of a rectangular box that is tangent to the tops of the warp and fill wire pairs and that extends to the centerline of the four individual wires that are bonded. An image of a warp/fill bond in an actual brazed weave and an illustration of the bond in the model is shown in Figure 22.

The shape of this bond is defined by the wire diameter and the gaps between wires. In the limit where the warp/fill wire gap approaches zero, then the volume of the warp/fill bond also approached zero. This is an artifact of the way that the warp/warp, fill/fill, and warp/fill bonds are defined, but it also means that the volume between the wires will be completely filled by the warp/warp or fill/fill bonds when the warp/fill gap approaches zero. The volume of the warp/fill bond in this model is defined as,

$$V_{w-f} = (g_{w-w} + 2r)\left(g_{f-f} + 2r\right)g_{w-f} \quad (19)$$

Using these above equations with the wire size and gap values, the volume of the 5 types of individual wires bonds can be calculated. The volume of the individual bonds for the standard and the optimized architecture weaves and a model with no gaps and the average gaps measured earlier in this chapter for each architecture are shown in Table 6.

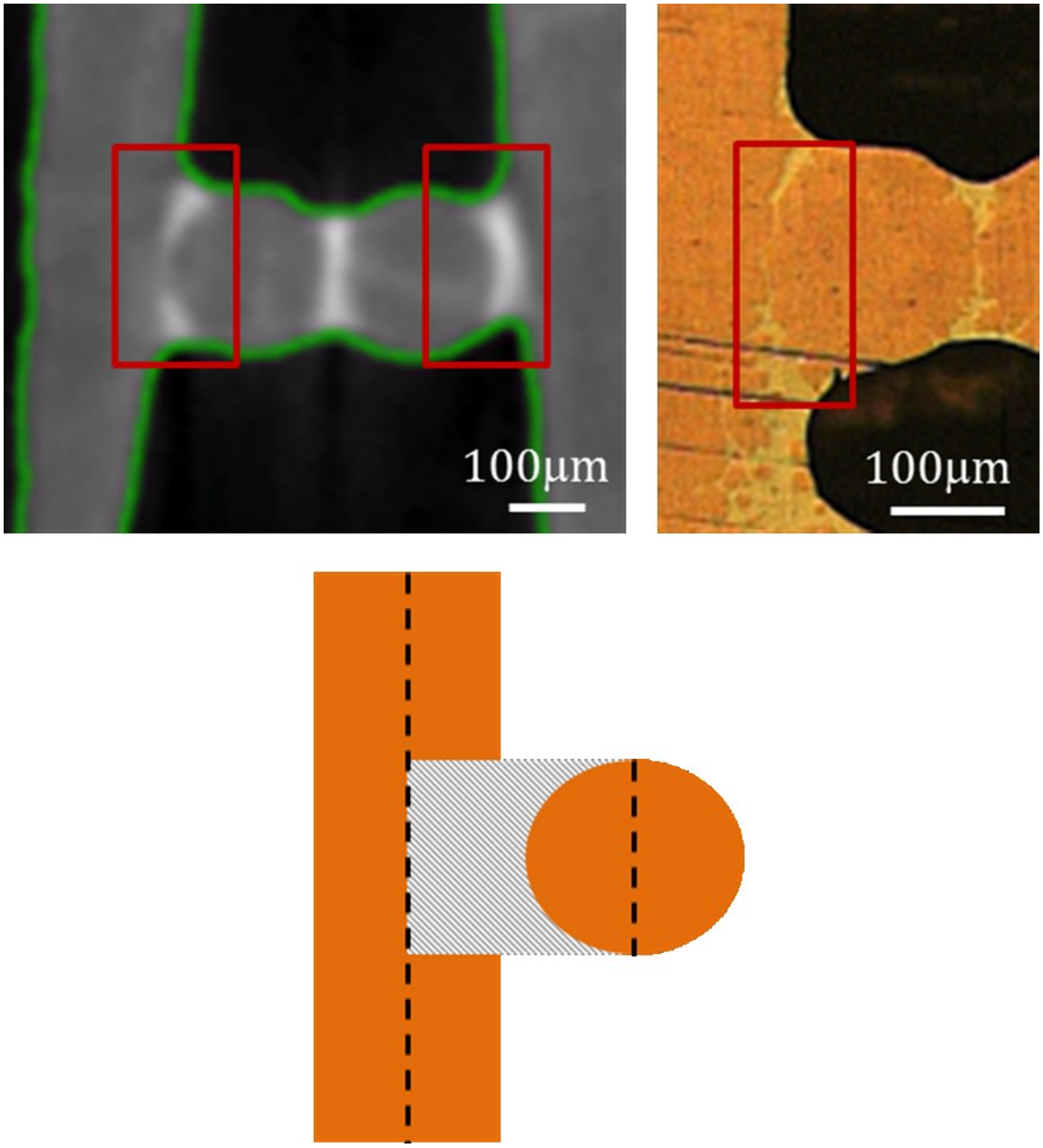

Figure 21: An x-ray microtomography image (courtesy of NRL) and an optical image of a cross section which shows the geometry of a z-wire bond to a neighboring orthogonal wire in the copper weaves after brazing at 900°C for 5 minutes in a forming gas atmosphere. The bond of interest is outlined in both images by a red box. Below is an illustration of the model of the bond, which extends to the centerline of each of the wires in the pair.

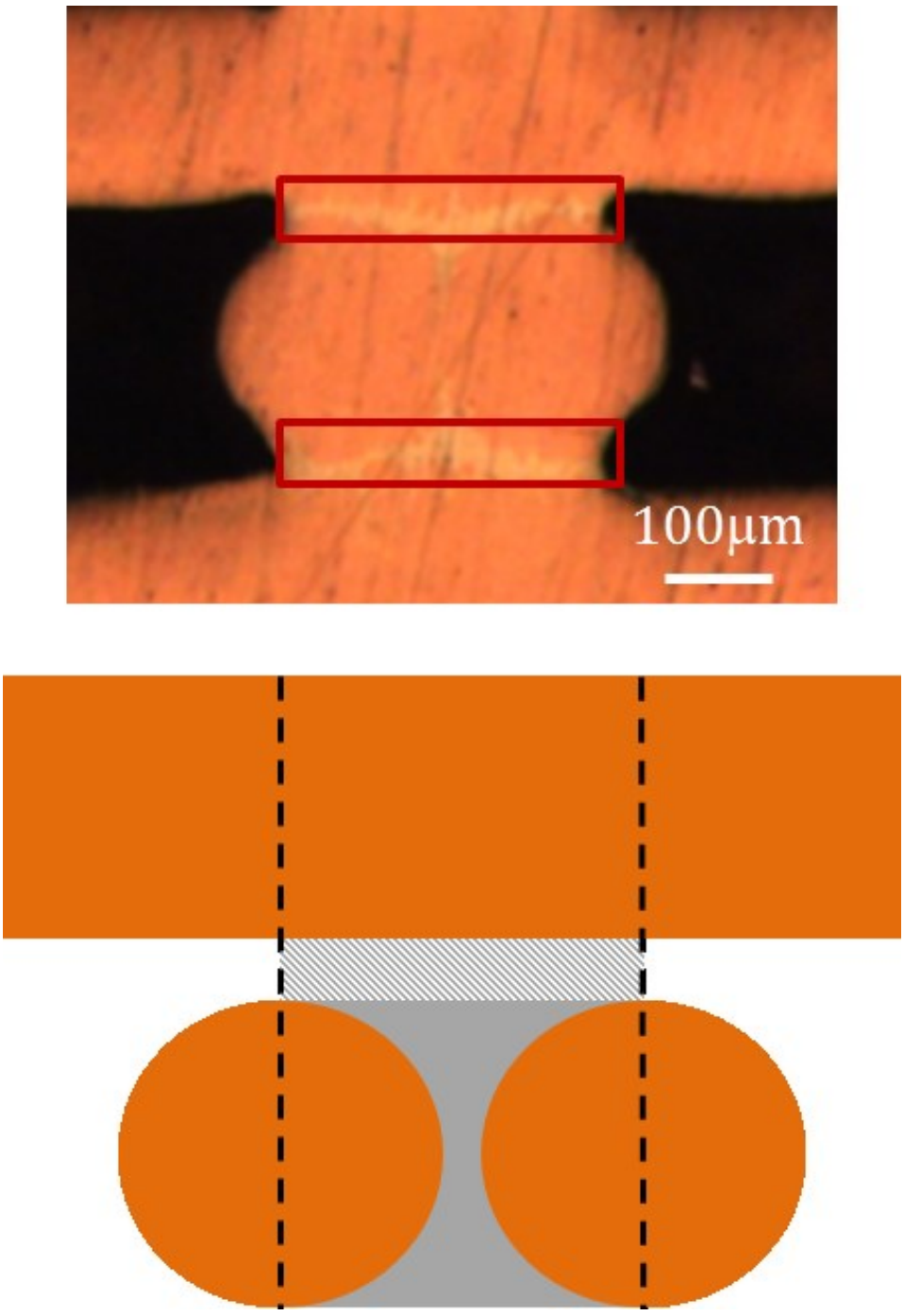

Figure 22: An optical image of a cross section which shows the geometry of a warp/fill wire pair bond in the copper weaves after brazing at 900°C for 5 minutes in a forming gas atmosphere. The bond of interest is outlined by a red box. Below is an illustration of the model of the rectangular box shaped braze junction, which extends to the centerline of each of the four wires in the pair.

Table 6: The volume of an individual warp/warp, fill/fill, warp/z, fill/z, and warp/fill bonds in the repeat unit for the standard and optimized architectures and for a model with no gaps between wires and a model that uses the average measured gaps from optical measurements

Bond Type	Individual Bond Volume (mm^3)			
	No Gaps		Measured Gaps	
	Standard	Optimized	Standard	Optimized
warp/warp	1.06E-02	1.06E-02	1.61E-02	1.97E-02
fill/fill	1.06E-02	1.06E-02	1.68E-02	1.55E-02
warp/z	1.77E-03	1.77E-03	2.42E-03	2.18E-03
fill/z	1.77E-03	1.77E-03	4.26E-03	1.77E-03
warp/fill	0.00E+00	0.00E+00	1.89E-03	2.04E-03

In order to determine the total volume of braze in the repeat unit, the volume of each type of bond must be multiplied by the associated number of each type of bond. The number of each type of bond in the repeat unit is shown in Table 7 and the total volume of each type of bond in the repeat unit for the standard and optimized architecture for the models with no gaps and with the measured gaps is shown in Table 8 and Figures 23-26.

Table 7: Number of individual warp/warp, fill/fill, warp/z, fill/z, and warp/fill bonds in the repeat unit for the standard and optimized architectures

Number of Each Type of Bond in a Repeat Unit		
Bond Type	Standard	Optimized
Warp/Warp	10	7
Fill/Fill	12	8
Warp/Z	40	28
Fill/Z	48	32
Warp/Fill	40	22

Table 8: Total volume of the warp/warp, fill/fill, warp/z, fill/z and warp/fill bonds in the repeat unit for the standard and optimized architectures for the models with no gaps and for the models with the average measured gaps

Bond Type	Total Bond Volume in a Repeat Unit (mm^3)			
	No Gaps		Measured Gaps	
	Standard	Optimized	Standard	Optimized
warp/warp	1.06E-01	7.43E-02	1.61E-01	1.38E-01
fill/fill	1.27E-01	8.49E-02	2.02E-01	1.24E-01
warp/z	7.08E-02	4.95E-02	9.69E-02	6.10E-02
fill/z	8.49E-02	5.66E-02	2.04E-01	1.45E-01
warp/fill	0.00E+00	0.00E+00	7.56E-02	4.49E-02
Total	3.89E-01	2.65E-01	7.40E-01	5.13E-01

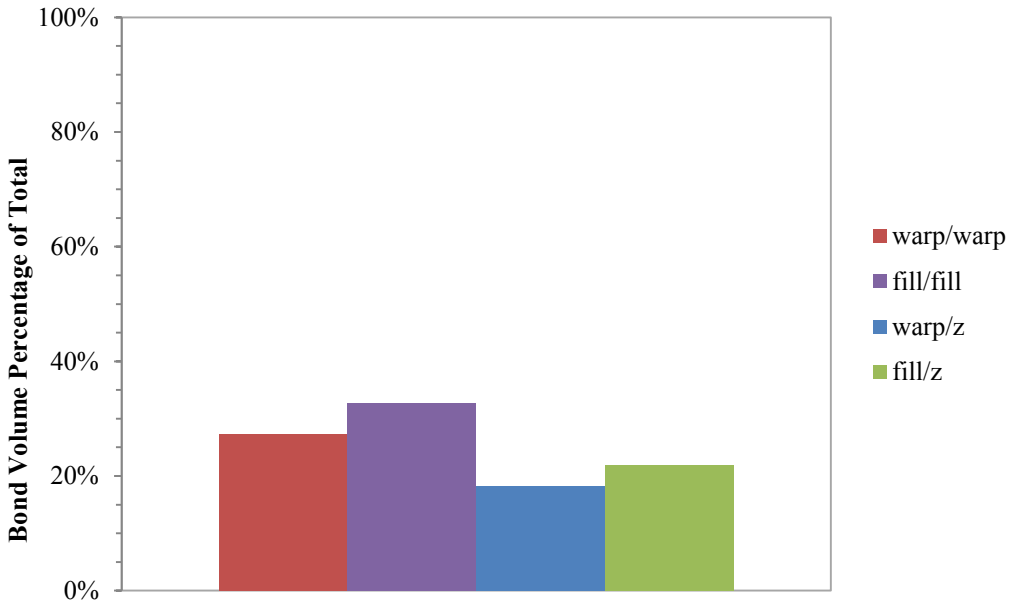

Figure 23: Braze distribution by bond type on a volume basis presented as a percentage of the total bond volume in a repeat unit for the standard architecture weave model with no unintended gaps.

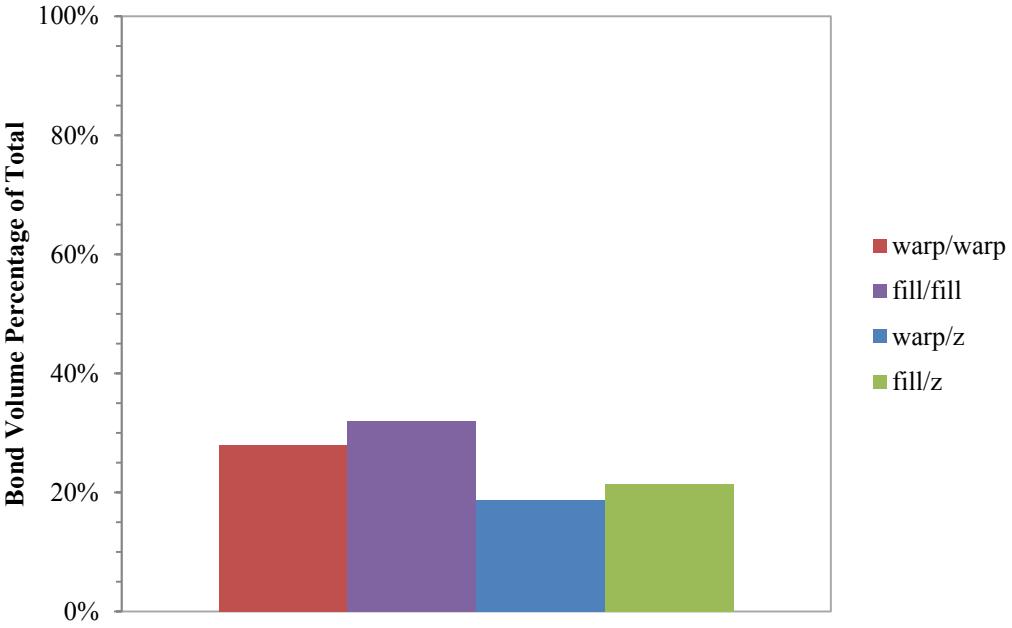

Figure 24: Braze distribution by bond type on a volume basis presented as a percentage of the total bond volume in a repeat unit for the optimized architecture weave model with no unintended gaps.

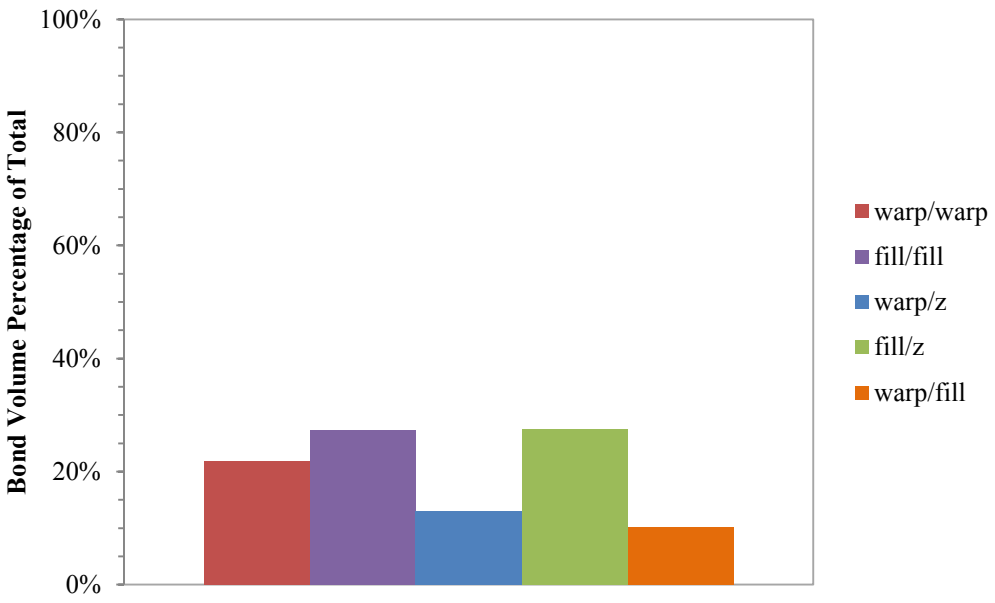

Figure 25: Braze distribution by bond type on a volume basis presented as a percentage of the total bond volume in a repeat unit for the standard architecture weave model with the average measured gaps between wires for each type of bond.

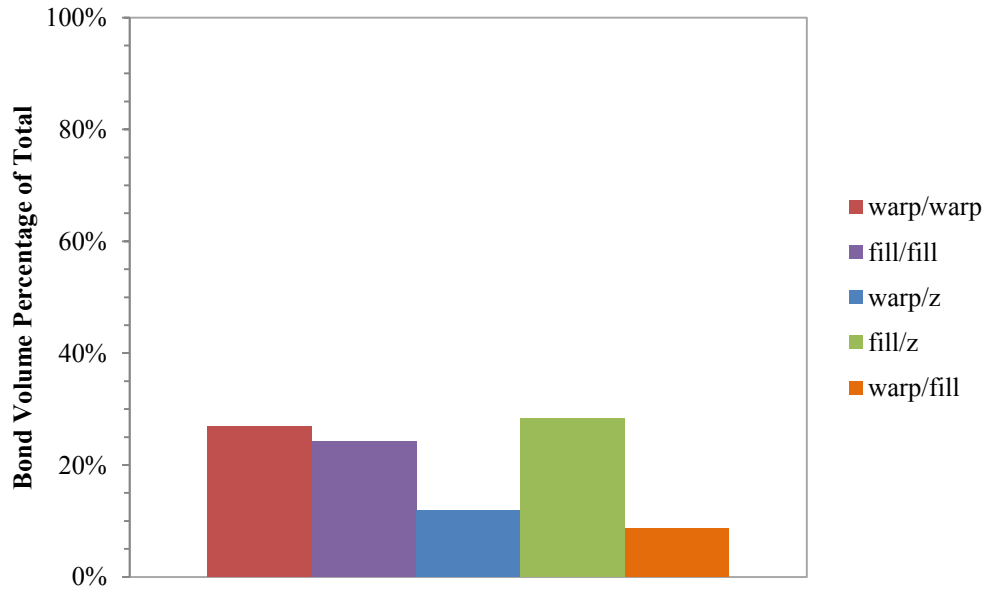

Figure 26: Braze distribution by bond type on a volume basis presented as a percentage of the total bond volume in a repeat unit for the optimized architecture weave model with the average measured gaps between wires for each type of bond.

Examination of the amount of braze required for each bond and each case reveals several things about the role of architecture, bond type, and gap size. As a result of the greater amount of wires in the standard weave and the corresponding greater number of bonds, the standard architecture requires more braze (by volume) to fully bond the lattice together. Additionally, the gaps in the weave increase the distance between the wires and the volume that must be filled in order to bond the wires together with the assumed geometry. This leads to an increase in the bond volume as the size of the gaps increase. In the model with no gaps, we do not see any braze that is being used for warp/fill bonds. This is a result of the way that the warp/fill bond is defined, that was described above, not an indication of the fact that there are no warp/fill bonds present. In fact, the model inherently assumes that the material is fully bonded. Instead, the warp/fill bonds are actually part of the warp/warp and fill/fill bonds in the zero gap model. The parallel wire bonds (warp/warp and fill/fill) are the greatest volume of braze in the repeat unit with more fill/fill bonds than warp/warp bonds. This is attributed to the greater number of fill/fill wire bonds available. The z-wire bonds constitute a smaller volume than the parallel wire bonds with more fill/z bonds than warp/z bonds as a result of the greater number of available fill/z bonds in the material. The incorporation of gaps into the model leads to changes in the distribution of braze amongst the bond types. The most prominent change is the sharp increase in the volume of fill/z bonds. This is attributed to the large gap size between fill and z-wires, which lengthens the fill/z bonds and drastically increases the volume of the bonds. The other significant change that can be observed is the presence of warp/fill bonds in the weaves. The warp/fill bonds begin to appear and

occupy nearly 10% of the volume of all bond material in the models that incorporate gaps. The warp/fill gaps are the second largest gaps in the model which causes the large increase in warp/fill bond volume. Finally, it is important to note that the introduction of the measured gaps dramatically doubles the volume of bond material by for both architectures.

The total mass of the wire and braze for the repeat unit for each of the four cases has now been shown. In order to use these calculations to estimate the required amount of braze to fully bond the weaves, they must be turned into a mass gain of braze, *MG*. The mass of each component in the repeat unit is calculated by multiplying each calculated volume by their corresponding density (ρ_{Cu} = 0.00896 g/mm^3 [67] and ρ_{Braze} = 0.00908 g/mm^3 [53]). Dividing the mass of the braze by the mass of the wire in the repeat volume will then yield the mass gain necessary for brazing all of the wire nodes in the weave. The mass of the wire and braze for each of the four cases and their associated percent mass gain calculations are found in Table 9.

The mass gain that is required to fully bond all of the wires in the materials provides an indication of the required amount of braze that is necessary to fully bond the 3D weaves and transform them into lattices. For both gap sizes, the models show that the standard architecture requires more braze to fully bond the weave and a larger mass gain, although the difference in mass gain with architecture for a particular gap size model is at most 2%. The model with no gaps requires less bonding material and therefore there is a smaller mass gain required to bond these weaves than the model with the gaps. It is important to consider the fact that in these models, idealized bond geometry is employed, all possible wire bonds are satisfied, and the gap size that is used as an average gap size

for all bonds of a particular type. These factors indicate that the correct mass gain for the actual material may likely lie between the estimates of the mass gain for the no gap and the measured gap model.

Table 9: Mass of the wire and braze in a repeat unit for the standard and optimized architectures for the models with no gaps and for the models with measured gaps. The associated percent mass gain of each of these four cases is also shown.

Mass (g)	Mass of Wire and Braze in a Repeat Unit			
	No Gaps		Measured Gaps	
	Standard	Optimized	Standard	Optimized
m_{wire}	1.87E-02	1.39E-02	2.17E-02	1.62E-02
m_{braze}	3.49E-03	2.38E-03	6.63E-03	4.60E-03
% Mass Gain	18.6%	17.2%	30.6%	28.4%

In order to empirically determine the approximate amount of braze needed, samples were prepared using different amounts of braze for both the standard and optimized pattern weaves in copper. The cross-sections of the warp-z plane of the standard weaving pattern for six different amounts of braze are shown in Figure 27.

From cross sections like those shown in Figure 27, it was determined that when low amounts of braze are used (7% mass gain) only a fraction of the wire junctions are bonded together and the majority of the bonding appears to be between pairs of parallel

wires. At the intermediate amounts of braze (11% and 15% mass gain) we see evidence of the second phase of bonding between warp and fill wires. At even high amounts, (>20% mass gain), we see evidence of bonding to the z-wires (phase 3) and then (>25%) filling in of the larger voids within the structure (phase 4). This would imply the ideal amount of braze that is required to fully bond the weaves and to maximize shear stiffness and permeability would be a mass gain in the mid 20% range. These results are in agreement with the analytical estimate of the amount of braze. These results were further confirmed through measurements of the in-plane shear stiffness and the permeability by Dr. Yong Zhang and Longyu Zhao, which are discussed in Chapter 4, and through serial sectioning and x-ray microtomography measurements that were performed by the Naval Research Lab (NRL) with the help of Dr. Richard Fonda and Dr. Amanda Levinson.

In order to examine the weaves that were brazed with various amounts of braze, NRL performed x-ray microtomography and serial sectioning in combination with 3D reconstruction techniques in order to provide 3D images and quantitative measurements of the bonding in the weaves. Seven brazed copper samples (four optimized architecture and three standard architecture) with different amounts of braze from 5-30% mass gain were analyzed by NRL.

A standard architecture sample with a 15% mas gain was initially examined at high resolution in order to determine the preferentially and the efficiency of the bonding in the weaves. An ideally bonded sample would only provide the efficiency of the bonding in the weaves, but would provide no indication of which bonds are more likely to be brazed first. A sample slice of the weave and the 3D reconstruction of the entire sample is shown in Figures 28-29.

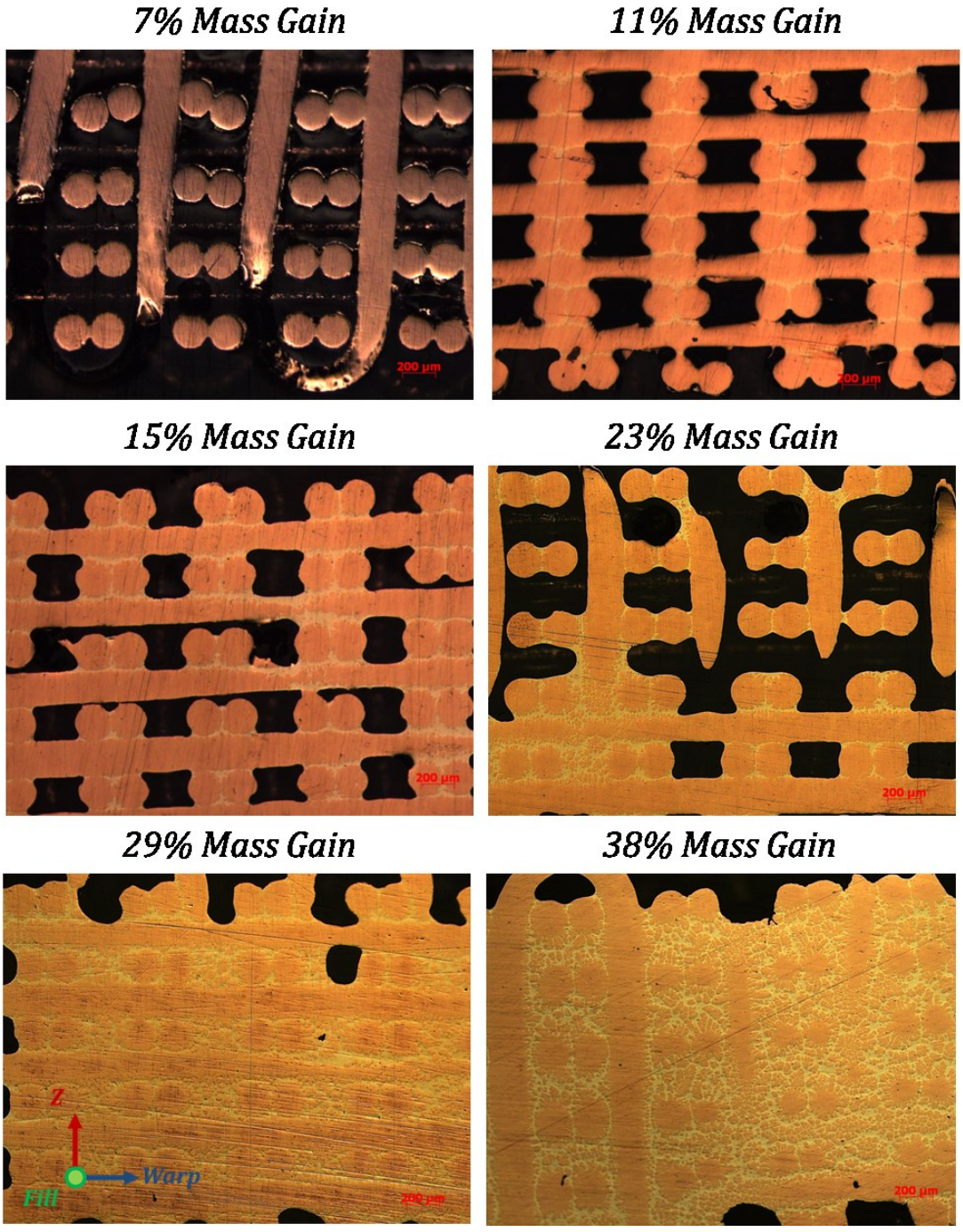

Figure 27: Cross sections of the warp-z plane of the standard weaving pattern in copper after brazing with different amounts of braze at 900°C for 5 minutes under a 95% N_2 / 5% H_2 atmosphere.

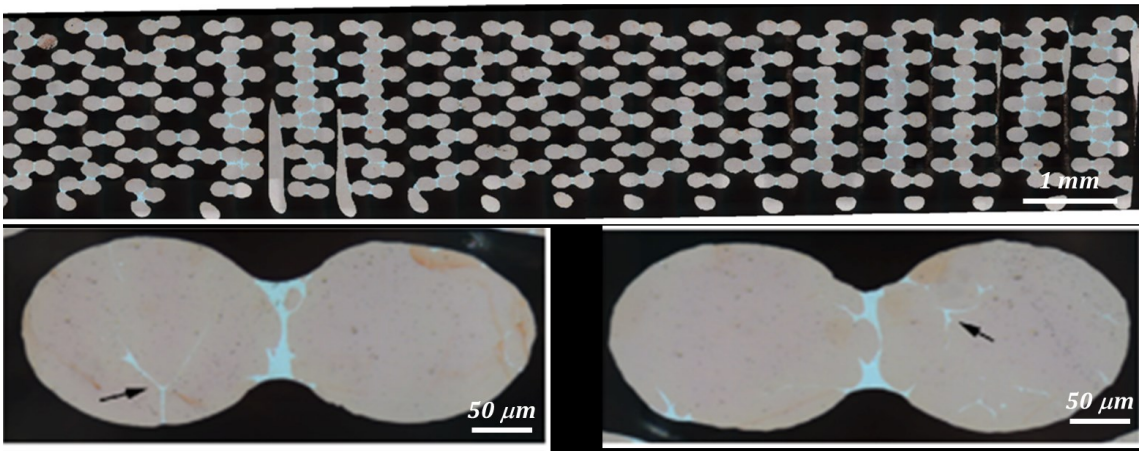

Figure 28: A single slice that was taken of the 15% mass gain brazed standard architecture copper weave sample. Below are two wire pairs that have been successfully bonded together. The shape of the brazed junction and the alloying and penetration of the braze with the wire can be seen in these images. (Courtesy of NRL)

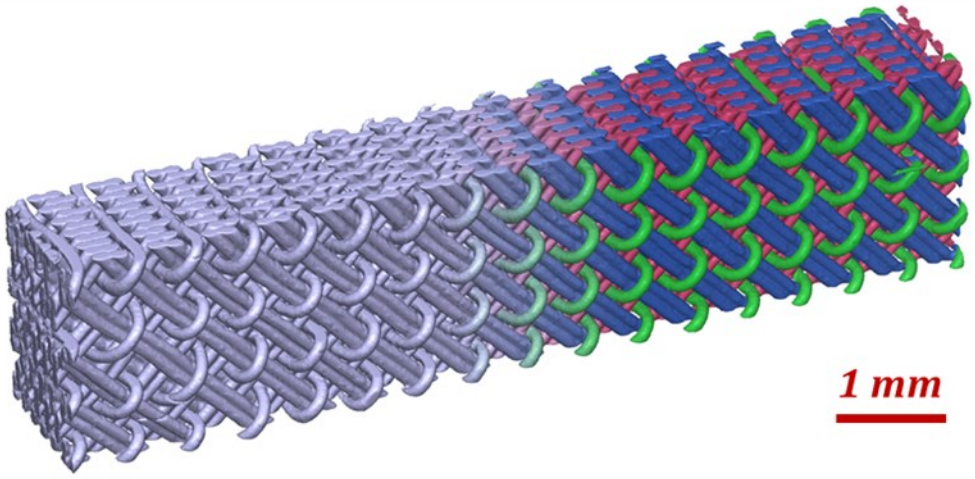

Figure 29: The 3D reconstruction of the 15% mass gain brazed standard architecture copper weave sample. This reconstruction was analyzed in order to look at the preferentiality and the efficiency of the bonding by brazing. (Courtesy of NRL)

The six other brazed copper samples were both standard and optimized architecture copper weaves with 6-35% mass gain were examined with x-ray

microtomography. An image of the the x-ray microtomography reconstructions are shown in Figures 30.

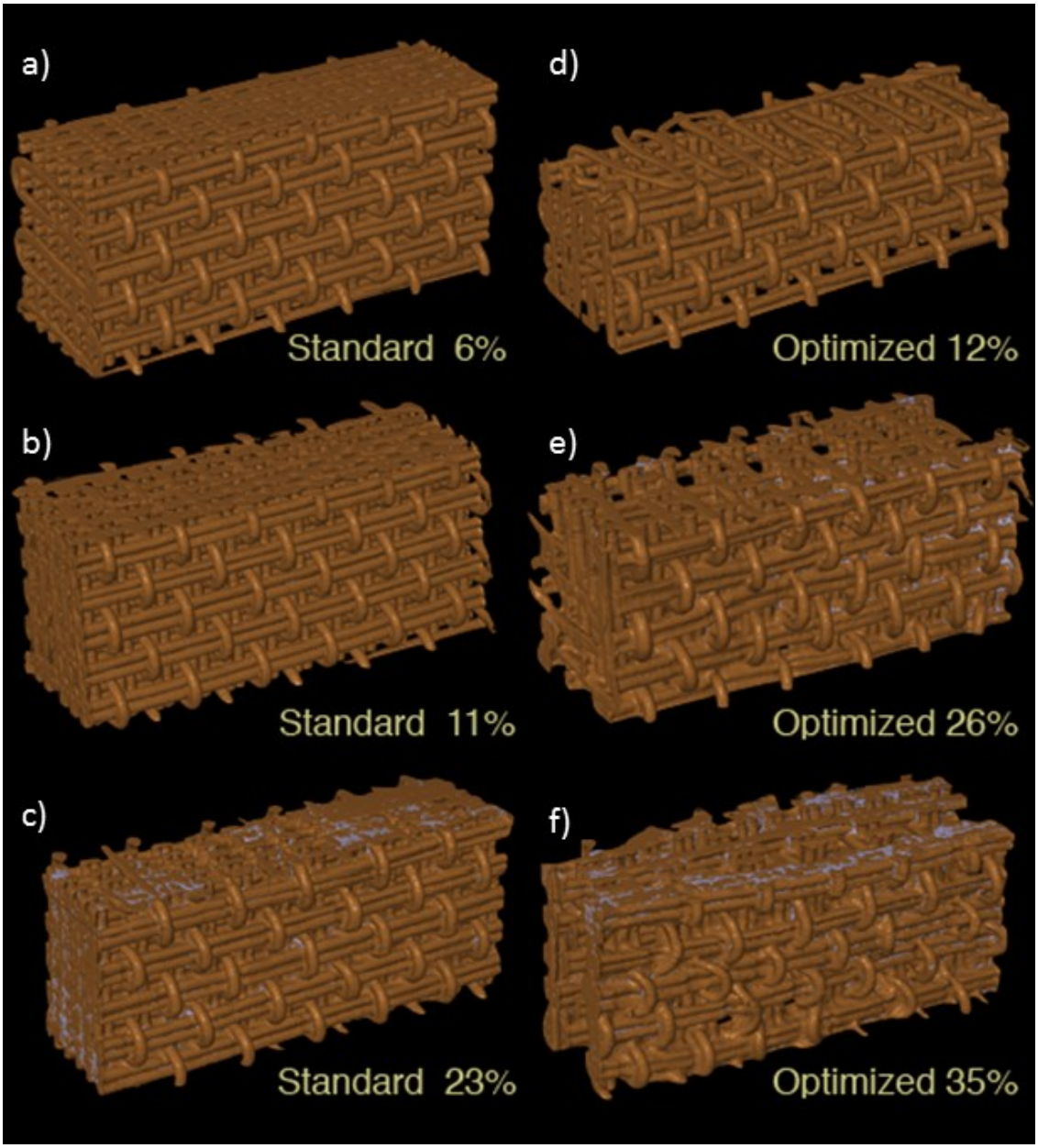

Figure 30: Images of the six additional serial sectioned samples after reconstruction. The reconstructions were analyzed to provide detailed analytical information of the location of the braze in the samples and to confirm the ideal amounts of braze that is necessary for each architecture. (Courtesy of NRL)

The serial sections and x-ray microtomogrpahy measurements of the brazed copper samples provided further evidence that the ideal amount of braze to bond most of the tangential wire junctions, without filling in the larger flow channels in the material is in the mid 20% mass gain range. At the lower amounts of added braze, the efficiency of bonding the z-wires to the fill wires decreases because the size of the gaps in the woven structures is larger. This confirms our hypothesis on the order preference of the order of bonding in the weaves. At higher amounts of braze, we begin to see clumping of braze at the surfaces of the material and eventually filling in of the flow channels [68].

In summary, we have brazed samples of both the standard and optimized patterns in copper and empirically determined the optimal amount of braze that is required to preferentially bond the weaves together without filling in the large flow channels in the weave. The empirically determined amount of braze that should be added is in the mid 20% of the mass of the copper weave that is being brazed. We also have found that for the copper weave and the silver-copper eutectic brazing alloy that a brazing cycle that rapidly heats the material to 900°C provides good fluidity for this system. Use of a reducing atmosphere containing from 5% hydrogen in argon was adequately sufficient to clean the surface of the copper and allow braze to wet the structure. The materials were also tested for both shear stiffness and permeability, which in conjunction with analytical modeling, x-ray microtomography, and serial sectioning results confirmed that we were able to successfully preferentially bond the weaves and form microlattices.

3.2.2: Brazing of Multilayer Weaves

We have shown that we can make microlattice materials by brazing of the copper weaves with silver-copper braze, but in order to determine if the material properties are an improvement over current commercially available materials, we must look at some of the possible applications. Load bearing thermal management devices are potential application and we will use it as a means to guide the manufacturing and property requirements of the materials.

Laser diode packages have a wide range of applications from simple every day devices such as laser pointers to demanding applications for military use. Demanding applications require increasingly higher power outputs, but due to the inefficiencies in these laser diode devices, the generation of more power leads to the detrimental generation of more heat in the device. In fact, most laser diodes have efficiencies of less than 20% and many have efficiencies of only a few percent [69]. In order to generate the right frequency and bandwidth of emitted light, as well as to prevent overheating and material breakdown, the laser diodes must be actively cooled [70].

Most demanding laser diodes applications involve packaging a cooled laser diode system for use on mobile vehicles. This places special demands on the cooling system and makes the weight of not only the device but the coolant and piping necessary for the device to operate an important consideration. A device that has greater cooling efficiency would provide the necessary heat removal with less weight, and if the material is load bearing it can replace other structural material thus eliminating further weight. As a result, a device that has a high heat transfer coefficient per flow rate (implying efficient

convective heat transfer to the working fluid while only using a small amount of fluid), a low pressure drop, and a uniform temperature across the device (no local high temperature regions) in addition to bearing loads would allow for greater laser diode performance.

In conjunction with Michael Schatz from Lincoln Labs at MIT, it was determined that a nominal heat transfer testing block for laser diode cooling should possess a geometry of 25.4 mm x 25.4 mm x 76.2 mm. Since the 3D weaves that we a currently fabricating have a maximum thickness (z-direction) of 3 mm and width (fill-direction) of 30 mm, we could not currently manufacture the geometry necessary to satisfy the requirements with our current 3D weaving process. In order to meet the size recommended by Lincoln Labs, it become necessary to not only bond the nodes of the as-woven material, but also to join layers of the material together by stacking and brazing in the z-direction.

In order to braze multiple layers of the material together, the processing steps developed for the brazing of single layers of the weave was used as guideline. In previous single layers brazing work, foils of braze were placed above and below a layer of weave and the liquid braze needed to only penetrate the weave by 1.5 mm (one half of a layer thickness). The same strategy was employed in multilayer brazing and 8 layers of woven material were stacked with foils of braze placed above and below each layer of woven material. The stack of braze and weave was then sandwiched between layers of 99.99% pure alumina plates to help maintain flatness and provide support for the part during brazing. The materials and the alumina plates were wrapped with NiCr wire in order to maintain the alignment of the materials during brazing. After wrapping with

wire, the braze foils and the strips of woven material were then realigned so that the exterior of each layer of weave was in alignment with all of the other layers. Due to the Cr_2O_3 on the surface of the NiCr wire that is not reduced by the 5% hydrogen atmosphere, braze did not wet the wire and therefore it could be placed in direct contact with the exterior of the weave and be easily removed after brazing. An example of a sample prepared and ready to be inserted into the furnace for brazing is illustrated in Figure 31. A sandwich of weave and braze was inserted into the furnace and processed using the same processing cycle that was described previously for the brazing of single layers of weave. An 8-layer optimized samples after brazing, EDM cutting, and hand polishing to 1200 grit on the four cut surfaces is shown in Figure 32.

When manufacturing multilayer woven materials, it was important to ensure that braze not only penetrated the whole structure, but also to check that braze was uniformly distributed throughout the structure and that the z-wire loops nested between layers and were properly brazed. Cross sectioning and polishing were performed to provide indications of the quality of the brazing in the multilayer brazed lattice structures. The images of the polished cross sections are shown in the Figure 33. From the polished cross sections, it can be seen that there is uniform penetration of the liquid braze throughout the whole structure and it appears that the z-wires do nest into one another during brazing. Globally, nesting does not occur throughout the entire sample, but it appears that significant amounts of the sample do show this behavior. Overall, our initial results indicate that we were able to successfully fabricate multilayer lattices of copper weaves.

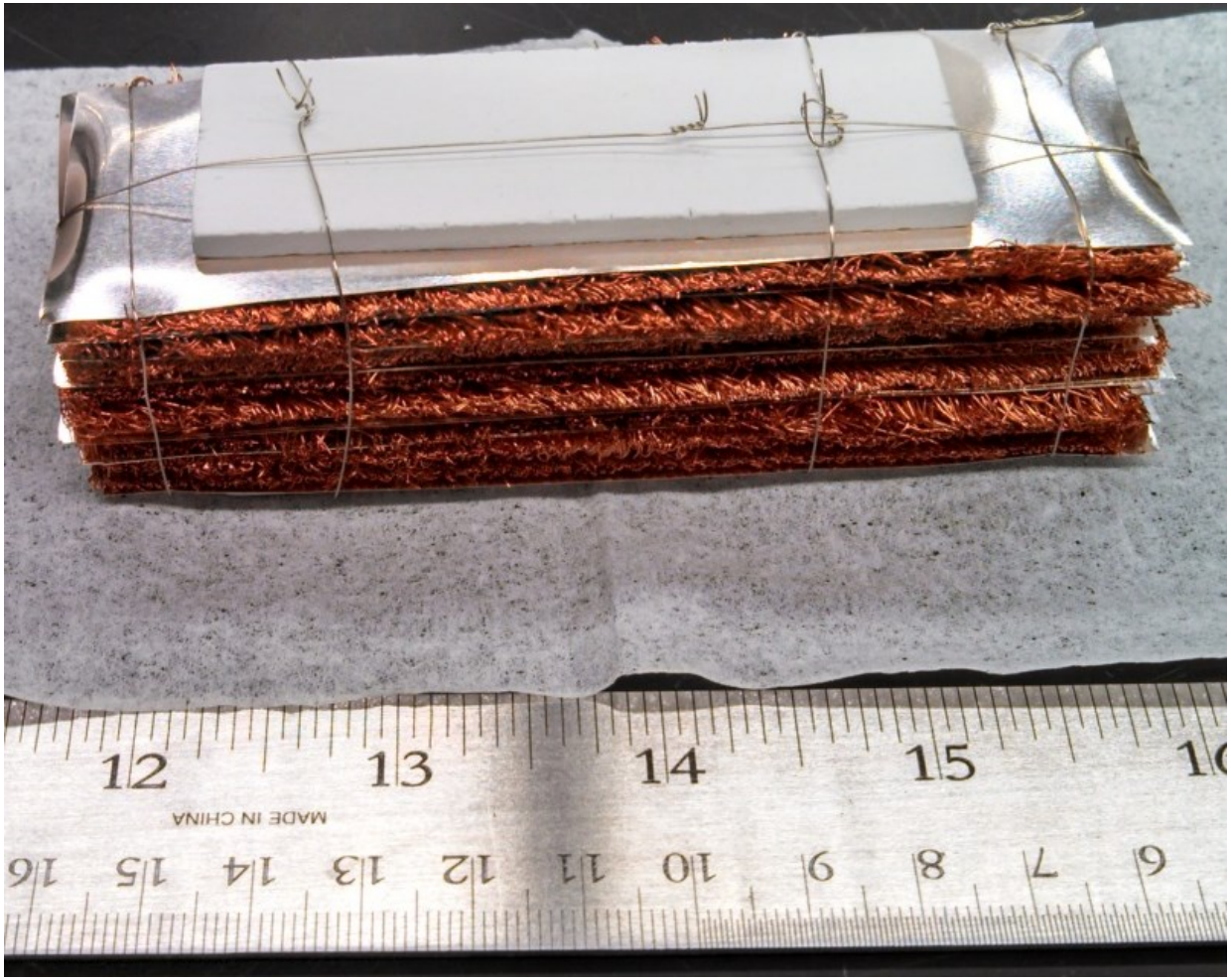

Figure 31: An 8-layer optimized sample prepared with 4 brazing foils for each layer of weave, before brazing. The samples is 110 mm long so that all edges can be trimmed and two samples can be fabricated. One sample will be 76.2 mm long and the other will be 25.4 mm long (warp direction).

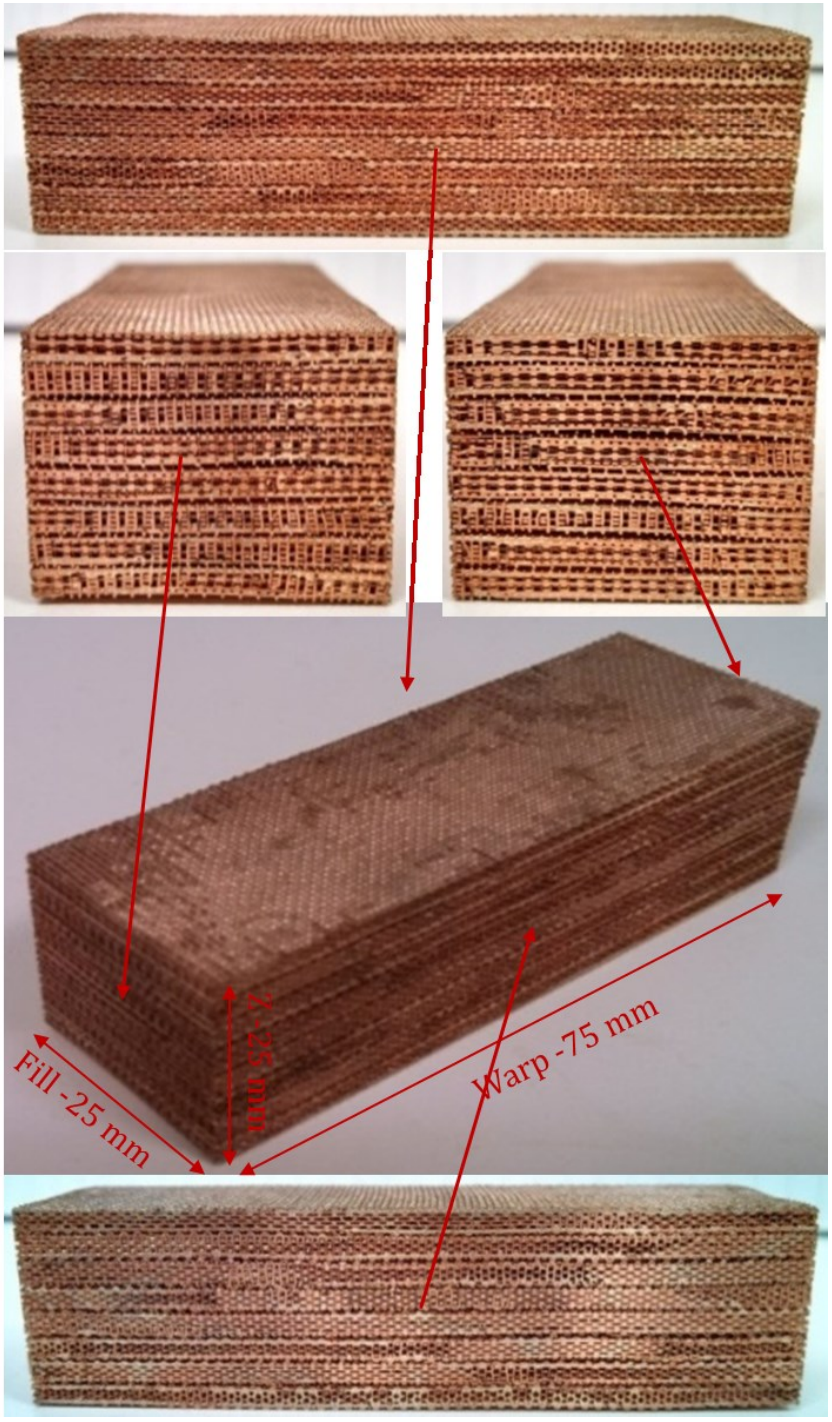

Figure 32: 8-layers of optimized copper weave brazed together at 900°C for 5 minutes in a 3% H_2/ 97% Ar environment. The material was then cut with a wire EDM into a 76.2 mm x 25.4 mm x 25 mm block and then all cut surfaces were hand polished to a 1200 grit finish in order to remove the recast layer.

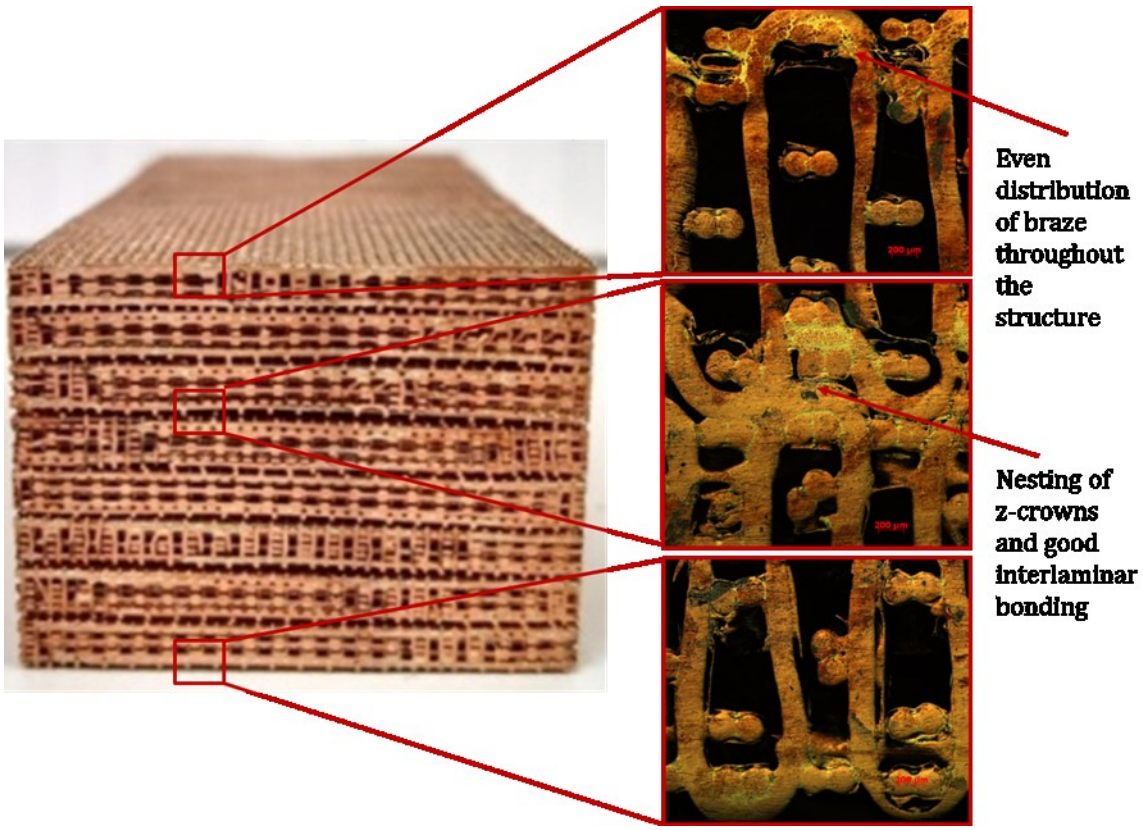

Figure 33: Cross sections of the 8-layer optimized woven copper microlattice structure. These cross sections reveal uniform distribution of braze throughout the structure and good interlaminar bonding and nesting of the z-crowns between layers.

In order to minimize surface contact resistance and allow for greater coupling of heat into the weave during thermal testing, a 1mm thick face sheet was also attached to the warp-z face of the material after it was EDM cut and polished to a 1200 grit finish. Face sheets were bonded for 5 minutes at 780°C with a single 25.4 mm x 76.2 mm x 0.045 mm foil of silver-copper eutectic braze. This lower temperature did not appear to allow the braze within the rest of the structure (from the first brazing cycle) to reflow since its melting temperature had increased due to interdiffusion and alloying with the

copper base metal. Also, it did not appear that the braze was able to wick into the structure in any significant manner due to its high viscosity at these temperatures. This brazing alloy was preferred because its thermal conductivity is close to the thermal conductivity of pure copper and silver [71]. In addition, alloys in between the composition of the brazing alloy and the wire possess a high thermal conductivity. An image of the woven structure with the brazed face sheet is in shown in Figure 34.

Figure 34: Image of the 8-layer optimized copper microlattice structure with a 1mm thick OFHC copper face sheet brazed to the warp-z face of the structure. The face sheet was bonded at ~800°C with the same silver-copper eutectic braze that was previously used to braze the structure together.

Several samples were manufactured in the 25.4 mm x 25.4 mm x 76.2 mm geometry in both the standard and the optimized weaving pattern (Figure 35). Additionally, other samples were also fabricated in a 25.4 mm x 25.4 mm x 25.4 mm size as well. Samples both with and without face sheets were also made in order to satisfy a

wide variety of testing configurations. In order to satisfy additional heat transfer applications, multilayer (8 layers in the z-direction) were fabricated and then sliced by wire EDM into thinner sections with the fill direction in the thickness. These samples also had a face sheets applied after they were sliced to the appropriate dimensions. All surfaces were then ground and polished to a 1200 grit finish by hand. Samples that were 3.2 mm, 6.4 mm, and 12.7 mm thick were prepared in both the standard and optimized architecture and are shown in Figure 36. This work shows one example of how the limitations of the current weaving process can be overcome and the available geometries and applications of final parts can be expanded through the using of brazing.

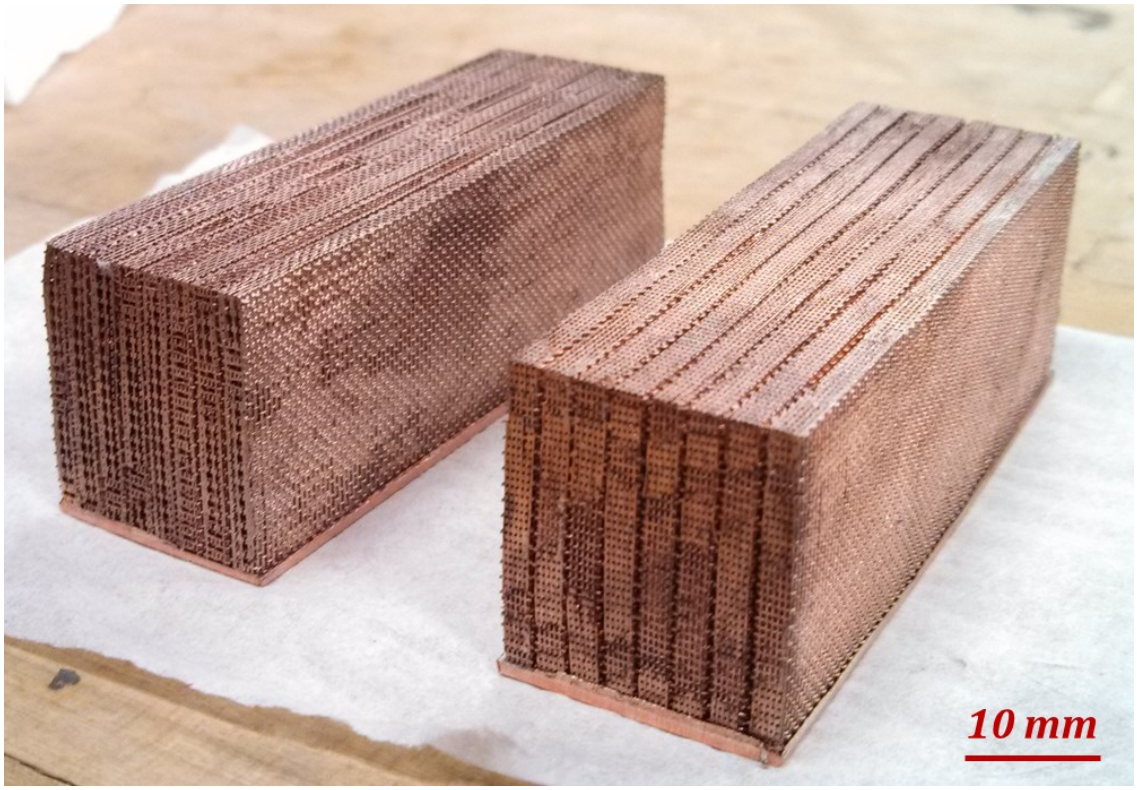

Figure 35: 25.4 mm x 25.4 mm x 76.2 mm (warp x fill x z) multilayer woven and brazed copper blocks. The optimized block is shown on the left and the standard pattern block is shown in the right. Both samples were brazed to a 1 mm thick OFHC copper face sheet after the initial brazing process (which was used to bond the layers together).

Figure 36: Sliced standard and optimized pattern woven samples in three different thicknesses. The samples were all 25.4 mm x 76.2 mm (z x warp) and the thickness (fill) was varied to be 3.2 mm, 6.4 mm, and 12.7 mm. After cutting to the appropriate thickness, the sample was then bonded to a face sheet using a silaver-copper eutectic braze.

3.2.3: Fugitive Weaves

Another current limitation of the weaving process is that certain positions in the weave must be occupied with wires to support the structure. In the standard pattern weave, all of the positions are filled, however in the optimized weaving pattern selected wires were left out of the weave to open up flow channels while leaving enough wires in the weave to support the structure during weaving. In an effort to increase the permeability of our structures even more than can be directly woven, we studied the use

of “fugitive” wires. Fugitive wires act as place holders during the weaving process and support the structure during weaving, but are later removed in order to allow for the development of new, more open designs and patterns.

In order to make stiff lattice materials from weave, we need to braze the structure together. This creates a difficult materials problem when selecting the fugitive wire material. Ideally, you would want the fugitive wire material to survive the bonding process and then be able to be removed. For the copper systems, this would mean that the material would have to survive at temperatures in excess of 900°C in a hydrogen environment, but also be able to be removed without ever exceeding 1000°C. In principal, one could etch selected wires out after brazing, be we decided to pursue a different tack. In an effort to create microscale lattice materials that have higher permeability than materials that could be woven, we decided to use silver-copper eutectic brazing wires as fugitive wire in our copper woven materials. This fugitive wire is not only removable to open larger flow channels, but the melting of the fugitive wires will also serve to bond the weave together to form a microlattice.

Materials were woven by Dr. Keith Sharp at SAERTEX in this fugitive architecture using our design that incorporated 250 μm diameter wires that are made of the same silver-copper eutectic brazing material that we currently employ to braze the copper weaves. The optimized pattern was modified to use fugitive wires in all of the fill positions in the middle 4 fill layers of the pattern. According to initial modeling, this design would increase the permeability another 120%, while only decreasing the shear stiffness by 15% as compared to the optimized structure. A model of the fugitive wire

weaving pattern in both orientations as well as mounted and polished cross-sections of the as-woven material (courtesy of Dr. Yong Zhang) are displayed in Figure 37.

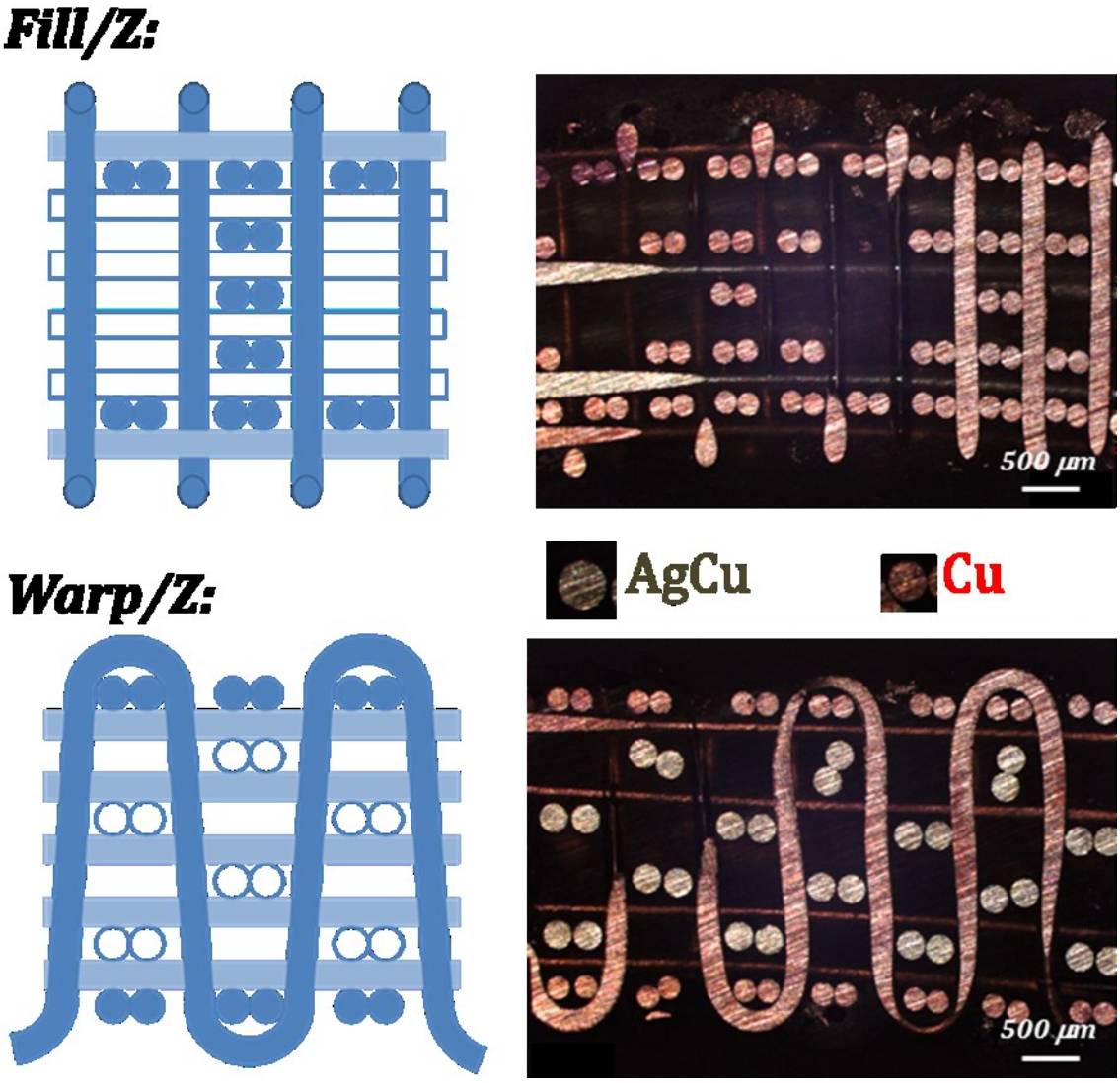

Figure 37: Modeled images of the fill/z and the warp/z planes of the fugitive wire weaves. The silver-copper eutectic braze wires are as open circles and rectangles in the model and can be seen in silver in actual material. Images of the actual material were originally captured by Dr. Yong Zhang.

The fact that the brazing wire is used to support the structure before bonding creates some difficulties in processing the material. Once the braze melts (which occurs at 780°C) the fugitive wires can no longer serve to support the structure. Also at these temperatures the copper wires are very soft and can easily sag. In order to process these materials, a strategy must be employed which allows the structure to retain its geometry, while also bonding the material together to form a microlattice.

In initial experiments, we processed the material with the same method as was previously used to make microlattice materials. Heating the material at 900°C resulted in the generation of microlattice materials, however, some of the pairs of copper wires moved from their intended positions due to capillary action pulling wires towards neighboring wires, which can be seen in Figure 38. This is not ideal and we would like to maintain the wire position before and after brazing.

Additionally, the material also possessed a curvature in the warp-fill plane that disappeared after brazing. The natural curvature in the as-woven material can be clearly seen in Figure 39. This curvature is not desired in the brazed materials, because it makes the material difficult to test and eventually integrate into applications.

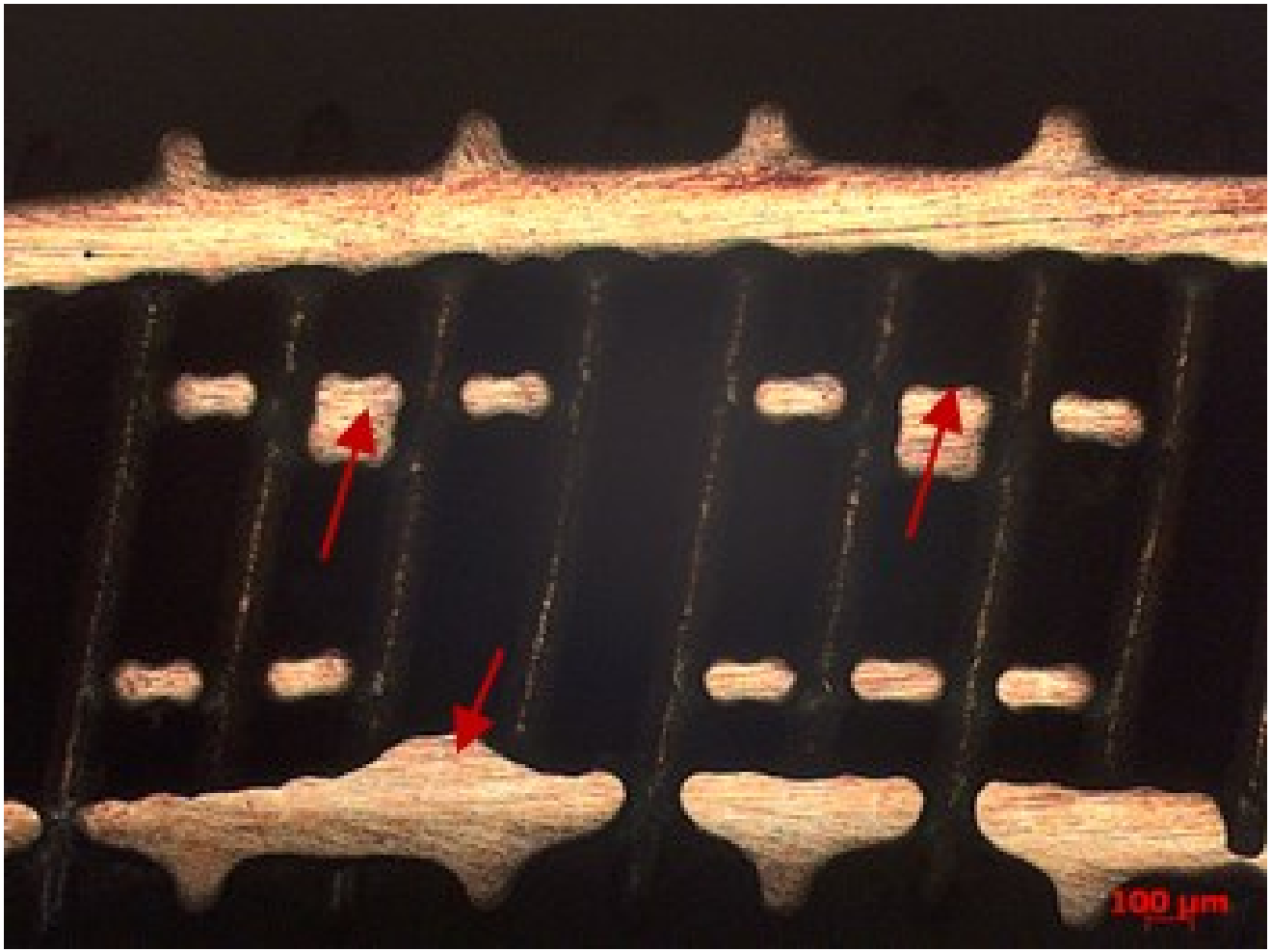

Figure 38: Cross section images of the fugitive wire sample after brazing at 900°C. The red arrows indicate how the wires have moved from their original positions.

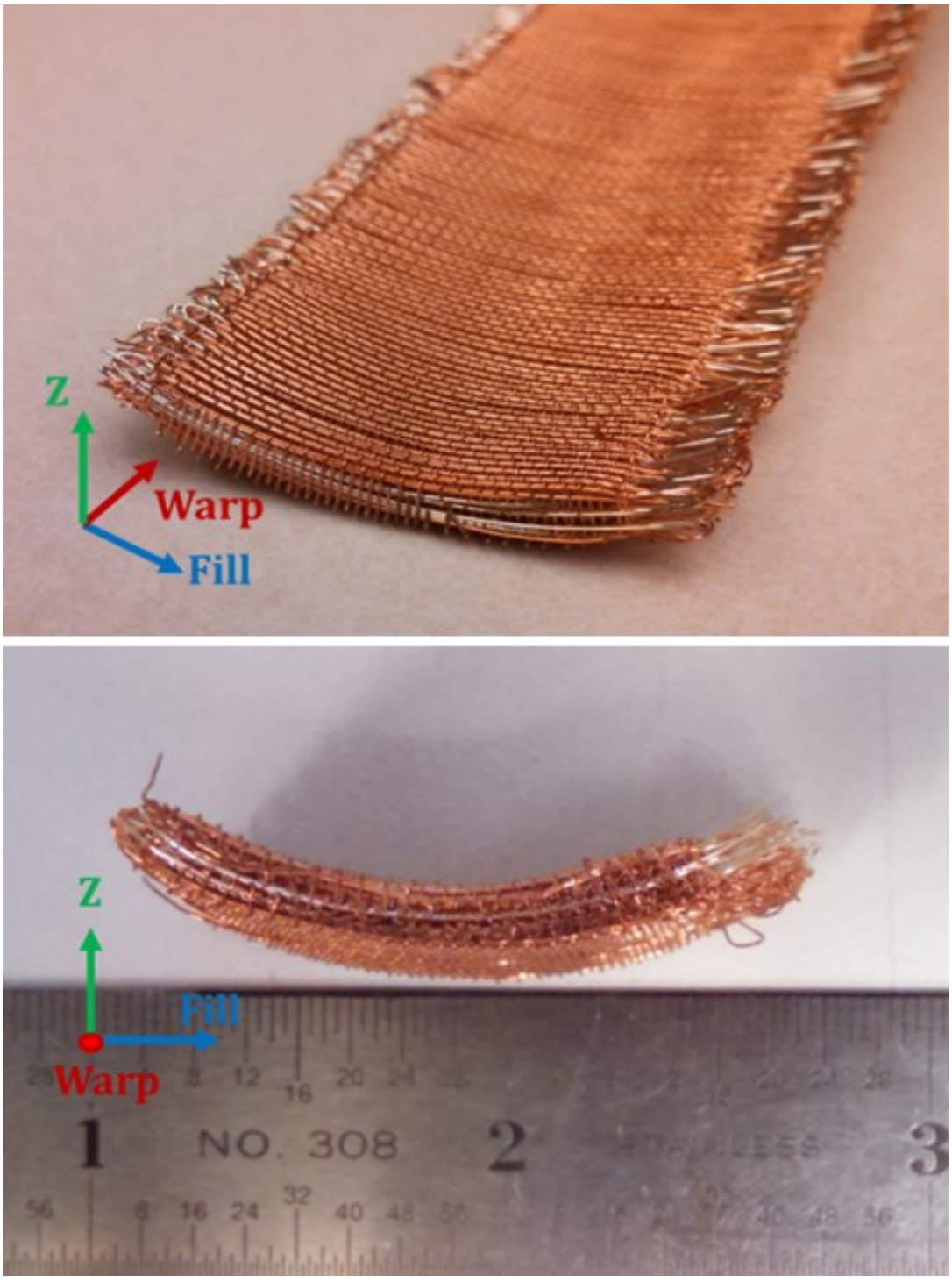

Figure 39: Images of the as-woven material with silver-copper eutectic wires (shown in silver) replacing some of the copper 'fill' wires in the middle layers of the weave. Note the natural curvature of the weave in the warp/fill plane along the fill direction.

In order to overcome the issues of wire movement, sections of the material were cut and oriented with the warp direction oriented vertically to avoid the influence of gravity. In this orientation, the wires are supported by wire to wire contacts in the vertical direction (warp/z contacts) which helps to maintain the structure. This is a feasible solution to maintain the architecture of the material during the brazing process, however, the natural curvature along the fill direction of the warp/fill plane is not relaxed. Therefore, in order to flatten the samples before brazing, the samples were annealed at 650°C for 3 hours under a 95% N_2 /5% H_2 atmosphere (shown in Figure 40). This temperature and duration was determined empirically after annealing several sections of the material.

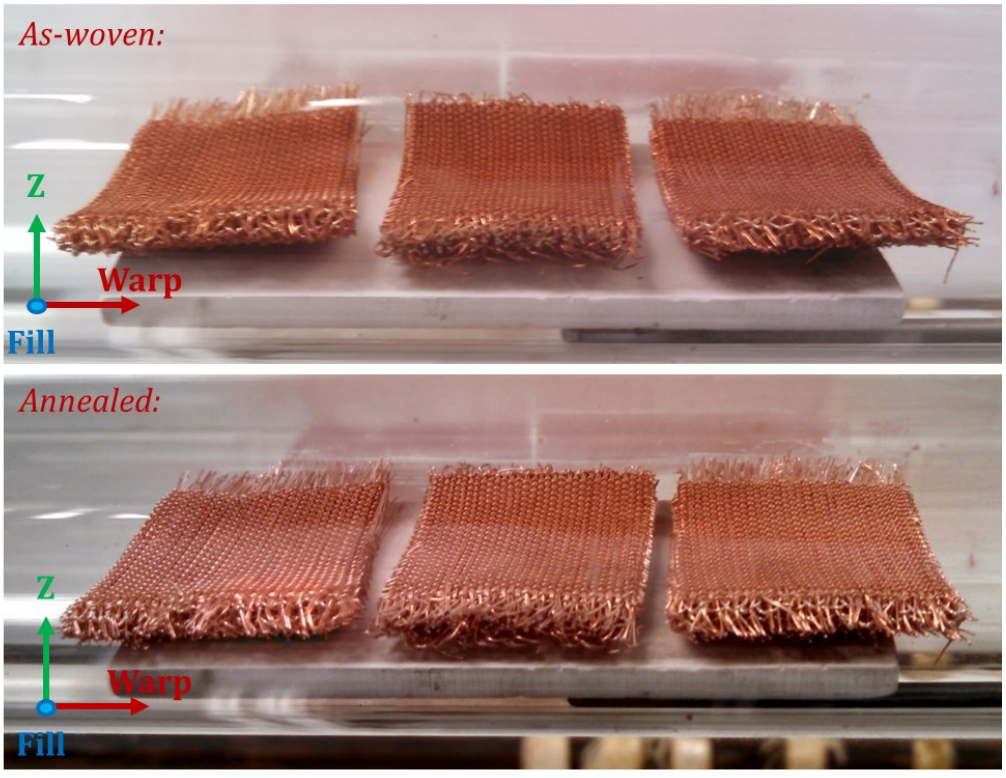

Figure 40: Images of three samples of the fugitive wire material before and after annealing at 650°C for 3 hours. The pronounced curvature of the as-woven material is relaxed after the annealing process which allows for brazing of the samples with the warp direction vertically oriented.

After annealing, the samples were then rotated so that the warp direction was then oriented vertically to ensure continuous wire to wire contact in the vertical direction even after the braze wires have melted. An image of the sample before brazing is shown in Figure 41.

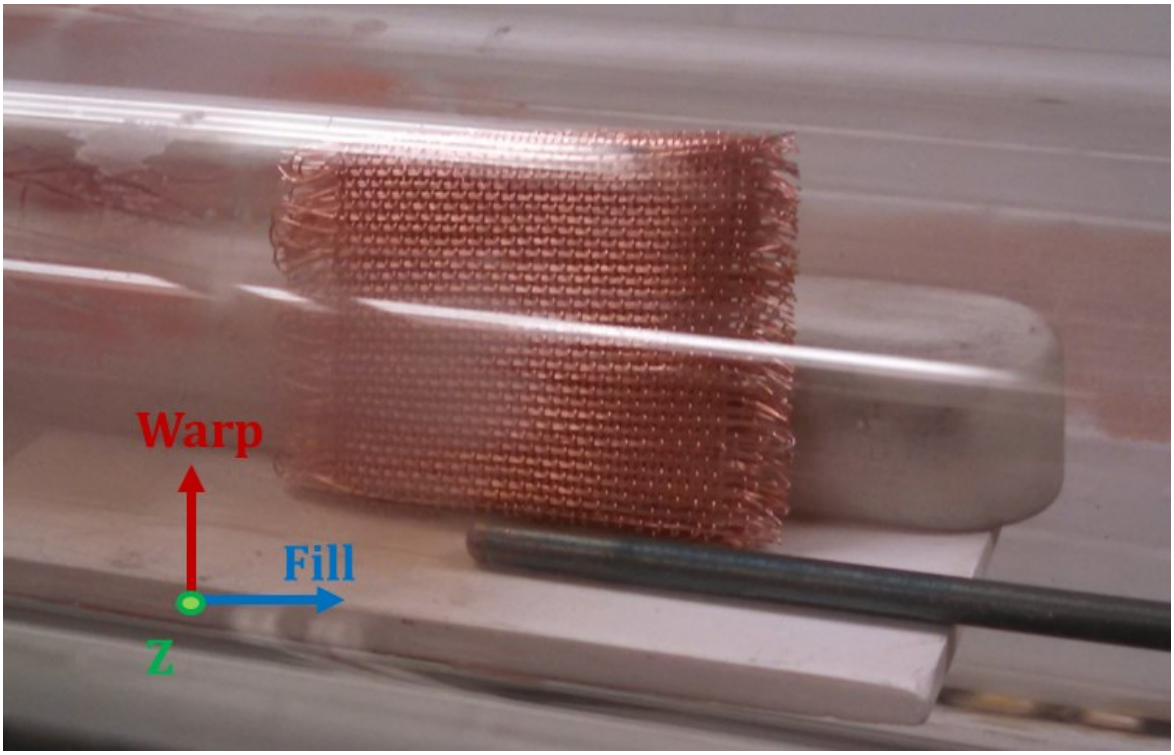

Figure 41: An image of a sample after annealing and before brazing with the warp direction of the material oriented vertically. Supporting materials are alumina and the thermocouple that is used to record the processing cycle temperature is shown in front of the sample.

During brazing the sample was once again supported on alumina substrates inside a quartz chamber that was evacuated and backfilled with a 95%/5% N_2/H_2 gas mixture at

1 psig. The sample was heated to 780°C and held at that temperature for 1 minute in order to ensure uniformity of the sample temperature and even brazing. The sample was then rapidly cooled back to room temperature before being returned to normal atmosphere. Some samples were also directly brazed after being mechanically flattened by hand. This eliminated the annealing step, but there were concerns that the architecture of the material was affected by this bending process, because more twisted wire pairs were observed in the mechanically flattened samples (Figure 42) than in the annealed samples (Figure 43) after brazing.

After brazing, the microlattices were cut into 16x16x3mm samples for permeability and shear stiffness using wire EDM in order to prevent damage. The cut faces were hand polished to 1200 grit finish in order to remove the EDM recast layer and to examine the microarchitecture of the material. Images of the material after brazing are shown in Figures 42-43. Cross sections of the material that was bent flat before brazing as well as the material that was annealed and then brazed are shown.

Comparing the annealed fugitive wire sample directly to the predicted architecture (Figure 44), shows that this process is capable of making bonded, microlattice, fugitive wire structures that are less dense and more permeable than structures than can be directly woven. These materials were further analyzed by Dr. Amanda Levinson and Dr. Richard Fonda at the Naval Research Lab using x-ray microtomography. A reconstruction of the annealed fugitive wire sample after brazing is shown in Figure 45. The results of the tomography confirmed that the annealed samples exhibited the desired fugitive architecture. Discussions of the mechanical properties and the permeability of these structures can be found in Chapter 4.

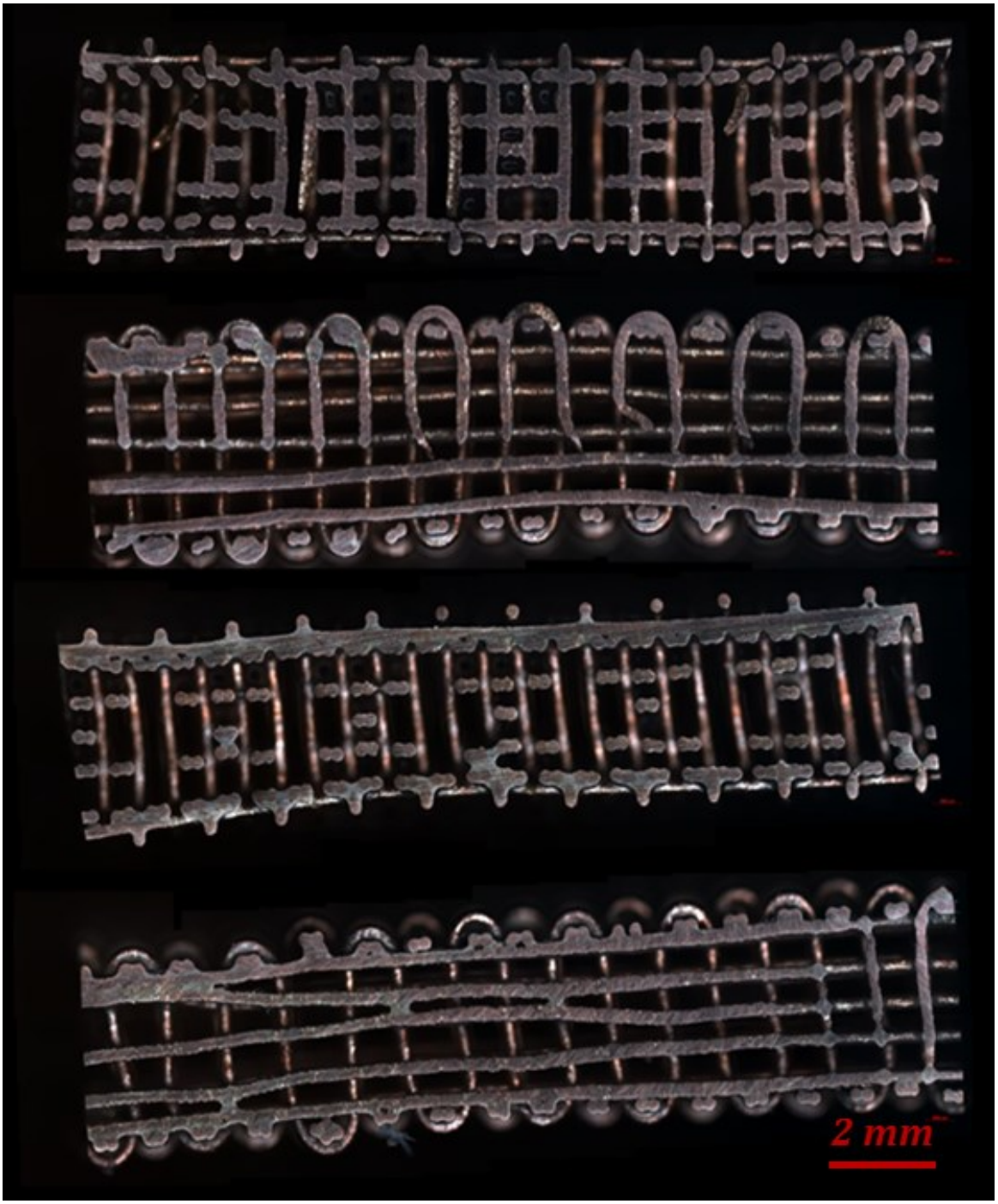

Figure 42: Images of the material after brazing at 780°C, cutting, and polishing. The images show all four faces of the warp/z or fill/z plane of the material. The sample was annealed at 650°C for 3 hours and brazedat 780°C for 1 minutes. It appears to maintain the as-woven architecture after the braze wires were removed.

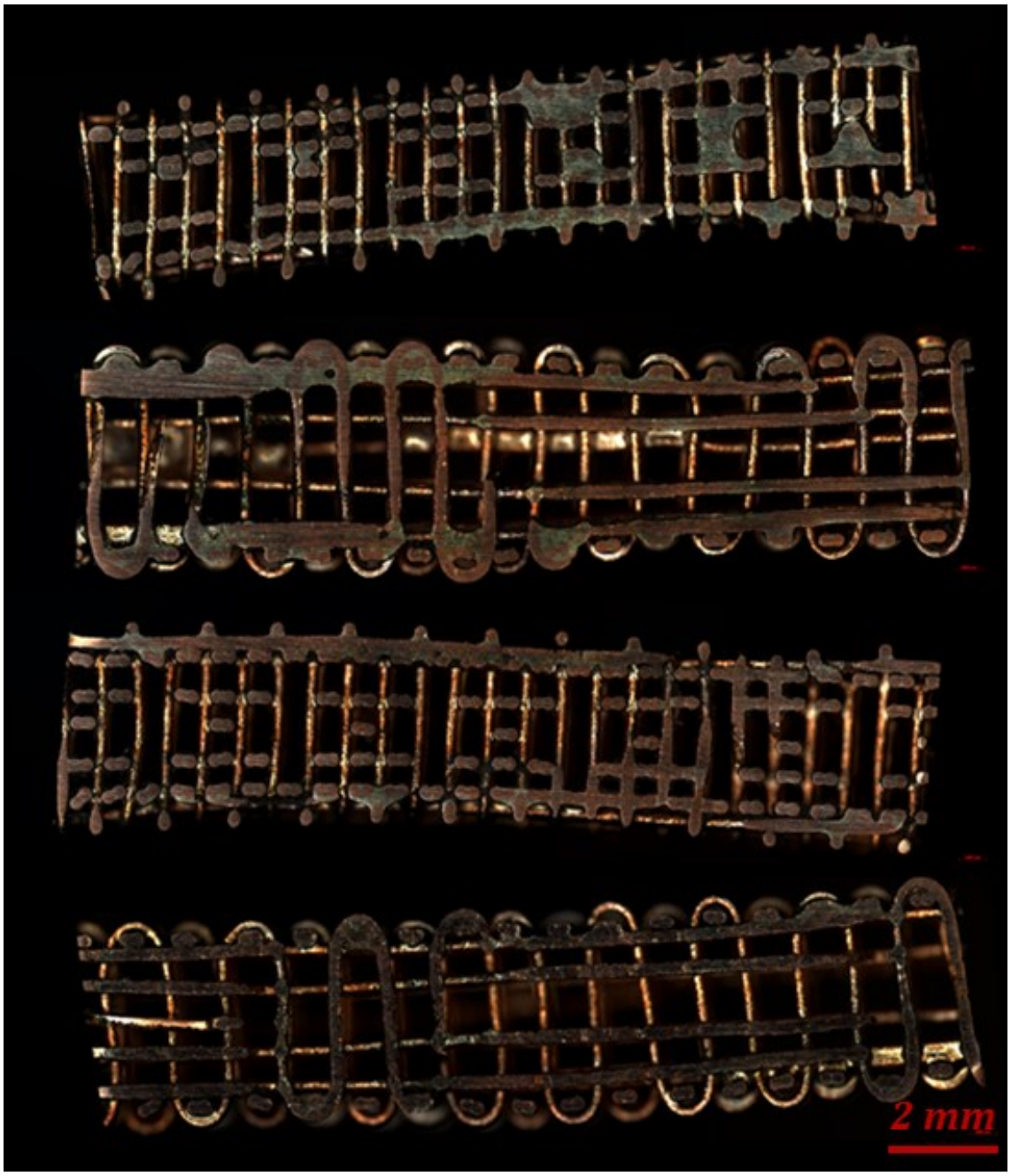

Figure 43: Images of the material after brazing at 780°C, cutting, and polishing. The images show all four faces of the warp/z or fill/z plane of the material. The sample flattened by bending by hand and brazed at 780°C for 1 minute. The sample on the shows evidence of braze clumping in the sample which indicates possible defects and deviations from the woven architecture.

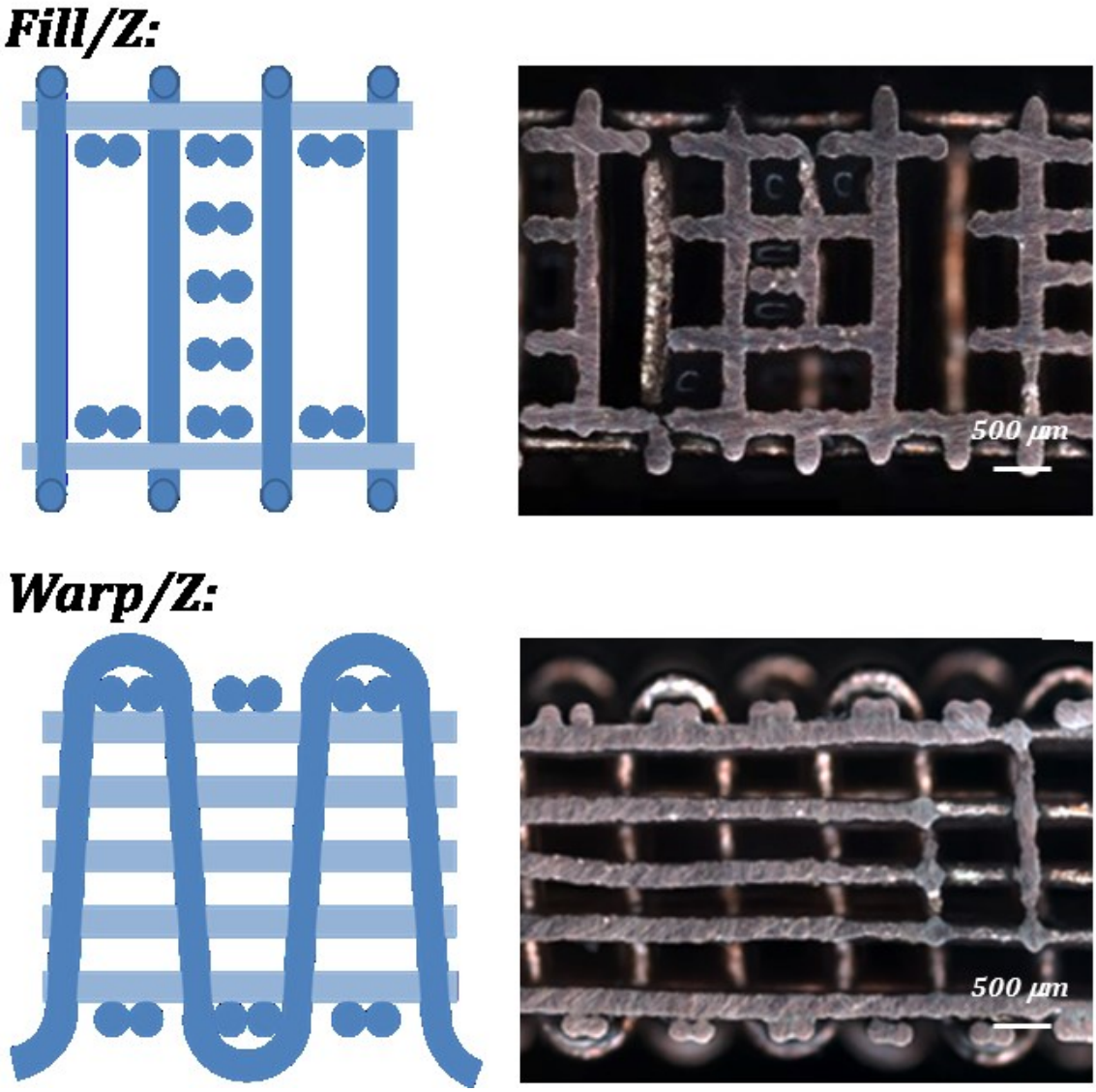

Figure 44: Modeled images of the fill/z and the warp/z planes of the fugitive wire weaves after brazing. The silver-copper eutectic braze have melted and migrate to the junction in the material to bond it together. The real material (shown on the right) was annealed at 650°C for 3 hours and then oriented with the warp direction vertical for brazing at 780°C for 1 minute.

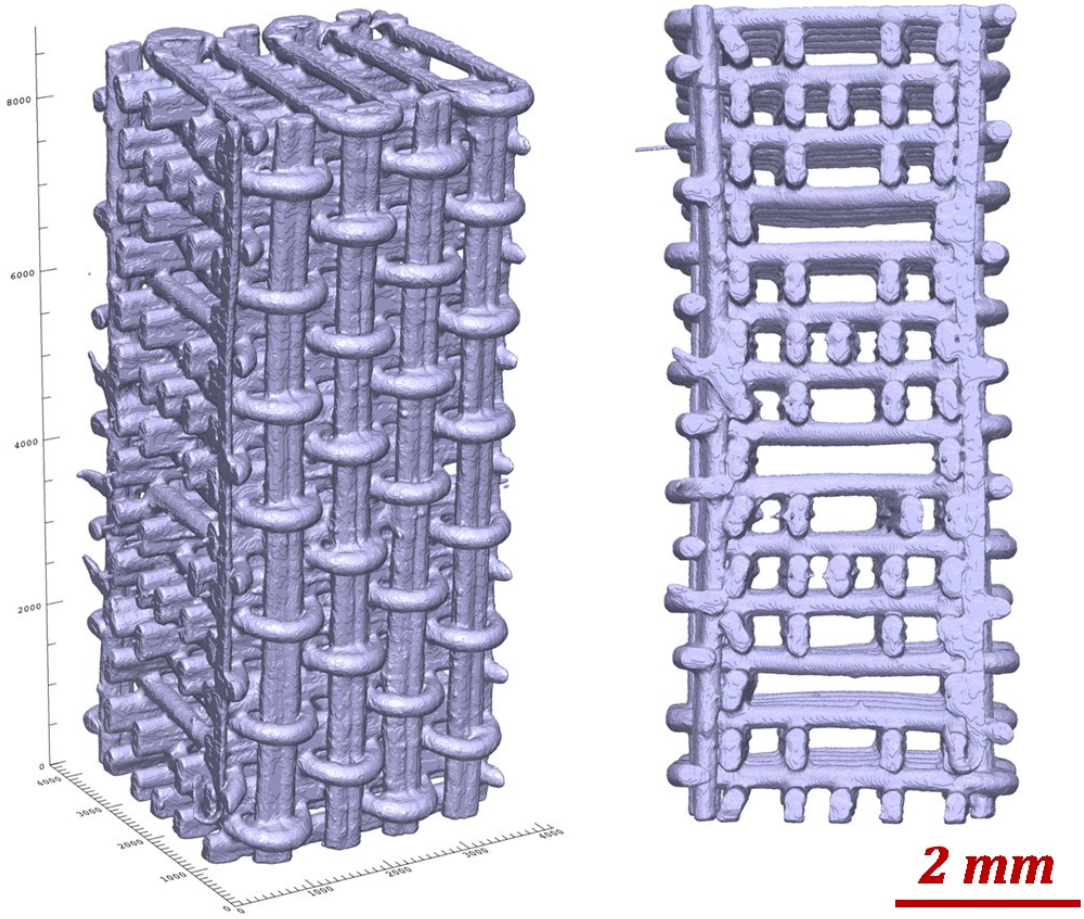

Figure 45: X-ray microtomography reconstructions of the annealed and brazed fugitive wires microlattice material. The sample was annealed at 650°C for 3 hours and then oriented with the warp direction vertical for brazing at 780°C for 1 minute under a 95% N2/ 5% H2 atmosphere. (Courtesy of NRL).

3.2.4: Brazing of NiCr Weaves

The above work has focused on the brazing of 3D woven OFHC copper microlattice materials. Preliminary work was also performed to braze the Chromel-A woven structures as well. Since the Cr_2O_3 surface oxide cannot be reduced by heating in a hydrogen environment, and chemical fluxing agents wanted to be avoided, a brazing

alloy was selected that would be able to successfully wet the surface of the NiCr wire without the need for a chemical fluxing agent. A single layer NiCr sample was prepared and sandwiched between 6 foils (~25% mass gain) of Nicrobraz brazing alloy. The sample was then heated to 1075°C for 5 minutes under a 98% N_2 / 2% H_2 atmosphere. After brazing, the sample was EDM cut to 16 mm x 16 mm and polished to 1200 grit by hand. The cross-sections of the material after brazing is shown in Figure 46.

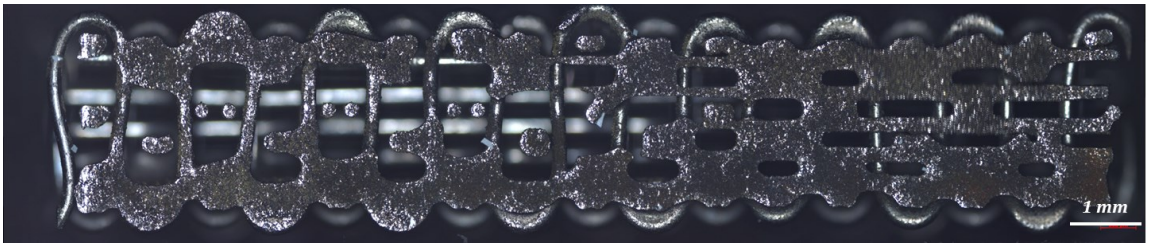

Figure 46: Warp/z plane of the brazed NiCr weave after brazing with 6 foils(~25% mass gain) of Nicrobraz at 1075°C. It appears that this alloy is able to penetrate the weave and preferentially bond the structure together, however, it does not appear to have to same uniformity of selectivity as the brazing alloy with the copper weaves.

This initial work on brazing the NiCr weaves shows that brazing is an option for preferential bonding of the NiCr weaves. The braze appears to successfully bond the weave together, but the alloy does not seem to wet the surface as well and the braze appears to clump in the junctions more than with the silver-copper alloy on the copper weaves. Fine tuning of the processing parameters and the brazing alloy should be performed and confirmed in combination with imaging, mechanical, and permeability testing.

Although brazing is the primary method for bonding the 3D woven copper structures, the necessary work to develop an appropriate brazing process for the NiCr

weaves is still in its infancy. This is a result of the fact that other bonding techniques were developed for the NiCr weaves which are the topics of the other sections in this chapter.

3.3: Vapor Phase and Transient Liquid Phase Processing

In order to make 3D woven metallic microlattice materials for high temperature applications, Chromel-A wires were woven. Chormel-A alloys are capable of use in air at temperatures up to 1200°C, although they often become brittle at these temperatures. Brazing was used to initially bond wires together (as discussed above), however, the addition of brazing material lowers the maximum use temperature of the microlattice material. Also, many of the brazing alloys also form brittle intermetallics that may also negatively affect the properties of the microlattice materials.

Previous work in the areas of MEMS [72] and periodic cellular materials [73] have shown that the properties of these materials can be drastically improved through use of a pack aluminization processing. In both of these examples, Ni-based materials (non-superalloys) were formed using conventional processing techniques. After the materials were formed into their desired shape (through LIGA-Ni processing or conventional sheet and tube drawing and forming), they were then pack aluminized to build up a Ni-Al surface coating. The material was then homogenized at high temperatures in order to diffuse the aluminum into the structure. Since both of these examples were for materials where the maximum thickness was less than 1 mm, the aluminum is able to diffuse through the full thickness of the material. The materials were then heat treated in order to

bring out the superalloy γ-γ' microstructure, which improves the overall high temperature properties of the material (particularly creep resistance). This allows for the creation of superalloy materials and structures with small dimensions that would be prohibitively difficult or expensive to manufacture with conventional rolling, shaping, or forming techniques due to the low ductility and high strength of superalloy materials.

As a result of the many advantages (creep resistance) of the material that results from this processing technique, our collaborators at Northwestern University pursued bonding and alloy modification of the NiCr weaves through vapor phase aluminization and transient liquid phase bonding. In this manner, they are able to form 3D woven, bonded, super alloy microlattice structures. A short summary of their work is included in this thesis for completeness.

3.3.1: Vapor Phase Aluminization

Chemical vapor deposition/pack aluminization process was selected for use in the formation of 3D woven NiCr microlattice materials. This technique can in principle be used to turn the NiCr woven lattice materials into a Ni-Cr-Al superalloy microlattice structure since, the diameter of the wire is sufficiently small (202 μm). Additionally, the aluminization process is very conformal, so the deposition of aluminum at near wire to wire junctions should also be possible. After homogenization, the wire junctions possess the same Ni-Cr-Al composition as the rest of the structure, and then the γ-γ' microstructure can be precipitated out during further heat treatment.

This portion of the project is being performed at Northwest University, and details of the processing can be found in the literature [74,75]. A brief summary is included here because it does highlight a method that would allow for the development of 3D woven Ni-based superalloy microlattice materials that could be useful for high temperature multifunctional applications. Due to the high strength and low ductility of these Ni-based alloys, procuring small diameters of wire and weaving them would be prohibitively difficult and expensive. Moreover, vapor phase processing can in principle also be used to bond wire nodes within the structure since the wires swell with the addition of the Al. Unfortunately, this bonding process is highly dependent on wire spacing, since it bonds adjacent wires by growing one wire into the other. Current work has only been able to achieve ~50% bonding efficiency [74].

3.3.2: Transient Liquid Phase Processing (TLP)

As discussed in the previous section, the vapor phase aluminization process is capable of successfully depositing aluminum onto the surface of the NiCr woven structures and has the ability to bond touching wires together. The main drawback of this process is that the bonding efficiency of the aluminization process is negatively affected by the gaps that are present in the material as a result of the weaving process. In order to overcome the difficulty of bonding these weaves with their inherent spacing, transient liquid phase (TLP) bonding was used. In this process, the addition of elements that form a deep eutectic with the base material forms a phase that is temporarily liquid (as its

composition changes through the eutectic), which can bond the structure. As a result, vapor phase elemental addition was combined with transient liquid phase (TLP) processing in order to overcome some of the drawbacks of the vapor phase aluminization process, while simultaneously increasing the number of elements in the superalloy, and expanding the available types of materials that could be processed in this way.

TLP processing has been shown in the literature as a method to make foams [76] and other porous structures [77] in NiTi-Nb hyperelastic alloys. As a result of their biocompatibility, they are frequently examined for biomedical applications such as scaffolds. Additionally, the starting powders and processing methods allow for fine tuning of the final composition and properties. In previous work, the NiTi-Nb eutectic is used in order to melt, and densify powders of the material. In this work, we also chose to use a deep eutectic alloy to coat, melt, and bond the wires together.

For the NiCr weaves, the wires were alumino-titanized through a vapor phase processing method that is analogous to the vapor phase process that was previously described. After the vapor phase processing, the material was then heated to the point at which the eutectic composition melted locally at the surface. In a manner analogous to the brazing process described earlier, the liquid metal than serves to preferentially bond neighboring wires together through capillary action. This method is able to bond wires together that possess larger gap spacing than the aluminization process that was described previously. Analysis by Richard Fonda, Amanda Levinson, and David Rowenhorst at NRL showed that the bonding efficiency reached efficiencies as high as 90%, but that bonding of the material depending on the type of bond that was being formed (warp/fill, fill/z, and warp/z). As the liquid bonds the wires together, it also alloys with the

neighboring wire material and forms an alloy with a higher melting temperature which solidifies the material. This structure can also be homogenized and solution treated to form the γ-γ' superalloy microstructure.

3.4: Additional Post-Weaving Processing Techniques

Other post-weaving techniques were also used in this project in order to bond and modify the 3D woven metallic microlattice materials. These techniques served to provide alternate methods to bond the materials together in a preferential manner, or to modify the surface of the wire to improve the overall characteristics of the material. In short, these other techniques open the door to a more broad range of possible properties and applications for these materials through the use of post-weaving techniques.

3.4.1: Electroplating

Electroplating of the copper wires with pure copper was perused by Longyu Zhao as a way to preferentially bond the wires together. The technique is based on the fact that electroplating of the wires is a rather conformal process and that as the wires were electroplated, they would grow into one another. This process was unfortunately limited by the wire spacing in the weaves in the same way that the vapor phase aluminization process was also limited by the gaps that are inherent in the weaving process. This

technique, however, did serve as a method that may be later used to roughen the surface of the wires. This gives us the opportunity to tune the friction characteristics of the wires, which are possibly important for damping applications. Additionally, this technique can be used to increase the surface area of the weaves if they are to be used as a chemical catalyst or filter.

3.4.2: Nitrocarburization

Another technique that was also examined in this work is nitrocarburization of the surface of the wire, which was done by Dr. Arthur Heuer and Dr. Hal Kahn at Case Western Reserve University. This process is a vapor phase process that is able to uniformly coat the surface of the wire. It is known to greatly increase corrosion resistance, improve hardness (and subsequently the wear characteristics), and to modify the surface friction [78]. This process is done at low temperature and does not bond the material together and it is designed for use on Ni-based alloys including the superalloy structures described above. The increased corrosion and wear resistance would allow for 3D woven microlattice structures to be used in demanding and highly corrosive environments. Modification of the surface and its coefficient of friction also provides another parameter which may be tuned after the material is already woven. This property in particular may allow for the tuning of the frictional damping properties of these microarchitectured materials for a variety of applications while simultaneously increasing their wear and corrosion resistance.

3.5 Summary

Overall, 3D weaving of metallic wires using the 3WEAVE® process has allowed for the creation of metallic microlattices with well-defined 3D architectures, in a variety of materials, with a process that is scalable and flexible. Through the use of a variety of bonding techniques it has been shown that selective bonding of these structures is possible, which leads to the manufacturing of mechanically stiff and strong materials. As a result, these materials can be viable candidates for multifunctional applications. Through the use of more advanced post-weaving techniques, the architecture, composition, tribology, and various other properties can be controlled. These are a few examples of the many design possibilities that are available to tune these 3D woven microarchitectured lattice materials for specific multifunctional requirements.

Chapter 4: Properties of Metallic Lattices

Although Chapter 5 will focus on the damping properties of out metallic lattices (which was a major focus of my research), a true advantage of these 3D woven metallic lattice materials are their multifunctionality. This chapter is intended to provide a broader view of the properties of 3D woven lattice materials that have been bonded together (predominantly through brazing). My role in the collaborative project has focused on the development of brazing protocols and measurements, but I have also manufactured the majority of the samples that were used to measure mechanical and thermal properties, and a summary of that collaborative work is included for completeness. An examination of the shear stiffness and permeability, for which the material was initially optimized, and the thermal properties of multilayer woven structures, both alone and combined with novel header designs, are discussed in this chapter.

4.1: Stiffness and Permeability

4.1.1: Shear Stiffness

In-plane shear stiffness measurements were used to empirically optimize the brazing process that was discussed in Chapter 3. The majority of the mechanical testing

performed in this subsection was carried out by Dr. Yong Zhang, but I prepared the lattice materials through brazing and EDM cutting to the appropriate size, and helped in developing preparation and testing protocols. In order to confirm the appropriate amount of braze, samples were prepared using different amounts of braze (~5-30% mass gain of braze over the mass of the original weave), for both the standard and optimized pattern weaves in woven OFHC copper. After brazing, samples were then cut into 16 mm (warp) x16 mm (fill) x 3mm (z) square panels using wire EDM. The cut faces of the sample were then polished by hand to a minimum of 1200 grit.

The samples were tested using a micromechanical testing system with a rigid frame and grips that placed the sample in shear. An image of a sample mounted in the shear loading grips is shown in Figure 47. Samples were potted in the grips using Loctite fast drying, high strength adhesive. The grip on the left side of the image is bolted to the frame of the mechanical testing machine. The grip on the right side of the frame is moved by a high precision actuator. That grip is supported in an air bearing for near frictionless linear movement. The Futek 100 N load cell is situated between the air bearing and the actuator, to measure the load applied to the sample in real time. Sequential images of the sample were captured every second by means of a 6 Megapixel Pixelink camera and Digitial Image Correlation (DIC) was used to calculate the displacement of the wires in the images. The output from the load cell and the DIC were then used to calculate the shear stress and shear strain behavior of the material. Unloading curves during the test were used to measure the shear stiffness of the material. The measurements of the shear stiffness of the brazed standard and optimized Cu weaves with various amounts of braze are shown in Figure 48.

Figure 47: Micromechanical sample tester configured for measuring the in-plane shear properties of 16mm x16 mm x 3 mm 3D woven microlattice materials. The sample is potted into the grips in the top and bottom of the image. The left grip is bolted to the frame and the left grip is pulled to the right by means of an actuator. The right side of the grip is supported in an air bearing and the load is measured on that side via a load cell. The strain of the sample is measured using DIC.

The measurements of the shear stiffness of the weaves with various amounts of braze show that as more braze is added, the shear stiffness of the weaves continues to increase (except for the second data point in the standard weave which decreases a small amount compared to the other sample with less braze). If we examine the standard architecture weaves, we can see that there is a large increase in the shear modulus from the first two samples with the smallest mass gains to the samples with the two highest mass gains. The sharp increase in shear modulus indicates that the brazing is bonding the wires together and efficiently increasing the shear modulus. In the two samples with the largest mass gain, there is a small increase in shear modulus as more braze is added. This

indicates that the ideal amount of braze is likely in the mid 20% range, where the increase in the amount of braze drastically increases the stiffness of the material. Unfortunately, only two measurements of the shear modulus of the optimized weaves were carried out, and there is insufficient data to provide similar indications of the ideal mass gain. Therefore, this data must be used in combination with the other results that were already shown and the permeability measurements which are shown in the next section.

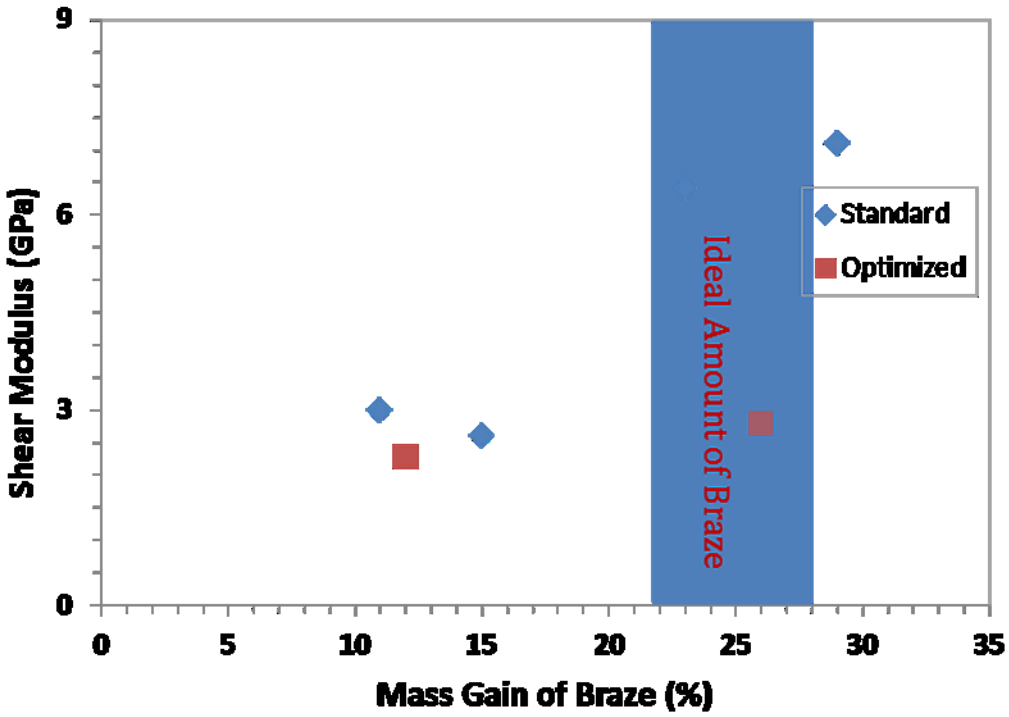

Figure 48: Measurements of the shear modulus of the standard and optimized architecture Cu weaves after brazing with various amounts of braze. The ideal mass gain is highlighted in blue and is centered around 25% mass gain.

4.1.2: Fluid Permeability

The shear stiffness measurements were complemented by measurements of the fluid permeability of the woven material. The measurements of these materials were performed by Longyu Zhao, but I brazed and cut the samples to the appropriate size and hand polished the faces of the sample to prepare them for testing. The working fluid that was used for the testing was polyethylene glycol (PEG) as a result of its high viscosity, which increased the resolution of the pressure measurements. The samples were sealed into the fixture using soft polymer foam in order to ensure that the fluid traveled through the sample and not through the space between the sample and the wall of the fixture. An image of the sample in the fixture is shown is Figure 49.

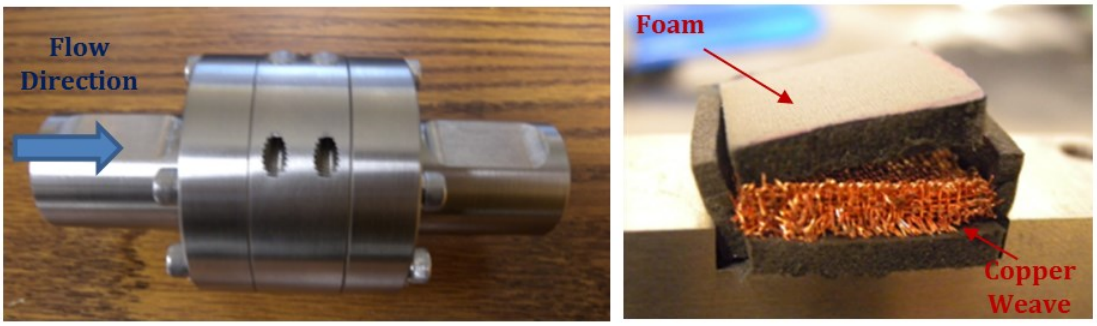

Figure 49: The permeability testing fixture is shown on the left after it was assembled and ready for fluid permeability testing. The image on the right shows a woven copper sample surrounded by sections of low density foam before being mounted in the fixture.

After the sample was loaded into the fixture, the cross-sectional area was measured using an optical microscope. The fixture was then assembled and the differential pressure

across the sample and flow rate were varied and measured for each test. The permeability was calculated in the laminar flow regime. The permeability measurements of the standard and optimized architecture brazed Cu weaves with various amounts of braze are shown in Figure 50.

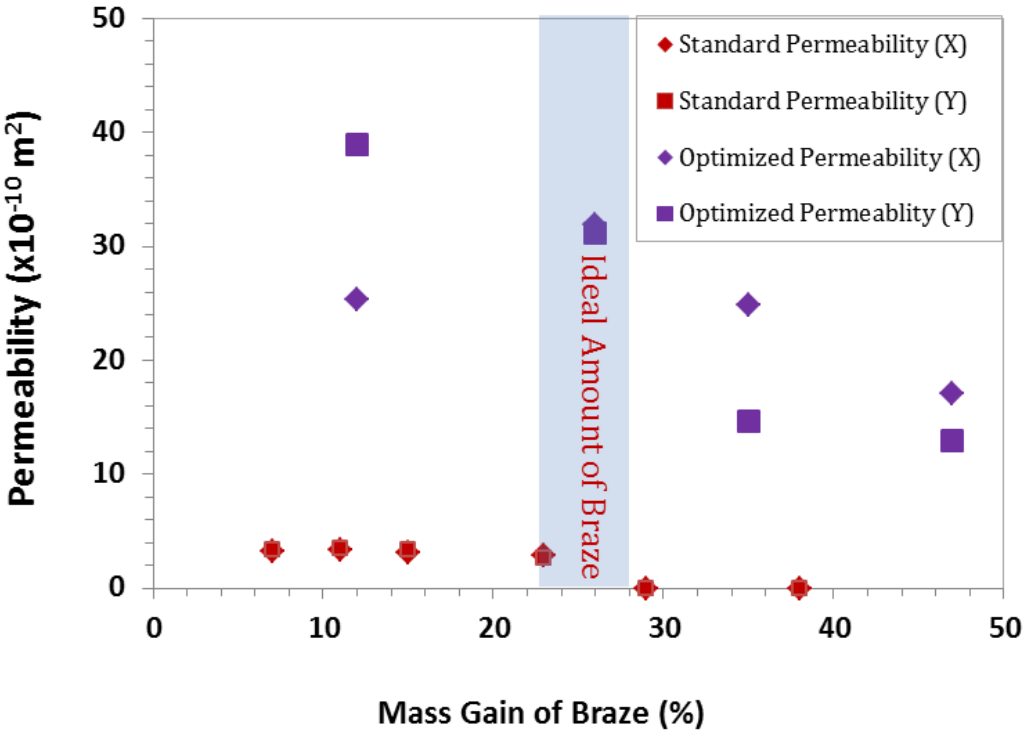

Figure 50: Measurements of the shear modulus of the standard and optimized architecture Cu weaves after brazing with various amounts of braze. The ideal mass gain is highlighted in blue and is centered around 25% mass gain.

The results of both the in-plane shear testing and the permeability testing of the standard and optimized brazed copper weaves for samples that were brazed with various amounts of braze, in addition to the brazed fugitive wire weaves are summarized in Table 10.

Table 10: Summary of the shear stiffness and permeability measurements of the standard, optimized, fugitive brazed copper samples

Amount of Braze	Permeability ($x10^{-10}$ m^2)			Mechanical Properties
Standard Pattern Brazed Copper Samples				
Mass Gain (%)	X	Y	Z	Shear Modulus (GPa)
6	3.23	3.65	3.35	N/A
11	3.37	3.60	3.51	3.0
15	3.05	3.21	3.31	2.6
23	2.85	3.04	2.56	6.4
29	N/A	N/A	N/A	7.1
Optimized Pattern Brazed Copper Samples				
12	25.3	38.9	N/A	2.3
26	31.9	31.2	N/A	2.8
35	24.8	14.7	N/A	N/A
Fugitive Wire Copper Samples				
-	45.3	47.8	8.8	2.4

The shear stiffness and permeability measurements show that for the standard structure a mass gain in the mid 20% range maximizes the shear stiffness and minimizes the decrease in permeability in the brazed structure. The results from the optimized structure showed that a similar percent increase in mass gain also resulted in an ideal amount of braze in order to maximize the shear stiffness and minimize the decrease in permeability. This is in agreement with the analytical predictions of the amount of braze

needed to fully bond the weaves and previous cross-sections of the material, which showed that the large channels in the material begin to fill in with braze after the smaller pores and cavities formed between tangential wires are filled with braze. From the cross-sectional images, 3D reconstructions, and the stiffness and permeability data, it appears that this occurs when we add more than 30% or more braze by mass. Additionally, the greatest gains in shear stiffness are the results of bonding of the tangential wires. Adding more braze fills in the channels of the material, but it only moderately increases the shear stiffness of the materials. As a result, filling in the channels results in a small increases in the shear stiffness of the material over the properly bonded cases [50,51].

The measurements of the fugitive wire samples shows that the concept of fugitive wires makes samples that are almost twice as permeable as the optimized structure, with a minor decrease in shear stiffness, with the further addition of braze. This may serve as a guide for further studies where more possible 3D woven microarchitectured material designs may be explored.

4.2: Thermal Transport of Cu Lattice Materials

As a result of the high thermal conductivity and surface area of the 3D woven microlattice copper materials, the thermal transport properties of these weaves and their applications as a thermal cooling device is of interest. A geometry of 25.4 mm x 25.4 mm x 76.2 mm was initially defined as a starting point for a heat transfer device with

applications for the cooling of laser diodes [70]. For these types of applications, a high heat transfer coefficient is important in defining the performance of a cooling device. Additionally, since the output wavelength of a laser diode is sensitive to the operational temperature, the device must exhibit high thermal performance without substantial temperature gradients (usually ± 1°C), a low pressure drop across the material (less than 1 psi), and requiring a low flow rate (1-10 L/min).

The testing of the thermal characteristics of these materials was performed mostly by Longyu Zhao, but I fabricated the multilayer lattice blocks both with and without facesheets, and fabricated the header structures that were coupled with the weave using both copper and ABS plastic. A testing fixture was designed that allowed heat to be applied to one of the 25.4 mm x 76.2 mm warp/fill faces of the sample by means of a kapton resistance heater. The fixture allowed for fluid to flow in a variety of orientations through the remaining five faces of the sample.

4.2.1: Serial and Bifurcated Flow:

The two primary flow patterns that were examined were 'serial' flow, in which the fluid flowed down the 76.2 mm warp direction of the material with the inlet being the two smaller 25.4 mm x 25.4 mm fill/z faces of the sample. In the alternate 'bifurcated' flow pattern, fluid enters the samples through the 76.2 mm x 25.4 mm warp/fill face that is opposite the heated surface. The fluid then exits the sample through both 25.4 mm x

25.4 mm fill/z faces of the material. An image of the fixture that was used to measure the samples is shown in Figure 51.

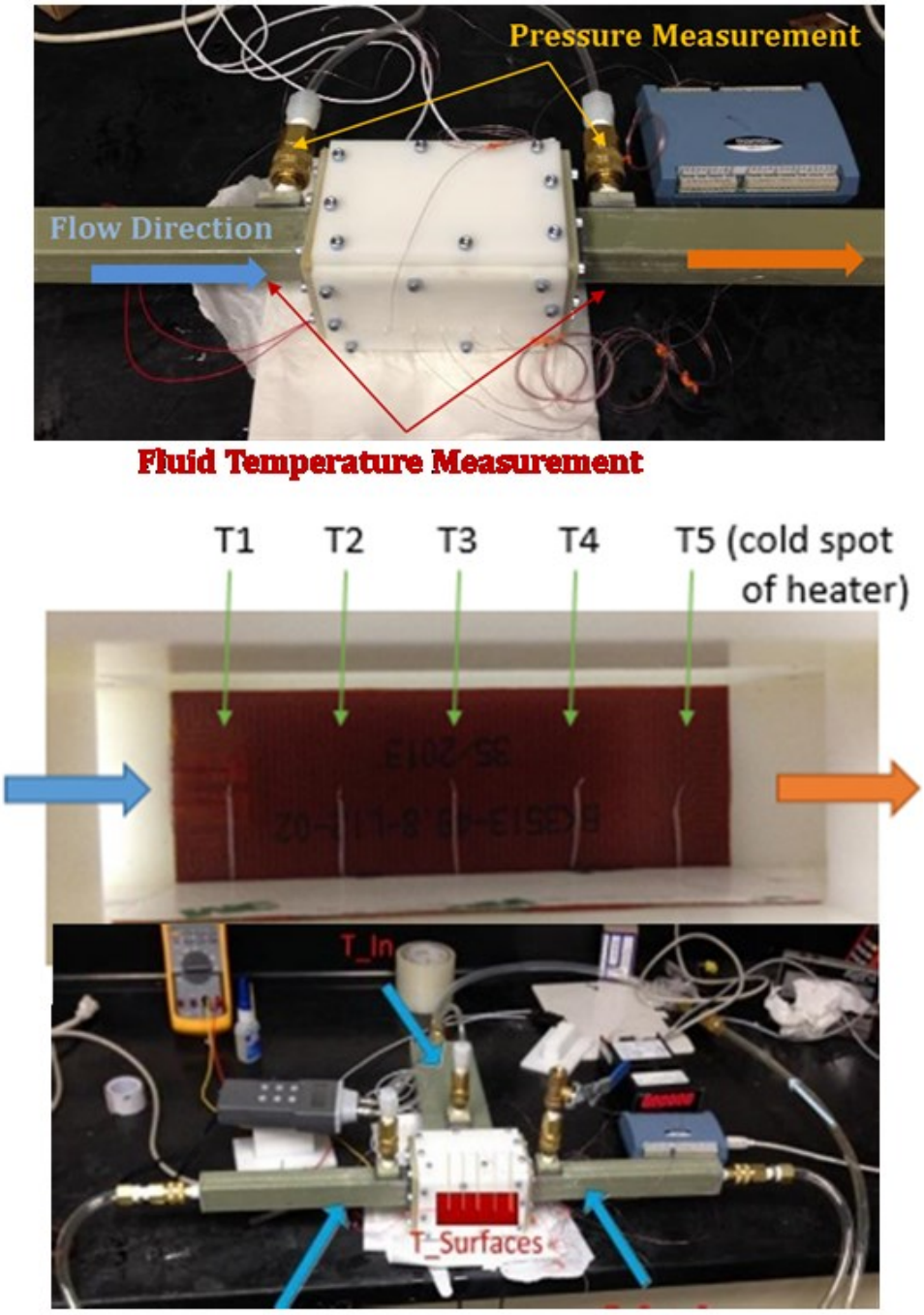

Figure 51: The heat transfer measurement fixture shown in two configurations. The image on the left shows the system arranged for serial flow and the bottom right image shows the system setup to measure bifurcated flow. The image in the upper right corner shows the kapton heater and the associated thermocouple that measure the surface temperature during a test. (Image courtesy of Longyu Zhao)

4.2.2: Impinging Flow with Weaves and Headers

A third flow pattern was also defined for the weaves and is referred to as the 'distributed' flow pattern. The intention was to increase the heat transfer coefficient and to decrease the thermal gradients across our copper weaves through the use of an impinging distributed flow design. This design was developed to take advantage of the unique properties of our copper woven micro lattices. In order to possess high heat transfer coefficients with low thermal gradients (which are properties that are frequently at odds in conventional heat transfer devices), we determined as a result of modeling and the experiments with the other two flow patterns, that it is important to put the impinging cold water as close as possible to the hot material in order to maximize the amount of heat that is transferred from the heat source to the working fluid. In order to put the cold incoming fluid as close as possible to the heat source, we decided to decrease the sample dimensions perpendicular to our heat source (fill direction) and to use an impinging flow design where fluid flows towards the heated surface (through the fill direction) and exits the system by flowing along the heated surface (along the warp direction) and out the sides (the fill/z plane). Through experiments in which fluid passed through the warp direction (linear flow), we found that the efficiency of the heat transfer decreases down the flow direction since the average temperature of the fluid increases down the length of the flow direction. The temperature difference between the device and the fluid becomes smaller as the fluid temperature rises because the convective transfer decreases. This decrease in convective efficiency leads to an increases in the thermal gradient from the inlet to the outlet of the device. In order to concentrate the flow near the hot surface, and to minimize the thermal gradient along the device, we developed a header to provide

distributed local flow of cold water into our lattices while making use of our current heat transfer measurement equipment for testing impinging flow in 25.4 mm x 25.4 mm x 76.2 mm samples.

Multiple designs were developed to control the fluid. We designed the system to be easily and quickly fabricated, to provide the maximum amount of cold water as close to the heated surface, to minimize thermal gradients across the heated surface in both in-plane directions, and to meet the dimensions that could be tested within our current testing fixture. A 3-D rendering of our selected design in shown in Figure 52.

In the selected design, a 1"x 3" wall of cold water impinges on the upper plate of the tube structure. Water is then distributed into the array of 3/16" tubes. Fluid that travels through the tubes impinges on the layer of copper weave that is brazed to the heated lower copper plate. Fluid then absorbs heat as it passes through the weave and exits through the smaller 1/8" holes in the lower plate into the central chamber between the upper and lower plate. The hot water then exits out the sides of the device. A schematic top down view of the lower plate is shown in Figure 53.

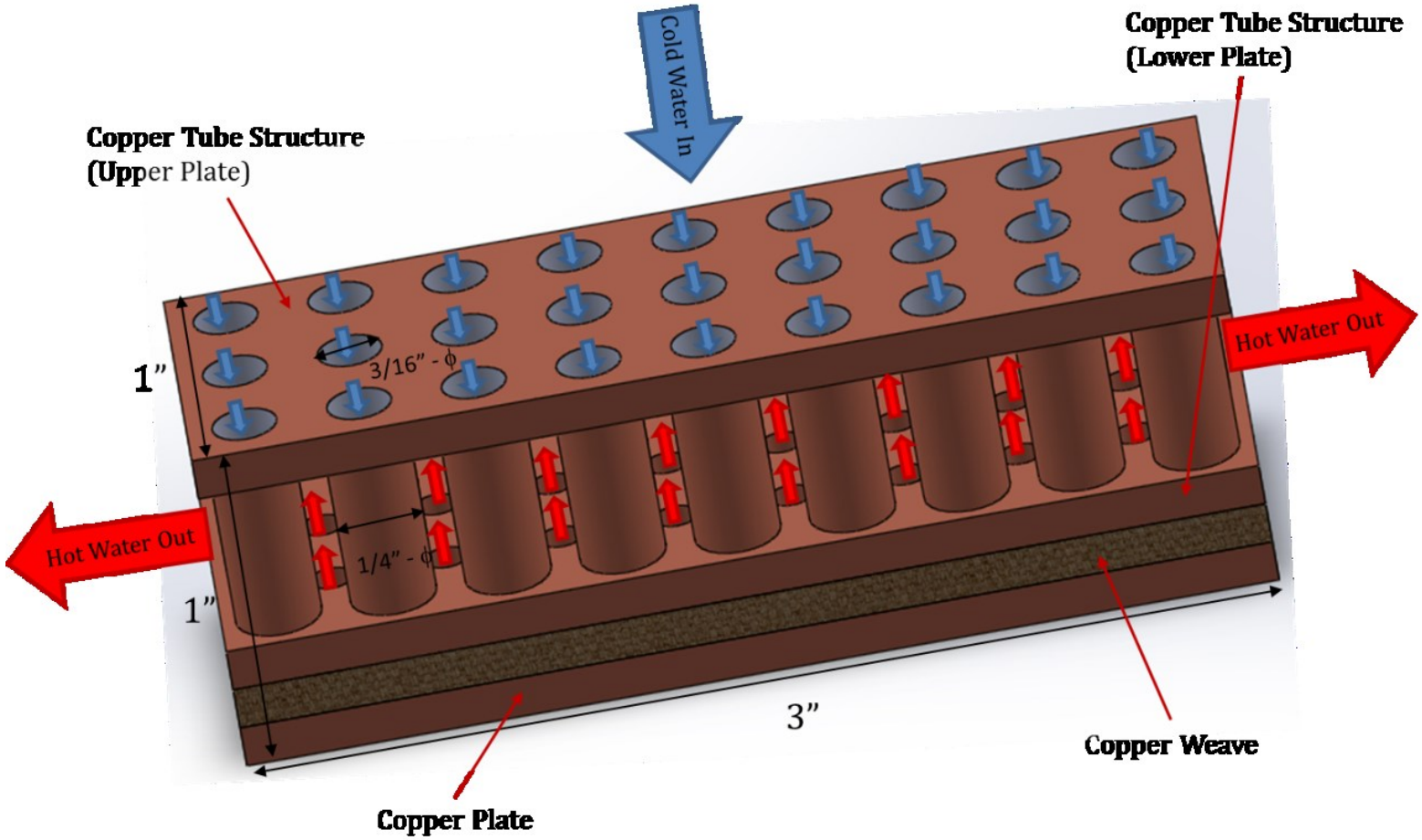

Figure 52: A 3D rendering of our Distributed impinging flow (DIF) heat transfer device with a single 1/8" thick layer of woven copper material. Cold water enters the system through the series of holes in the upper plate and flows thorough tubes in the structure (which is shown in Cu, but was also made in ABS plastic). Cold water than enters the copper woven material and absorbs heat as it flows to the exit holes in the lower plate. Fluid that leaves the weave though the holes in the lower plate then flows out the ends of the device as shown by the large red arrows.

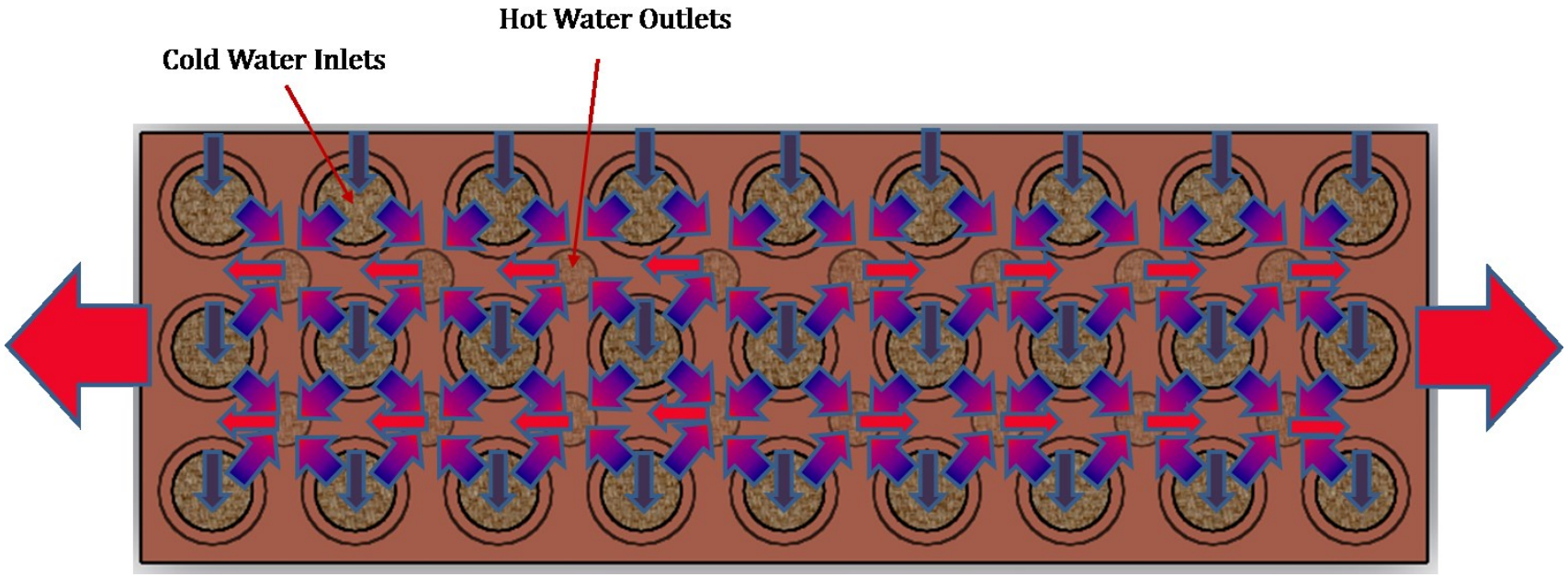

Figure 53: Top down view of the lower plate illustrating the path of water through the system. Arrow color indicates relative temperature of the fluid with blue representing cold water and red representing hot water. Cold water enters the weave through the larger holes in rows 1, 3, and 5, flows through the weave while absorbing heat, and then finally exits through the holes in rows 2 and 4, and then flows out the ends of the device as indicated by the red arrows.

In order to evaluate the role of sample thickness (perpendicular to the heated surface) while also aligning the samples in the best direction for flow, three samples thicknesses were examined: 12.7 mm, 6.4 mm, and 3.2 mm with the fill direction oriented perpendicular to the heated surface. These samples required the attachment of 20 gauge OHFC copper facesheets to better couple heat into the woven architecture and to compare with the previous results from the other flow patterns. The details of the sample fabrication can be found in Chapter 3.

In order to provide the impinging distributed flow for the fabricated woven structures, the JHU machine shop fabricated the upper and lower plates in 0.125" thick OFHC copper plate and counterbored all holes for the tubes 0.0625" deep into the inner surfaces of the plates. In order to bond the tubes into the counterbores, individual foils of braze were cut from 0.0018" thick foils of silver-copper eutectic braze (Lucas-Milhaupt LM-721 VTG alloy) and were inserted into the counterbores followed by the copper tubes. The assembled structure was than heated to 900°C under a 95% N_2/5% H_2 forming gas atmosphere and held at that temperature for 5 minutes. The structure was then cooled to room temperature under the forming gas atmosphere. Images of one of the plates with the braze foil inserted into it before brazing, the sample in the furnace during brazing, and the final tube structure on a 1/8" thick woven sample is shown in Figures 54-55.

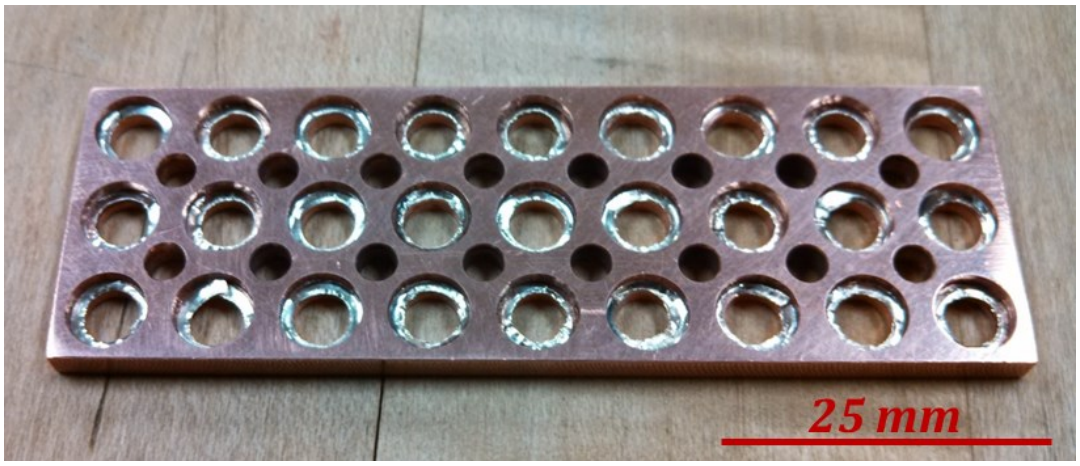

Figure 54: Lower plate of the distributed impinging flow copper tube structure with the 0.0018" thick foils of silver-eutectic braze inserted into the counterbores.

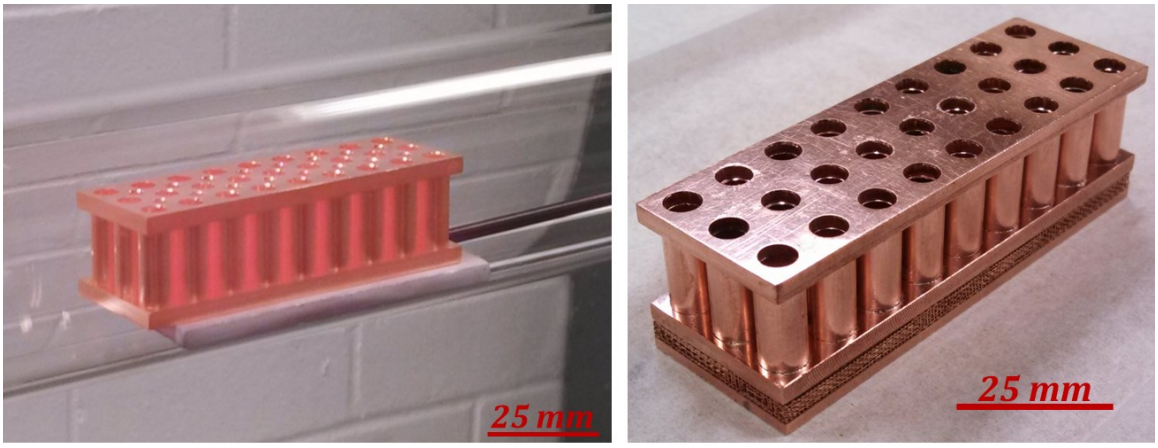

Figure 55: Image of the assembled OFHC copper distributed impinging flow tube structure during brazing at 900°C under a 95% N_2 / 5% H_2 atmosphere (left) and assembled after brazing on top of a 0.125" brazed copper sample (right).

In addition to manufacturing these headers in copper, I also manufactured the same tube geometry through 3-D printing of ABS plastic with a Stratasys Fortus 400mc. Machining, brazing, and polishing of the copper parts was both labor intensive and costly to produce. In order to quickly and inexpensively produce many different header

geometries, 3D printing was used. The 3D printing of these headers was accomplished in a usually 2 days or less, whereas the manufacturing of the copper header took several weeks. After 3D printing parts were mechanical polished to 400 grit to remove printing marks on the top and bottom surface, cleaned with isopropyl alcohol, and chemically polished to ensure that they were water tight. These parts were manufactured in three different heights (9.5 mm, 15.9 mm and 19.1 mm) to match the three different woven structure thicknesses while preserving the 25.4 mm x 25.4 mm x 76.2 mm geometry that the testing fixture was designed to accept. These samples maintained the same hole diameters and spacing of the original copper design and changes in thickness were performed by changing the length of the tubes.

Due to the limited sizes that were readily available in OHFC copper, the initial copper structure was manufactured with inlet diameters that are larger than the outlet diameters. Also, there were more inlets than outlets due to the initial geometry restrictions. Initial modeling results indicated that matching the diameter of inlets and outlets would decrease pressure losses in the system without affecting the heat transfer properties. As a result of the ease and speed of manufacturing by 3-D printing, we manufactured not only the three structures that were based on the initial copper structure, but also three structures (in the same thicknesses) with the same inlet and outlet diameter as the original structure's inlet diameter. Images of the inlet of the 3-D printed structure, the outlet of the structure that matches the copper structure, the outlet of the structure with the same inlet and outlet diameter, and the six structures with their matching woven structures are shown in Figures 56-59.

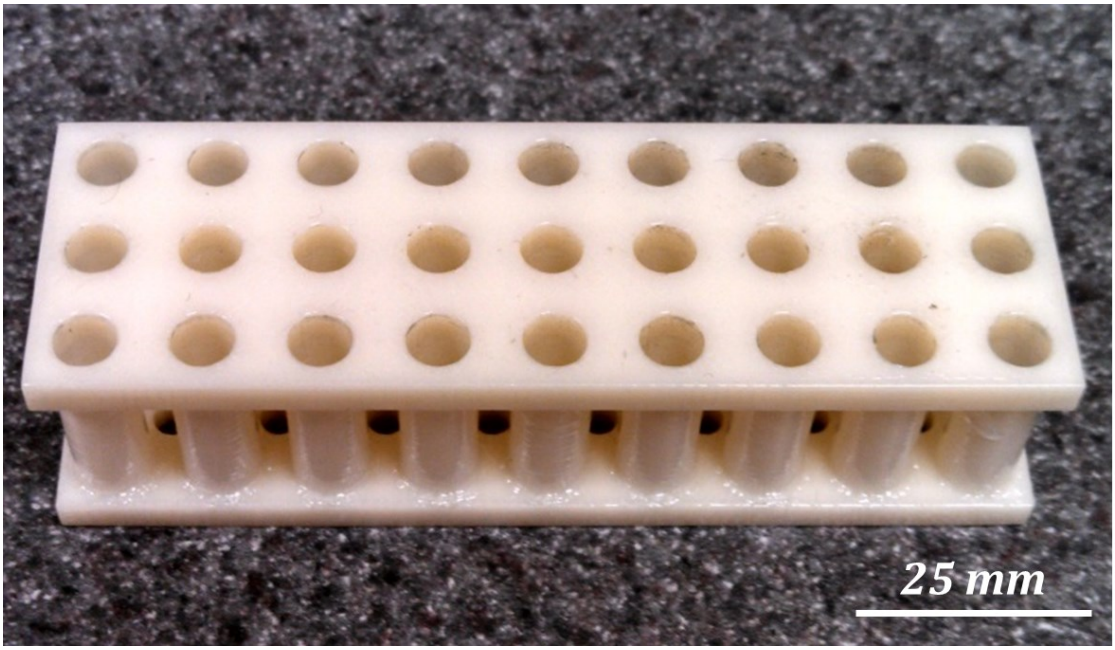

Figure 56: 3-D printed ABS plastic distributed impinging flow structure (0.75" tall) showing the inlet side of the device. The inlet side of the device looks identical for Header Design #1 and #2 of the 3D printed header strucutres since the size and the arrangement of the holes was fixed.

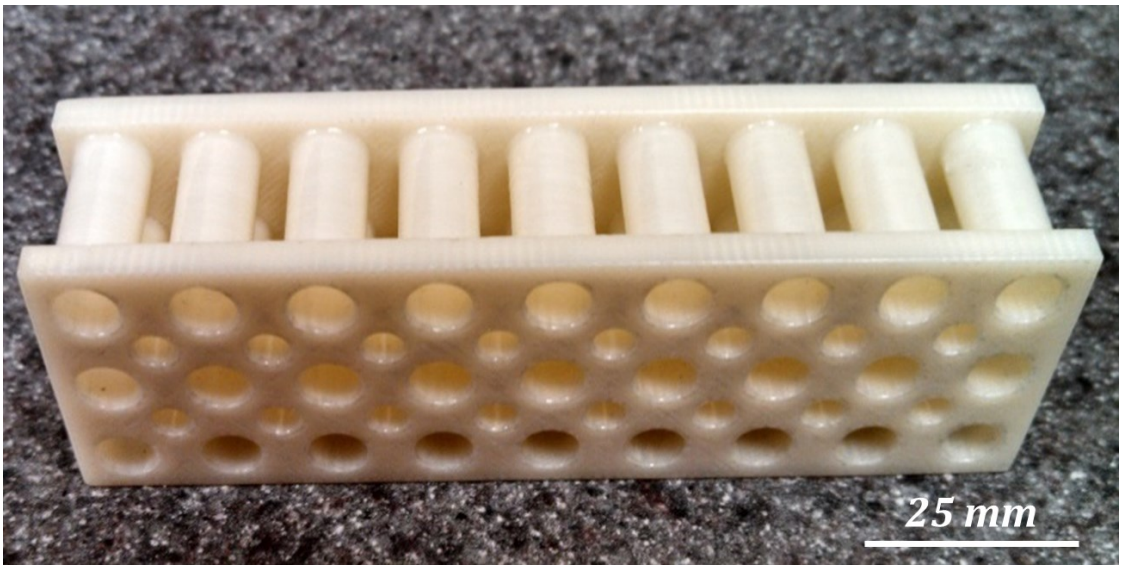

Figure 57: 3-D printed ABS plastic distributed impinging flow structure (0.75" tall) showing the outlet side of the device that matches the copper structure geometry. This geometry is denoted as Header Design #1.

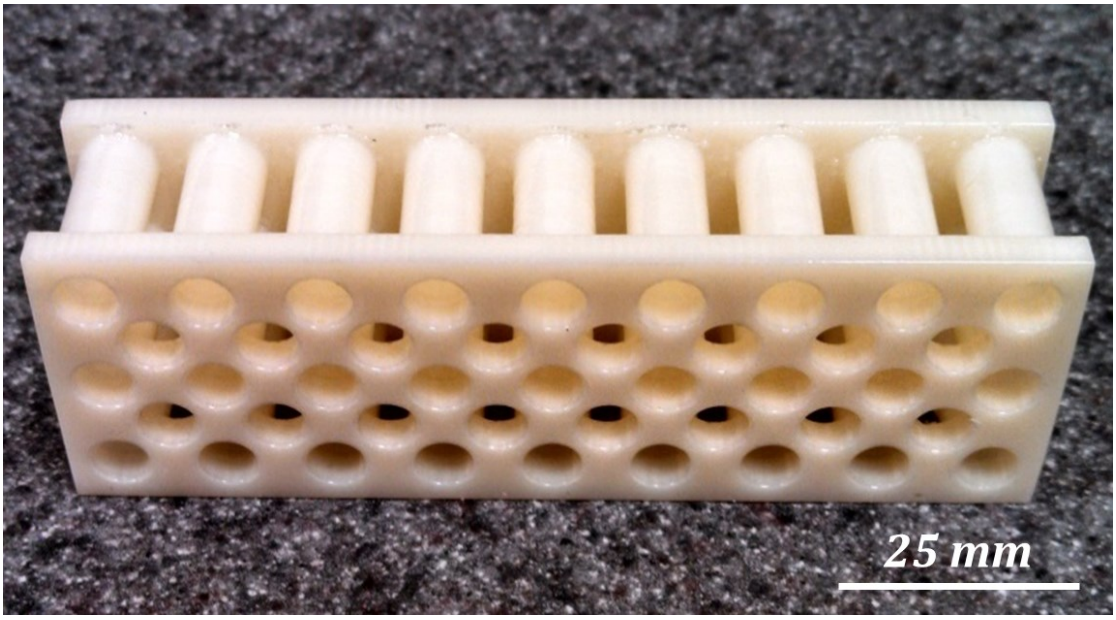

Figure 58: 3-D printed ABS plastic distributed impinging flow structure (0.75" tall) showing the outlet side of the device where the inlet and outlet diameter are the same as the inlet diameter of the previous device. This geometry is denoted as Header Design #2.

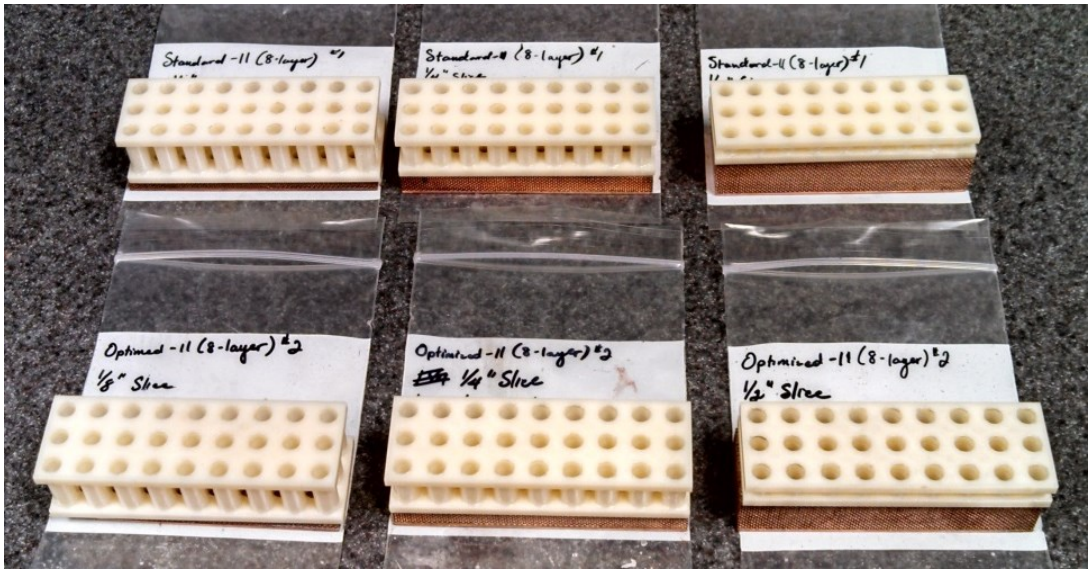

Figure 59: 3-D Printed ABS plastic distributed impinging flow structures of various heights on top of their associated woven copper structures.

Two other designs were also developed in order to provide enough data to properly verify our modeling and provide the opportunity to further optimize the designs. Header Design #3 matched the total inlet and outlet area. The center locations of the inlet and outlet holes were not changed from the two previous designs, but in this case the inlet diameter was decreased to 1/8" to ensure that there would be sufficient web thickness with the increased outlet diameters. The outlet diameter was changed to 5/32" so that the overall area was as close as possible (to the nearest 1/64"). The top and bottom of one of the printed structures is shown in the Figure 60.

Design #4 was made to test the effects of rotating the inlets and outlets by 45° about the z-axis in relation to the weave. Due to the current width limitations of the weave, we were unable to fabricate sections of the weave that were orientated at 45° so we elected to modify the design of the plastic distributed impinging flow structure. The design used inlets and outlets that were the same size (1/8") in diameter and as a result of the rotation the in plane spacing of the tubes changed (by a factor of $\sqrt{2}$ since it is a diagonal of the previous square arrangement). In order to maintain the 1"x3" footprint of the structure one row was lost from the pattern. Subsequently though, the inlet and outlet diameter and total area are equal in this design. The top and bottom of one of the printed structures is shown in Figure 61.

These different structures were likewise printed in the same three thicknesses and the structures are shown in Figure 62.

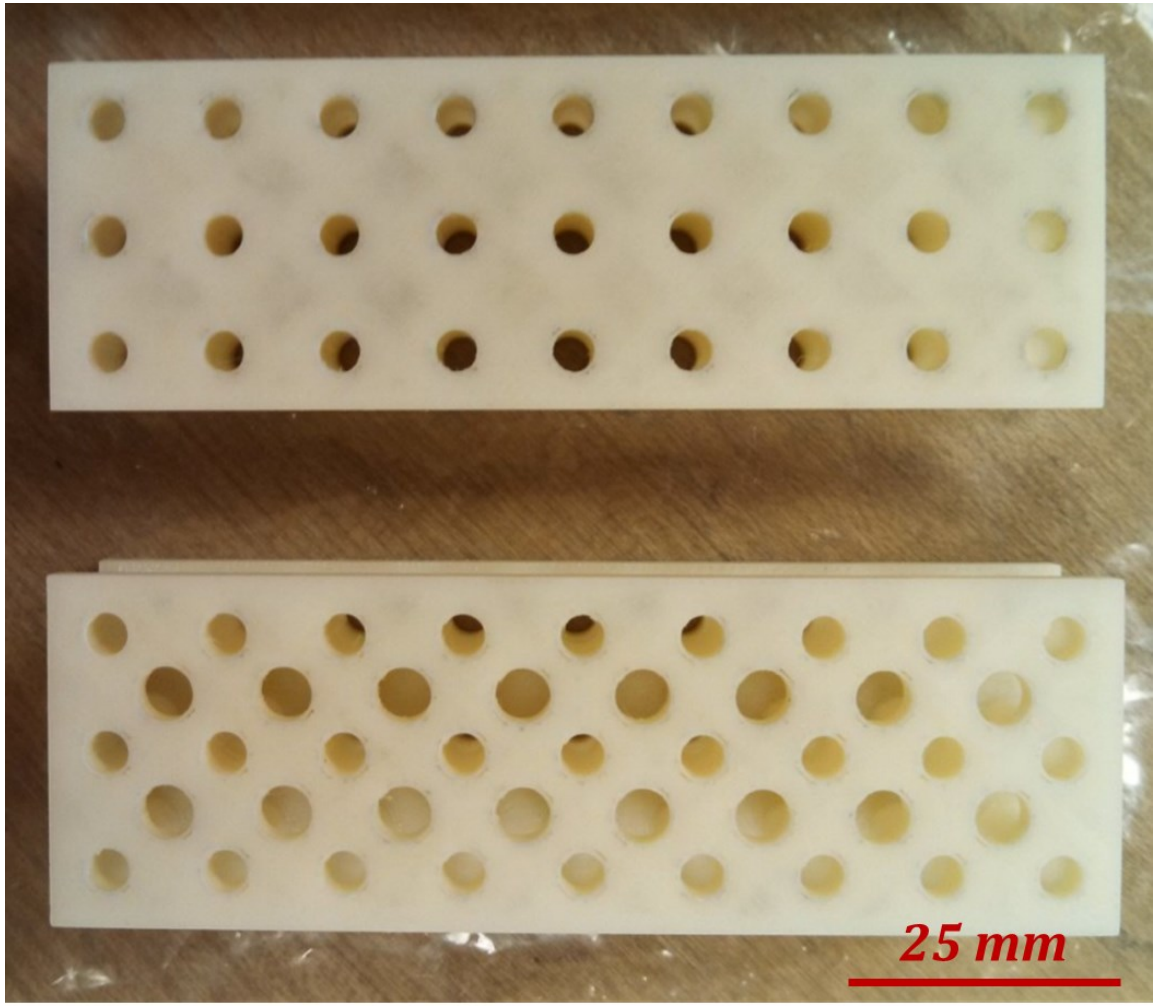

Figure 60: 3-D printed ABS plastic distributed impinging flow structure (Design #3) where the total inlet and outlet area was matched. The upper inlet surface is shown in the upper part of the image and the bottom surface of the structure is shown in the lower half of the image.

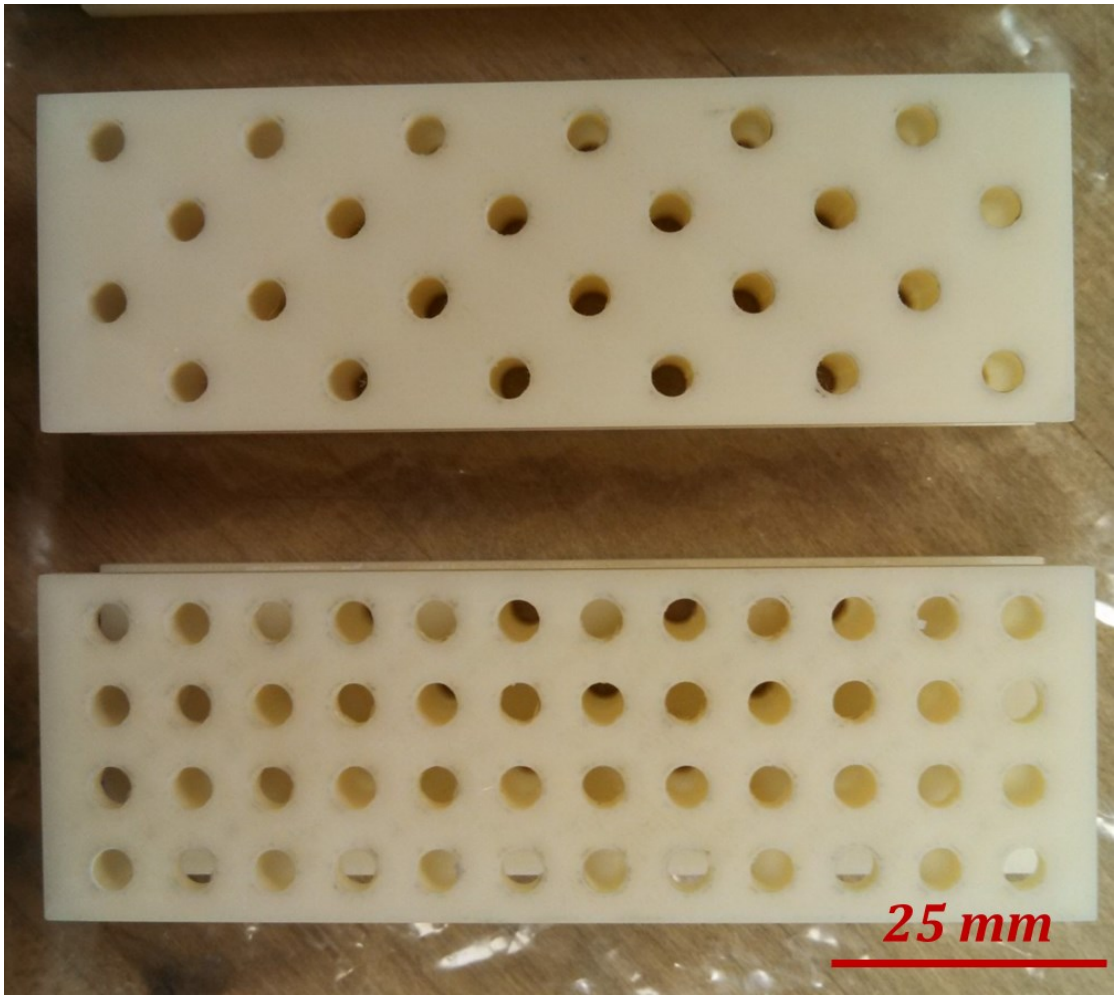

Figure 61: 3-D printed ABS plastic distributed impinging flow structure (Design #4) where the pattern used previously was rotated 45° and the inlet and outlet diameter and total area were matched. The upper inlet surface is shown in the upper part of the image and the bottom surface of the structure is shown in the lower half of the image.

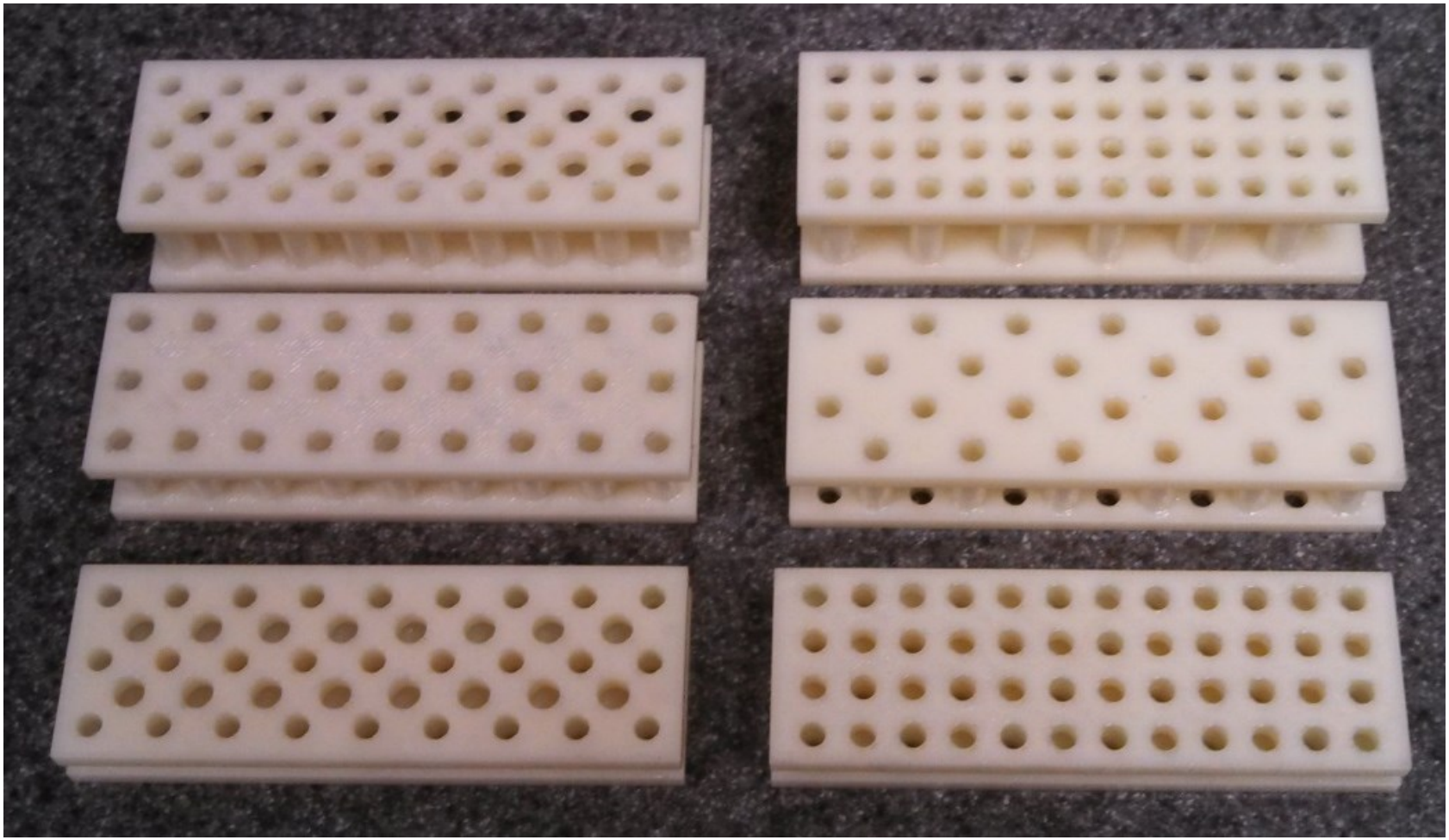

Figure 62: The three different thicknesses (0.375", 0.625", and 0.75") for each of the new patterns. Design #3 is shown on the left and Design #4 is shown on the right with structures decreasing in thickness from top to bottom.

For each test, the differential pressure, flow rate, inlet and outlet fluid temperatures, and the temperature profile of the heated surface of the sample were measured. These values were used to calculate the Nusselt and Reynolds[79] number for our materials for the different flow orientations. The Nusselt number is a dimensionless parameter that describes the convective heat transfer that occurs at a surface. It is defined as,

$$Nu = \frac{hL}{k_f} \tag{20}$$

where, h is the convective heat transfer coefficient, L is the thickness of the woven structure (25.4 mm in our case), and k_f is the conductivity of the liquid. The Reynolds number is another dimensionless parameter that is defined as the ratio of inertial to viscous forces in a moving fluid. As a result it can be used to indicate the onset of turbulent flow and more generally can be used to examine the flow rates of a fluid. The Reynolds number is defined as,

$$Re = \frac{\rho v L}{\mu} \tag{21}$$

where, ρ is the density of the fluid, v is the average velocity of the fluid, L is the thickness of the woven structure, and μ is the dynamic viscosity.

The calculations of the Nusselt and Reynolds numbers for our 25.4 mm x 25.4 mm x 76.2 mm woven microlattice materials in the axial and bifurcated flow patterns were calculated for a series of flow rates and the results of these measurements by Longyu Zhao are found in Figure 63. The measurements of the distributed flow pattern (header and weave) was measured for the ABS Design #1 header (0.75" thick) combined

with the 0.125” thick optimized copper weave. Measurements of the other copper and ABS header and weave samples are currently in progress.

Overall, the 3D woven microlattice structures exhibit greater heat transfer abilities (larger Nusselt number) than fins and foams for similar flows. Additionally, the uniform surface temperature of the axial and bifurcated flow make these attractive for applications that require uniform cooling. The distributed flow designs appear to also outperform the bifurcated flow designs since the thickness of the material has been tuned for increased performance for our application. These thermal properties, combined with the strength and damping properties, make these 3D woven metallic microlattices a material with many promising multifunctional applications.

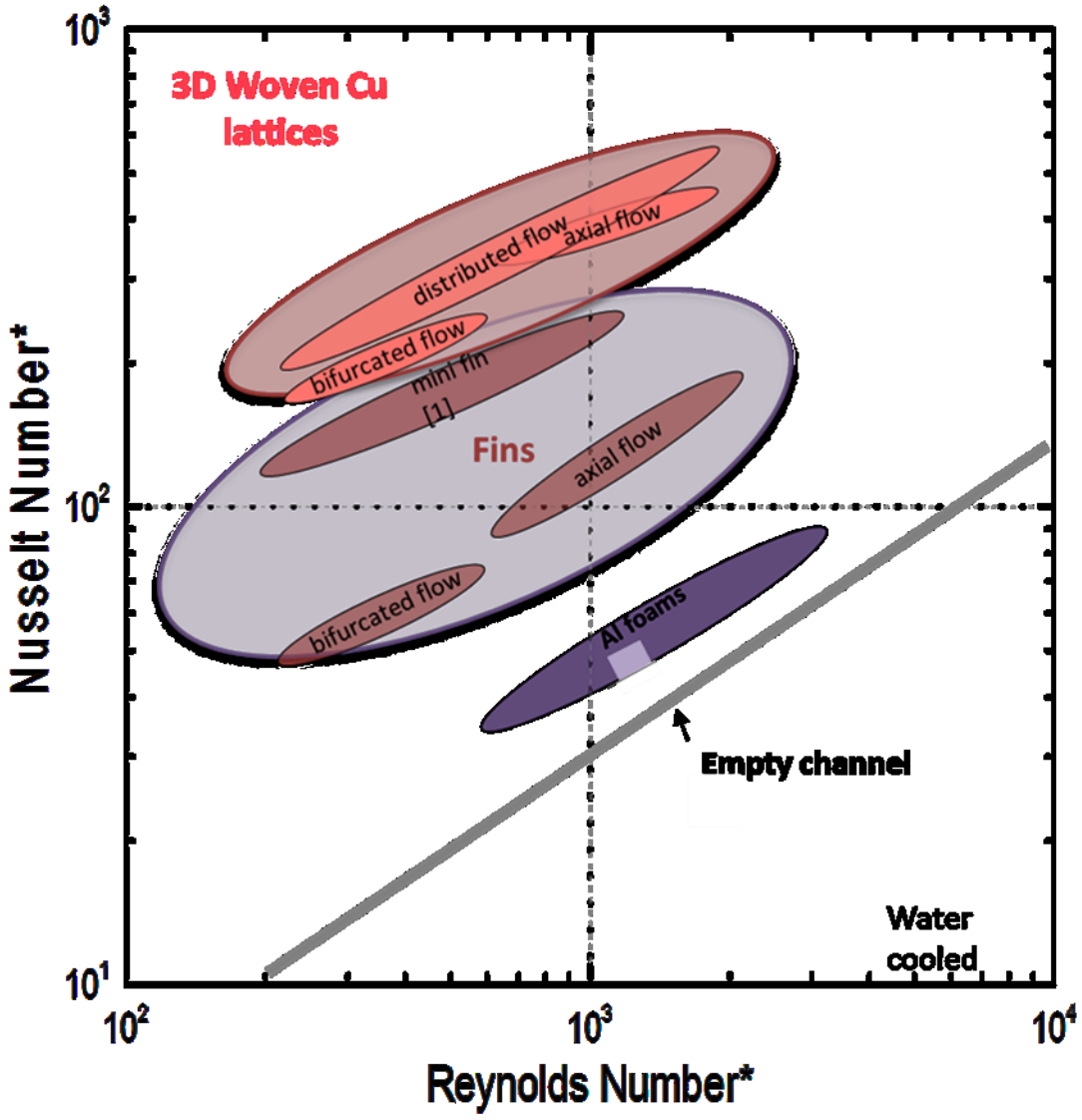

Figure 63: A plot of the Nusselt number, which is a dimensionless parameter that described the convective heat transfer, and Reynolds number, which is a dimensionless parameter that describes the flow rate, for the 3D woven lattices for the 3 different flow patterns: axial (flow along the warp direction of the material), bifurcated (flow in through the fill direction and out through the z-fill plane), and distributed (flow through the header structures into the weaves and out through the sides of the header). These values are compared with mini fins, Al foams, and an empty channel, which are other common heat transfer devices for similar applications. (Courtesy of Longyu Zhao)

Chapter 5: Damping Properties

Damping of vibrations in high speed rotary devices, such as turbines, is an area of great interest, because mitigation of these vibrations leads to longer life and fewer fatigue failures [80]. Dissipation of vibrations that are present during dynamic loading has been examined by others and can be found in the literature [81–83], and polymers are commonly used to dampen vibrations. Polymeric materials have high loss factors, but they are limited in their applicability as a result of their low operating temperatures since many vibration reduction environments, such as turbines, would subject these materials to high temperatures. The use of fluid dampers, another common vibration mitigation option, is also limited in their ability (due to degradation or evaporation of the fluid) to fulfill these high temperature damping needs. Therefore, a vibration reduction solution that does not rely on fluids or polymers would be of great interest for a large number of high speed machinery applications.

There have been a few reports in the literature of solutions that were developed for high temperature oil free vibration reduction applications that did not make use of polymeric materials. In one, a randomly oriented metallic wire mesh was compressed and used as a bearing damper in the space shuttle main engine high-pressure fuel turbo pump [84]. Rotodynamic instability of the rocket engine turbopump was manifested as a damaging subsynchronous whirling motion, and the knitted wire mesh was shown to improve the stability of the turbopump, which was quantified as a reduction in the reaction forces at the supports of the pump [84]. In another example, General Electric

(GE) developed oil-free dampers for applications in turbomachinery [85,86] through the use of a knitted mesh of interlocking loops of copper wires. This wire mesh was compressed into a toroidal shape with 25% mesh density and was employed as a bearing support damper. The resulting damping properties of the component depended on the excitation frequency, which limited the overall translation of the part to other applications.

In this dissertation, I measured and studied the damping properties of 3D woven metallic lattice materials subjected to sinusoidal loading in the frequency range of 1 to 200 Hz. The damping properties of these lattice materials were measured for both as-woven and bonded lattices. The results were quantified using the loss factor, η, since it is the most comprehensive way to quantify the energy dissipation (damping) capabilities of a material or system [87]. Examination of the resulting behavior was further studied using high speed camera imaging and FEA modeling.

Investigations into the damping properties of the weaves indicated that three mechanisms were responsible for the high measured damping values: (i) internal damping (the inherent damping of the material) of the individual wires contributes to the overall damping, but its contribution is small compared to the high measured loss factors in the weaves; (ii) frictional wire on wire sliding is another mechanism that transforms the kinetic energy of the applied vibrations into heat modeling and measurements together indicate that this mechanism appears to be a major contributor to the overall measured loss factor, since there are a large number of contact points in the weaves; (iii) modeling revealed that the weaves also possess an inertial damping mechanism as well.

Inertial damping is the result of individual wire segments in the weaves like a classic physics vibrating string.

In order to evaluate the performance of these materials for use as a high temperature damping material, the loss factors of the NiCr weaves were measured in air at temperatures up to 300°C in the DMA and after exposure to temperatures as high as 1200°C in a furnace. Cu weaves were also measured after exposure to temperatures as high as 300°C in air and 925°C in a forming gas environment. The temperature exposure leads to a decrease in the measured loss factor in all of the materials. The micro and macroscopic changes that occur upon temperature exposure were quantified using careful disassembly of the weave and optical analysis combined with modeling. The measurements were then used to calculate changes in geometry and springback, which are believed to contribute to the change in damping performance. The changes in the weaves with temperature exposure were examined in light of the changes that occur in the internal, inertial, and frictional damping mechanisms. From the examination of the data, it appears that the changes with temperature that are observed have the greatest effect on the frictional damping mechanism, by changing the magnitude and distribution of forces in the weave. Finally the high temperature damping properties of these materials are compared to other materials.

5.1: Room Temperature Damping Properties

5.1.1: Room Temperature Damping Measurements

The room temperature measurements of our 3D woven metallic microlattice materials are the focus of this section. Samples for these dynamic tests were cut by wire EDM from bulk 3D weaves in order to ensure that the sides were straight and parallel in order to increase sample uniformity and to aid in repeatability of the measurements, in addition to minimizing the damage caused by the cutting process. The loading was performed in a single cantilever orientation in a TA Instruments Q800 Dynamic Mechanical Analyzer (DMA). The grips were tightened against the material by applying a 0.3 *N-m* torque to the bolt that pushes against the top edge of each grip. This value was selected in order to securely mount the sample without deforming the sample underneath the clamp. During a test, the samples were subjected to a sinusoidal oscillation with an amplitude of 20 μm. The amplitude was chosen from initial quasi-static testing in the DMA to ensure that the testing was performed in the elastic regime and that internal wire stresses remained below the yield strength. An image of a NiCr sample in the single cantilever bending fixture of the DMA is shown in Figure 64. The DMA applies a sinusoidal oscillation and the load is monitored during the oscillation. The software in the DMA compares the phase delay, ϕ, between the maximum stress and strain in order to calculate the storage modulus (the stored elastic energy in the material during loading) ,k_s', and the loss modulus (the energy that is dissipated during loading), k_s'', for the tested sample at each applied frequency. An illustration of a sinusoidal stress and strain response with a resulting phase delay is shown in Figure 65.

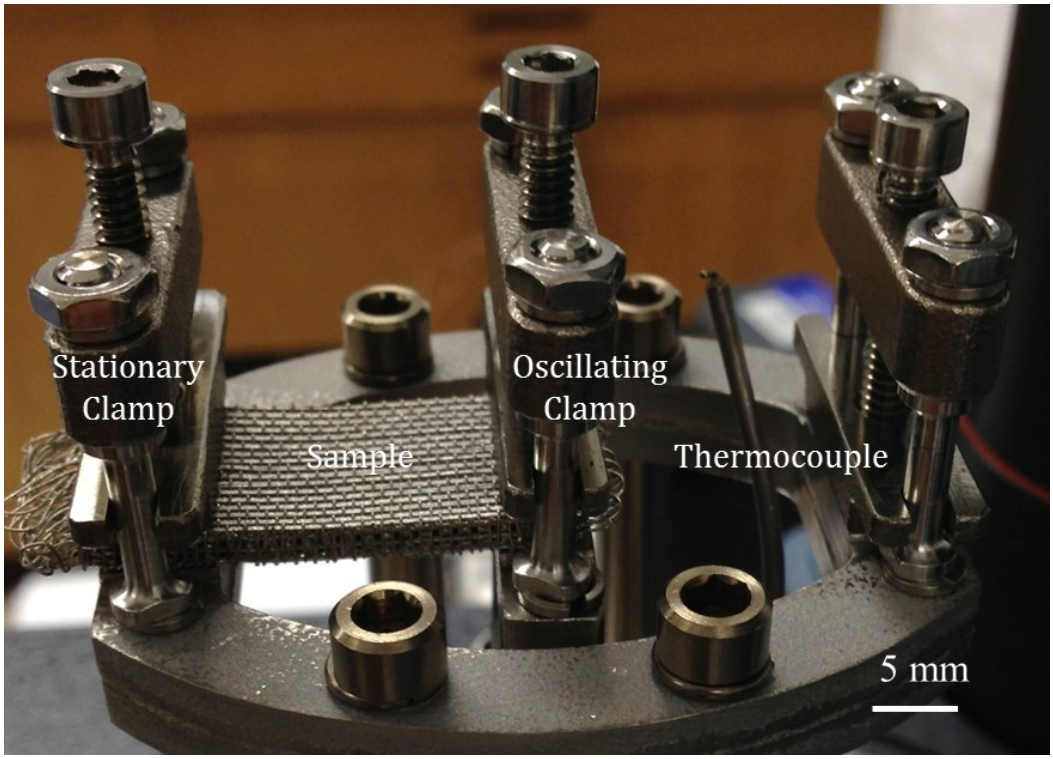

Figure 64: A 15mm wide optimized pattern NiCr sample mounted in the TA Instruments Q800 DMA for dynamic testing. The sample is in a single cantilever orientation where it is clamped in a fixed connection on the left edge and the right edge of the sample is clamped in an oscillating clamp that moves vertically up and down.

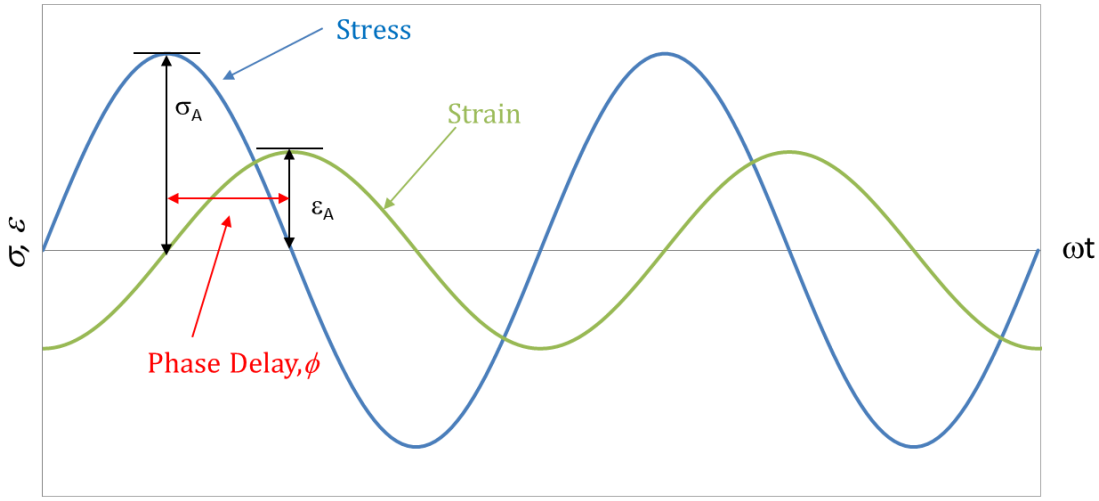

Figure 65: An example of a time dependent sinusoidal stress and strain response for a material that exhibits damping. The phase delay, ϕ, is measured as the delay between the maximum stress and maximum strain. The tangent of the phase delay in the response is the loss factor.

The ratio of the loss modulus to the storage modulus was employed in order to quantify the damping capabilities of the material at a given frequency. This ratio is equivalent to the tangent of the phase lag, ϕ, between the force and displacement oscillations in the idealized parallel spring and dashpot system as is shown in (see p.60 in [88]). This value is referred to as the loss coefficient and it is described by the expression,

$$\eta = \tan\phi = \frac{k_s''}{k_s'} = \frac{P_a"}{P_a'} \tag{22}$$

where, P_a' is the force at the peak displacement (in-phase reaction), and P_a'' is the force at the zero displacement (out-of-phase reaction) [14,88,89].

Each sample was tested in four different possible orientations by flipping and rotating the samples between tests to ensure repeatability, resulting in at least 40 measurements for each sample for each test. An illustration of the relationship between the four discrete sampling orientations are shown in Figure 66.

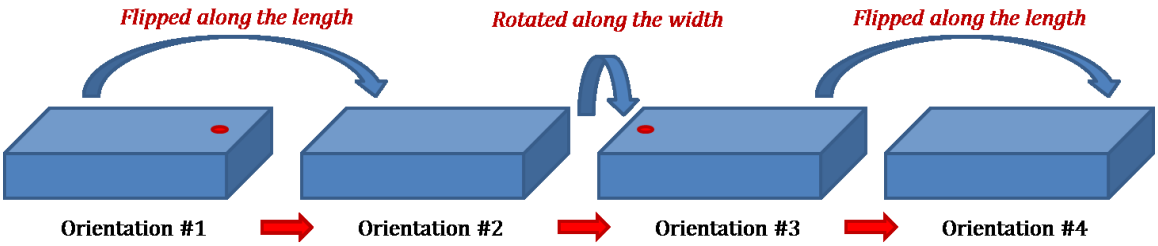

Figure 66: A summary of the four discrete sample orientations that were tested for each case and sample in the DMA and the relationship between the orientations. The dot on the top surface of the sample is a fiducial marker to help the reader understand the change in orientation.

The results of multiple samples (at least two for each case, but often more than two samples were tested) were compared and then averaged in order to arrive at a loss factor for a particular case. No systematic frequency dependence was found in the loss coefficient of the unbonded materials.

Most samples tested in this work were 15 *mm* in width so that the test would sample the largest possible volume of material that could be tested in the DMA. In order to ensure that the sample width did not influence the results, samples were prepared in two widths, 10 and 15 *mm* and they had a minimum length of 25 *mm*, which was determined by the spacing of the grips. 10 and 15 *mm* wide samples represent the practical testing limits for these materials. The maximum width is determined by the maximum width of the grips and the minimum width is to ensure that the sample has sufficient integrity to remain intact during handling and testing. An example of the loss factors for both 10 and 15 *mm* wide standard architecture NiCr sample are shown in Figure 67.

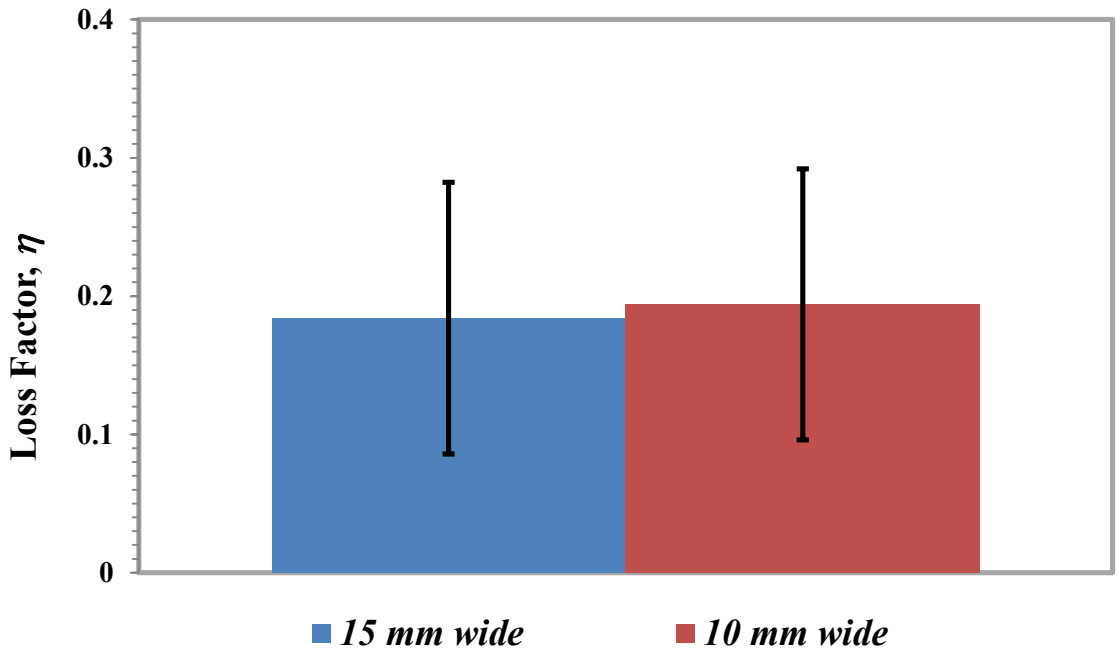

Figure 67: Average of the DMA measurements of the standard architecture as-woven NiCr samples from 1-200 Hz that were cut to a width of both 10 and 15 mm in order to evaluate the role of sample width. It is clear from these measurements that there is no real measurable difference between the damping properties of the two different widths.

Measurements of the average loss factor of both sample widths did not show any measureable difference, which indicates that the damping properties for these measurements are not sensitive to the sample width for this range of sizes. The sample length had an unsupported length (measured as the inner dimension between the two clamps) of approximately 17.5 *mm*+/- 1 *mm* and differences in the length were accounted for in the system calibration that was performed before each test. The remaining material was clamped underneath the grips of the DMA.

Samples of both Cu and NiCr weaves were measured in their as-woven state for both the standard and optimized (optimized for permeability and shear stiffness, not damping) architectures. In order to more directly compare the results to the literature and

to ensure that our single cantilever bending orientation was comparable to the literature values, a plate of copper was prepared with the same dimensions (3mm thick and 15 mm wide) as the woven samples. All of these samples except for the copper plate were tested in at least four distinct orientations and multiple samples were tested for each architecture. The individual measured loss factors for frequencies from 1-200Hz are shown in Figures 68-72. The average loss factor (average of all data points for a particular case) and standard deviation of all of the data for each case is summarized in Figure 73.

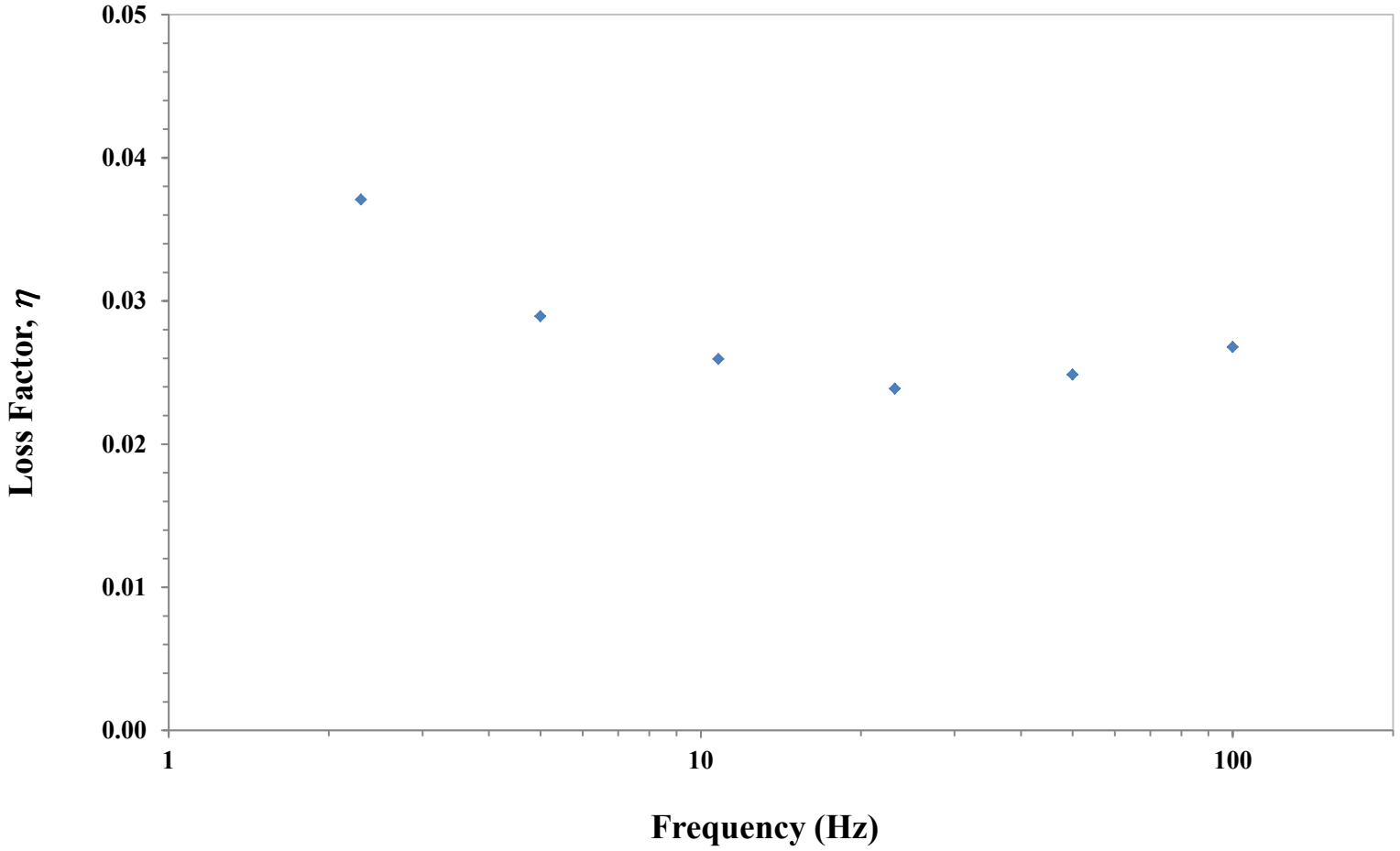

Figure 68: Room temperature DMA measurements of the loss factor of an OFHC Cu plate from 1-100 Hz.

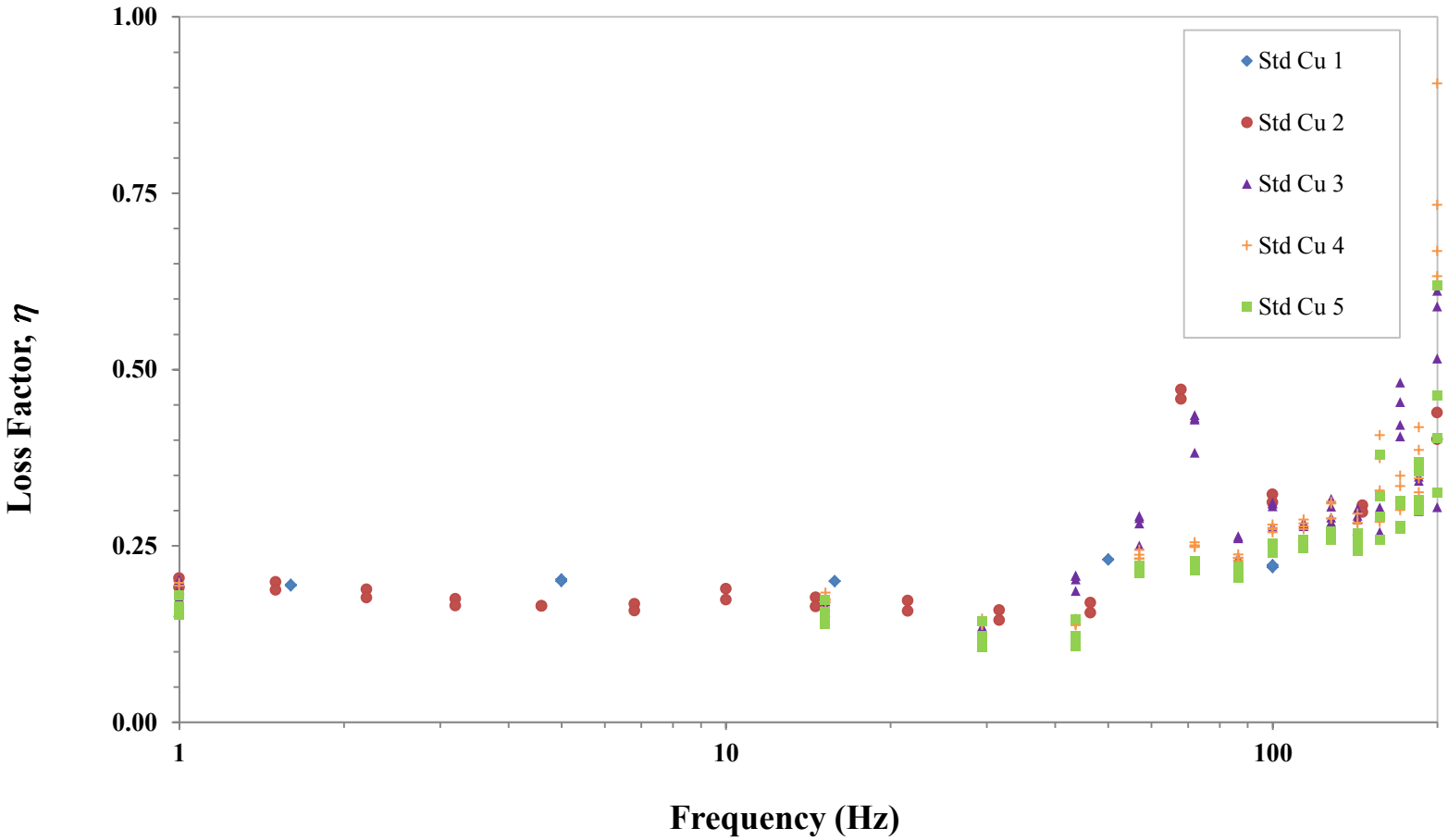

Figure 69: Room temperature DMA measurements of the loss factor of three as-woven 15 mm wide standard architecture Cu weaves from 1-200 Hz. Each sample was tested with the fill direction aligned along the bending axis and each sample was tested multiple times.

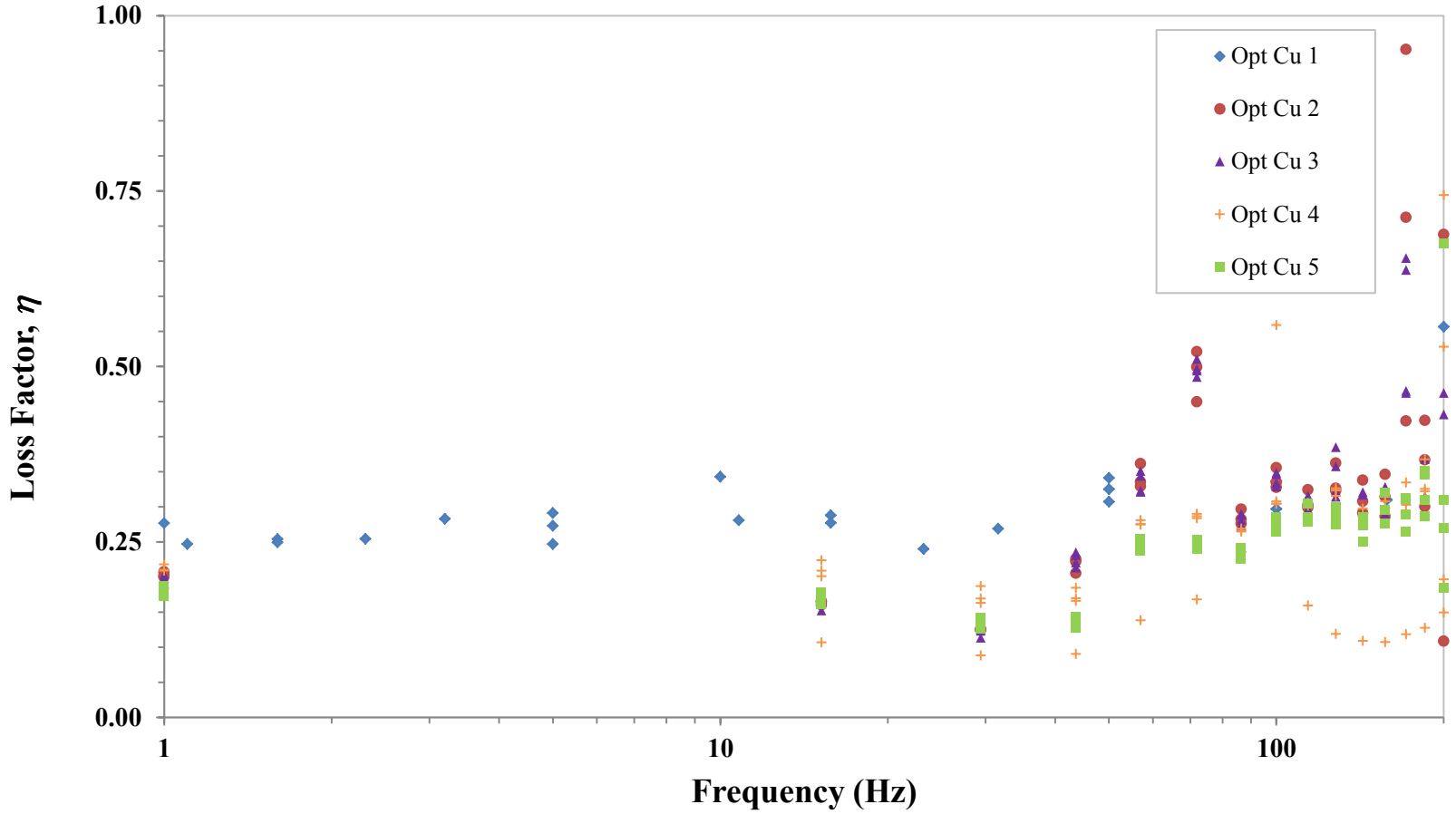

Figure 70: Room temperature DMA measurements of the loss factor of three as-woven 15 mm wide stiffness and permeability optimized architecture Cu weaves from 1-200 Hz. Each sample was tested with the fill direction aligned along the bending axis and each sample was tested multiple times.

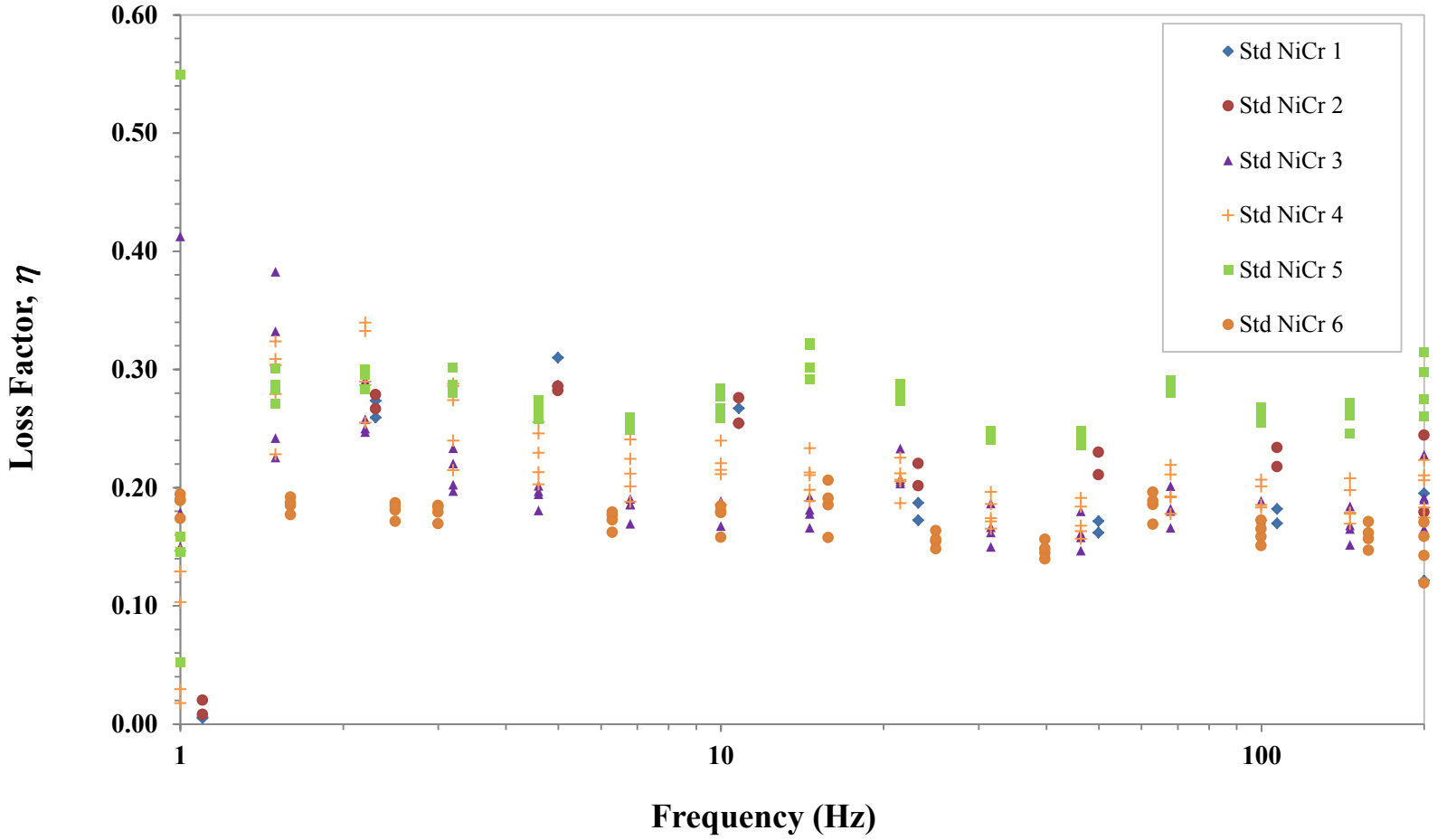

Figure 71: Room temperature DMA measurements of the loss factor of six as-woven 15 mm wide standard architecture NiCr weaves from 1-200 Hz. Each sample was tested with the fill direction aligned along the bending axis and each sample was tested multiple times.

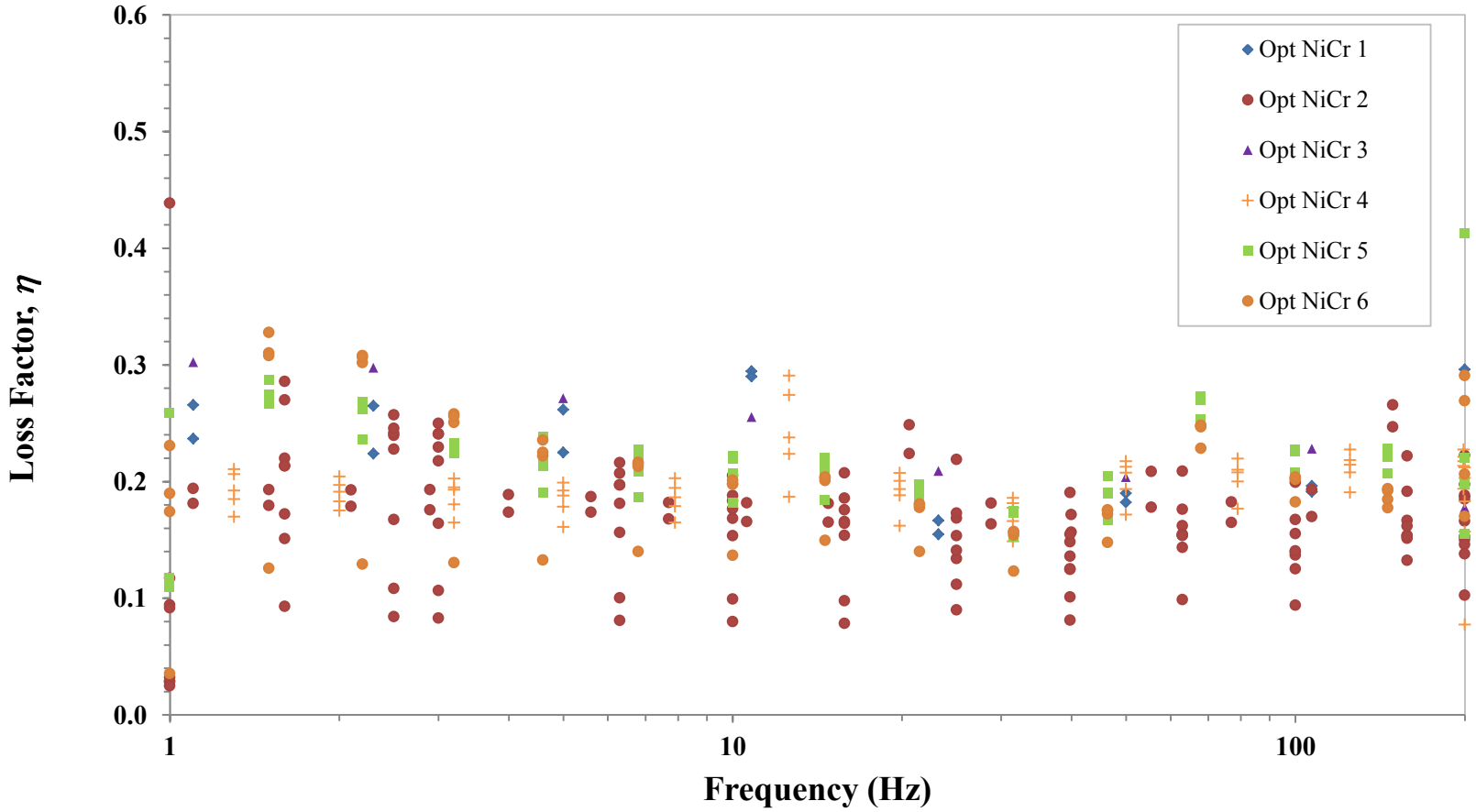

Figure 72: Room temperature DMA measurements of the loss factor of six as-woven 15 mm wide stiffness and permeability optimized architecture NiCr weaves from 1-200 Hz. Each sample was tested with the fill direction aligned along the bending axis and each sample was tested multiple times.

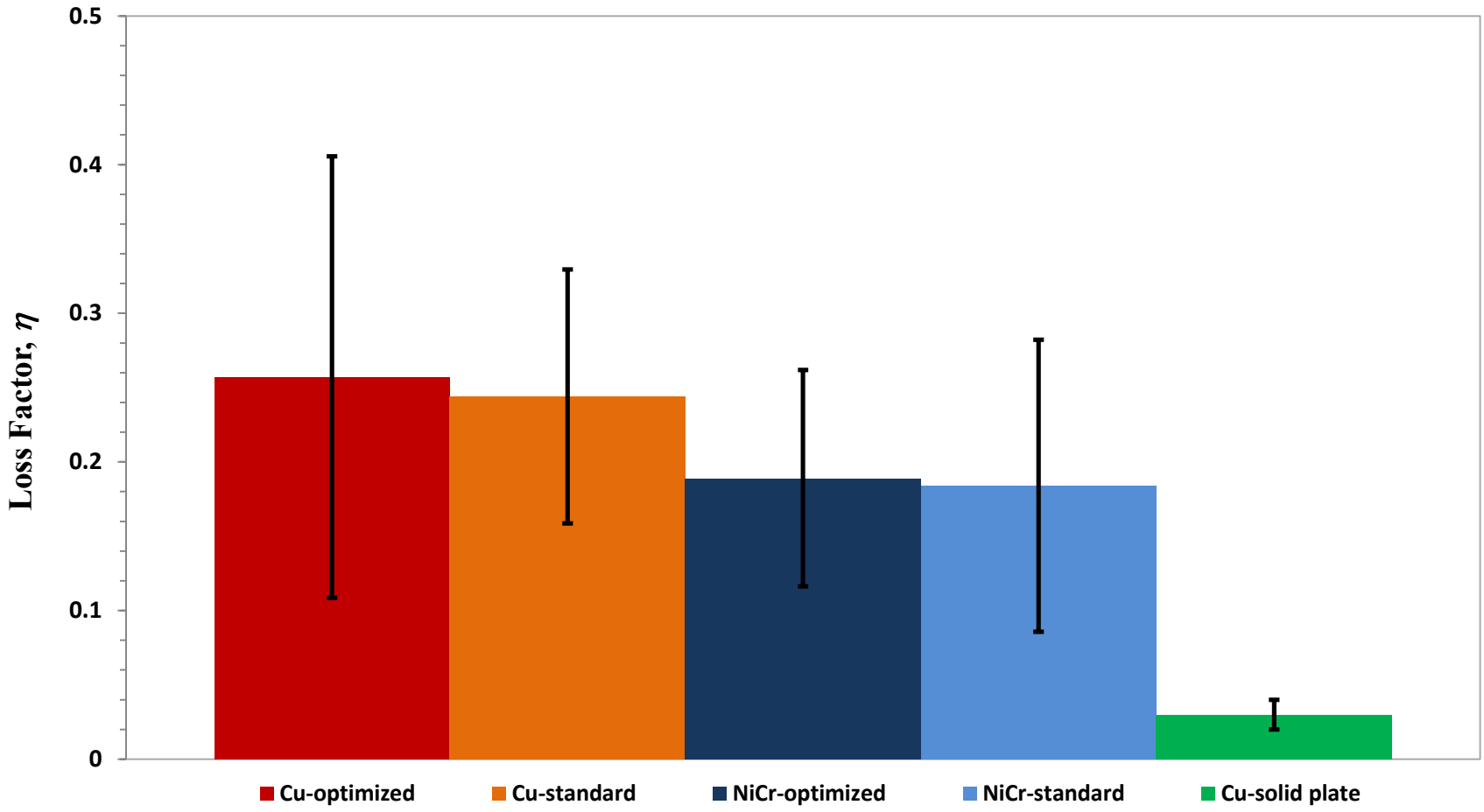

Figure 73: A plot of average mechanical loss coefficient from 1-200 Hz for the as-woven Cu and NiCr woven materials and a solid Cu plate of the same dimensions. The error bars are calculated as ± 1 standard deviation on the population of each data set.

The measured values for the mechanical loss coefficient for the 3D woven materials are much greater than the values of the solid metallic materials from which they are made (internal damping) and they are comparable to many common polymers. The measurements of the average loss coefficient of the OFHC copper plate had a value of 0.03. Asbhy reports a maximum loss factor for solid copper of 0.008, which is below the measurement capabilities of the technique. Our measurements of the copper plate indicate that the damping of the solid copper is rather small, although they are not in exact agreement with the literature values (an average value of <0.01 was not measured). It is believed that the discrepancy is a result of the fact that the DMA is not designed to measure the damping properties of solid metallic materials with the substantial stiffness of copper, but for polymeric materials, which possess a significantly lower stiffness. Solid NiCr has a maximum loss factor of 0.002, but it was not measured due to difficulties in sourcing the appropriate NiCr material in plate form [90].

The mechanical properties (specifically shear stiffness) of these materials can be improved through the bonding processes discussed in the previous chapter, which would improve the multifunctional capabilities of these materials. Copper samples were bonded by brazing using the optimal amount of braze (discussed previously) and NiCr samples were bonded by Northwestern University by vapor phase aluminization. The measurements of the individual standard and permeability optimized brazed Cu and aluminized NiCr samples is shown in Figures 74-77, and the average mechanical loss factor of these bonded samples is shown in Figure 78, and the summary of all of the average room temperature measurements of loss factor and standard deviation for both as-woven and bonded materials are shown in Table 11.

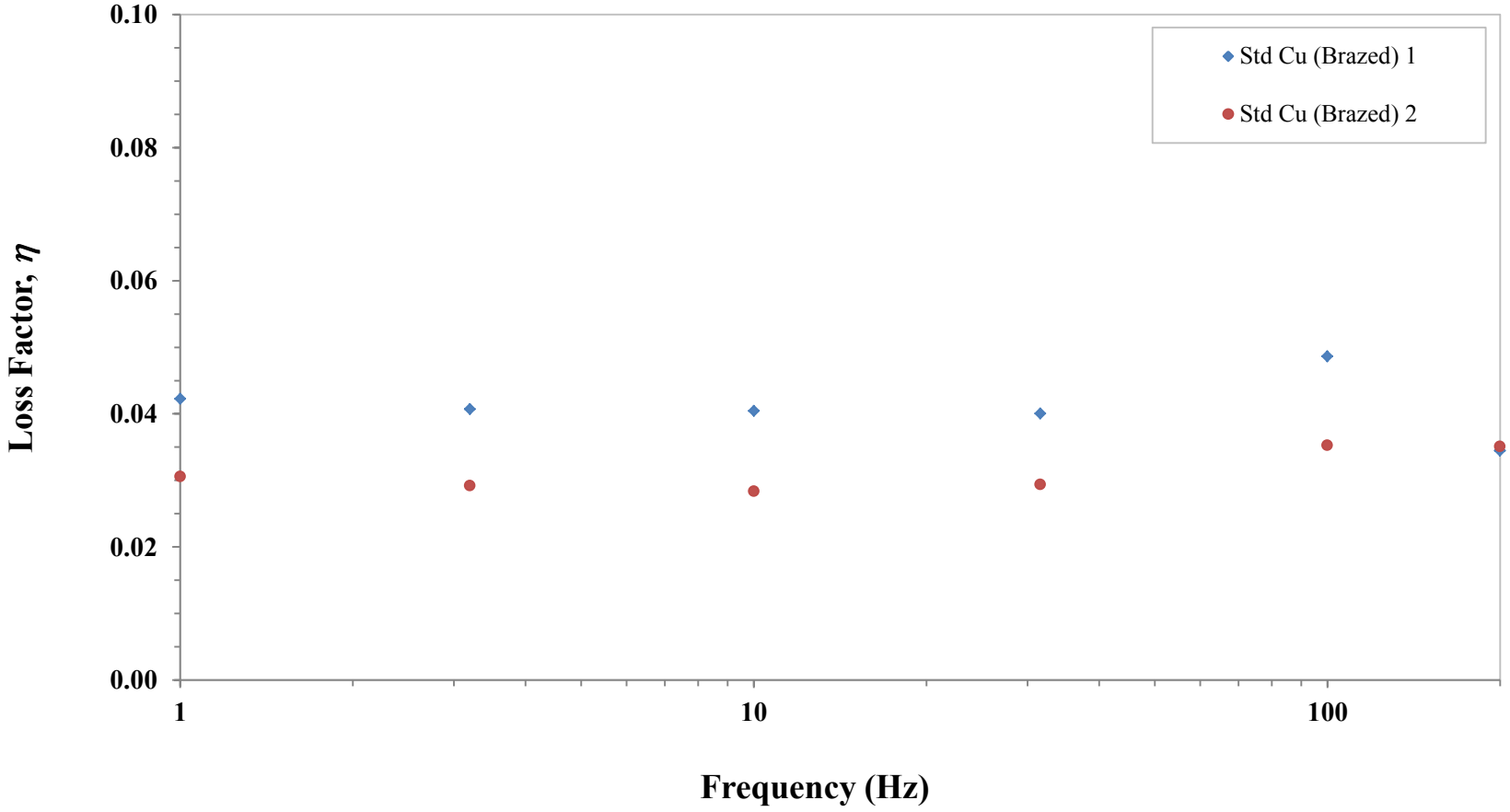

Figure 74: Room temperature DMA measurements of the loss factor of two as-woven 15 mm wide standard architecture brazed Cu weaves from 1-200 Hz. Each sample was tested with the fill direction aligned along the bending axis.

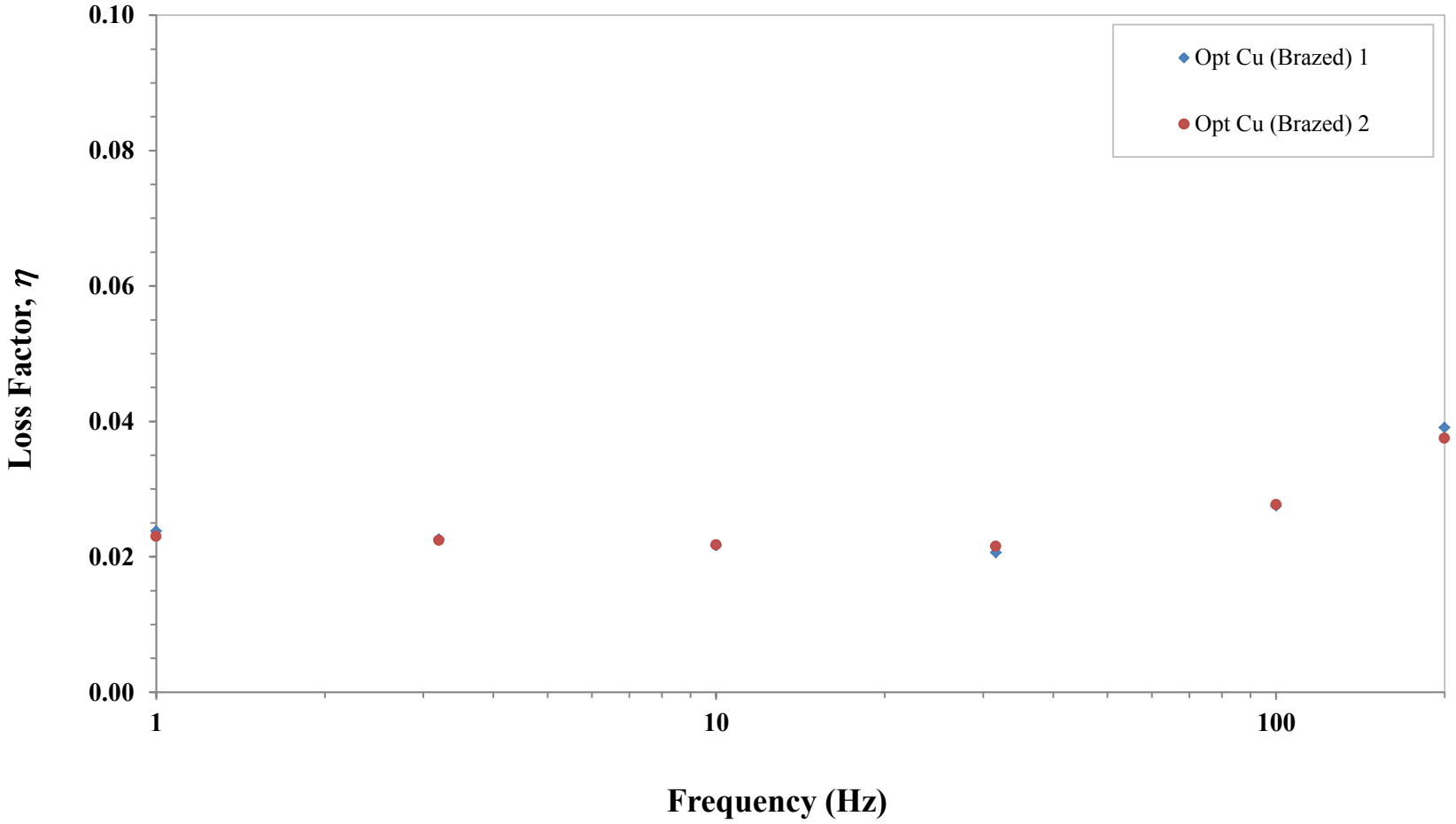

Figure 75: Room temperature DMA measurements of the loss factor of two as-woven 15 mm wide stiffness and permeability optimized architecture brazed Cu weaves from 1-200 Hz. Each sample was tested with the fill direction aligned along the bending axis and each samples.

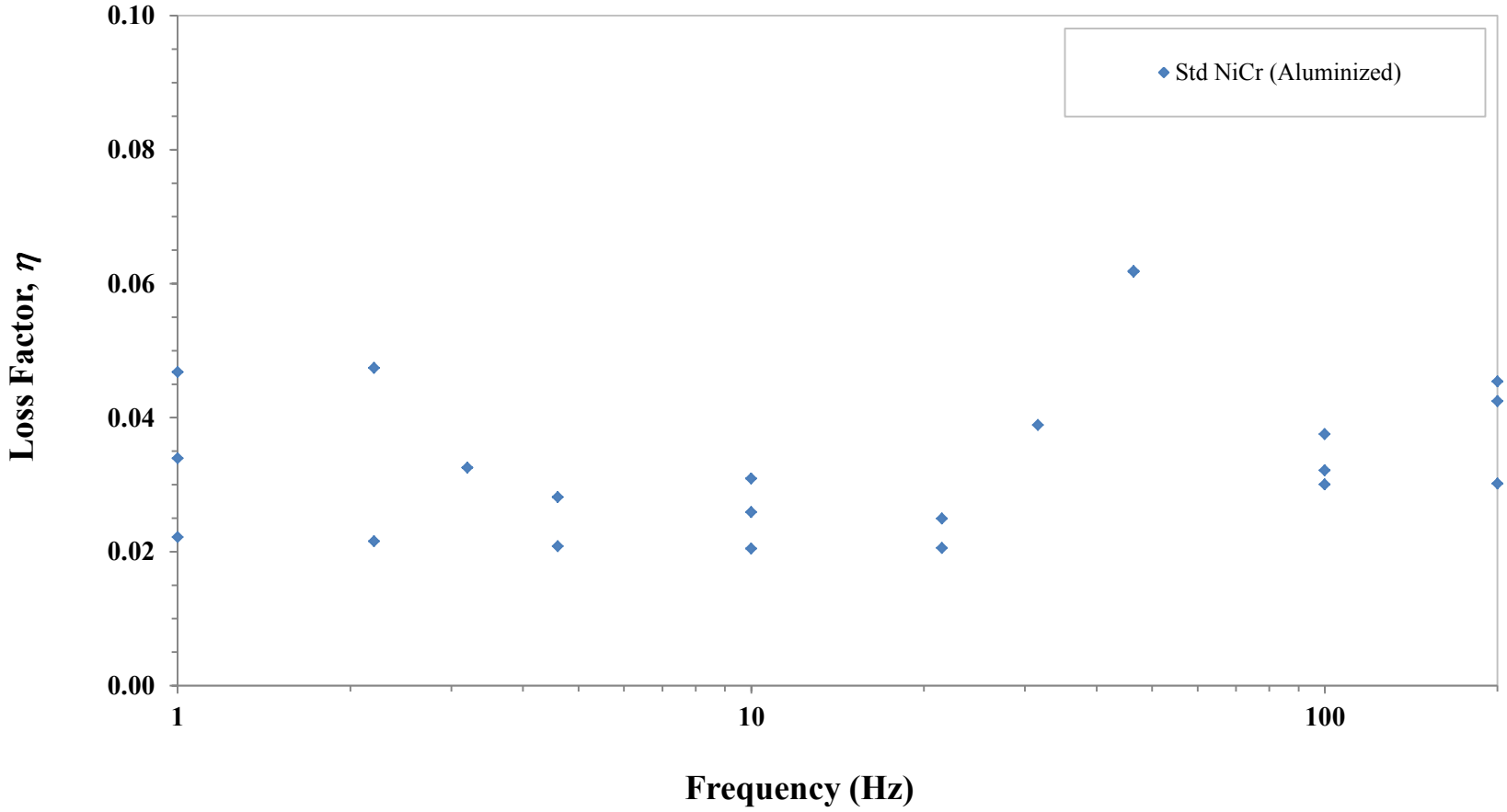

Figure 76: Room temperature DMA measurements of the loss factor of an as-woven 15 mm wide standard architecture aluminized NiCr weave from 1-200 Hz. The sample was tested with the fill direction aligned along the bending axis and it was tested multiple times.

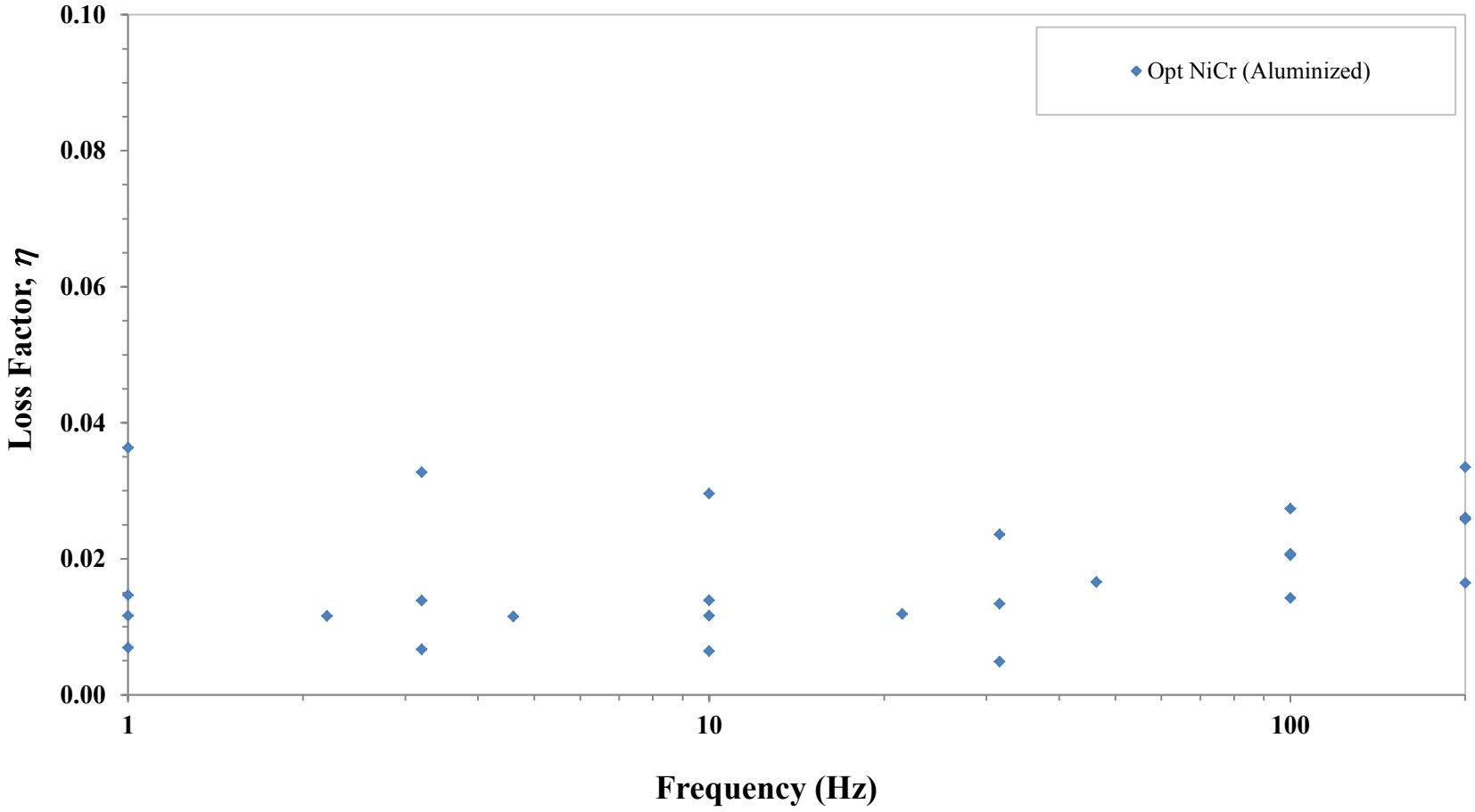

Figure 77: Room temperature DMA measurements of the loss factor of an as-woven 15 mm wide stiffness and permeability optimized architecture aluminized NiCr weaves from 1-200 Hz. The sample was tested with the fill direction aligned along the bending axis and it was tested multiple times.

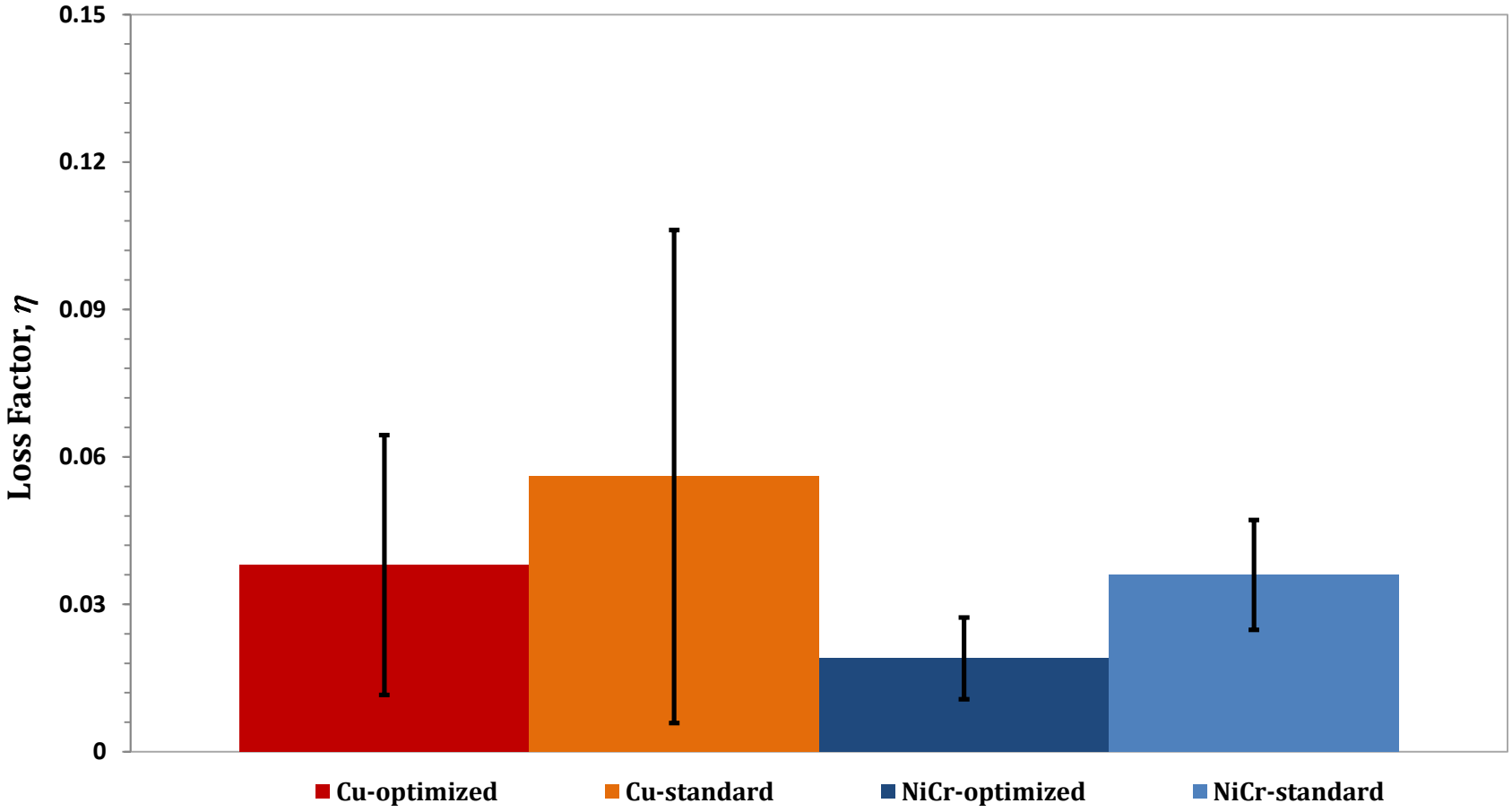

Figure 78: DMA measurements of the average mechanical loss coefficient for frequencies of 1–200Hz for fully bonded 3D woven lattice materials. Copper samples were bonded by brazing and NiCr samples were bonded by vapor phase aluminization by Northwestern University.

Table 11: Summary of the room temperature DMA measurements

Material	Loss Factor, η	Standard Deviation, σ
Copper Plate	0.03	0.01
Standard Cu	0.24	0.09
Optimized Cu	0.26	0.15
Standard NiCr	0.18	0.10
Optimized NiCr	0.19	0.07
Standard Cu (Brazed)	0.06	0.05
Optimized Cu (Brazed)	0.04	0.03
Standard NiCr (Aluminized)	0.04	0.01
Optimized NiCr (Aluminized)	0.02	0.01

It is obvious that bonding results in a decrease in the mechanical loss coefficient of these materials. It is reasonable to assume that bonding pins the wires at their junctions inhibiting frictional sliding, which is one of two dominant damping mechanisms in these materials. The materials still exhibit damping that is higher that their solid parent materials, which implies that damping in these materials is attributed to mechanisms other than purely frictional sliding. FE modeling results, conducted by Stefan Szyniszewski, suggests that an inertial damping also contributes to the damping in these materials and may be less affected by bonding.

5.1.2: Modeling of the Damping Properties of 3D Woven Metallic Weaves

In order to develop a greater understanding of the mechanisms that lead to the high measured damping properties in these materials, a model of the 3D woven NiCr optimized pattern samples was made by Stefan Szyniszewski in LS-DYNA [91]. The modeled sample had dimensions of 10 x 17.5 mm (in order to mimic the DMA experiment) and it was generated with all wires explicitly included. An image of the damping model that was used to simulate the dynamic mechanical properties of these materials is shown in Figure 79.

As discussed in Chapter 3.1, optical examination of the as-woven samples revealed stochastically distributed gaps between the wires. In order to evaluate the effect and importance of these gaps, a series of finite element models were created with discrete average gap spacing that would allow us to evaluate not only the importance of gaps, but also the role of different types and sizes of gaps. The different types of gaps that were included in the model were: (i) a tightly-packed or zero-gap model where all wires are tangent and there are no unintended gaps between wire junctions; (ii) a model featuring uniform gaps (based off the measured average gap spacing in the real material) in a particular direction

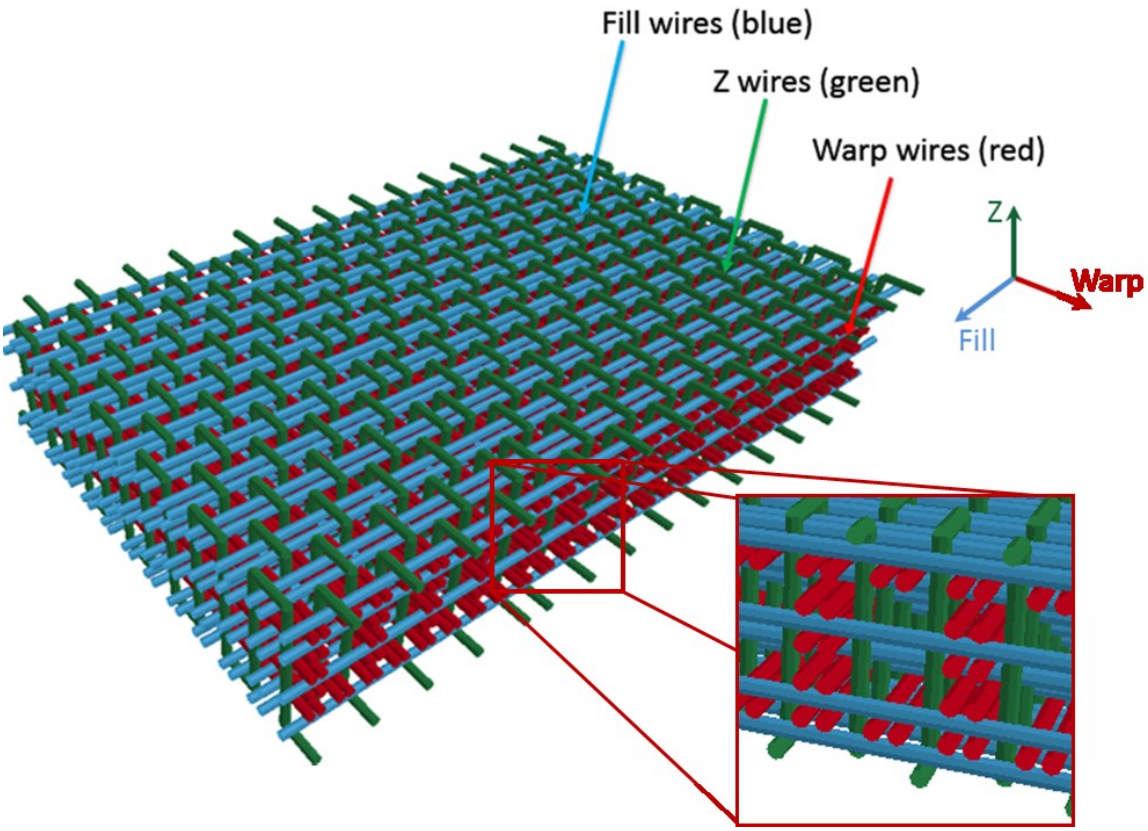

Figure 79: LS-DYNA model by Stefan Szyniszewski of the as-woven 3D woven microlattice material. The model was had a clamped boundary at one end and the other end of the material was subjected to an oscillation in order to mimic the DMA testing of the material. Wire spacing and coefficient of friction were varied in order to evaluate their effects on the damping properties.

between all wires in the warp and fill directions (no gaps in the z-direction) ; and (iii) a model where the measured average vertical gaps were also included was simulated. The gaps in the model were assumed to be uniform although the distribution of gaps in the manufactured sample is stochastic, as discussed in [51] and previously in this work. The uniform gap sizes in each direction were based on the average gap spacing that was measured from mounting real as-woven material samples in epoxy, sectioning them, and measuring the resulting spacing between wires under an optical microscope. The mean spacing values from the optical measurements that were employed in the model were 99

μm in the warp direction, 10 μm in fill direction, and 47 μm vertical (z-direction) gaps between warp and fill wire pairs.

In addition to assuming that the gap sizes were uniform in the finite element model, all simulated wires were also perfectly straight and free of residual stresses. This simplification means that solutions may not match the measured damping loss factor values from the experiments, however, the models can help provide insight into the damping mechanisms at play and their dependence on the wire spacing and coefficient of friction (two variables that can be controlled through manufacturing and post processing).

In the finite element model, the nodes on one end of the model were fully clamped and an oscillatory load was imposed on the opposite end by means of a virtually massless vertical elastic shell. This was intended to mimic the same boundary conditions that were present in the DMA experiments. The mass of the plate that applied the load to the material was less than 0.1% of the specimen's mass in order to ensure that its inertia did not affect the simulation results. A sinusoidal load was applied at 70 Hz to the top of the loading plate in such a manner that the oscillatory amplitude of 20 μm was achieved. Contact and friction between wires was accounted for in the model, and they were simulated with a general contact algorithm (CONTACT AUTOMATIC GENERAL [91]). A static coefficient of friction $f_s = 0.44$ [92] and dynamic coefficient of friction $f_d = 0.20$ [93] was employed in the simulations and the ratio of the dynamic to static coefficient of friction was confirmed to be consistent with the ratios given for other metallic materials [94]. The transition from static to dynamic coefficient of friction was modeled using an exponential decay function that decays to the dynamic coefficient of friction for contact sliding velocities larger than 25 mm/s. The elastic modulus of the

individual NiCr wires was measured by Dr. Yong Zhang to be E = 130 GPa from the initial elastic loading during tensile tests of a single NiCr wire. The internal damping of the NiCr wire was small in comparison to the measured damping loss factor of the materials. In order to save on computational costs, it was not included in the model and was assumed to be negligible.

The results of the simulations for the two sets of coefficients of friction and the three types of uniformly distributed gaps with their calculated loss factors is shown in Table 12.

Table 12: A summary of the various gap spacing and coefficients of friction that were simulated with the optimized pattern NiCr damping model with the simulated loss factors

	No gaps	Horizontal gaps only	Average measured gaps
Average gap spacings (microns)	warp = 0 fill =0 z=0	warp = 99 fill =10 z=0	warp = 99 fill =10 z=47
Measured coefficient of friction (f_s = 0.44, f_d = 0.20)	**0.15**	**0.13**	**0.06**
Increased coefficient of friction (f_s = 0.88, f_d = 0.40)	**0.19**	**0.14**	**0.06**

These simulations of the stiffness and permeability optimized architecture NiCr lattice predicted absolute loss coefficients that were only about half of the experimental values in the model with no gaps, and even lower values for the models that included gaps.

These low values may be attributed to the fact that the model assumes the wires are perfect and does not account for the stochastic irregularities, such as twists and bends, that are known to be present in the woven material. The computational model employed idealized geometries of the wires (all warp and fill wires were straight, and z-wires had perfect 90° bends), while real samples have wires which are bent and twisted, which increases the wire to wire frictional contact surface area for damping (wire to wire contact is present in 60-70% of all possible junctions), despite the average measured gaps. The model also does not include residual stresses in the wires (specifically the z-wires) which can change the contact forces involved in frictional damping. Zhao et al. [50] and Zhang et al. [51] have recently demonstrated that manufacturing irregularities and the stochastic nature of wire geometries need to be considered to accurately model the permeability and stiffness of 3D woven lattice materials. This indicates that in order for the models to match the experimental work, they must take into account some of these irregularities. Nevertheless, the damping model with the assumed perfect geometries was still able to provide us with a greater understanding of the sensitivity of the damping loss factor to two key parameters: coefficient of friction and average gap size.

The modeled damping values were found to be dependent on the chosen coefficient of friction and it was also found to depend on the assumed gap sizes, because frictional energy dissipation is dependent on whether or not there is wire to wire contact. Doubling the coefficient of friction increased the simulated loss coefficient by one third for both the zero-gap model and when gaps were only incorporated in the warp and fill directions (although this case should exhibit a smaller dependence on the coefficient of friction). By contrast, simulations that included gaps in all three directions showed no

appreciable change in the simulated loss coefficient when the friction coefficient was doubled. In this case, the number of frictional contact points was decreased as the gap size increased. It is surmised that the number of frictional contact points in the model underestimates the number of contact points in the real material, since it doesn't account for twists and bends that are present in the real material which serves to increase the number of contact points for the same average gap spacing. Overall, this result indicates that friction-based damping is activated in tightly packed lattices, while inertial-based damping is always present. It is worth noting that the coefficient of friction for Cu (f_s^{Cu} = 1.1 [94]) is larger than that of NiCr (f_s^{NiCr} = 0.44[92]) and that the measured loss coefficients for the Cu lattices were consistently and significantly higher than for the NiCr lattices. This suggests that even with inherent manufacturing irregularities, damping of the woven lattice materials is influenced by friction.

The mean gaps sizes were further investigated by using average gaps that were equivalent to the experimental samples. The simulated loss coefficient of these samples was 0.06. Doubling the z-direction gaps (from 47 to 94 μm) decreased the simulated loss coefficient from 0.06 to 0.05. This shows that this type of gap plays a small role in the simulated loss coefficient. Changing the z-direction gaps to 23.5 μm (half of the average gap size in the real material) also caused a slight decrease in the loss coefficient to 0.05. The variations between the simulated loss coefficients indicated that for the modeled loading frequency the inertial damping is not sensitive to uniformly distributed gap sizes, as long as there is sufficient space for the wire movement to occur.

In order to confirm the accuracy of the motion in the model, a high speed camera was used to examine the weaves while they were in the DMA. Samples were cycled in the DMA at 70 Hz with an amplitude of 20 μm. The side of the sample was examined with the camera during the test. Samples were cut with the bending axis aligned along the warp direction and the fill direction. An example image from each of the tests is shown in Figures 80-81.

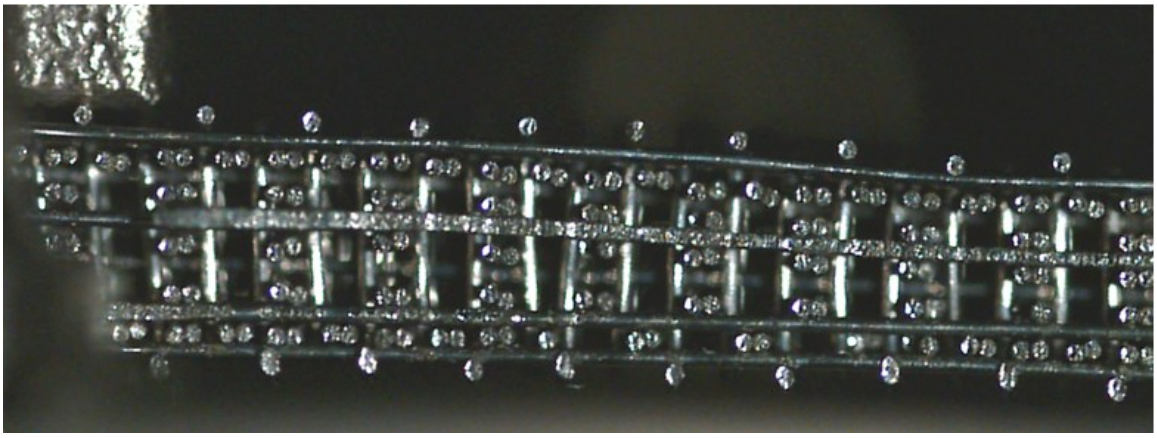

Figure 80: An image from the high speed video that was taken of the as-woven optimized pattern NiCr weave during DMA testing. The moving clamp can be seen on the left side of the image. The exposed edge is the fill-z plane of the material which served as the bending axis of the sample. The majority of the testing in the DMA was carried out in this orientation.

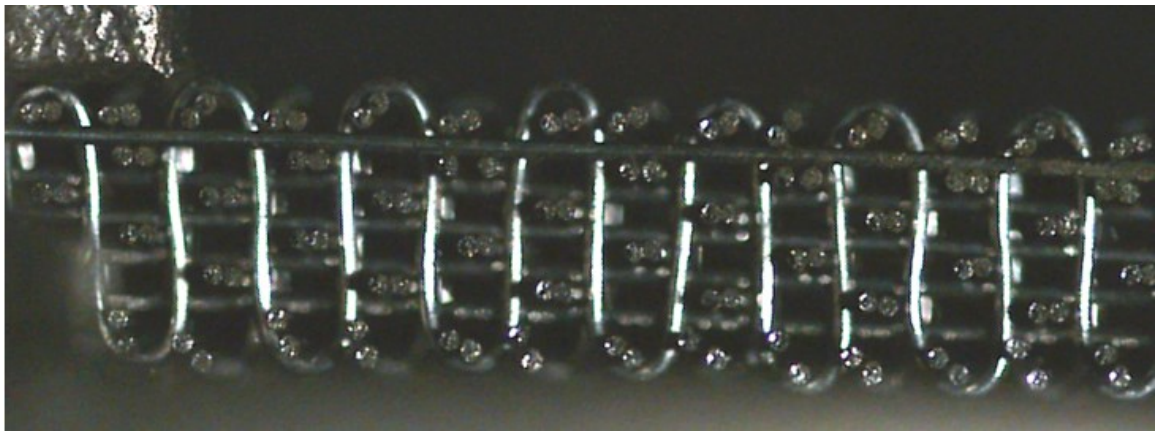

Figure 81: An image from the high speed video that was taken of the as-woven optimized pattern NiCr weave during DMA testing. The moving clamp can be seen on the left side of the image. The exposed edge is the warp-z plane of the material which served as the bending axis of the sample.

The obtainable resolution of the images precluded DIC tracking in order to quantify the individual movements of wires in the weave, however, it observations of the videos revealed that all of the individual elements in the weave moved in unison. Small individual wire movements were not noticed in the videos. In the damping model, nearly homogenous movement of the weave is detected and slight differences in the movement are only detectable when the movements are heavily magnified as shown in Figure 82. Therefore, the results of the high speed video were in agreement to what was seen in the damping model.

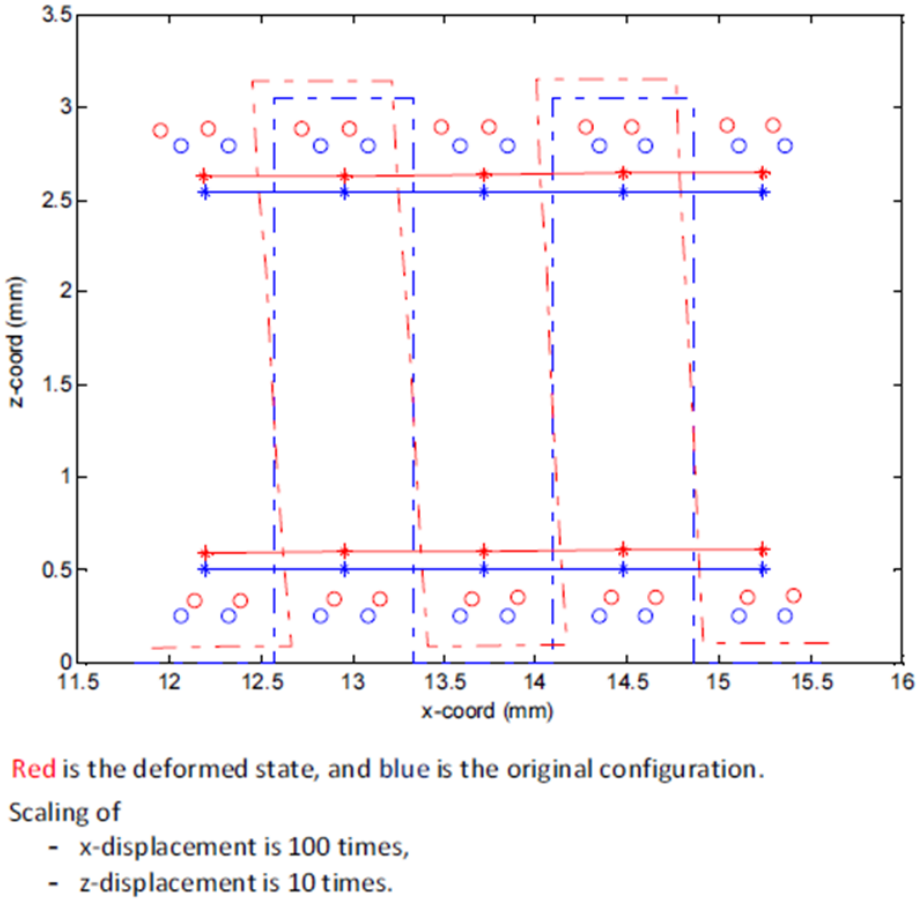

Figure 82: A trace of the movement of the z-wires and the outer layers of warp and fill wires in the weave during a damping simulation. It is important to note that the in-plane displacements are so small that they need to be magnified by 100x to be readily seen.

The experimental measurements of the room temperature damping properties of the 3D woven metallic lattice materials indicate that they are a promising damping material with the potential to be used in high temperature applications. The majority of conventional damping materials with comparable loss coefficients, such as polymers, are restricted to significantly lower temperatures, whereas the NiCr wires have a maximum service temperature of 1175°C [67]. The modeling that was performed as part of this work by Stefan Szyniszewski provides insight into the damping mechanisms that are

present in this material and their dependence on gap spacing and coefficient of friction. Two damping mechanisms are present in this material. Frictional energy dissipation is highly dependent on not only the coefficient of friction, but also the gaps and defects in the material (which affects the number of frictional contact points). Inertial damping is however always present in this material and it is the result of out of phase movements of individual wires in the weave or energy dissipation through vibrations of individual wire segments suspended between orthogonal wires (akin to the classical physics example of a vibrating string). This modeling provides insight into the damping mechanisms and how to possibly optimize the underlying micro-architecture of these materials. This indicates that there is a possibility to design 3D woven metallic lattice materials with increased and possibly even tunable damping properties.

5.2: High Temperature Damping

5.2.1: Measurements of the High Temperature Damping Properties

In order to evaluate the possibility of using the metallic 3D woven microlattice materials for high temperature damping applications, we must measure the damping characteristics of the materials at elevated temperatures. In the previous section, testing was performed in a TA Instruments Q800 DMA. This device has the ability to perform damping measurements in air at temperatures up to 300°C. The damping properties of

the as-woven material were measured at temperatures up to 300°C in the DMA. Results of these measurements were compared to measurements of samples that were heat treated for equal amounts of time in a tube furnace in air in order to evaluate the effect of the sample being constrained by the clamps during heating. In order to evaluate the effects of even higher temperature exposures and to better control the environment, our custom tube furnace was used to heat Cu weaves in air to temperatures as high as 300°C (925°C in reducing atmosphere) and NiCr weaves to 1200°C. These temperatures were selected since the maximum in air service temperature of Cu is less than 300°C [67] while, the maximum service temperature of the Chromel-A NiCr alloy that was used to make the NiCr weaves is 1175°C-1200°C [67,90,95–98]. The thermal effects on the damping properties of most samples were characterized before and after temperature exposure at room temperature in the DMA, due to the limitations of maximum temperature and environment that are available in the DMA.

For the in-situ characterization of the temperature dependence of damping, the stiffness and permeability optimized NiCr weave was selected since it has the highest as-woven damping and was the highest temperature capability in air. Initially a series of room temperature measurements were gathered in order to affirm that the as-woven sample agreed with other samples from the same wire and architecture. The furnace enclosure was placed over the sample and it was heated at a rate of 10°C/min until the first temperature setpoint was reached. The temperature was then held for 10 minutes before damping measurements were performed in order to ensure that the temperature of the sample was uniform. Testing was performed by heating the sample to temperature setpoints in 100°C increments, beginning at room temperature and ending at 300°C.

After the sample returned to room temperature it was then once again measured. The loss factor measurements at frequencies from 1-200 Hz during temperature exposure in the DMA for the stiffness and permeability optimized NiCr weave are shown in Figure 83 and the average and standard deviation at each temperature setpoint are summarized in Figure 84.

The measurements of the stiffness and permeability optimized weave at progressively higher temperatures indicates clearly that as the material is exposed to progressively higher temperatures, the average measured loss factor decreases. Additionally, the measurements of the material after exposure to 300°C in air are nearly the same as the material at 300°C. This indicates that the change is permanent and that measurements of the material after exposure to high temperatures can provide an indirect indication of the damping properties of the material while they are at higher temperatures.

In order to compare the role of the sample being clamped in the DMA and the validity of ex-situ heating measurements, another optimized architecture NiCr weave was measured before and after exposure to 300°C in air in our custom tube furnace. The measurements of and comparison of the in-situ and ex-situ techniques are shown in Figures 85-86.

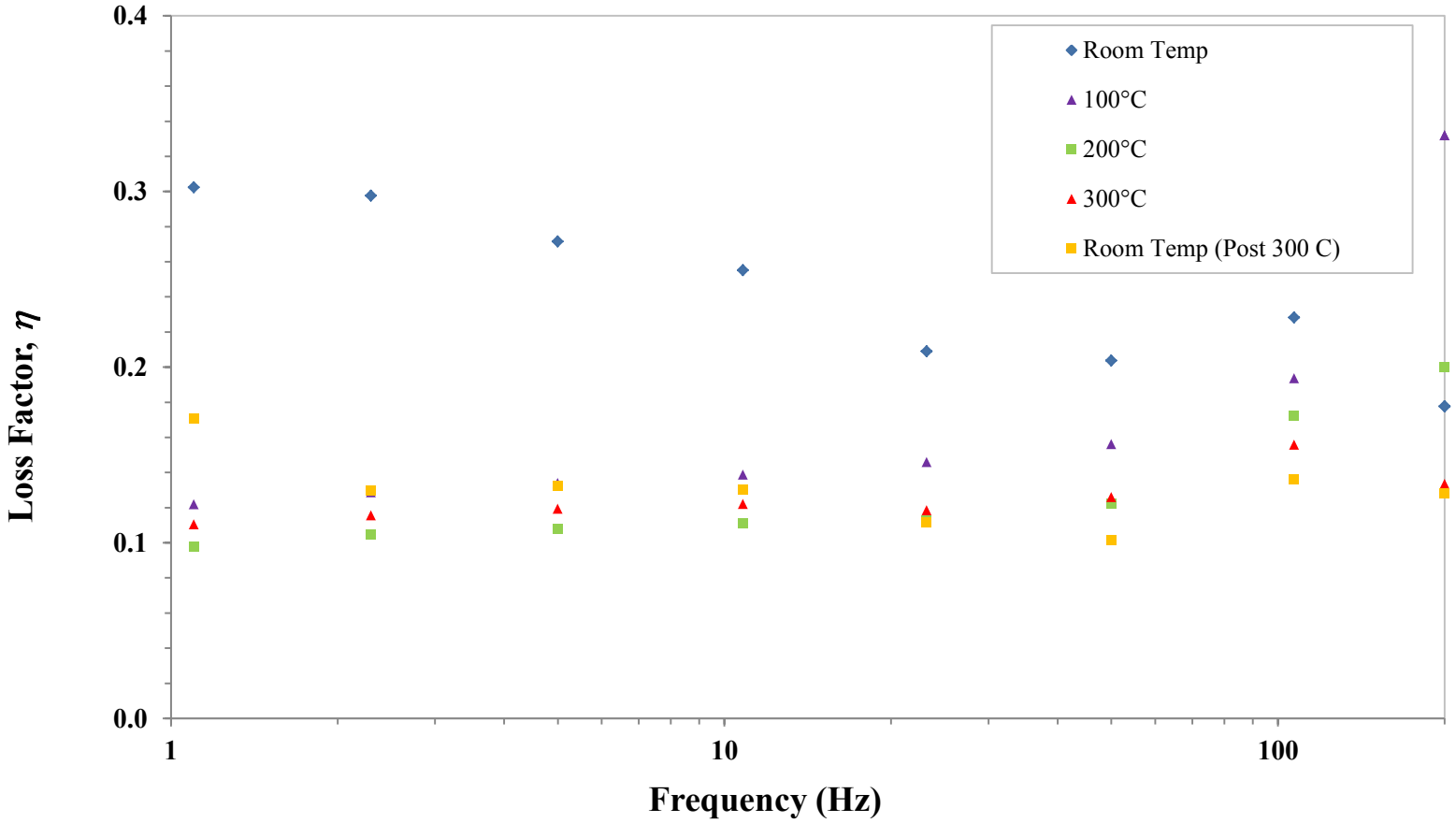

Figure 83: In-situ loss factor measurements from the DMA of an as-woven stiffness and permeability optimized NiCr 3-D weave for frequencies from 1-200 Hz. Measurements were taken in 100°C increments as the sample was heated in the DMA in order to quantify the damping changes in the weaves at various temperatures.

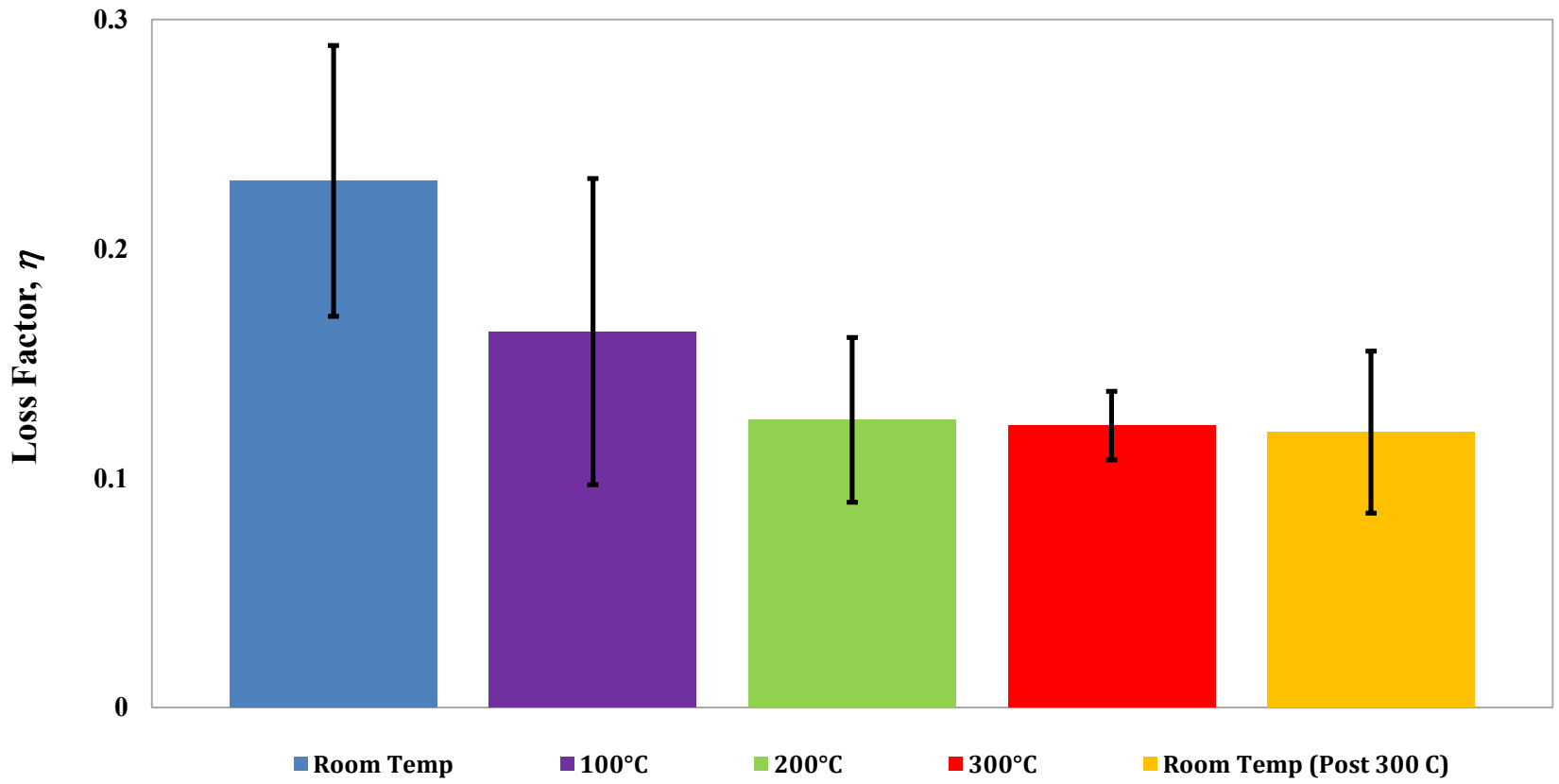

Figure 84: Average of the in-situ loss factor measurements from the DMA of an as-woven stiffness and permeability optimized NiCr 3-D weave for frequencies from 1-200 Hz. Measurements were taken in 100°C increments as the sample was heated in the DMA in order to quantify the damping changes in the weaves at various temperatures.

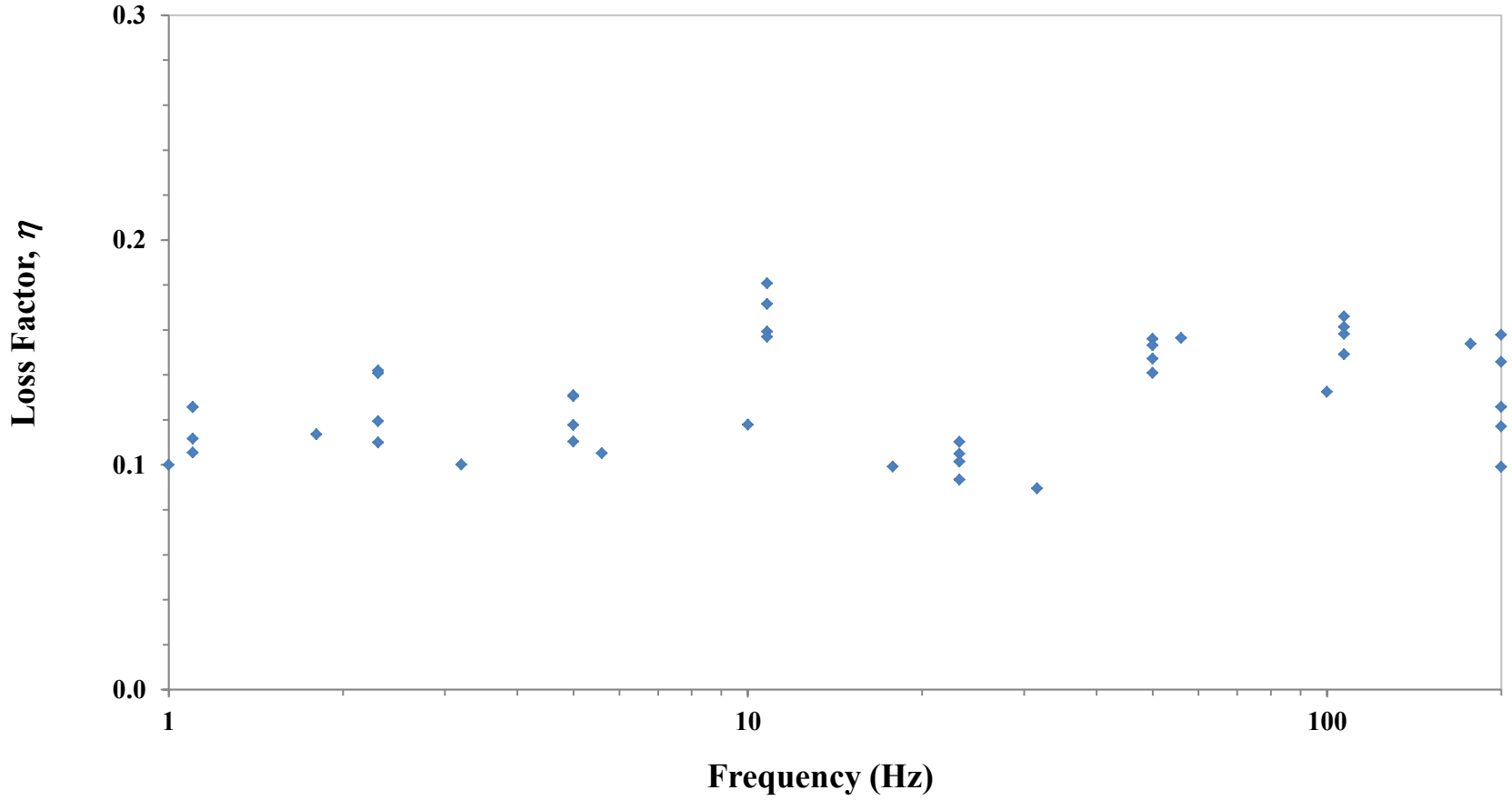

Figure 85: Ex-situ measurements of the loss factor of a post 300°C in air exposure for 5 hours of a stiffness and permeability optimized NiCr 3-D weave for frequencies from 1-200 Hz.

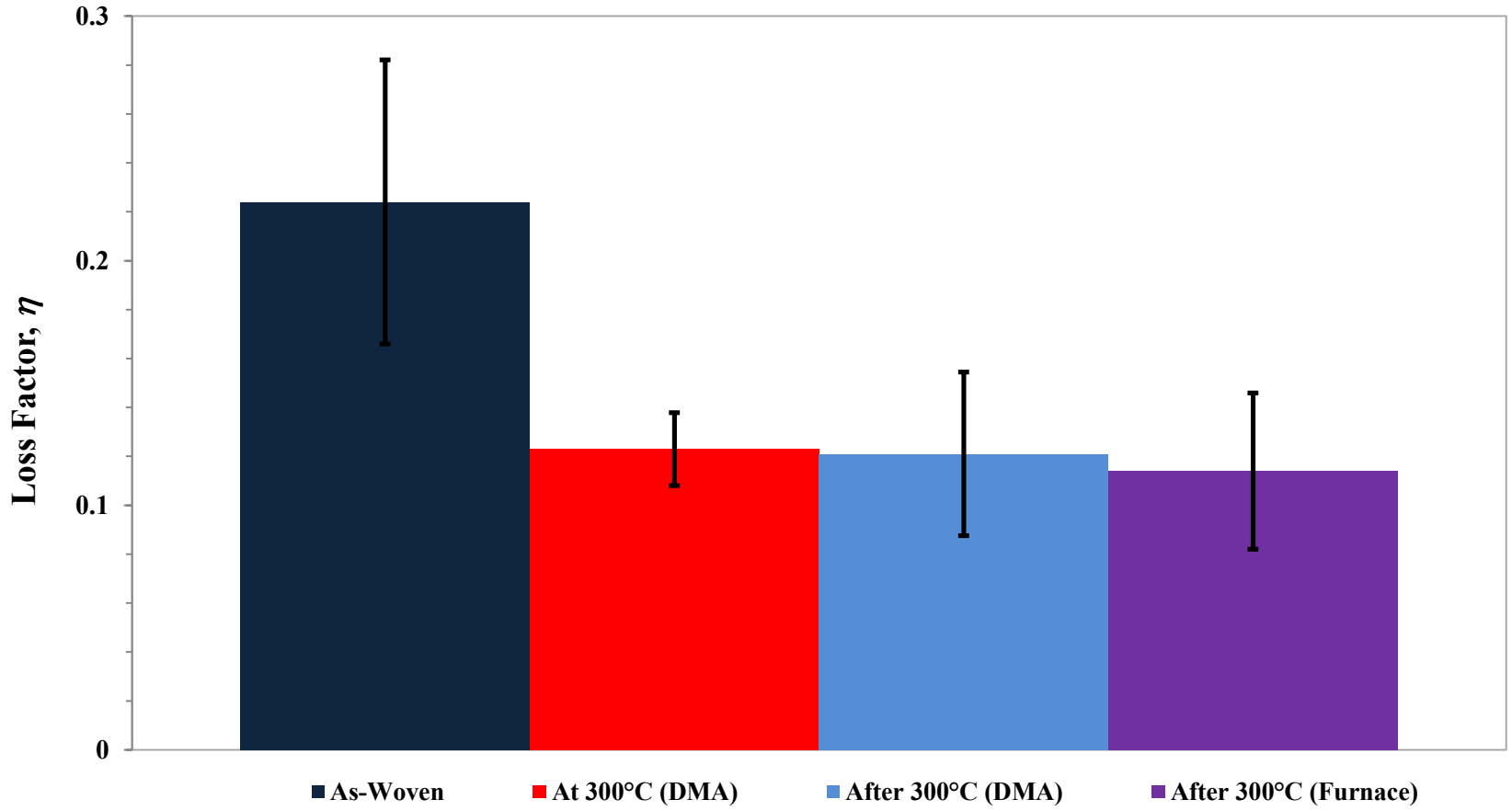

Figure 86: Average loss factor measurements from the DMA of the optimized pattern NiCr weaves. Measurements were taken in at least four orientations for all values from 1-200 Hz for all data points except for the measurement at 300°C which was taken in one orientation only. One standard deviation of the data is indicated by the uncertainty bars. Measurements were taken of the as-woven material before during and after a 300°C exposure in the DMA. Measurements were also taken on different samples before and after exposing the as-woven material to 300°C in a furnace for 5 hours.

Examination of these measurements of the optimized pattern NiCr samples revealed that the damping properties decrease from the as-woven state when the material is exposed to elevated temperatures whether the material is heated in the DMA or in our tube furnace. At 300°C (as measured in the DMA), the damping decreases by nearly 50% (η decreases from 0.22 to 0.12). When the material returns to room temperature after being exposed to 300°C in the DMA, the loss factor remains the same as was measured at temperature ($\eta = 0.12$). Another as-woven sample was measured before and after exposure to 300°C by heating in a tube furnace in air and these measurements confirmed that the measured loss factor of the material after exposure to 300°C in both the DMA and the tube furnace leads to the same ~50% decrease in the measured loss factor after the material returns to room temperature. As a result of these measurements and the greater range of temperatures, and environmental control of the tube furnace, all of the other temperature exposure measurements were performed by ex-situ heating with measurements before and after temperature exposure in the DMA.

For the ex-situ characterization of the damping dependence on temperature exposure, samples were measured in their as-woven state in the DMA in four orientations. The NiCr samples were then heated in our custom tube furnace to temperatures of 300°C or 1200°C for 5 hours in air. The Cu samples were likewise heated in air to their maximum in air service temperature of 300°C. In order to provide data that could be compared to the exposure of NiCr to 1200°C, the Cu weaves were also measured before and after exposures to 925°C in a forming gas (95% N_2/5% H_2) atmosphere to prevent oxidation of the material. This temperature was selected since it is 88% of the absolute melting temperature of the Cu wire and 1200°C is also 88% of the

absolute melting temperature of the NiCr wire. The ex-situ testing at 300°C was employed to not only evaluate the effects of clamping the samples during heating (discussed previously), but also to compare the effects of exposing the Cu and NiCr weaves to the same temperatures in air. The measurements of the loss factor at frequencies ranging from 1-200 Hz for the standard and stiffness and permeability optimized architectures for both the Cu and NiCr weaves are shown in Figures 87-93. The average of the loss factor and the corresponding standard deviation for each case are summarized in Figures 94-96 and Table 13.

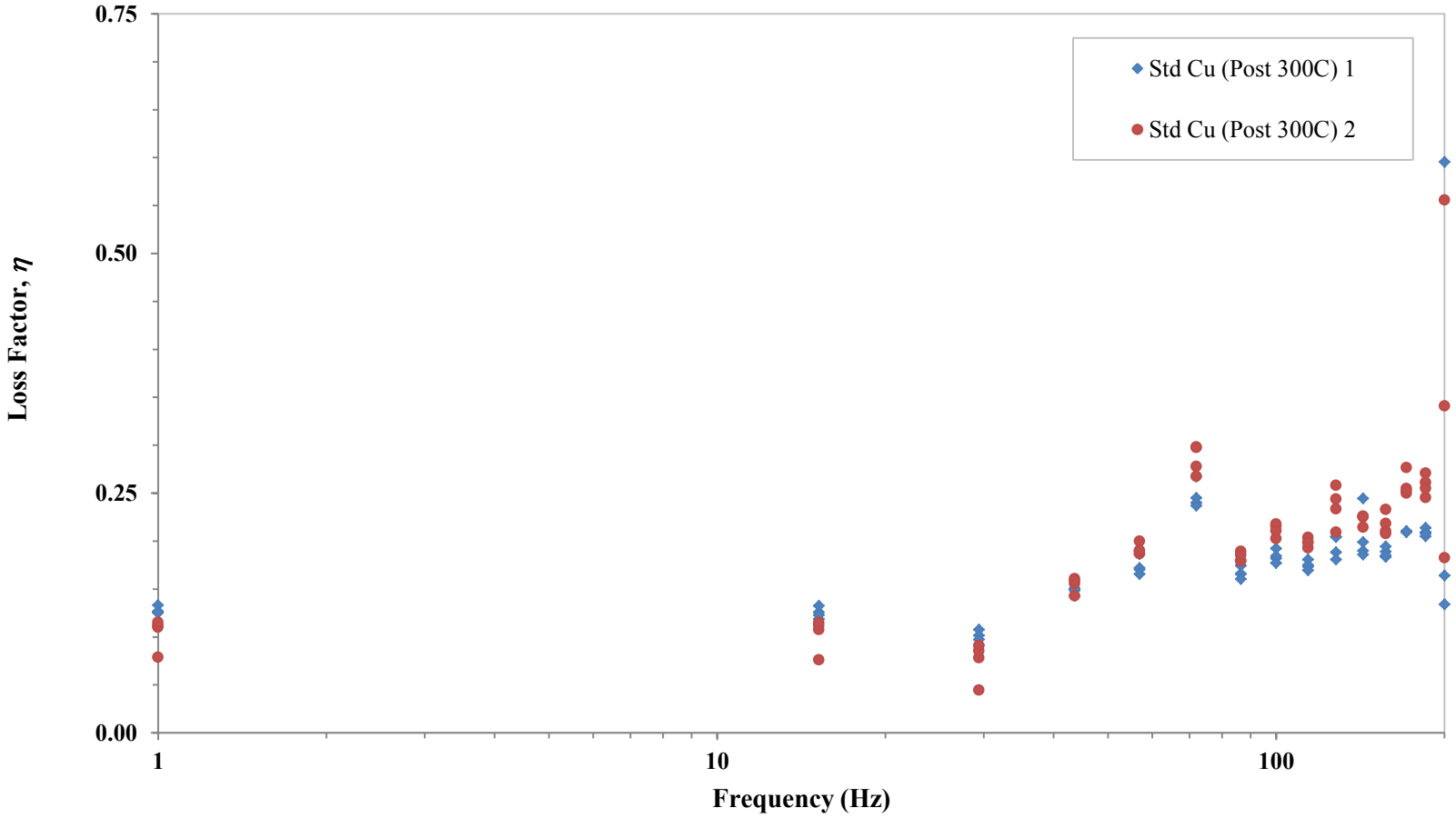

Figure 87: Ex-situ measurements of the loss factor after a 5 hour exposure at 300°C in air of the standard architecture Cu 3-D weaves for frequencies from 1-200 Hz.

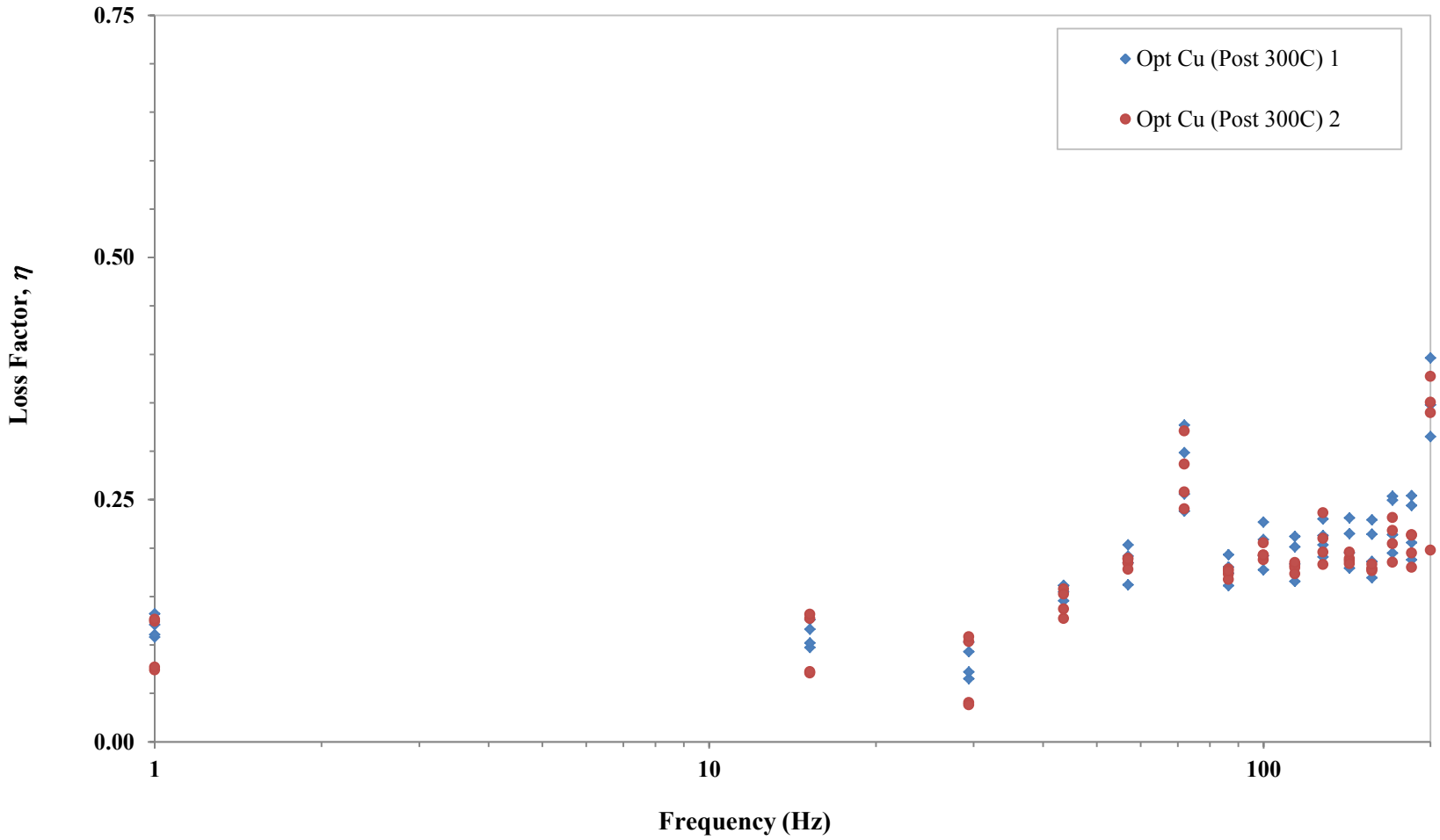

Figure 88: Ex-situ measurements of the loss factor after a 5 hour exposure at 300°C in air of the stiffness and permeability optimized architecture Cu 3-D weaves for frequencies from 1-200 Hz.

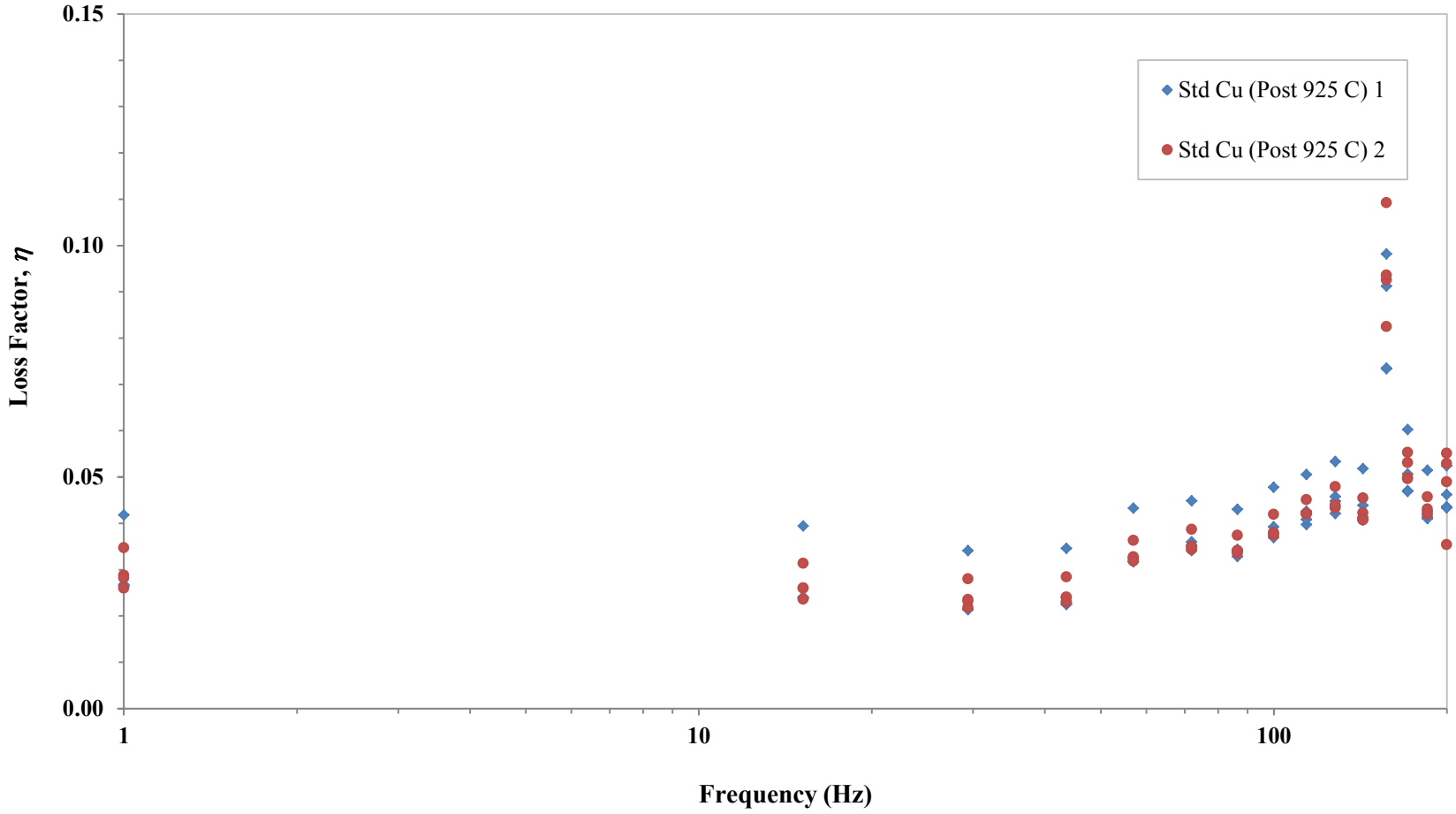

Figure 89: Ex-situ measurements of the loss factor after a 5 hour exposure at 925°C in a forming gas (95% N_2 / 5% H_2) of the standard architecture Cu 3-D weaves for frequencies from 1-200 Hz.

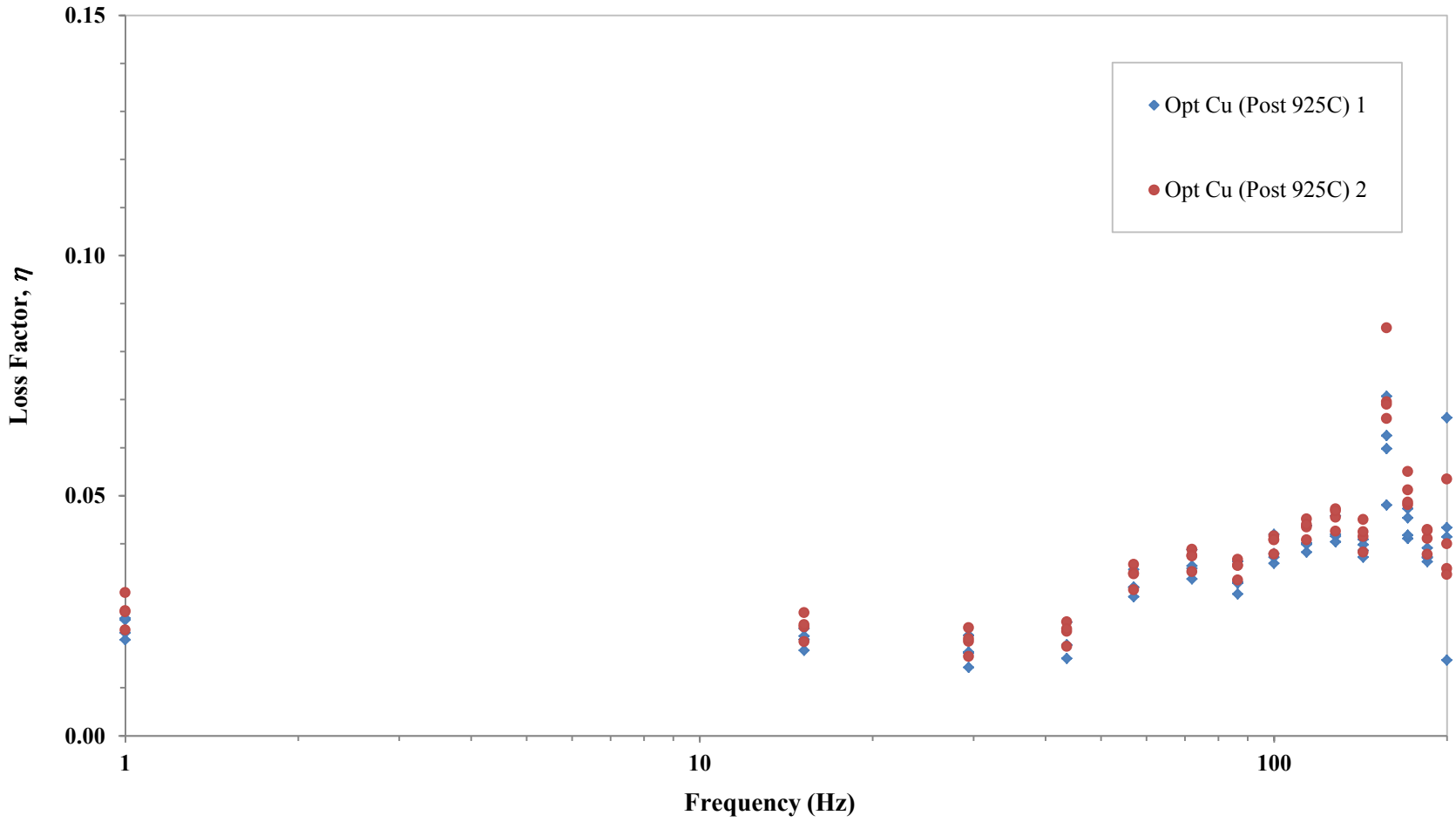

Figure 90: Ex-situ measurements of the loss factor after a 5 hour exposure at 925°C in a forming gas (95% N_2 / 5% H_2) of the stiffness and permeability optimized architecture Cu 3-D weaves for frequencies from 1-200 Hz.

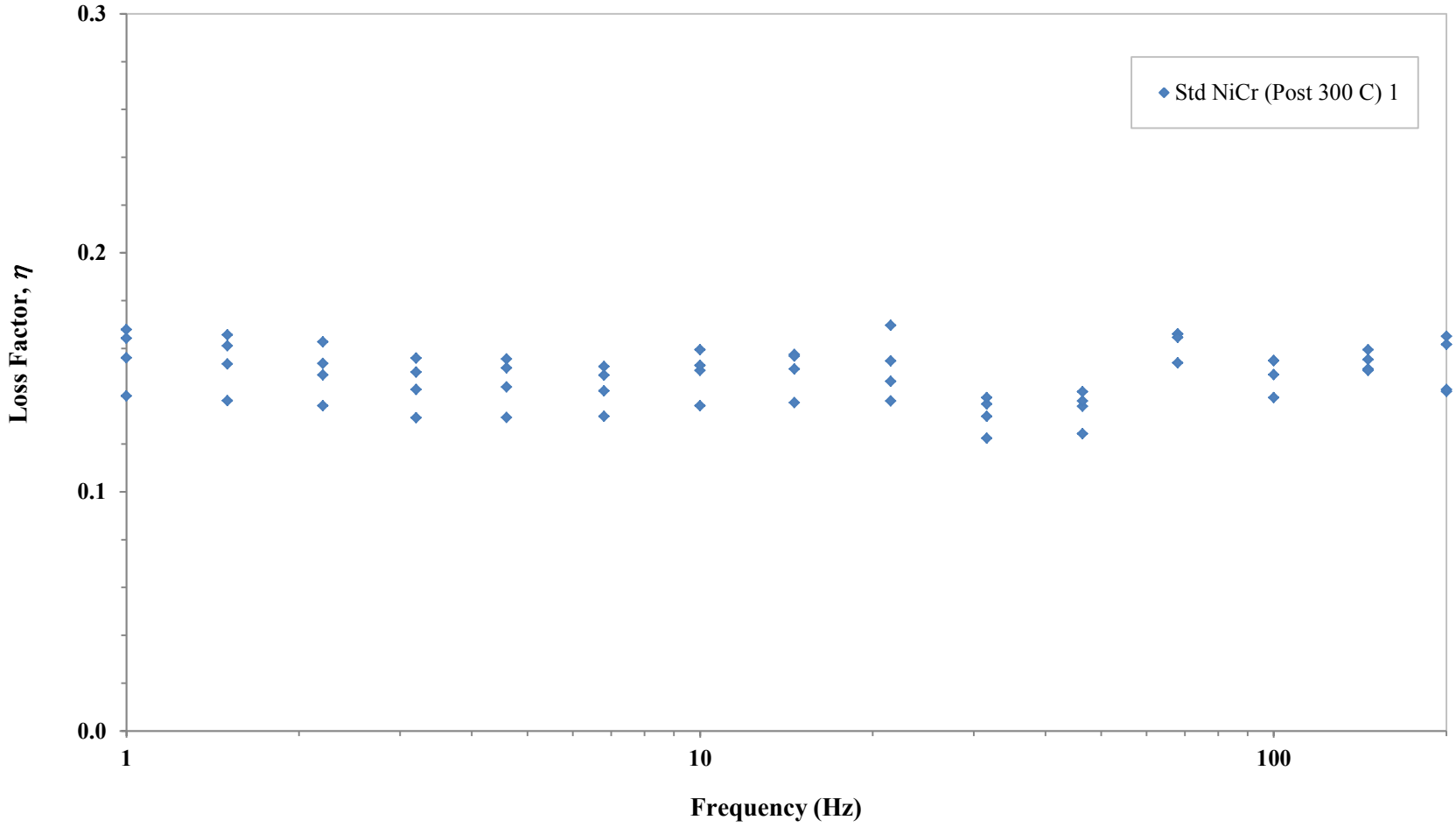

Figure 91: Ex-situ measurements of the loss factor after a 5 hour exposure at 300°C in air of a standard architecture NiCr 3-D weave for frequencies from 1-200 Hz.

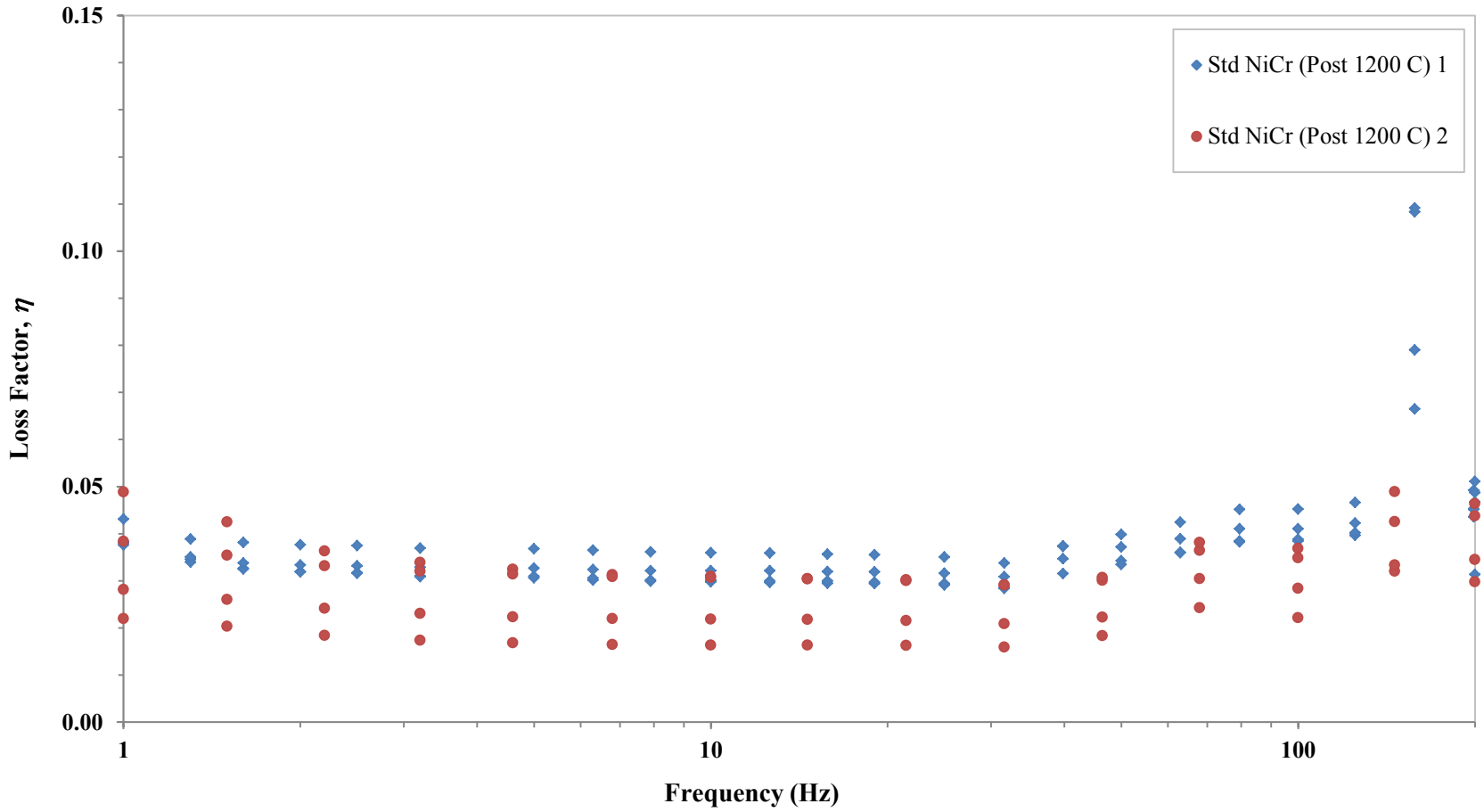

Figure 92: Ex-situ measurements of the loss factor after a 5 hour exposure at 1200°C in air of the standard architecture NiCr 3-D weaves for frequencies from 1-200 Hz.

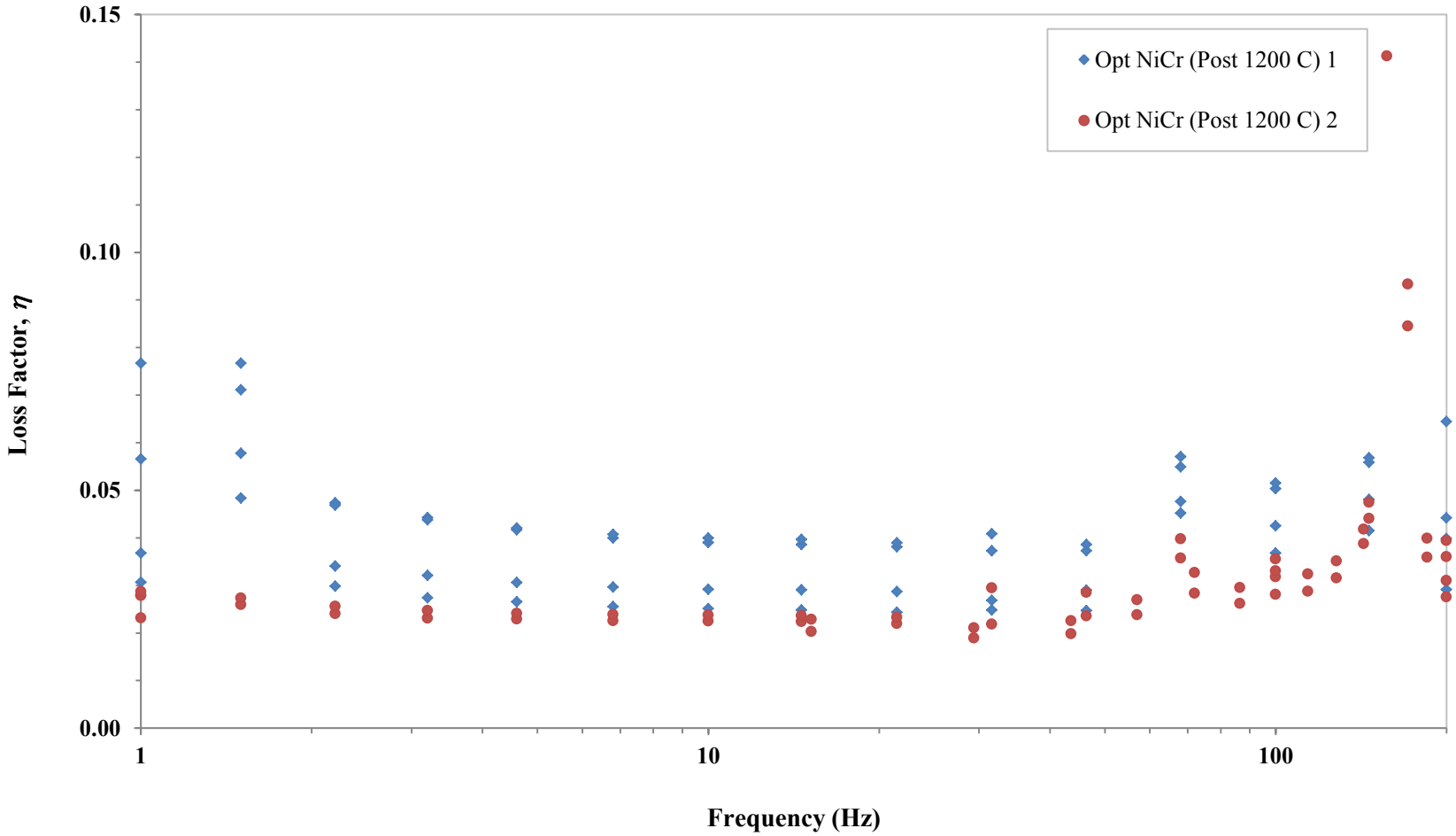

Figure 93: Ex-situ measurements of the loss factor after a 5 hour exposure at 1200°C in air of the stiffness and permeability optimized architecture NiCr 3-D weaves for frequencies from 1-200 Hz.

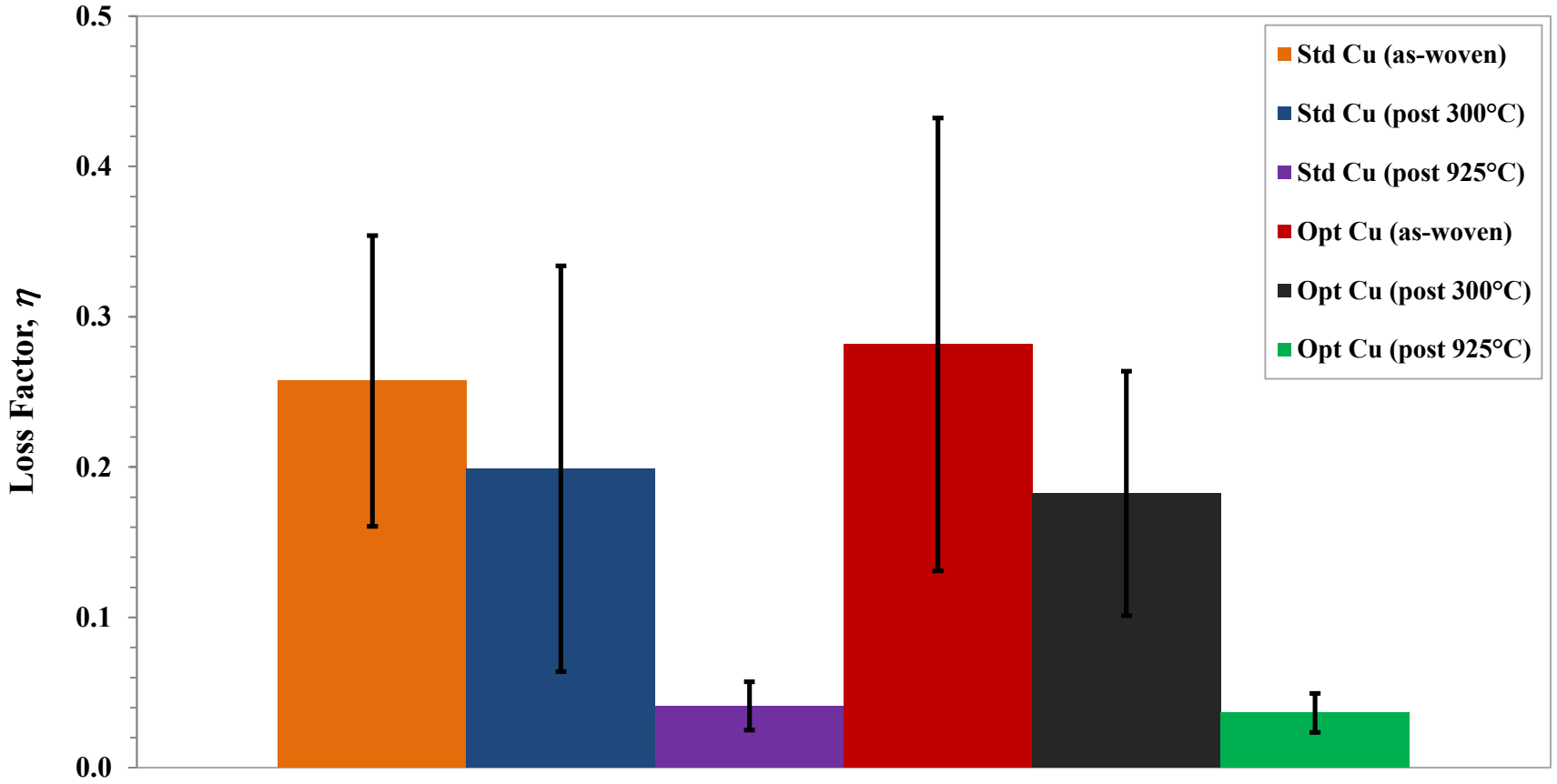

Figure 94: Average of the ex-situ measurements of the loss factor for frequencies from 1-200 Hz for the standard and stiffness and permeability optimized Cu 3-D weaves in the as-woven, post 300°C in air, and post 925°C in forming gas (95% N_2/ 5% H_2) states. The uncertainty bars indicate one standard deviation of the average of all of the measurements for a particular case.

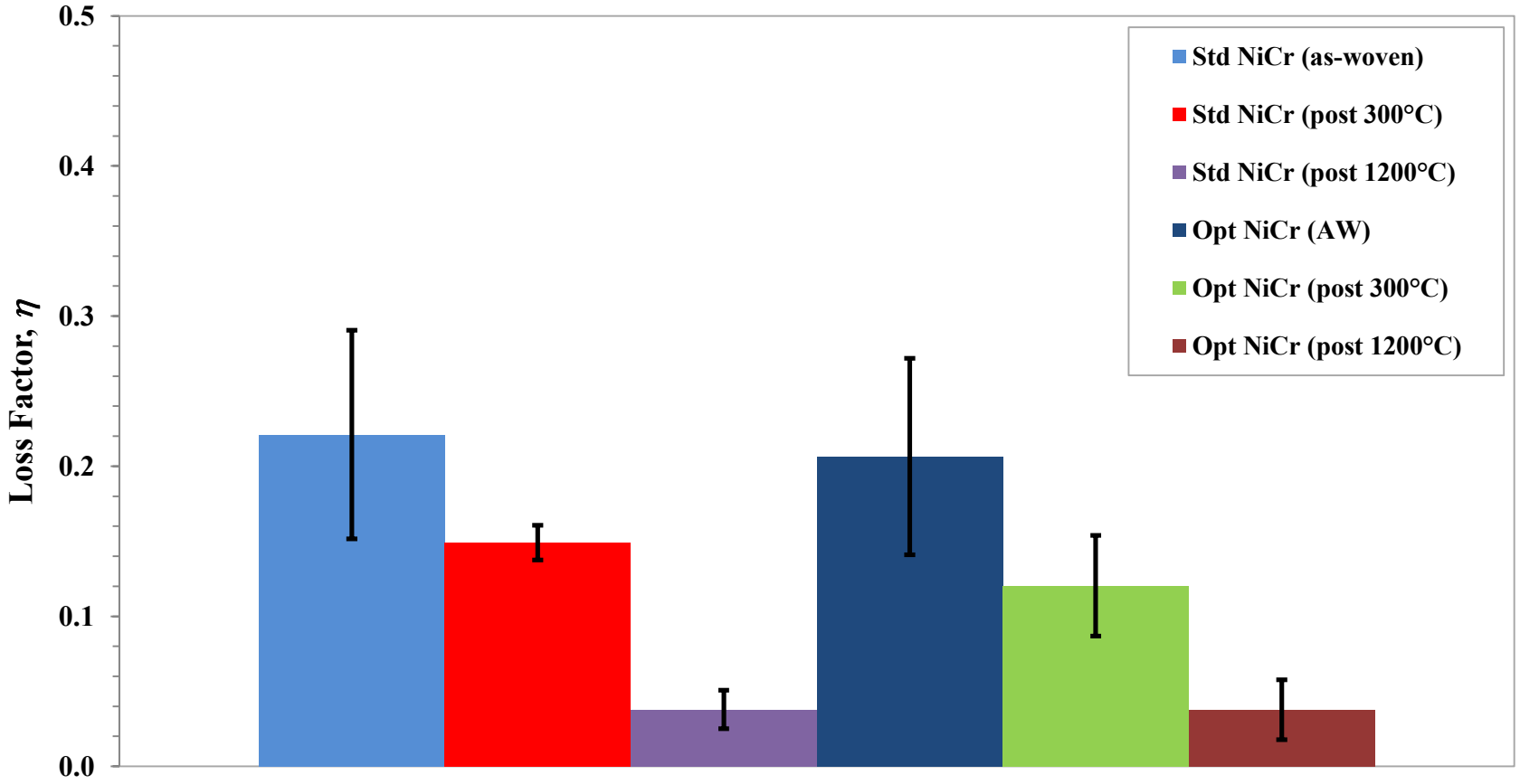

Figure 95: Average of the ex-situ measurements of the loss factor for frequencies from 1-200 Hz for the standard and stiffness and permeability optimized NiCr 3-D weaves in the as-woven, post 300°C, and post 1200°C in air states. The uncertainty bars indicate one standard deviation of the average of all of the measurements for a particular case.

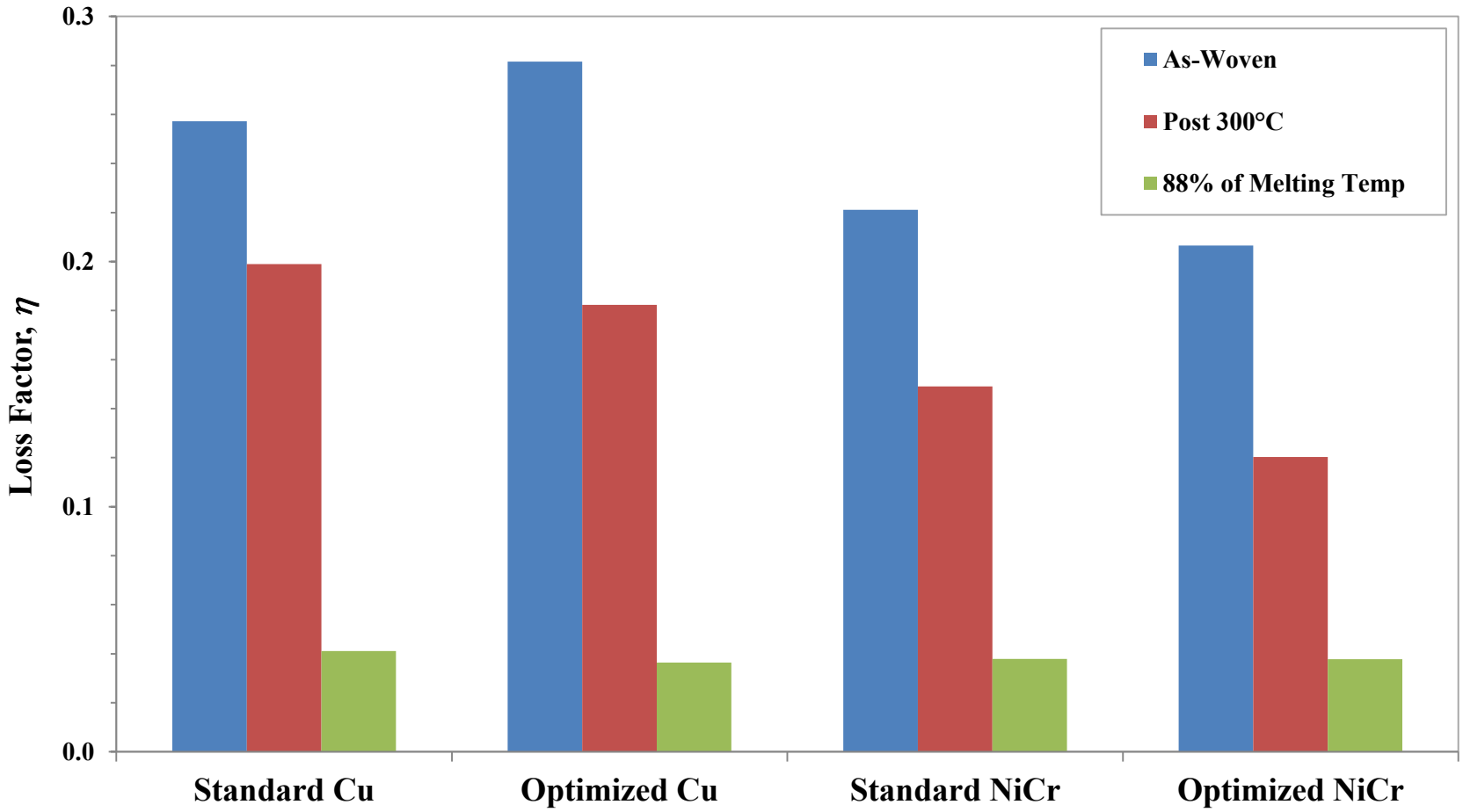

Figure 96: Comparison of the average of the ex-situ measurements of the loss factor for frequencies from 1-200 Hz for the standard and stiffness and permeability optimized Cu and NiCr 3-D in the as-woven, post 300°C in air, and post 88% of their melting temperature (925°C in forming gas for the Cu weaves and 1200°C in air for the NiCr weaves) states.

Table 13: Average of the ex-situ measurements of the loss factor for frequencies from 1-200 Hz for the standard and stiffness and permeability optimized Cu and NiCr 3-D in the as-woven, post 300°C in air, and post 88% of their melting temperature (925°C in forming gas for the Cu weaves and 1200°C in air for the NiCr weaves) states

As-Woven	Standard Cu	0.26	0.10
	Optimized Cu	0.28	0.15
	Standard NiCr	0.22	0.07
	Optimized NiCr	0.21	0.07
Post 300°C	Standard Cu	0.20	0.14
	Optimized Cu	0.18	0.08
	Standard NiCr	0.15	0.01
	Optimized NiCr	0.12	0.03
88% Of Melting Temp	Standard Cu	0.04	0.02
	Optimized Cu	0.04	0.01
	Standard NiCr	0.04	0.01
	Optimized NiCr	0.04	0.02

The ex-situ measurements of the Cu and NiCr weaves reveal that for all of the wire and architecture combinations, the loss factor deceases with the maximum temperature to which the material is exposed. Initially, the Cu weaves exhibit higher loss factors than the NiCr architectures and the difference between architectures is smaller than the difference between the materials choice. After exposure to 300°C in air, all of the samples showed a decrease in the measured loss factor of 25-45%. Comparing the decreases in the optimized architecture copper weaves after exposure to 300°C to the

optimized architecture NiCr weaves, we can observe that the decrease in the copper weaves is only ~35%, compared to the ~45% decrease in the NiCr weaves (25% for the standard copper weaves and 35% for the standard NiCr weaves). This is likely attributed to the fact that the yield stress of the NiCr wire is higher and will likely exhibit greater spring back, which leads to higher residual stresses (that are believed to be relaxed during temperature exposure). Exposure of as-woven samples to even higher temperatures in an appropriate environment that was selected to be 88% of the absolute melting temperature of the wire materials that make up the weaves, revealed even larger decreases in the loss factor. In fact, all of the samples had a measured loss factor of 0.04 after exposure to these temperatures. It is interesting to note, that the modeled weaves with the average measured gap spacing exhibited a loss factor of 0.06, which is comparable to the measured loss factor of the weaves after exposures to high temperatures. This may indicate that the weaves after exposure to the highest measured temperatures are well represented in the model of the weaves.

What is important to consider with all of these measurements of the materials after exposure to their maximum service temperature is that the decrease in the mechanical loss factor for all of the weaves limits the final applicability of these weaves for high temperature damping applications. However, even after exposure to 1200°C for 5 hours, the NiCr weaves still retained damping abilities that were competitive with many polymers, but with a much higher maximum use temperature. In order to compare the results with other damping materials, a plot of the mechanical loss factor and the maximum service temperature of many common damping materials is shown in Figure 97.

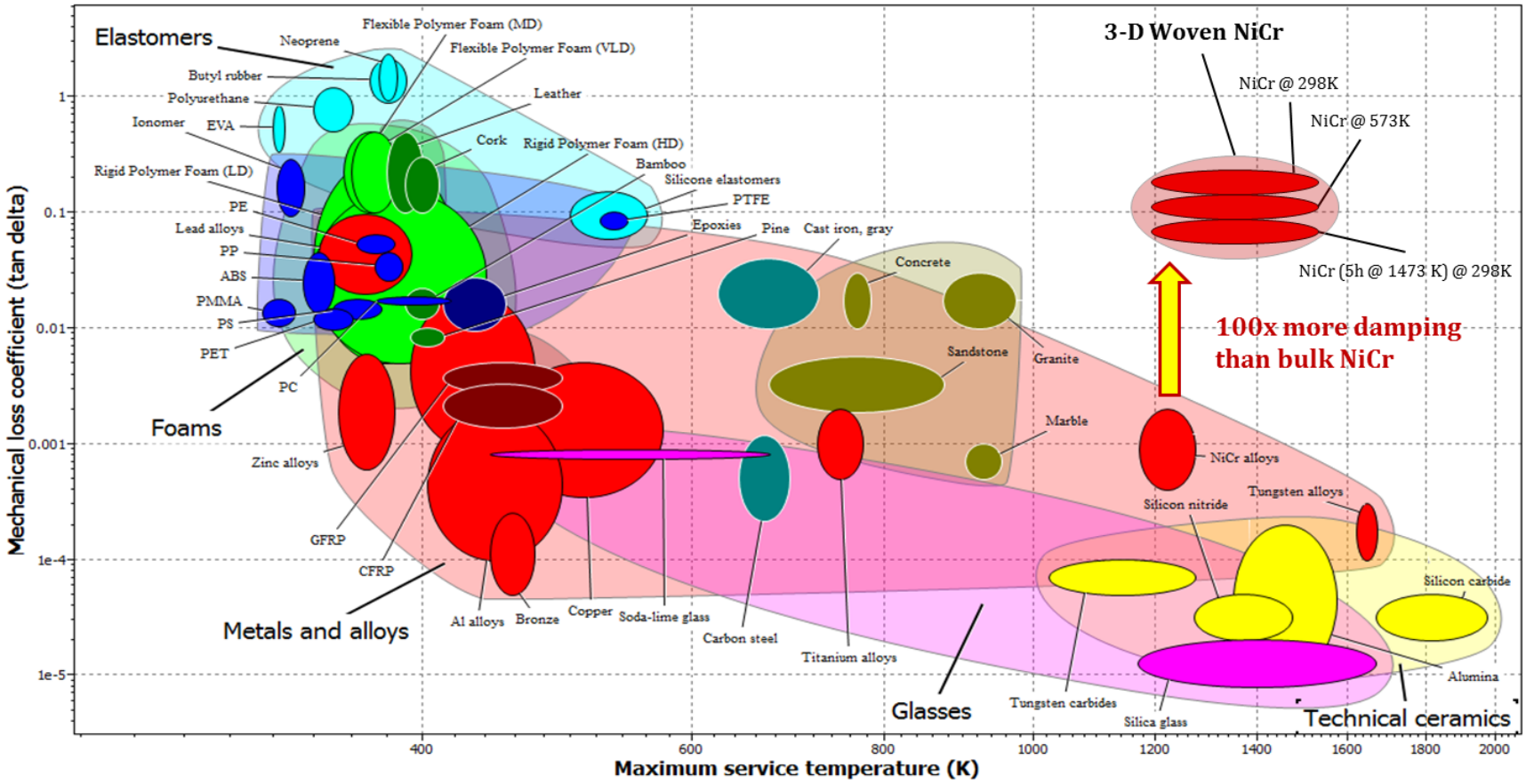

Figure 97: A Plot of the mechanical loss coefficient and the maximum service temperature of the material which shows how the 3D woven Optimized Pattern NiCr Weaves compare with many common polymers, metals, and ceramics. The 3D woven materials possess damping abilities that are comparable with many common polymers, which are frequently used in room temperature damping applications, but they also maintaining the ability function in the temperature range where only high temperature metals and ceramics can survive.

The measurements of the weaves both in-situ and ex-situ indicate that temperature exposure causes a permanent changes in the materials that leads to a decrease in the measured loss factor across the measured range. In order to design and optimize these architecture materials for damping, a greater understanding of the changes that occur during temperature exposure in the as-woven weaves is necessary. There are three main damping mechanisms that are responsible for the high damping abilities of the weaves. In the weaves, frictional and inertial damping dominate the response of the material, although internal damping of the wires themselves is always present. In order to understand the measurements of the changes in the materials with temperature, we will examine the role of each of these mechanisms in the weaves and how they may be affected by thermal exposure.

5.2.2: Effects of Temperature on Internal Damping

Internal damping in the 3D metallic weaves is the damping of an excitation that is performed by each wire individually and is independent of the architecture of the weave. The internal damping is the values for all of the materials (except for the weaves) that are previously shown in the mechanical loss coefficient and maximum service temperature plot. The contribution of internal damping to the overall damping of the material is small (since internal damping's contribution is orders of magnitude less than the role of the other two mechanisms) and exposure to high temperatures should not affect the internal damping of the material in a significant way, and any changes that would occur, would not affect the damping in a measurable way. Therefore any changes in the internal

damping could not be used to explain the large observed changes in damping in the weaves.

5.2.3: Effects of Temperature on Frictional Damping

Frictional damping in the 3D woven metallic weaves is the conversion of mechanical energy, through frictional sliding between adjacent wires, into heat. Frictional energy dissipation can be understood with the classic physics model of a block sliding along a surface as is shown in Figure 98.

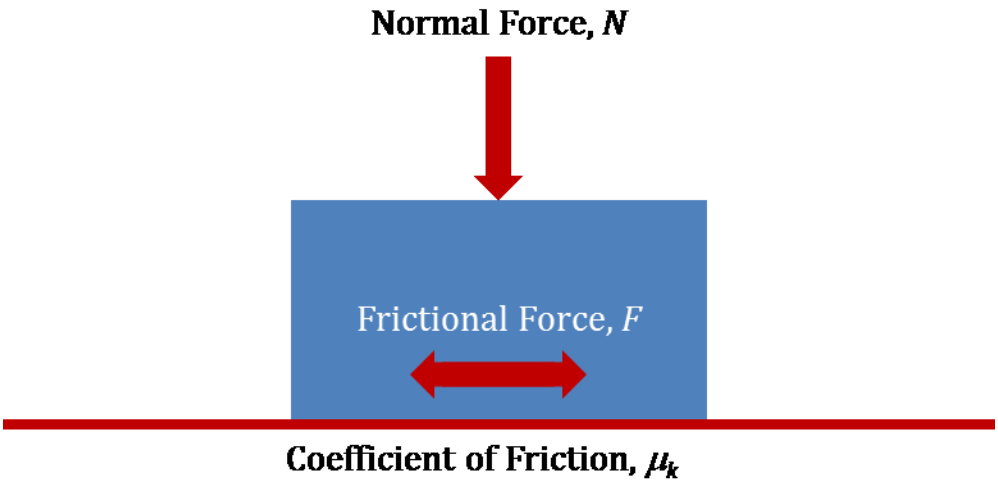

Figure 98: A simple modeling illustrating the transformation of kinetic energy into heat by a block sliding on a surface through kinetic friction. This model represents the frictional dissipation of energy that between wires in the weave that is responsible for vibration damping.

The frictional force, F_k, between the block and the surface is dependent on the normal force, N, between the block and the surface and the kinetic coefficient of friction, μ_k, between the two surfaces as [99],

$$F_k = N\mu_k \tag{23}$$

In order to relate the frictional forces to the damping, one must relate the frictional forces to the energy dissipated in a cycle, or the work done. In the case of reciprocal sliding (as is the case for the wires in the weave), the work done is

$$W = F_k d \tag{24}$$

Substituting in for the expression for the frictional force required to slide the block across the surface in a reciprocal motion,

$$W = N\mu_k 4A \tag{25}$$

where, A is the amplitude of the oscillation. The amplitude is multiplied by four, since the block must travel through the distance of four times the amplitude to complete one cycle.

Since there are many points of contact in the weave which contribute to the frictional energy dissipation, the work done must be multiplied by the number of frictional contact points in the weave. Within the weave there are warp/warp, fill/fill, warp/fill, warp/z, and fill/z contacts, which can contribute to frictional energy dissipation. The amount of contact and the normal forces between these wires is complex and variable. In this thesis, we have decided to focus our efforts on the interactions between the fill and z wires. The spring back of the z-wires against the fill wires increases the normal force for frictional energy dissipation and will be shown is dependent on temperature exposure. As a result, the expression for the energy dissipated in the weave for a single cycle becomes,

$$\Delta U = W = N\mu_k 4A\chi \tag{26}$$

where χ is the number of fill/z contact points in the weave sample.

In order to translate the frictional energy dissipation of the fill/z wires into a contribution to the loss factor of the material, the loss coefficient can be estimated as [14,88,89,100],

$$\eta = \frac{\Delta U}{2\pi U_{max}} \tag{27}$$

where, η is the loss factor, ΔU is the energy dissipated in a cycle (in this case from the frictional sliding of the fill and z-wires), U_{max} is the elastic energy stored at the maximum load. The elastic energy stored in a beam in single cantilever bending loaded at the end (which is the case for the DMA test), U_{max}, can be written as [101],

$$U_{max} = \frac{P^2 L^3}{6EI} \tag{28}$$

where, P is the load applied to the end of the beam, L is the length of the beam (17.5 mm), E is the elastic modulus of the beam, and I is the moment of inertia. For simplicity, the moment of inertia will be simply estimated as that of a beam of rectangular cross section which is,

$$I = \frac{bh^3}{12} \tag{29}$$

where, b is the width of the beam (15 mm) and h is the thickness of the beam (3 mm).

Combining all of the expressions together results in an expression for the loss factor that depends on the geometry and material properties in addition to the normal force between the wires, the load required to deflect the material, the amplitude of the oscillation, and the number of frictional contact points (which depends on the architecture), and it is written as,

$$\eta = \frac{A\mu_k N\chi Ebh^3}{\pi P^2 L^3} \tag{30}$$

This expression shows us what parameters are important in order to maximize the loss factor. The variables in the equation are not entirely independent, and for instance, the load required to deflect the beam to the desired amplitude, *P*, is dependent to varying extents on all of the other parameters in the equation. This however does provide guide for how to improve the loss factor and what may be affected by temperature exposure.

In the interest of this section, we are concerned with developing an understanding of the specific changes in frictional damping between the fill and z wires that occur with temperature exposure. The above equation for the loss factor indicates that the possible changes that occur could be changes in the coefficient of friction, the number of contact points in the weave, and the normal force.

From the literature [56,57,102], we know that a hard, gas tight oxide layer encapsulates the surface of the NiCr wires in the weaves which is present before, during,

and after high temperature exposure. This oxide layer is present in all measured cases of DMA testing and governs the kinetic friction coefficient between the wires. The damping properties still decrease due to temperature exposure, which indicates that a change in the coefficient of friction at the interface between wires is not the governing mechanism for the decrease in damping. Additionally, the heat treatments of copper were performed in air at intermediate temperatures (300°C) and in a reducing atmosphere at high temperature (925°C). The reducing atmosphere would prevent the growth of an oxide on the surface of the copper wires, yet the damping decreased further in these cases, providing further evidence that the coefficient of friction at the surface is not the main factor that is changing the damping properties of the weaves with temperature exposure.

The number of contact points in the weave that can contribute to frictional energy dissipation should be directly related to the architecture of the weave. In a perfect model, this is indeed the case, and the standard weaves have approximately ~50% more contact points than the optimized weaves. The linear dependence of loss factor on the number of contact points would imply that there should be a 50% increase in the loss factor from the optimized to the standard weaves. Examination of the measured loss factors in the real weaves clearly does not indicate that this is the case and in fact, using the as-woven loss factors of the standard and optimized architecture weaves as an example for the Cu and NiCr wires shows that the difference in loss factor between architectures is small and the dominant architecture depends on the wire material used. This is a result of two main factors. First, the modification of the number of contact points will also affect the load required to bend the weave in the single cantilever orientation (a competing variable in

the loss factor calculation). Secondly, in the real weaves, defects (gaps and twists) will increase or decrease the number of contact points in a stochastic manner and modify the normal forces for contact. As the wires move in the weaves during testing, the normal forces and number of contacts may also shift.

The role of number of contact points in controlling the loss factor is difficult to observe in the as woven materials, but examination of the in air heat treated samples after 300°C exposure shows that the standard architecture weaves possess a higher loss factor than the optimized weaves. The exact reason for this is not known, but it is surmised that the wires are able to settle into a stable configuration when they are exposed to elevated temperatures and effects of the architecture are then made more prominent. Unfortunately, the measurements of the weaves at 88% of their absolute melting temperature do not have enough resolution to provide further confirmation of this hypothesis.

The normal force of frictional damping is another major variable that is correlated to the loss factor for the frictional dissipation of energy in the weaves. As a result of the weaving process that was discussed earlier, the z-wires in the weaves exert a force against the fill wires when they spring back after the z-loops are formed. In order to quantify the contribution to the frictional damping and how the spring back force changes with temperature, we decided to examine the z-wires in the NiCr weaves before and after elevated temperature exposure. Both analytical and finite element models were used to estimate the forces that the z-wires exert on the neighboring fill wires. In trying to quantify this normal force, it was found that two other factors are affected by temperature exposure: relaxation of the curvature of the overall shape of the z-wire; and in-plane

expansion of the z-wires in the warp direction. These may also contribute to changes in the normal force in addition to the number of contact points in the weave.

5.2.3.1: Quantification of the Change in Z-Wire Geometry with Temperature:

In order to understand the decrease in damping with temperature exposure, we investigated the changes that occur in the z-wires of the NiCr weaves with exposure to increased temperatures. We know from the literature that exposure of the NiCr weaves to high temperatures in air will not affect the NiCr alloy that we have chosen since the surface is self-passivated by a gas tight Cr_2O_3 surface in the as-woven samples and will not be further affected by the temperature exposure [57]. This suggests that the changes in the damping properties of the weaves are not the result of changes in the coefficient of friction of the surface. It was hypothesized that an annealing process takes places which relaxes residual stresses in the weaves. The z-wires are subjected to the largest strain during the weaving process, while the warp and fill wires remain straight and are strained little if at all. Therefore, we investigated the changes in residual stress in the z-wires before and after temperature exposure in the NiCr weaves (both standard and optimized patterns).

In order to measure the residual stresses in the z-wires, the weaves had to be cut to expose the internal wires, and this was done using wire EDM in order to minimize the damage that results from cutting. Samples were cut to a length of 25 mm through the fill-

z plane and then they were subsequently cut along the warp-z plane in order to expose the profile of the z-wires as shown in Figure 99.

Figure 99: An as-woven section of the standard pattern NiCr weave with the 1" long section used residual stress analysis shown on the right edge of the image.

After EDM cutting, any stray pieces of wires were carefully removed with tweezers to expose the profile of the z-wire in the weave. The specimens were then mounted in a custom spring clip and placed under a 5x objective of a Zeiss upright microscope. The sample orientation was adjusted in relationship to the objective so that the entire cross section was parallel with the imaging plane and images were captured across the entire plane without having to readjust the focus of the microscope, which could cause distortions. Images of an entire z-wire at the surface were captured using the microscope's digital camera and a 0.63x adapter ring in full color bitmap format. After all of the images (usually between 120 and 150 images) of each cross-section were captured, the images were stitched together in order to form a montage of the z-wire in the weave with Microsoft® ICE [103]. This allowed me to perform analysis on a single stitched image of an entire z-wire instead of on smaller individual images. An example

montage and one of the single images that was used to form the montage is shown in Figure 100. A z-wire that was at the located at the surface of the weave was carefully removed with tweezers by working across the wire from side to side and slowly releasing it from the weave. Once a z-wire was removed, it was sandwiched between two glass slides and another montage of the wire was gathered. The removed wires exhibited a complex curvature of both the warp-fill plane (as seen in the image) and the warp-z plane (not shown in the image). An example montage of a z-wire that was shown in Figure 100 after being removed from the weave is shown in Figure 101. This removed wire exhibits the pronounced curvature of the warp-fill plane in the z-direction.

In order to evaluate the accuracy of the Microsoft® ICE stitching algorithm's ability to properly reconstruct the montage, a set of sample images was sent to Amanda Levinson at NRL, since this type of image stitching is frequently performed in their lab during serial sectioning [104,105]. She stitched the images using their software and compared their result with the results from the ICE software. The ICE software used three different stitching parameters ('planar 1', 'planar 2', and 'planar 3') which were all compared with NRL's stitched image. The settings control the limitations on the stitching algorithm. 'Planar 1' only allows the images to be moved, in-plane, with respect to one another in order to stitch together and form a montage. 'Planar 2' allows for rotation of the images in order to match and form a composite image. The 'Planar 3' setting also allows the algorithm to scale the individual images in order to form a composite. The original stitched image from NRL and the comparison between their composite image and the different images stitched using Microsoft® ICE are shown below in Figures 102-105. In order to compare the images, an image stitched with

Microsoft® ICE and the image stitched by NRL were overlaid on one another and aligned in the center of the image. Differences between the NRL image and the ICE images appear as bright regions in the overlay.

The results of the image stitching comparisons indicated that both the 'planar 1' and 'planar 2' settings generated results that agreed with the standard image from NRL. These images exhibit good matching without any noticeable bright regions, indicating a lack of matching. The 'planar 1' setting is the most restrictive setting in the sense that in only allows for translation of the individual images in order to create the composite image (no scaling or shearing of the image is allowed). The 'planar 1' setting was the most representative option for the image stitching, since images were taken using a planar translation along the wire without rotating or using different magnifications. The 'planar 1' setting stitches the images by only allowing translations (no scaling or rotation is allowed) and was selected for stitching all of the images that were gathered.

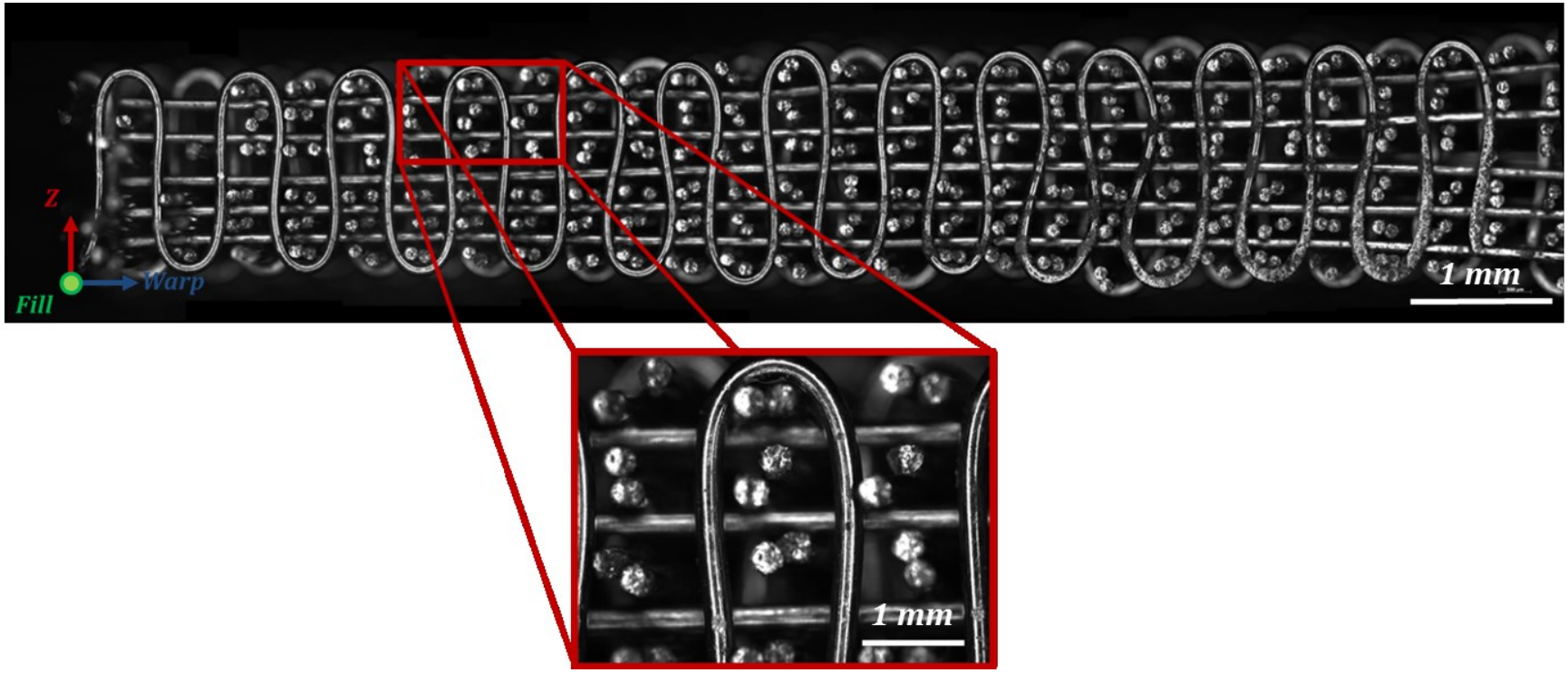

Figure 100: An example montage of the cross section of the standard pattern NiCr weave with the z-wire in the focal plane of the image. This image is a composite of 106 images that were stitched using Microsoft ICE. One of the images that was used to make the montage is shown as in inset.

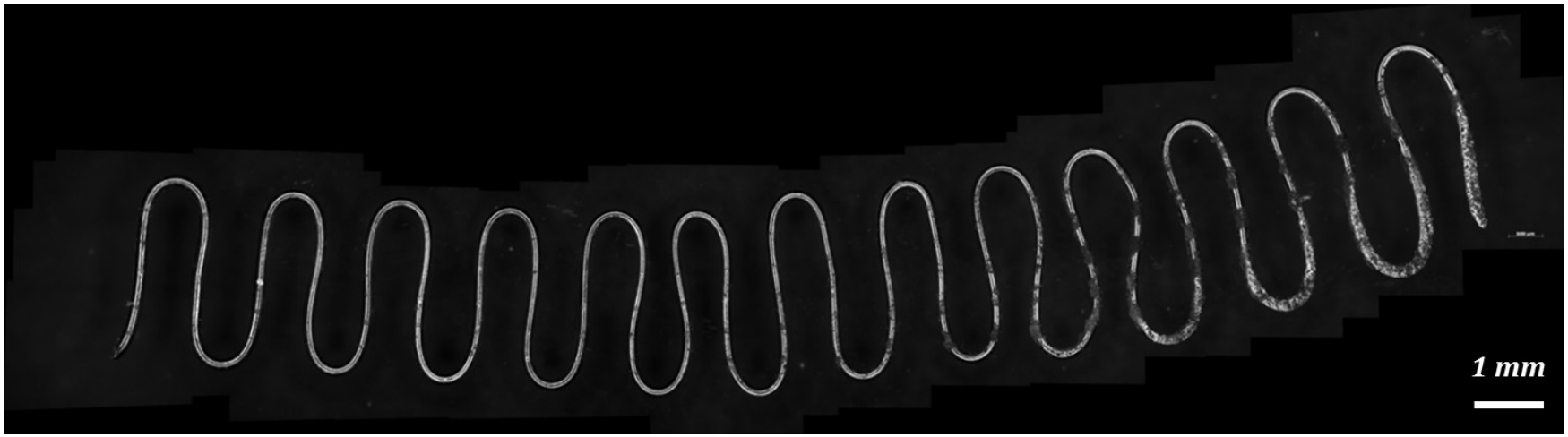

Figure 101: The same z-wire that was shown in the weave after it was removed from the weave and imaged between glass slides. The pronounced curvature in the warp-fill plane can be easily recognized in the image. This curvature is evidence that of residual stress that was present in the as-woven weaves as a result of the z-wire crimping that takes place in the weaving process.

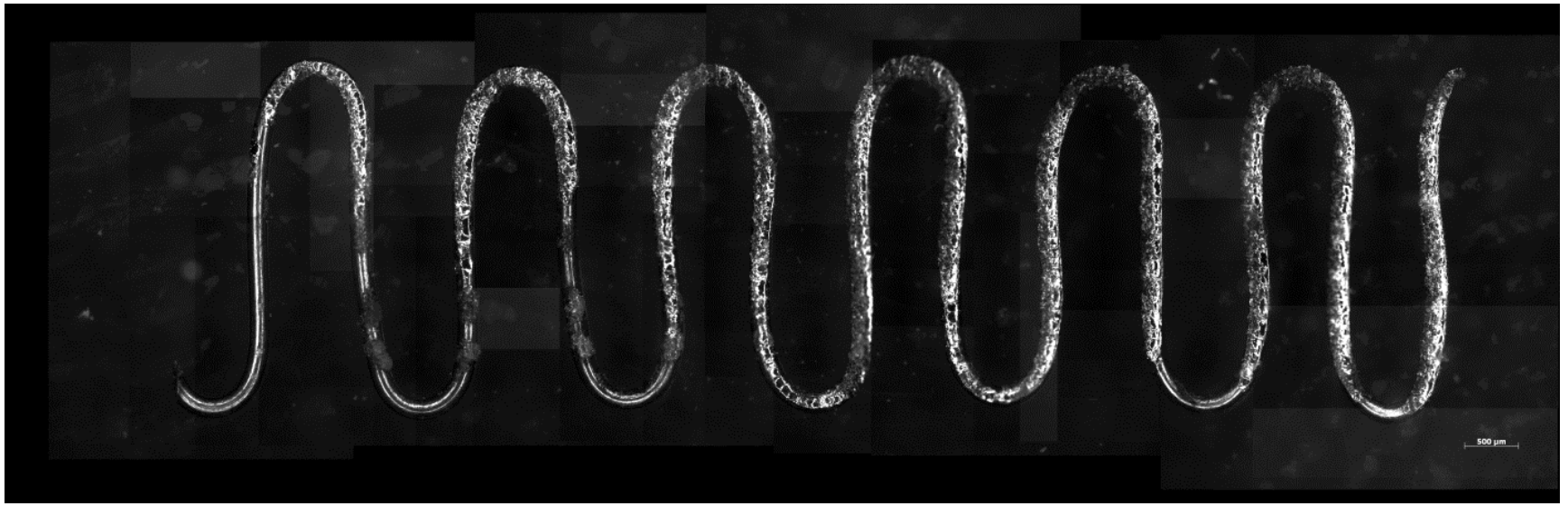

Figure 102: A montage of a small section of a NiCr z-wire that was stitched back together from a series of sequential images by Amanda Levinson at NRL.

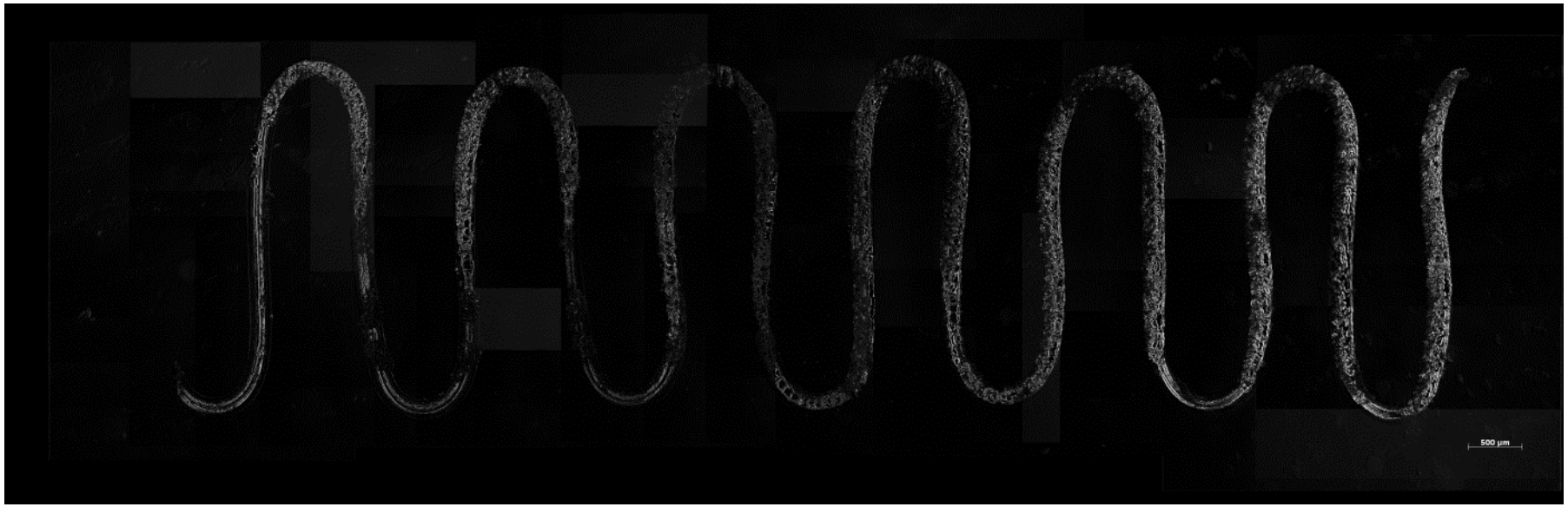

Figure 103: An overlay of two montages of a small section of a NiCr z-wire. One image was stitched by Amanda Levinson at NRL while the overlaid image was stitched at JHU with the Microsoft® ICE software using the planar 1 setting.

.

Figure 104: An overlay of two montages of a small section of a NiCr z-wire. One image was stitched by Amanda Levinson at NRL while the overlaid image was stitched at JHU with the Microsoft® ICE software using the planar 2 setting.

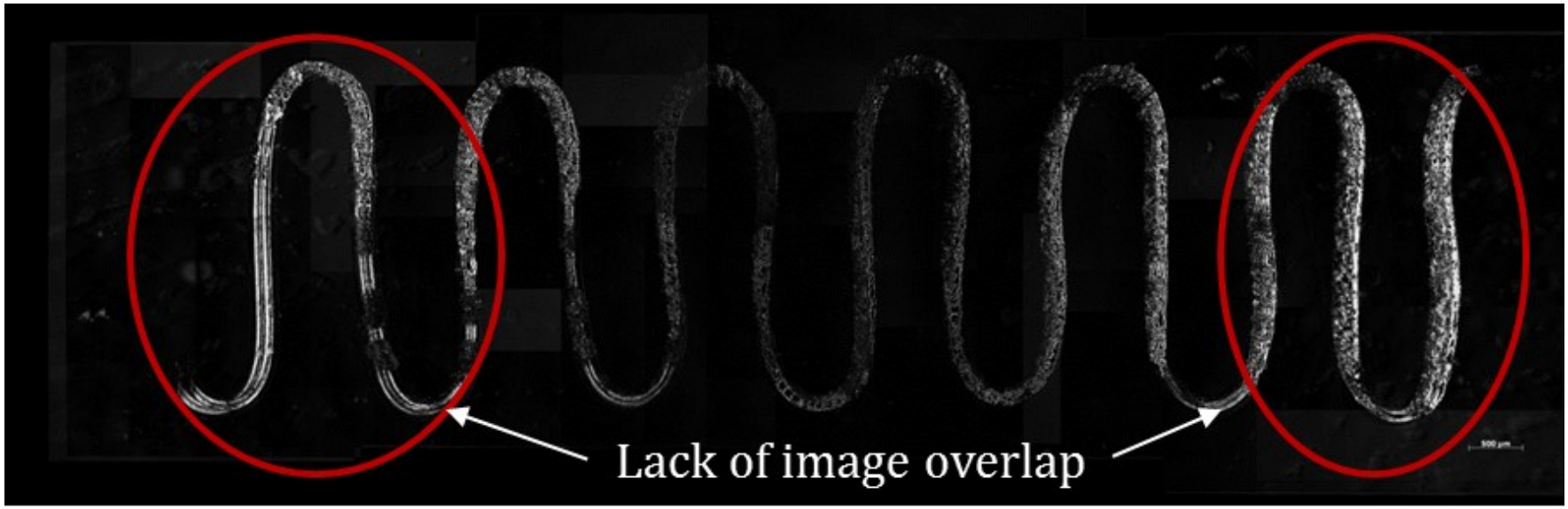

Figure 105: An overlay of two montages of a small section of a NiCr z-wire. One image was stitched by Amanda Levinson at NRL while the overlaid image was stitched at JHU with the Microsoft® ICE software using the planar 3 setting.

In order to quantify the data in these images, Image Pro Plus 8 was used to manually superimpose circles on the z-loops of the z-wires. Each image was calibrated using the 500 μm mark in the bottom right corner of each image. Circles were then superimposed on the z-loops from left to right alternating between the top and bottom. The size and position of the loops was determined by fitting the circles (defined by three points in the program) to the centerline of each z-loop. The nine, twelve, and three o'clock points that fell on the centerline of each wire were used to define the circle for a top loop and the three, six, and nine o'clock positions on a bottom loop were used to define a circle for the bottom loop. Each set of images for an individual z-wire had matching loops, ie. 'loop 1' for the image of the wire in the weave is the same 'loop 1' in the z-wire that was removed from the weave. The radius and center location for each z-loop was recorded in the calibrated image, and the values were exported to Microsoft® Excel for further analysis. An example image of the same z-wire both in and out of the weave with the superimposed circles on top of each of the z-loops can be seen in Figure 106.

The measurements of at least three z-wires from both the standard and the optimized pattern NiCr weaves were captured. Another set of standard and optimized pattern NiCr samples were also prepared with wire EDM and heat treated to 300°C in air in a tube furnace for 5 hours. At least three z-wires from each of these heat treated samples were also measured. All of these samples were analyzed with Image Pro Plus 8 as well and the data was exported to Microsoft® Excel.

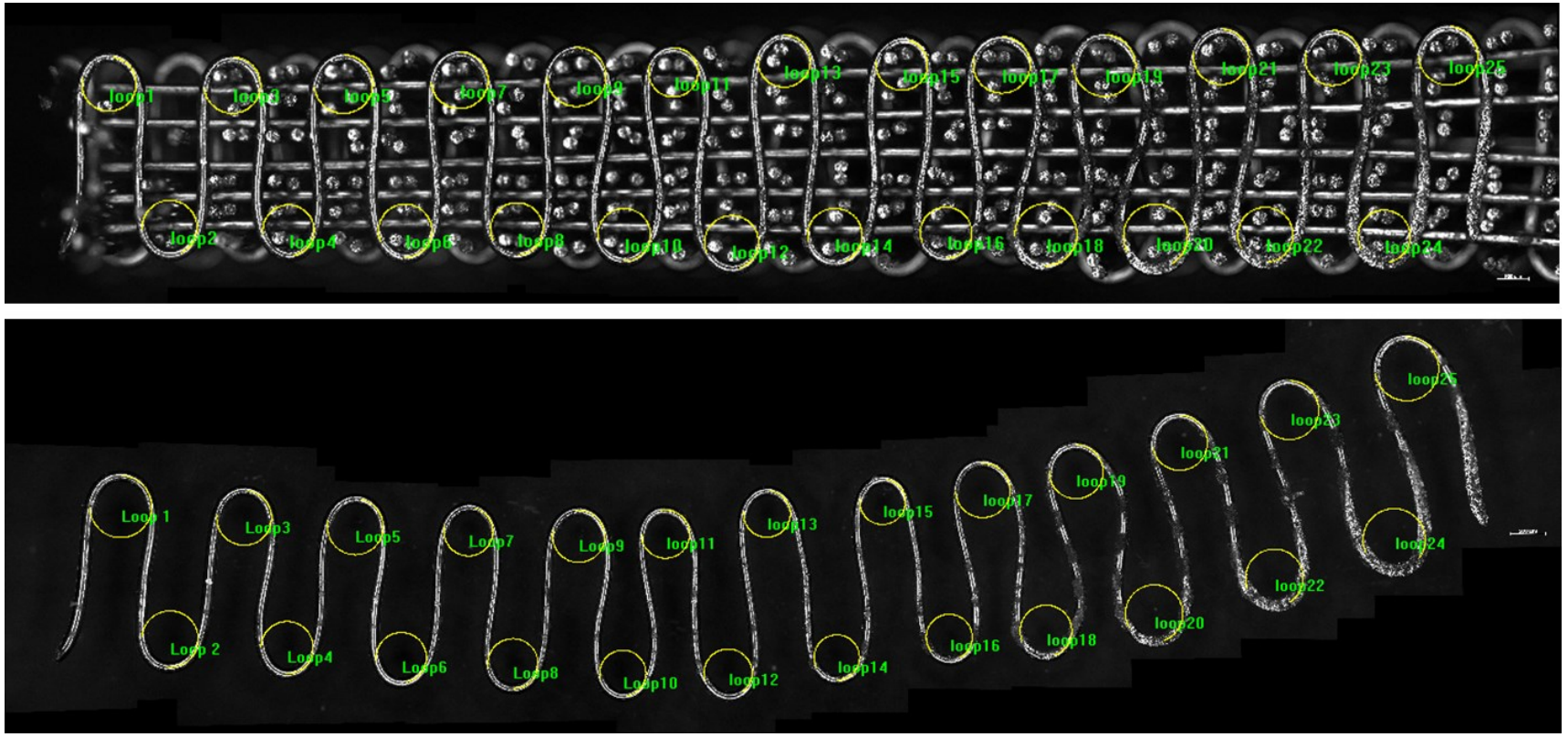

Figure 106: A montage of the same z-wire both in an out of the weave with superimposed circles on the z-loops. These superimposed circles are used to estimate the radius of curvature of each individual loop and to determine the relative positions of the individual z-loops in the and out of the weave.

The quantification of the changes in the z-wires with temperature exposure was used to develop an understanding of how the geometry of the weaves and the spring back of the z-wires changes for both architectures. Additionally, it was used to estimate the contribution of the z-fill frictional damping to the overall loss factor. This measurements help provide understanding and a basis to develop more complex damping models and eventually to optimize these materials for high temperature damping in the future.

5.2.3.2: Analytic Modeling of the Forces in the Z-Wire:

In order to quantify the frictional force between the fill and z-wires and how it changes with temperature, I developed an analytical model for the contact forces using geometry gathered from the individual z-wires both in and out of the weave. These geometries were used to develop representative models for each case. In the analytical models, the vertical sections of the z-wires were treated as beams that were subjected to single cantilever bending. In this case I assumed that the z-loop served to fix the wire in position on one end and all of the residual stress in the wire is balanced by a reaction force that is provided by the fill wires that are at the top and bottom of the weave. I further simplified the microstructure of the weave from the real geometry and assumed that the z-wire does not have a complex geometry (the real z-wires have an omega shape), but that it is straight and inclined at an angle to make contact with the fill wires. The simplified model of the warp/z plane is shown in Figure 107. In this illustration, the open circles indicate positions that are not occupied by wires in the optimized

architecture. The light blue wires are warp wires that occupy the planes behind the z-wire plane.

In the real geometry, the z-wire has a few limited points of contact with the fill wires through the thickness of the weave. These contact points allow for the transfer of stored elastic energy in the z-wires to the fill wires. This force may provide a normal force for frictional damping between the z-wires and the fill wires that will vary as a result of temperature exposure. The force exerted by the z-wire on the fill wires is indicated by the red arrows in Figure 107. These forces are the result of the spring back in the z-wires that is constrained by the fill wires.

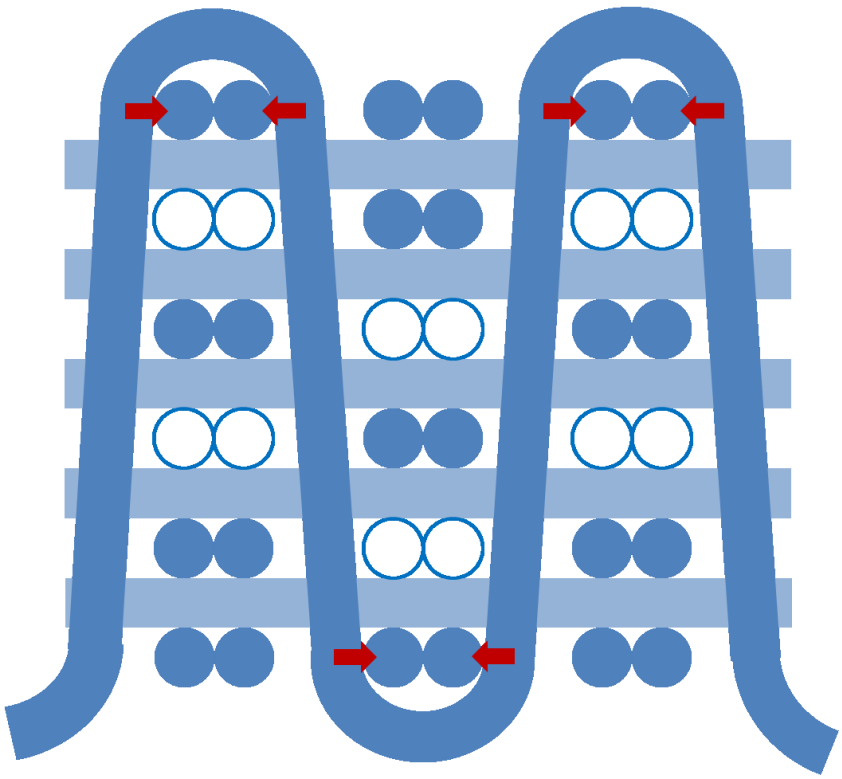

Figure 107: Conceptual model of the cross-section of the warp/z plane. The model assumes that the z-wire does not propagate vertically through the weave, but instead it is oriented at an angle. The red arrows indicate the points in the weave where the z and fill wires come into contact and the forces that the z-wire exerts on the fill wires. The open circles indicate positions that are empty in the optimized weaving pattern.

In this simple model, a z-wire can be treated as a beam with a point load at one end (which is accurate for the contact area between two tangential cylinders) of its length that induces bending. We will assume that the other end of the wire is fixed. This assumption is based off the idea that the z-wire is more compliant than the z-loop. An illustration of the model is shown in Figure 108.

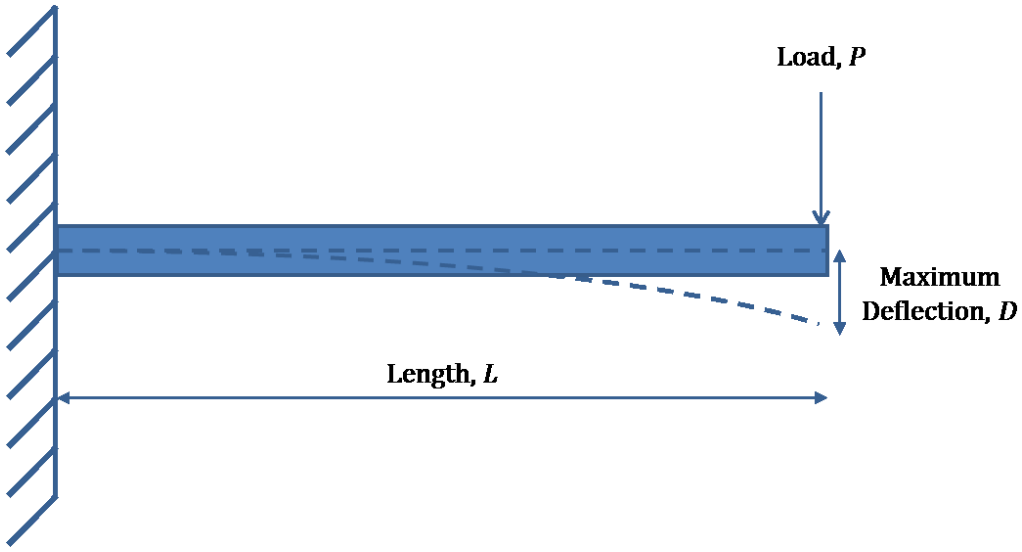

Figure 108: Illustration of a single cantilever beam with a point load at its end with the opposite end fixed. This simplification forms the basis of the analytical model of the z-wires when they are in the weave.

The description of the deflection of this type of geometry is found in many standard engineering textbooks [101]. The maximum deflection along the length of the beam is written as,

$$D = \frac{-PL^3}{3EI} \tag{31}$$

where, D is the maximum deflection at the end of the beam, P is the point load at the end of the beam, L is the length of the beam, E is the elastic modulus, and I is the moment of inertia. Since the load is the desired value, the above equation can be rearranged as,

$$P = \frac{3EID}{L^3} \tag{32}$$

Since the geometry of the wire is a long cylinder that is in bending along its length (bending axis is the z-axis), the area moment of inertia for the circular cross-section of the wire, I, is approximated as,

$$I = \frac{\pi r^4}{4} \tag{33}$$

where, r is the radius of the wire cross-section. Substitution into the equation for the load yields,

$$P = \frac{3\pi EDd^4}{64L^3} \tag{34}$$

In order to approximate the length of the beam, L, the three center positions of the superimposed circles on the z-loops were used for the image measurements that were discussed in the previous section. A representation of the superimposed circles on the z-loops is shown in Figure 109.

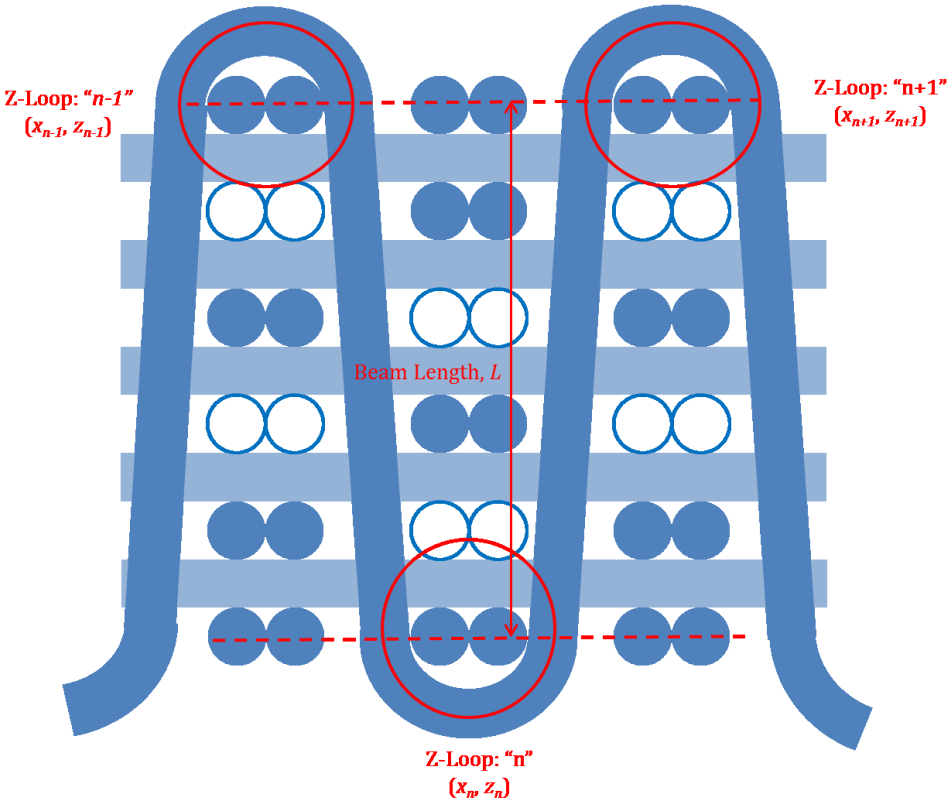

Figure 109: An illustration of the warp/z plane. The red circles are analogous to the superimposed circles of the z-loops from the image measurements described previously. The length of the beam that is being deflected is assumed to be the spacing between the z-loop centers on opposite sides of the weave.

The centers of the z-loop circles are a good approximation of the z-coordinate of the tangential contact points where the z-wire contacts the top or bottom fill wires. In

order to calculate the length of the beam, L, the z-coordinate (in this case z_n) is subtracted from the average z-coordinate of the pair of z-loops on the other side of the z-wire that are immediately to the left and right of the interrogated loop (in this case the average of z_{n-1} and z_{n+1}). Mathematically the length of the beam, L_n, is described as,

$$L_n = \left| \frac{z_{n-1} + z_{n+1}}{2} - z_n \right| \tag{35}$$

where, z_n is the z-coordinate of the loop that is contacting two of the interrogated z-wire beams, and z_{n-1} and z_{n+1} are the z-coordinates of the z-loops that are on the other side of the weave that make contact with the other two z-wire beams.

Calculations of the lengths of the z-wire segments, which are referred to as the beam length, are summarized in the Figure 110 for each of the cases: standard pattern as-woven, standard pattern after heating to 300°C, optimized pattern as-woven, optimized pattern after heating to 300°C. It is interesting to note that this is a measure of the average vertical spacing of the weave from the center of the fill wires that make up the top and bottom of the weave (assuming the fill wires fall in the middle of the z-wire loops). It can therefore be used to indicate how densely packed the weave is in the vertical direction. It appears that this spacing is greater in the standard weave than in the optimized pattern weave. This is likely due to the fact that the standard weave has more wires in the z-direction and because the weaves are not perfectly packed, there is increased spacing the z-direction. Also, the spacing decreases after heating indicating that the wires in the weave may settle into a more compact configuration during heating.

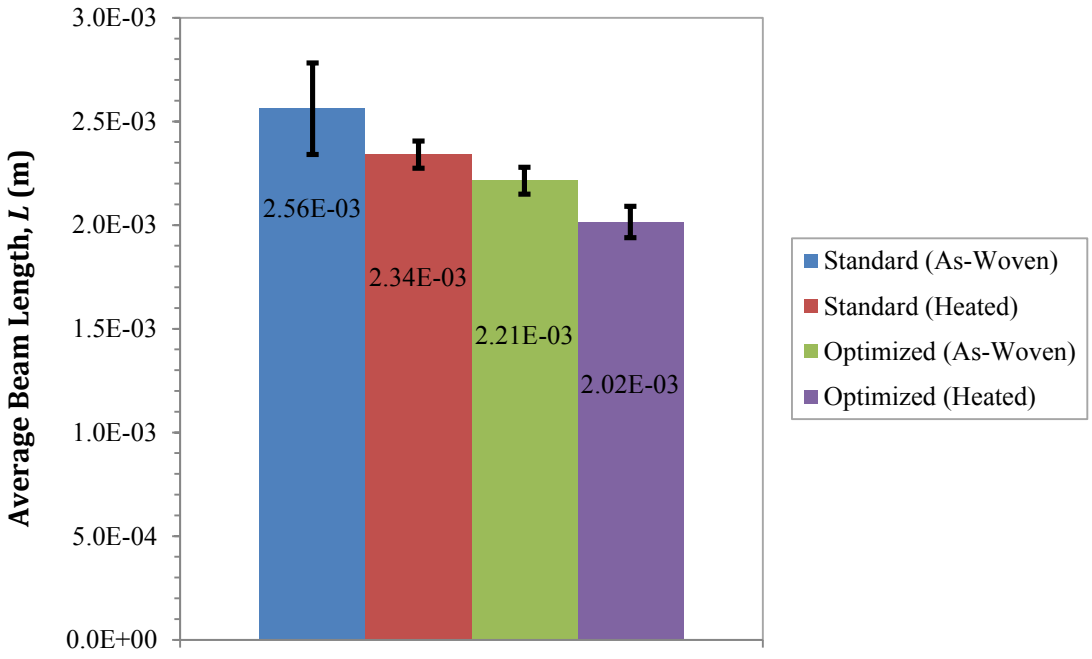

Figure 110: A summary of the calculations of the length of the z-wire beams that is used in the analytical model. The theoretical minimum spacing is calculated by assuming that warp and fill wires are stacked on top of one another with no spaces in between and that the outer fill wires are positioned at the center of each z-loop.

The elastic modulus, E, of the 80-20 NiCr wire (d = 202μm) was measured in the microtensile testing machine by Dr. Yong Zhang and was determined to be 125 GPa. The strain measurement was done using the MATLAB based DIC tracking software.

The displacement measurements, D, was calculated by comparing the position of the z-loops before and after the wire was removed from the weave. In order to measure the local displacement, the position of two neighboring loops on the same side (top or bottom) of the z-wire were compared in and out of the weave. This provides a local

measurement of the displacement between two neighboring loops. The measured distance is shown schematically as ,λ, in Figure 111.

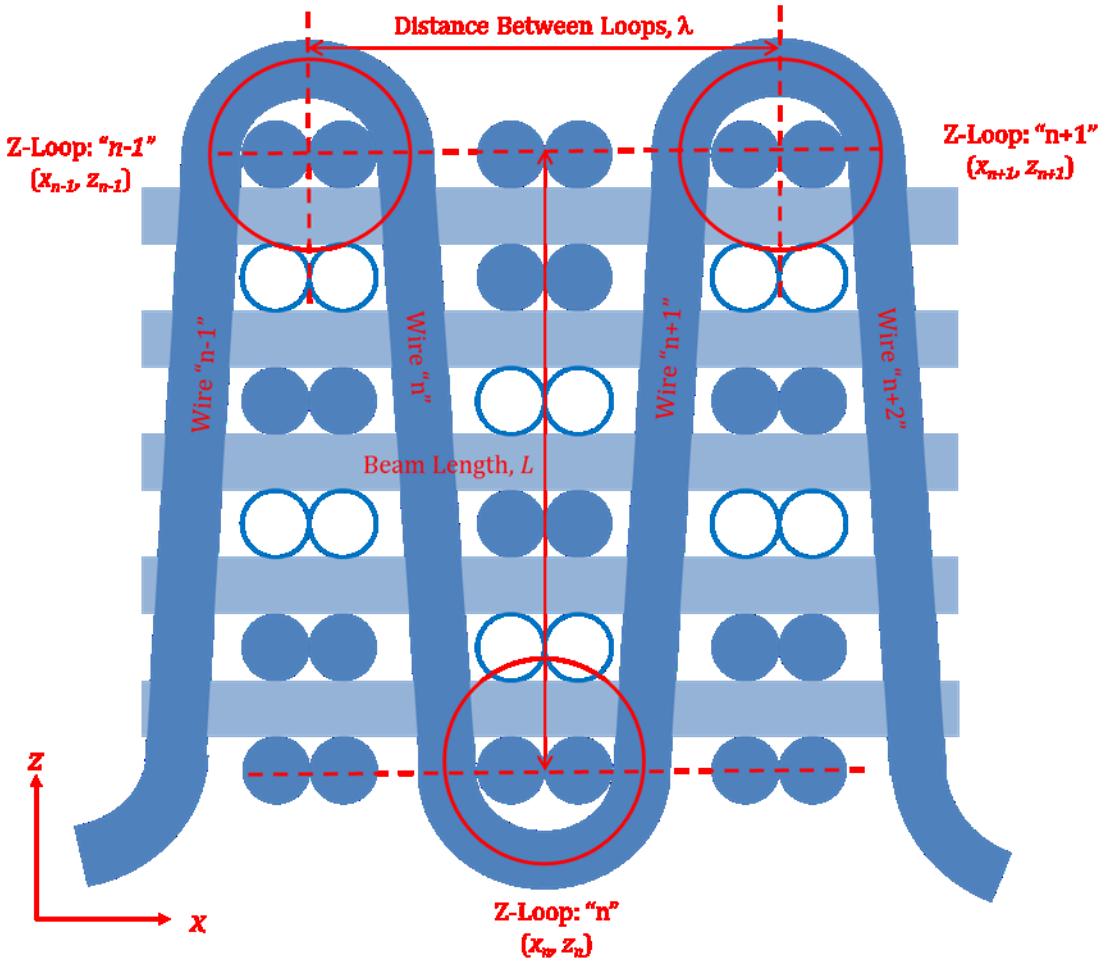

Figure 111: An illustration of the warp/z plane of the weave showing how the measurement of the distance between neighboring loops is calculated. This measurement is performed on wires both in the weave and after they are removed from the weave. Individual loops are compared in the samples to calculate a displacement.

In order to calculate the displacement for the z-wire "beams" that are connected to loop "n", we assumed that the displacement was symmetric on either side of loop "n". In

this case we chose to use the convention that the wire beam "n" was to the left of loop "n" although the choice is arbitrary. The distance between the neighboring loops, $L_{n+1,n-1}$, that are opposite the current loop of interest, loop "n", is the written for the z-wire in the weave as,

$$\lambda_{n+1,n-1} = \sqrt{(x_{n+1} - x_{n-1})^2 + (z_{n+1} - z_{n-1})^2} \tag{36}$$

Analogously, the distance between the neighboring loops after they are removed from the weave, $L'_{n+1,n-1}$, is written as,

$$\lambda'_{n+1,n-1} = \sqrt{(x'_{n+1} - x'_{n-1})^2 + (z'_{n+1} - z'_{n-1})^2} \tag{37}$$

where, the prime indicates the length and coordinates for the z-loops after they have been removed from the weave. Note that the distance between loops is a composite of the x and z changes and not just the x-direction contribution. For a beam in single cantilever bending, the load is applied perpendicular to the unloaded beam. If the z-wires were aligned with the z-axis then we could simply use the x-direction changes only. In the case of the weaves, the z-wires are not necessarily vertical, and the z-wires curve in the z-direction around the fill axis, which changes the orientation of the z-wire loops. In order to account for these changes, a composite (in the x- and z-direction) displacement is used.

The displacement between loops "n+1" and "n-1" as a result of being removed from the weave is twice the displacement of wire beam "n", denoted as D_n. The expression for D_n is written as,

$$D_n = \frac{\lambda'_{n+1,n-1} - \lambda_{n+1,n-1}}{2} \tag{38}$$

The wire in our case was initially in the 'straight' shape when the load (from the tangent fill wire) was applied. When the wire was removed and the load changed to zero, the wire assumed a 'bent' shape. This is the opposite of the beam model shown above since the beam is straight when no load is applied, but bent when the load is applied. The force balance in both our case and the model, however, should be equivalent.

The calculation of the individual forces for each wire and the overall average result are summarized in the Figure 112 for each sample (standard and optimized) and condition (as-woven and heated). There does not appear to be any discernable pattern as to the loads that are exerted by the z-wire on the fill wires for a particular case, but the data suggests that the loads are compressive in the warp direction and they are in the range of a 64-140 mN. The standard deviation of the measurement was calculated for each z-loop pair for each wire and heat treatment (~100 data points for each case).

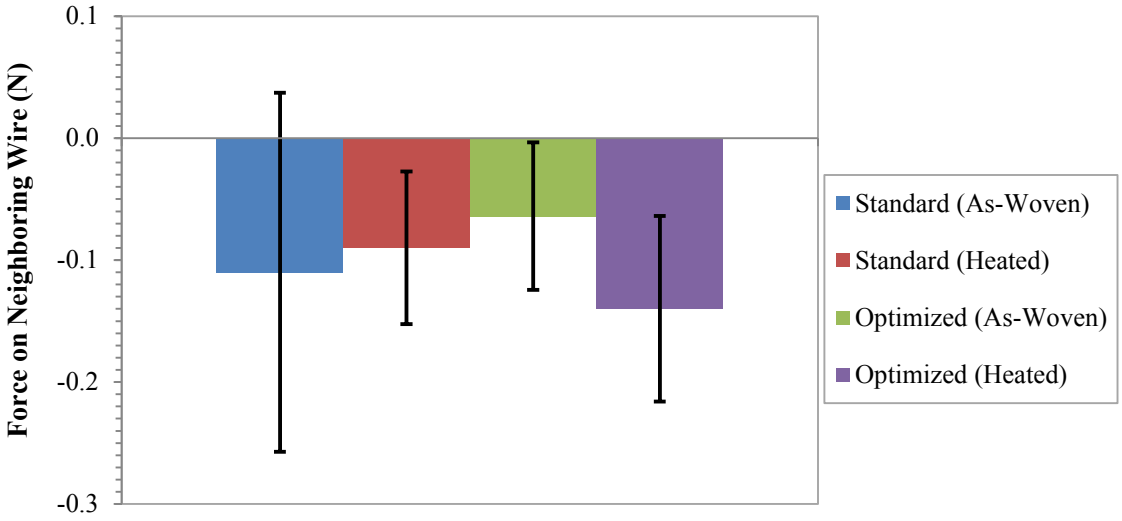

Figure 112: A plot of the absolute value of the average forces calculated using the analytical model for each case. It appears that the forces that are calculated from this analytic method are in the range of 64-140 mN. Error bars in the measurement indicate one standard deviation.

In order to increase the accuracy of the model, the change in the radius of curvature of each z-loop was also taken into account for each individual z-loop and it was included in the displacements. It was assumed in the previous model that the majority of the stored elastic energy was in the long vertical sections of the z-wires, but some elastic energy is also stored in bending the z-loops. The radius of the z-loops, which is measured by calculating the radius of the circles that were superimposed on the z-wire loops, was measured for all of the z-loops for both the as-woven and heat treated cases for both NiCr architectures. The difference in radius for the z-loops once they were removed from the weave minus the radius of the z-loops when they were in the weave is shown in Figure 113.

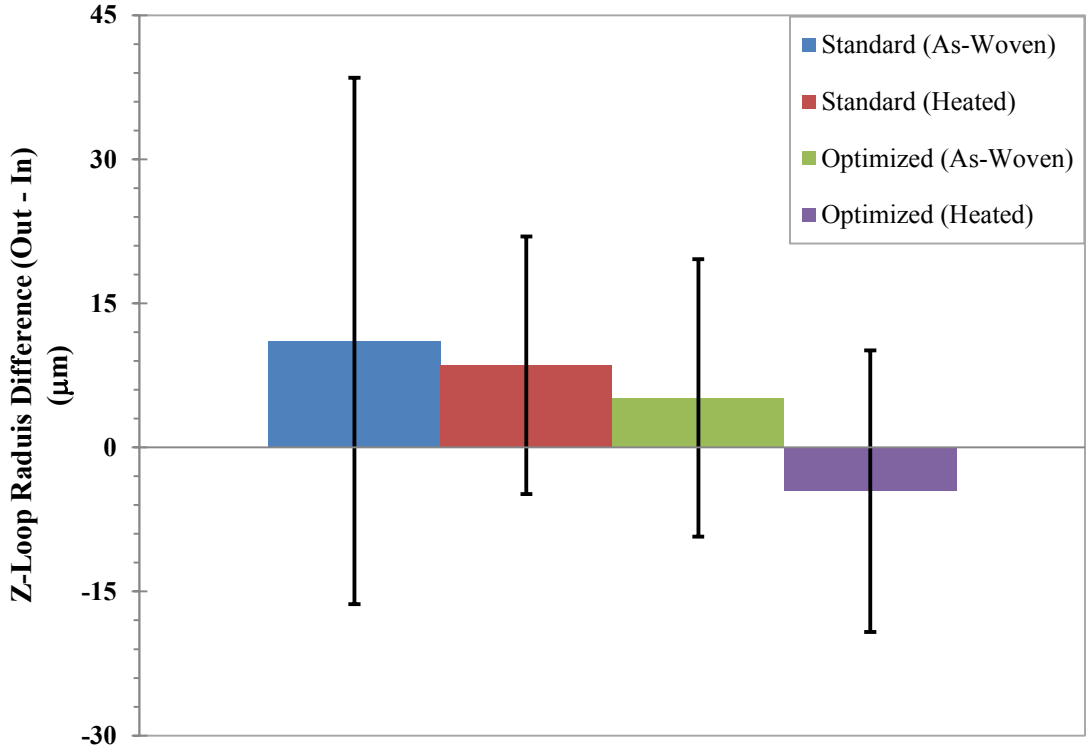

Figure 113: The difference in the radius of the z-loops for the wires that were removed from the weave minus the radius of the same exact z-loops when they were in the weave. The difference is an indication of the stored elastic energy in the z-loops that is a result of the weaving process.

This change in the radius needs to be accounted for since it may lead to an increase or a decrease in the apparent displacement of the end of the vertical section of the z-wire loop in the model, D_n. If the radius of the z-loop increases as the wire is removed from the weave, then the displacement of the z-loops will be an overestimate of the real displacement. Therefore, the change in the radius of the z-wire loops was subtracted from the displacement between a pair of z-wire loops and the values for the forces we recalculated. The results of these calculations can be found in Figure 114.

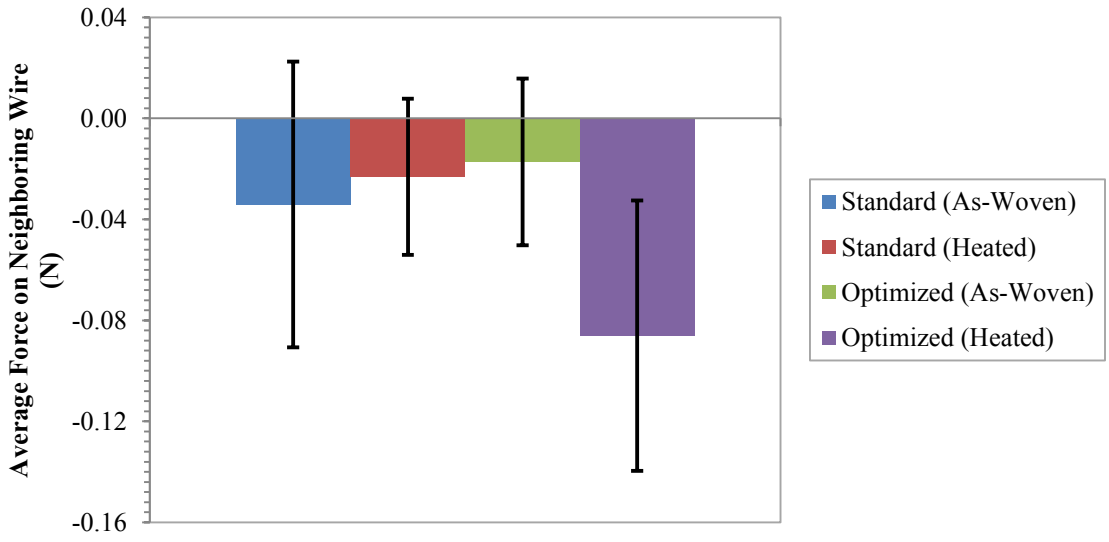

Figure 114: A plot of the absolute value of the average forces calculated using the analytical model for each case and accounting for changes in the radius of each z-loop. It appears that the forces that are calculated from this analytic method are in the range of 17-86 mN. Error bars in the measurement indicate one standard deviation.

Comparing the estimates of these forces when we account for changes in the radius of the z-loops with the model where we only account for displacement in the vertical sections of the z-wires shows that changes in radius of curvature affects the overall magnitude of the forces and decreases the estimated force by approximately half. Accounting for the deformations in the z-loops, doesn't affect the overall order of forces (ordering from maximum to minimum force) between the different architectures and heat treatments. What this implies is that the z-loops are storing elastic energy as well as the vertical sections of the z-wires.

Although this simple model does provide indications of the magnitude of the forces, the simplifications of the geometries and deformations should be accounted for

more completely. In order to develop a more complete model, finite element analysis was used to develop wire models and account for more of the geometric features of the z-wires which will allow is to compare and quantify the results with the analytical model.

5.2.3.3: Finite Element Modeling of Forces in the Z-Wires:

A finite element model was also developed to generate a more detailed understanding of the forces that are present in the weaves and to more fully account for the changes in the geometry of the wires in the model. 3D CAD models of the wires were built in SolidWorks and ABAQUS was used in order to mesh the models and to model the elastic deformations. Models of individual wires were constructed by using the relative center locations and the radii of the z-loops (that came from the image analysis that was discussed previously) and connecting those circles with double tangent lines. The circles were then foreshortened to semi circles that were connected by the tangent lines. This geometry that was made of semi-circles and lines was then extruded into a 3-D solid using this wire model as a center line with the diameter of the wire (202 μm). Wire models were constructed for individual wire samples for their configurations both in the weaves, and the geometry that they take on once removed from the weave. An image of one of the full wire models for the cases of the z-wire in and out of the weave is shown in Figure 115.

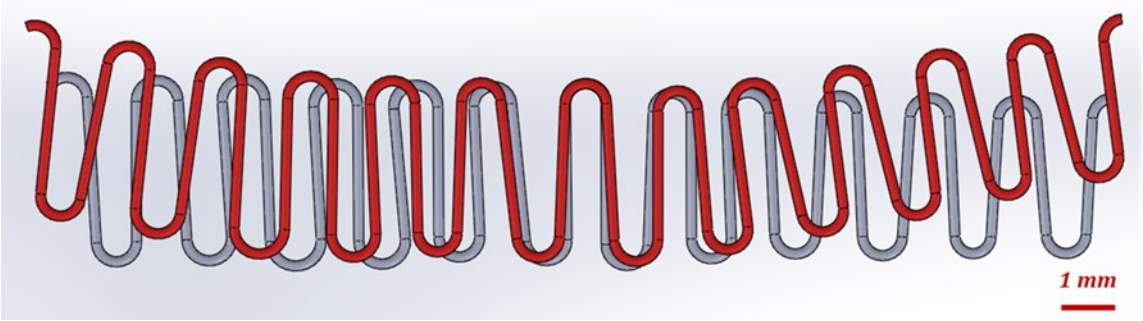

Figure 115: An example of the full z-wire models for the wires both in the weave (shown in grey) and out of the weave (shown in red). The models are overlaid on top of one another with a common point of tangency in the top center of both wires. The natural curvature of the weave is clearly evident in this image.

Since the overall properties of the weaves are our primary concern and not the individual properties of a single wire, we elected to represent the wires with individual subsections of the overall weave. The models were made for each of the four cases: standard pattern as-woven, standard pattern heat treated (300°C), optimized pattern as-woven, and optimized pattern heat treated (300°C). In addition, models were also made to represent the loops on the top of the weave separately from the loops on the bottom of the weave. It was found that when the wires were removed from the weave, they exhibited a curvature in the z-direction around the fill axis. The details of this will be discussed in the following section. The top and bottom was determined by examining the curvature of the z-wire for a particular case and the 'top' was assumed to be the direction in which the overall z-wire geometry was curved. Geometries for the 'top' and 'bottom' of the weave were then developed in order to account for these differences.

Models of a 'top' and 'bottom' for each of the four cases were constructed (eight in total) in order to represent the geometry of the loops when the wire was removed from the weave. The boundary conditions were applied in order to bend the wire models back

into the geometry that it assumed when the wire when was in the weave. An image of the models for a representative sub-section of the z-wires is shown in Figure 116 for the wire both in the weave and out of the weave.

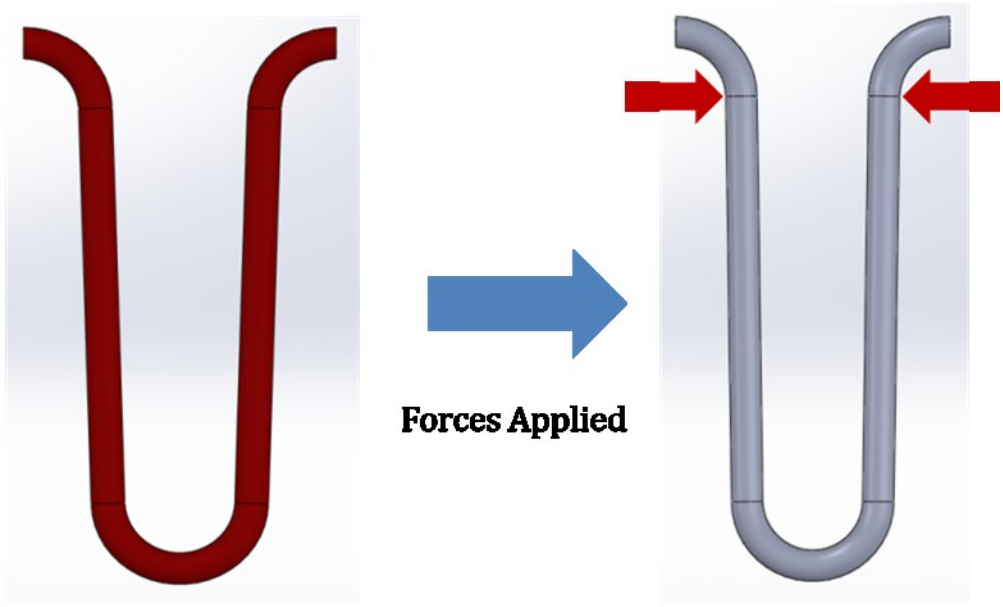

Figure 116: An example of representative subsections of the weave for a z-wire loop out of the weave (shown in red) and in the weave (shown in grey). The subsection for the wire in the weave shows the location where forces are applied in the model. Forces are applied at the point of tangency between the loop and the vertical section of the wire.

The models that were made in SolidWorks using the average geometries were imported into ABAQUS, where they were gridded with ~50,000 tetrahedral elastic elements before applying boundary conditions and running the simulation. The boundary conditions fixed the center of the wire at the bottom of the loop to remain in the plane, but it allowed the bottom z-loop to move towards or away from the two half z-loops if necessary. The faces of the z-loops that were cut were constrained to in-plane motion as

well. Finally, the boundary conditions applied deformations at the point where the z-wire loops met the top of the vertical section of the z-wire. The applied boundary conditions and the wire before and after deformation (with the finite element grid on the wire models) are shown in Figures 117-118.

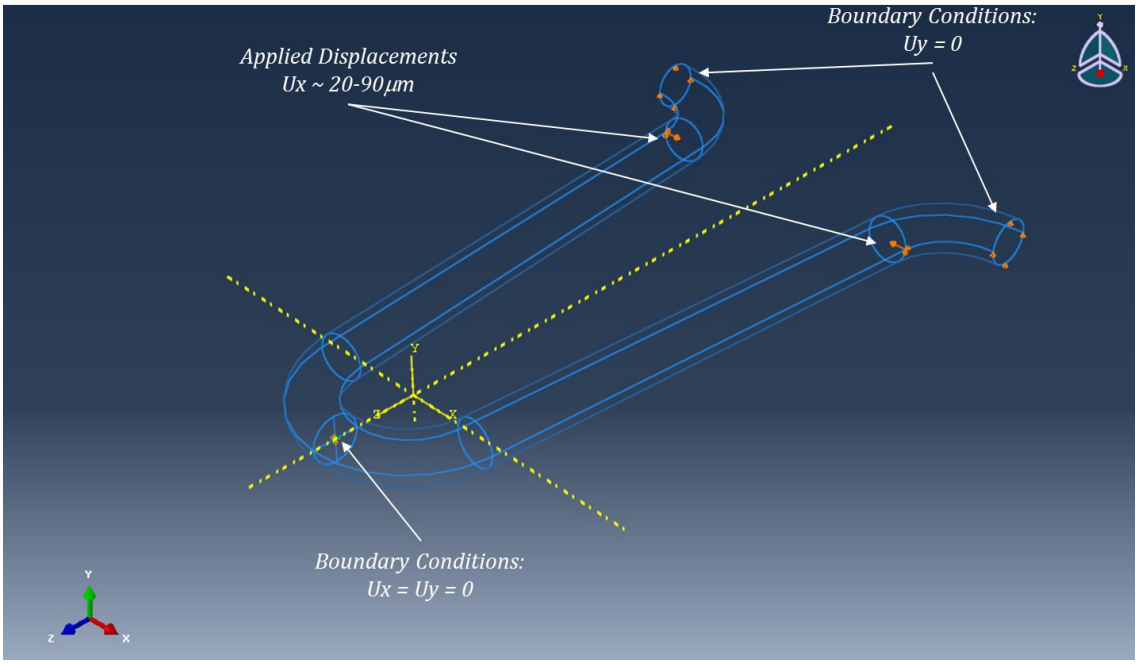

Figure 117: A representative subsection after being imported into ABAQUS and applying boundary conditions. The boundary conditions prevent out of plane deformations of the z-wire and displacements were applied at the point of tangency between the z-wire loops and the straight section of the z-wires.

The simulations were run on all eight of the wire geometries. The reaction forces were assumed to be two points of contact which were equal and opposite, and which were applied at the point of tangency between the semi-circle and the tangent line. The

reaction forces that were necessary to cause these displacements in the ABAQUS simulation for all eight cases are shown in Figure 119.

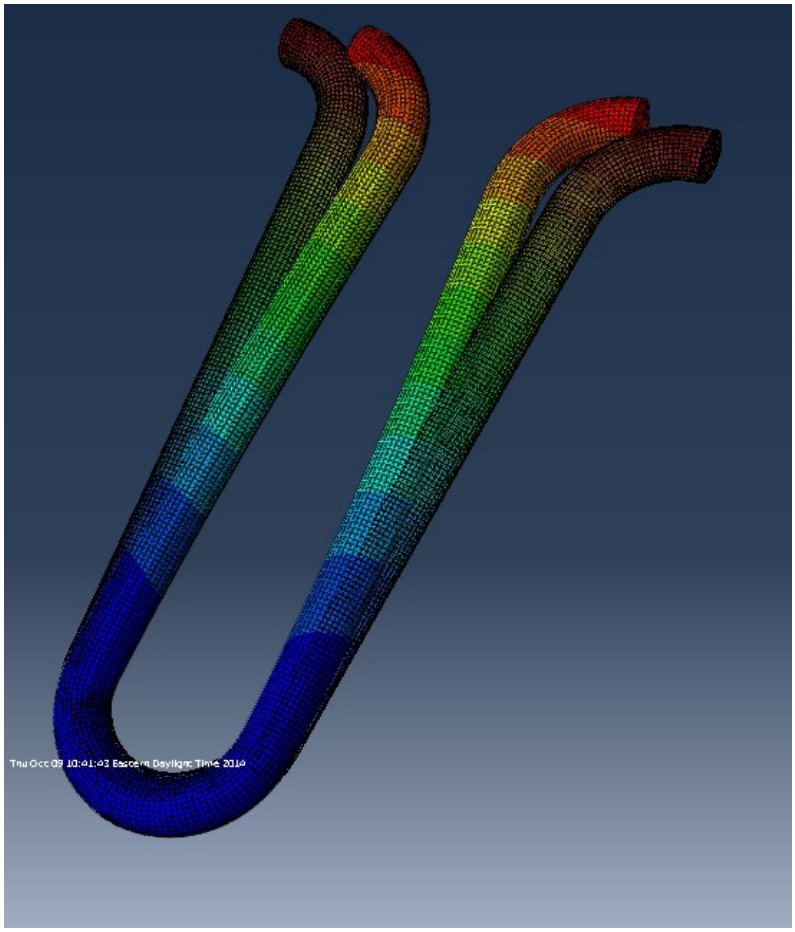

Figure 118: A representative subsection of the z-wire loop both after being removed from the weave and after the forces were applied to bring the wire back into the same position it would be in the weave. This also shows the elastic elements that were used to grid the wire subsection. Note that the deformation is scaled (13x) in order to exaggerate the motion.

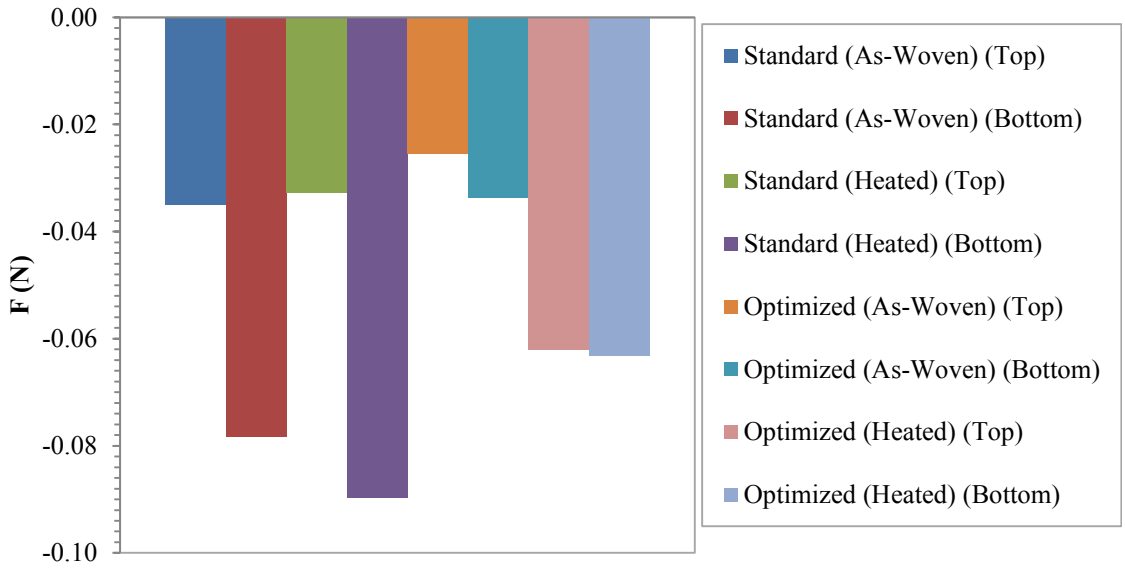

Figure 119: A plot of the absolute value of the average forces applied by the fill wires on the z-wires. The cases are broken into top and bottom loops for each case. The overall forces are in the range of 26 – 90 mN.

The results of the FE model shows that the resulting forces are on the order of 26 to 90 mN (which is nearly the same as the forces that were calculated with the analytical model when the radius change of the z-loops was included), and that the magnitude of the reaction forces are higher in the bottom of the weave than in the top of the weave in all cases. This difference in spring back on the top and bottom of the weave leads to the overall curvature in the weaves (which is the topic of a later section), but we can use this estimate and the previous estimate of the forces to now estimate the contribution to the loss factor from the z-fill contact forces that we have estimated.

5.2.3.4: Estimate of the Loss Factor Contribution of the Fill/Z Frictional Dissipation

In order to estimate the contribution of the fill/z frictional sliding to the overall observed loss factor measurements, we can use the expression that was derived previously for the loss factor,

$$\eta = \frac{A\mu_k N\chi Ebh^3}{\pi P^2 L^3} \tag{39}$$

For the NiCr weaves, in order to complete the estimate of the contribution to the loss factor of the frictional sliding between the between the fill and z-wires, there are several constants in the equation that must be estimated or extracted from measurements.

Many of the constants used in this estimate were used previously in other models and calculations. The amplitude of the oscillation, *A*, was extracted from the FE simulations performed by Stefan Szyniszewski and were determined to be on the order of 1-2 μm. As a result, a value of 1.5 μm was used in the calculation. The kinetic coefficient of friction between the NiCr wires, μ_k, was the same value (0.2) that was previously measured by Hal Kahn at Case Western Reserve and the value that was also used in the FE simulation performed by Stefan Szyniszewski. The value for the elastic modulus was measured by Yong Zhang and was determined to by 125 GPa from a single wire test with the strain measured using DIC. Since the sample is aligned with the fill direction along the bending axis, the elastic modulus in that direction would be governed

by the stiffness of only the fill wires (without bonding material, only the fill wires will bear any substantial load that would contribute to the elastic modulus). The fill wires occupy ~5% of the cross sectional area of the warp/z plane. Therefore, the single wire modulus was normalized by the density of the fill wires in the warp/z plane in order to calculate a reduced modulus of 6.3 GPa, which was the value used for E in the calculations. The load required to deform the beam was extracted from the DMA measurements of the maximum reaction force during a cycle at the moving clamp. This value was on the order of 3 N for all of the NiCr weave samples. The sample dimensions (b, h, and L) were extracted from previous measurements of NiCr test samples and the sample dimensions used in this calculation were: 15 mm wide, 3 mm thick, and 17.5 mm long. The number of contact points in the sample, χ, was estimated from the sample spacing between z-loops, and the dimensions of the sample. Measurements of the as-woven z-loop center to center spacing in the NiCr weaves had a value of ~1.8 mm between z-loop centers on the same side. The model assumes that there are two point of contact on each of those wire segments. Extrapolating the number of contact points in both warp and fill directions provides an estimate of the number of contacts in the sample to be 162.

For both the analytical model (accounting for the change in the radius of the z-loops) and the FE model, the loss factor was calculated for the minimum, average, and maximum estimated normal force. The results are summarized in Table 14.

Table 14: Summary of the loss factor contributions of the frictional dissipation of the fill/z wire contacts

Model	N_{min} (N)	η	N_{avg} (N)	η	N_{max} (N)	η
Analytical (w/ z-loop radius)	0.02	0.01	0.05	0.04	0.09	0.07
FE Model	0.03	0.02	0.06	0.04	0.09	0.07

The results of these estimates of the loss factor show that, for the estimated forces between the fill and z-wires, the frictional dissipation of that interaction is a substantial contributor to the overall damping found in these materials. For the estimates associated with the average normal force, the contribution of the fill/z wire frictional sliding could account for ~25% of the measured damping of the as-woven weaves. Although there does not appear to be any discernable pattern between the change in forces with temperature (i.e. the force increases or decreases with temperature for both architectures), it does indicate that changes in the fill/z wire interactions can lead to significant and measureable changes in the loss factor.

Overall, the measurements and modeling of the frictional damping between the fill and z-wires has shown that the contribution of this damping mechanism is significant to the overall damping abilities of the material, but the measurements of the weaves before and after heat treatment does not reveal a clear change in the normal force that would describe the decrease in damping with temperature exposure. Even though these forces may change with temperature exposure in a systematic way that leads to the observed change in damping, the estimates of the forces may not appropriately reveal

these changes as a result of some of the assumptions in the models. Specifically, the number of contact points and the idealized geometry of the z-wires may fail to capture the exact changes that occur with temperature exposure. This is due to perturbations in the architecture that are difficult to quantify on average, such as wire twists, wire contacts, and non-orthogonal wire geometries. These measurements and estimates of the effect of the frictional damping between the fill and z-wires on the loss factor provide indications that changes in these contact forces can significantly affect the damping abilities of these materials, but these changes are likely one of several factors that affect the damping with temperature exposure. The measurements of other geometric changes in the weaves and their possible role in the decreased damping will be explained in the remainder of this chapter.

5.2.3.4: Measurements of the Curvature of the Z-Wires

In our evaluation of the changes in the z-wires when removed from the weaves before and after temperature exposure, I observed that the z-wires as a whole exhibited a curvature along the warp direction around the fill axis. In order to quantify this curvature, the center location of each z-wire loop for each case was plotted and a least squares quadratic fit was applied to each wire data set to quantify the shape. The curvature for each wire was then quantified as the coefficient of the x^2 term in the curve fit. An example plot of the z-wire loop markers and the curve fit are shown in Figure

120. The plots of the z-wire loop locations for each measured wire and the quadratic fits to each wire are shown in Figures 121-124 for each case and the coefficients of the 'x^2' term in the quadratic fits is summarized in Table 15.

The coefficient of the x^2 for each wire was averaged with the other wires in each data set and the standard deviation of each dataset was calculated. The coefficient serves to quantify amount of curvature in in overall geometry of each z-wire. This curvature is the result of asymmetric stored elastic energy (spring back) that is allowed to relax when the z-wire is removed from the weave. When the z-wire is in the weave, the surrounding warp and fill wires serve to restrain the z-wire in a particular position. Once that wire is removed from the weave it is in its natural state with no applied external loads. As a note, we do not know what is the top or the bottom of the weave before we begin removing wires. Therefore the choice of the 'top' or the 'bottom' for each dataset was initially arbitrary. After measuring the curvature of the wires, the convention was used that the z-wires, on average, curved such that the ends pointed up. The datasets shown above were corrected for orientation by calculating the overall average for a dataset. If the average coefficient of the quadratic was negative, then every z-coordinate in the dataset was multiplied by negative one in order to correct the orientation. This correction had to be applied to both the standard and optimized as-woven datasets. The average curvature for each data set with the standard deviation is shown in Figure 125.

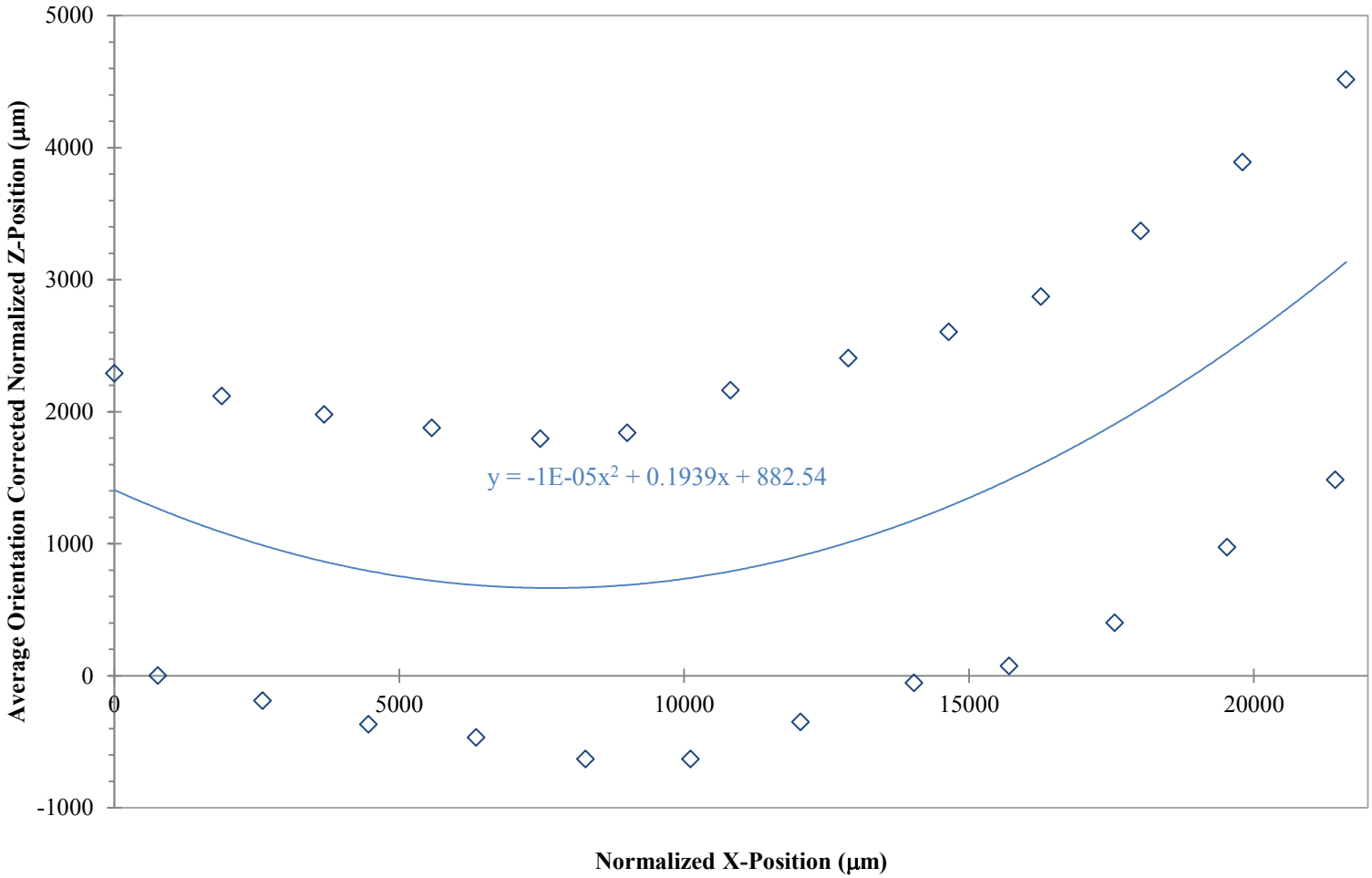

Figure 120: An example data set showing the z-loop center locations of a z-wire that was removed from the weave and the quadratic curve fit to the data. The coefficient of the 'x^2' term in the quadratic equation was used to quantify the curvature.

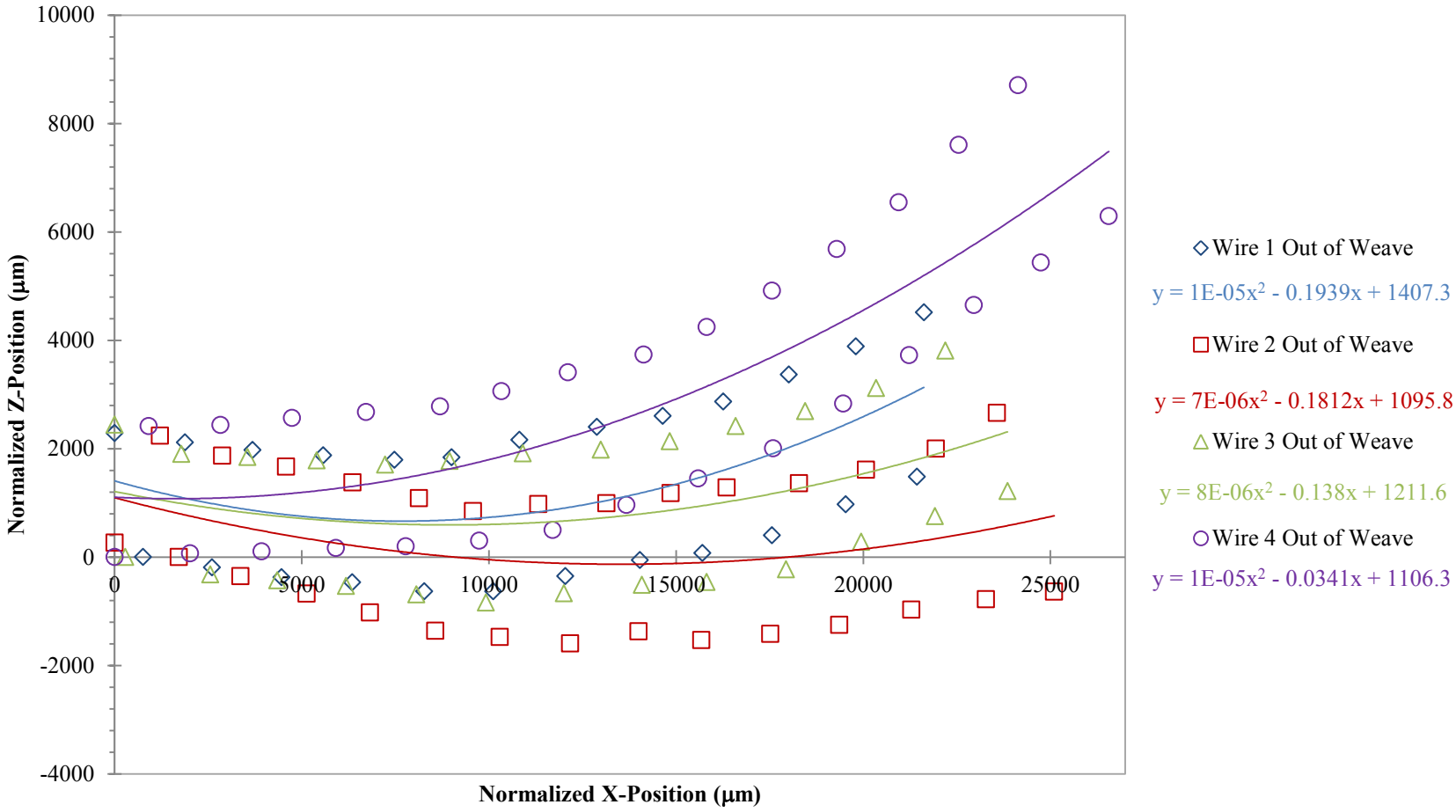

Figure 121: The individual position of each z-wire loop center after being removed from the weave for the as-woven standard pattern NiCr weave for 4 different wires. Quadratic equations were fit to each wire data set using a least squares fitting procedure and the fits and equation of the fit are shown for each wire.

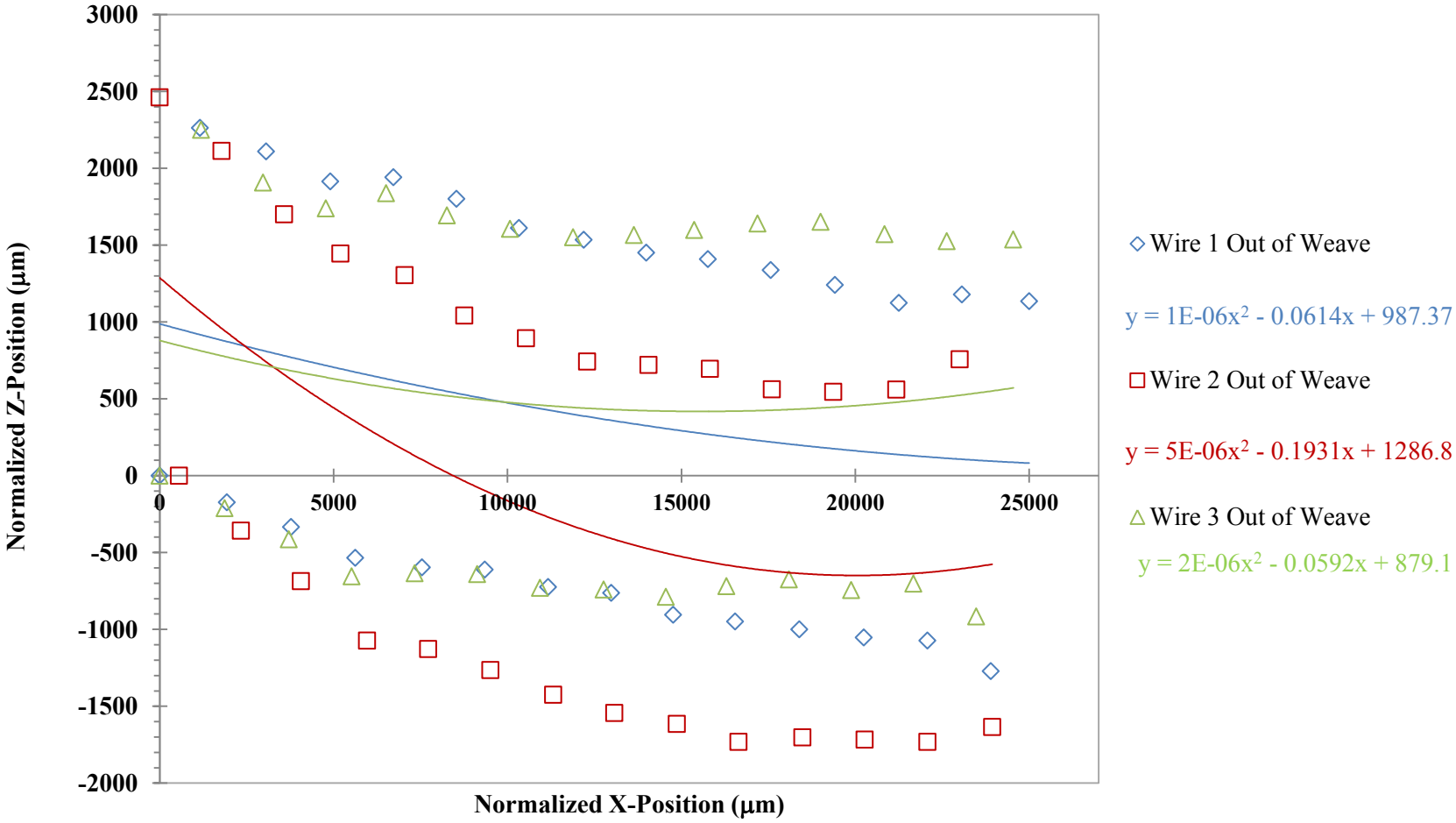

Figure 122: The individual position of each z-wire loop center for 3 wires after being removed from the standard pattern NiCr weave that was heat treated to 300°C for 5 hours in air. Quadratic equations were fit to each wire data set using a least squares fitting procedure and the fits and equations for each fit are shown.

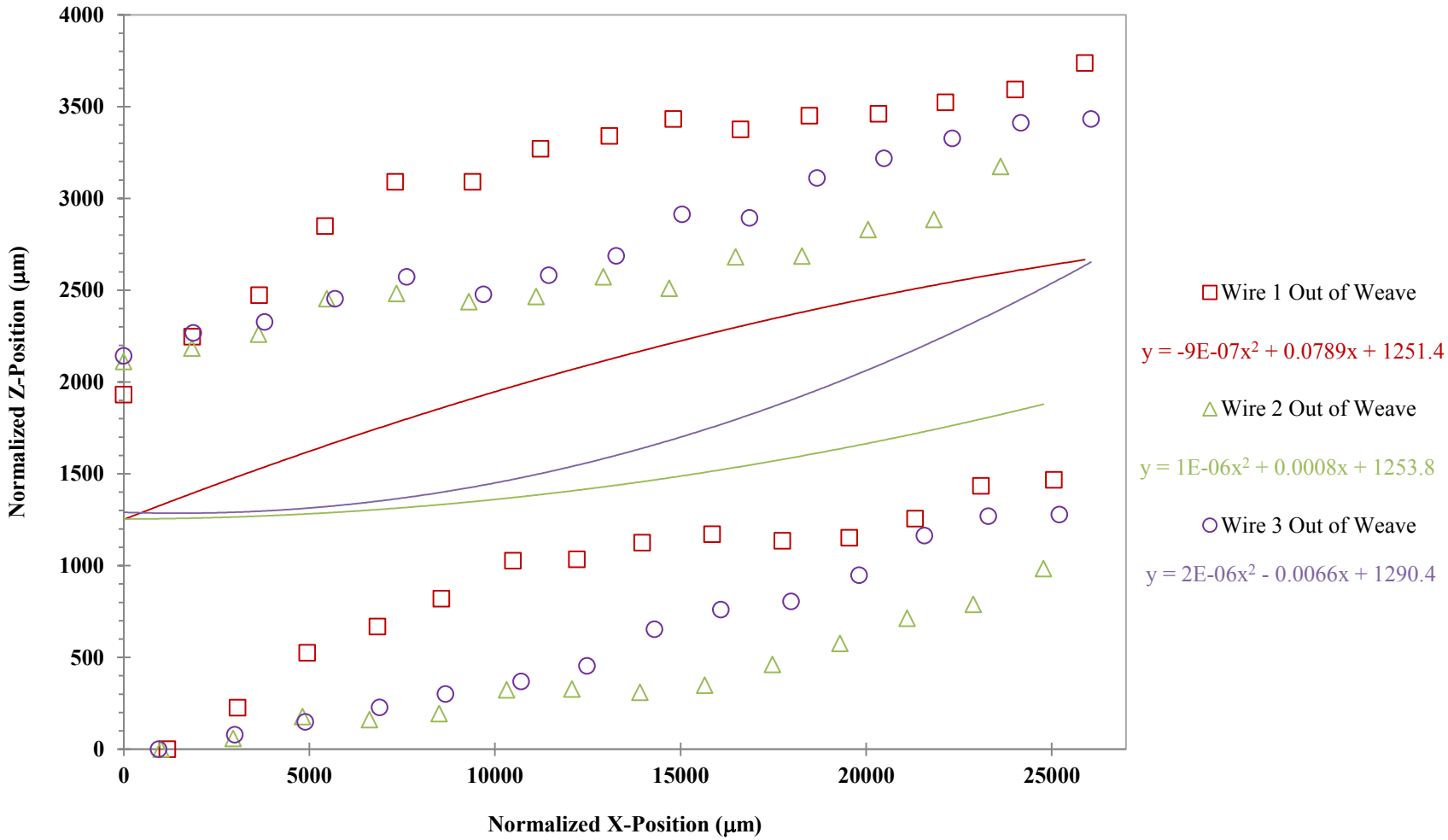

Figure 123: The individual position of each z-wire loop center after being removed from the weave for the as-woven optimized pattern NiCr weave for 3 different wires. Quadratic equations were fit to each wire data set using a least squares fitting procedure and the fits and equations are shown.

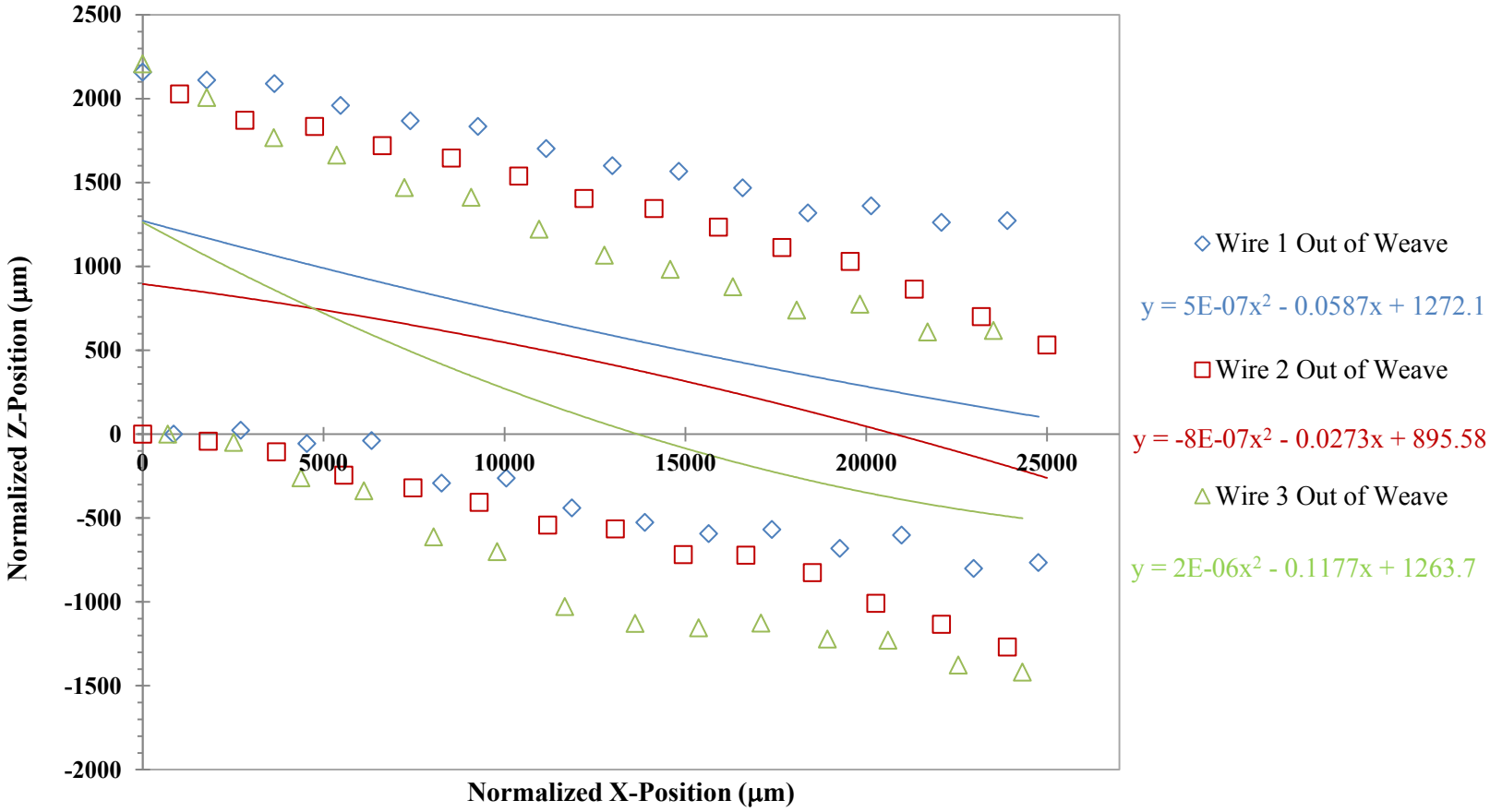

Figure 124: The individual position of each z-wire loop center for 3 wires after being removed from the optimized pattern NiCr weave that was heat treated to 300°C for 2 hours in air. Quadratic equations were fit to each wire data set using a least squares fitting procedure and the fits and equations for each fit are shown.

Table 15: Summary of the coefficients of the 'x^2' quadratic fits for the removed z-wire curvature measurements

	Z-Wire Curvature (10^{-6})			
	Standard As-Woven	Standard Heated	Optimized As-Woven	Optimized Heated
Wire 1	10	1	-0.9	0.5
Wire 2	7	5	1	-0.8
Wire 3	8	2	2	2
Wire 4	10			
Average	9	3	0.7	0.5

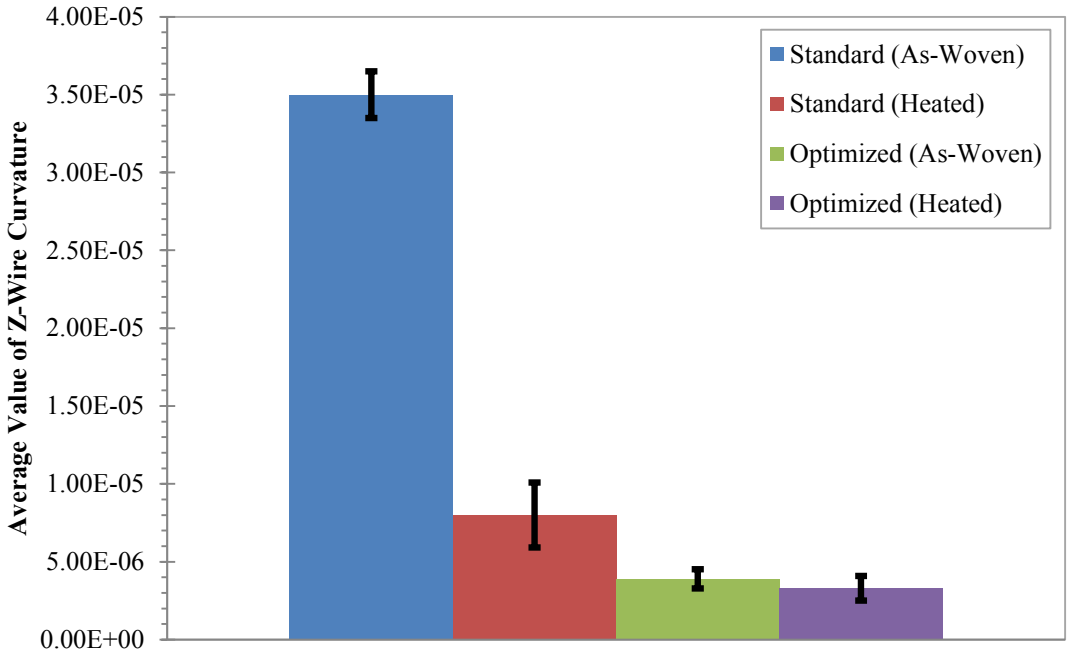

Figure 125: The absolute value of the quadratic fitting parameter for the z-loop position data sets was averaged for each pattern and condition. The values for each data set are shown with bars indicating one standard of deviation.

Examination of the overall curvature of the z-wires shows that the curvature in the standard weave is significantly greater than the curvature in the optimized pattern weaves. This indicates that the asymmetry in the residual stress in the of the top and bottom z-wires of the standard weave is greater than the asymmetry in the residual stress in the z-wires of the optimized weave. This is likely a result of the higher forces on the reed that are required when weaving the standard weave and the fact that the larger number of fill wires provide a greater resistance to the spring back of the z-wires (since there are more contact points and hence a greater frictional force to resist the spring back). This is also manifested as a smaller z-loop spacing in the warp direction as is shown in Table 16.

Table 16: Summary of the z-loop spacing in the NiCr weaves

Z-Loop Center to Center Spacing (μm)	Standard NiCr	Optimized NiCr
Warp Direction	1750 ± 100	1805 ± 78
Z Direction	2615 ± 230	2214 ± 67

In both architectures, the curvature of the heat treated wires is smaller than the global curvature of their as-woven equivalents. As the z-wires are heated in the weave, they are annealed in the flat configuration in which they are held by the fill wires. As a result, the heat treated samples exhibit less curvature than the equivalent as-woven z-wires. The smaller curvature in the heat treated samples should lead to a lower stress between z-wires and the neighboring wires, changes in the number of contact points, and a possible shift in the direction in which the load is applied. It is reasonable to assume

that this curvature change will modify the magnitude, direction, and distribution of the normal force for frictional damping between the z-wires and the fill wires. This complex redistribution could lead to a decrease in the frictional dissipation at these junctions. This could also help to explain the observed decrease in the damping properties after exposure to high temperatures, however, the complex nature of these changes does not allow us to directly tie the changes in curvature to a change in the observed loss factor.

5.2.3.5: Measurements of the Angular Change of the Z-Wires:

In order to quantify the changes in the geometry with temperature exposure of the z-wires, while they are still in the weaves, in a manner that accounts for the difference in the effective thickness change of the weave, I chose to quantify the changes in the z-wire geometry by connecting the z-loop centers with a series of triangles and monitoring the changes in the angles of the triangles in order to account for changes in the weaves. In this way, changes in the weave can then be quantified in terms of angles which are independent of the effective thickness of the weave. A model of how the calculation of the triangles was performed is shown in Figure 126. The calculation of the angle, α, was performed for all z-wire samples. In order to expand the technique, wires both in and removed from the weave were examined with this technique. Datasets were separated into the triangles with subsequent identifying angles for the top and bottom of the weave separately (in order to also help quantify the curvature). Top and bottom angles were

assigned based on the curvature of the z-wires in a set as was described previously. The average angle, α_o, was examined for the z-wires before they were removed from the weaves for both patterns (standard and optimized) and both states (as-woven and heat treated) in order to examine baseline difference in the angles between the z-loops when the z-wires are in the weaves. The results of these measurements can be seen in Figure 127.

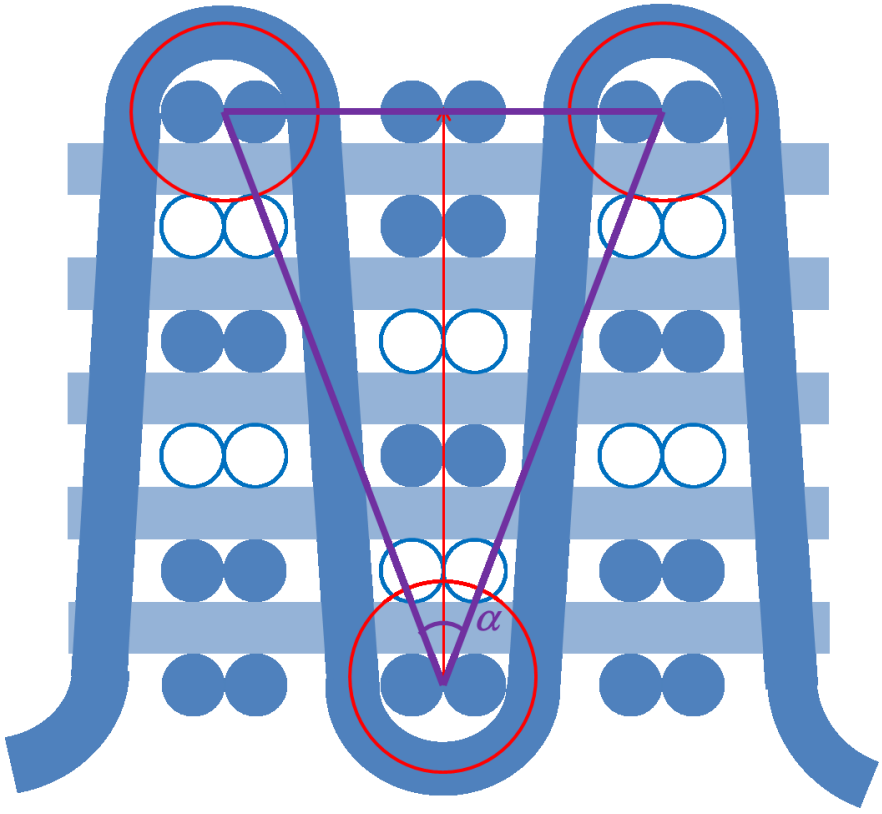

Figure 126: A model of the warp/z plane showing a triangle superimposed on the weave with the vertices of the triangle connecting the z-loop centers. This triangle serves to quantify the changes in the weave in a way that is independent of the thickness of the weave.

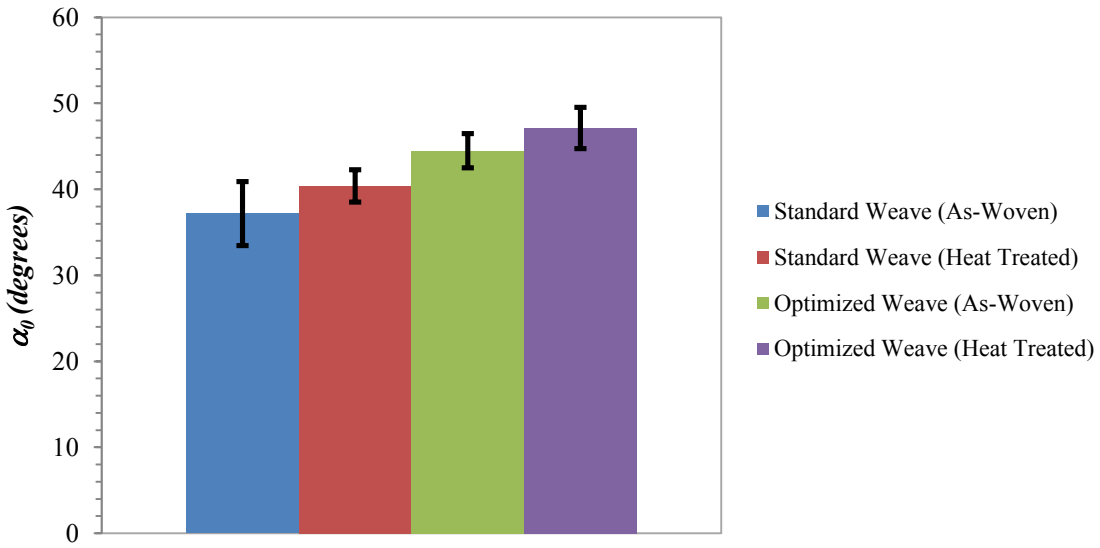

Figure 127: A plot of the characteristic angle, α, for the z-wire in the NiCr weaves. Both patterns and states(as-woven and heat treated) are shown in the plot and it can be seen that the angle increases when the material is heat treated and that the angle is larger in the optimized weaves than in the standard weave.

Examination of these measurements and calculations indicates two major things. First, there is a small increase in the characteristic angle, α_o, for these weaves when they are heat treated. This indicates that there is most likely an increase in the spacing of the weave along the warp direction which is necessary to accommodate the decrease in the thickness of the weave as was shown in Figure 110. Additionally, the characteristic angle is overall larger in the optimized weave than in the standard weave. This implies that the crimping of the z-wire loops is not as tight in the optimized weave as it is in the standard weave. This was seen in both the Cu and NiCr weaves. This is likely due to the fact that there are fewer fill wires in the optimized pattern to resist the spring back of the z-wires. Also, it may be the result of the fact that with fewer wires in the weave and more open space in the optimized, the pressure the reed exerts on the fill wires to crimp the z-wires into the loops may have to be lower in order to prevent twisting.

After the z-wires were removed from the weave, the same measurement was repeated. The results of these measurements are shown in Figure 128.

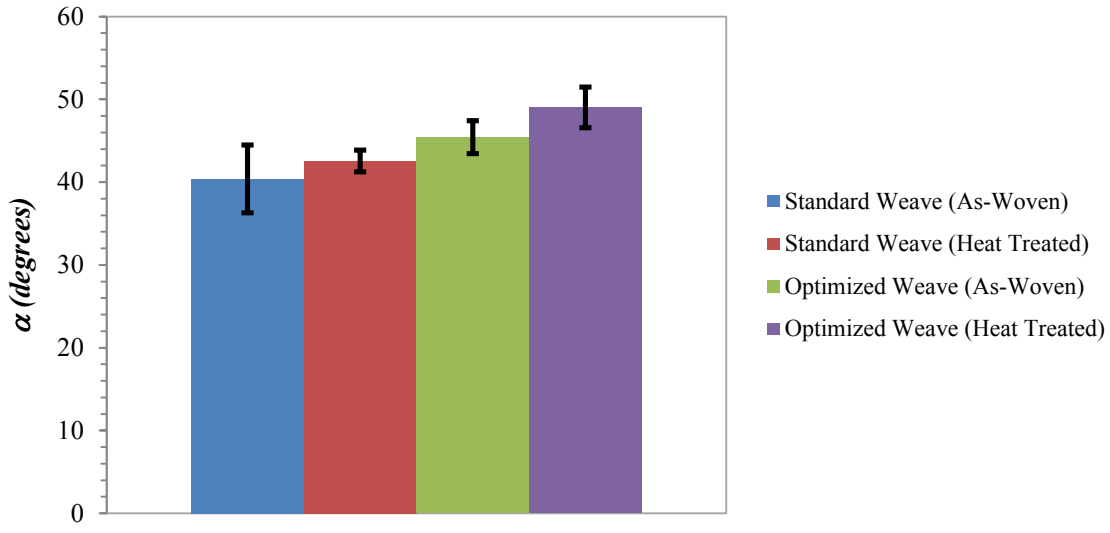

Figure 128: A plot of the characteristic angle, α, for the z-wire once it was removed from the NiCr weaves. Both patterns and states(as-woven and heat treated) are shown in the plot and it can be seen that the angle increases when the material is heat treated and that the angle is larger in the optimized weaves than in the standard weave, which is in agreement with the measurements of the z-wires in the weave.

Examination of the angle, α, for the z-wires after they were removed from the weave show an overall increase for all cases. This is shows that there is a relaxation of residual stress in the warp direction for all of the z-wire when they are removed from the weave. The fact that the overall distribution of the angle for each of the four cases remains the same (standard as-woven < standard heat treated < optimized as woven < optimized heat treated) implies that the differences in α as a result of residual stress are smaller than the changes in α that occur as a results of the heat treatment or differences in architecture. In order to directly examine the differences in α between the wires in the weave and when

they were removed, the difference was calculated and it is shown in Figure 129. The magnitude of the difference in the angle between the wires after they were removed from the weaves compared to the wires in the weave is relatively small (1 – 3°). Additionally, there does not appear to be any pattern in the data that indicates that with heat treatment there is a clear change in the angle of the weave from this data. In fact, these results, particularly Figure 127 are direct evidence of an increase in the z-loop spacing and α, which indicates that the weaves relax the residual stress in the z-wires by spreading in the warp direction when they are heated. This is likewise accompanied by a decrease in the effective thickness of the weave after heating. These results suggests that the decrease in damping that is found in these materials is a combination of several changes in the weave geometry and not one single change.

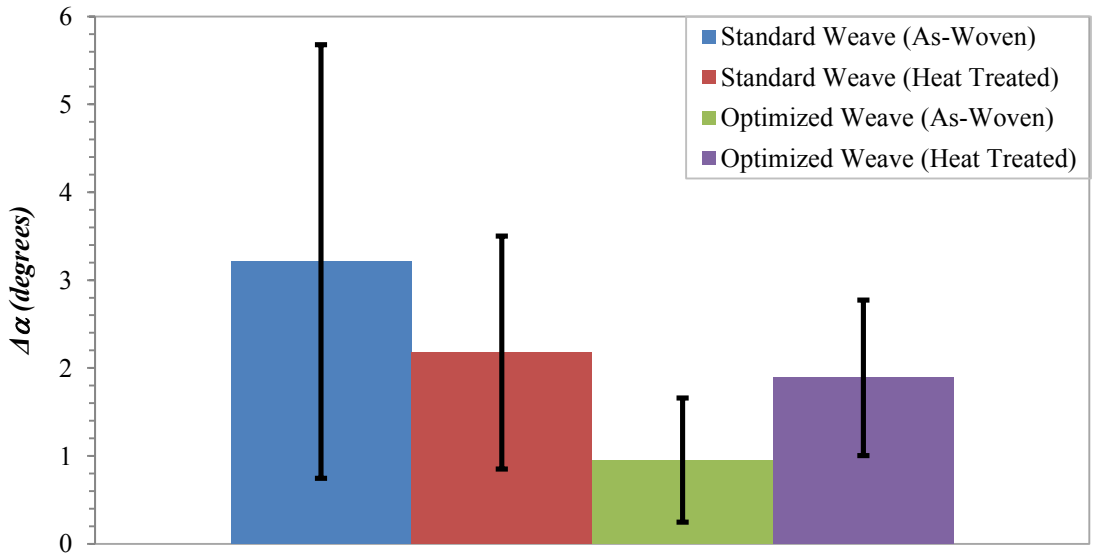

Figure 129: A plot of the difference in the average characteristic angle, α, for the z-wire once it was removed from the weave minus the z-wire in the weave for the NiCr weaves. Both the as-woven and heat-treated cases of both architectures are shown. The difference in the characteristic angle, α, are small and are on the order of 1-3°,

As was done previously with the FE models of the weave, a closer examination of the results, where the top and bottom of the weave were treated as separate data sets, can provide further insight into the asymmetric differences in the weave as a result of weaving pattern and heat treatment that cause changes in the curvature of the z-wire. In this case, the difference in angle between the top and bottom of the weave was examined since it is directly related to the curvature of the wire that was discussed before. The average angle for the all of the top z-loops for a particular case and all of the bottom z-loops for the same case were averaged and the difference between the top and bottom (which is related to the curvature of the z-wire) is what is shown. The data was also analyzed such that the difference was calculated for each wire individually before the average value was calculated. The results were the same in both cases indicating that the processing method does not change the results. The difference between the top and bottom weave angles for each of the four cases for the NiCr z-wires both in and out of the weave are shown in Figures 130-131.

In order to evaluate the residual stress in terms of the curvature of the weave we must compare the difference in angle between the top and bottom of the weave for each case both in the weave and after the z-wire was removed from the weave. The difference was calculated as the difference in characteristic angle for the z-wire once removed from the weave minus the z-wire angle difference in the weave. This is denoted as the $\Delta\Delta\alpha$ for the weave and it is related to the relative amount of the curvature in the z-wire normalized by the initial curvature in the weave (which should be relatively small since the z-wire is fixed into position by the fill wires). This value is related to the asymmetric

residual stress in the weave. The results of these calculations for the four different cases of the NiCr weaves are shown in Figure 131.

These results agree with previous results that the standard weave has a larger amount of asymmetric spring back than the optimized weave. Additionally, the heat treated state for both weaves exhibits less curvature than the as-woven states implying that the curvature (which is a result of an asymmetric residual stress in the weaves) relaxes with exposure to temperature.

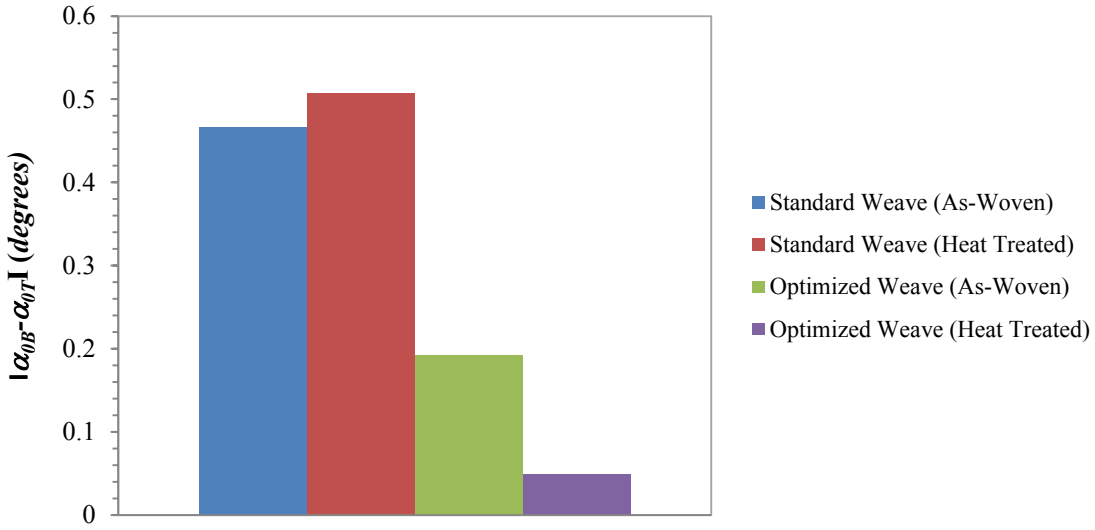

Figure 130: The absolute value of the difference in characteristic angle, α, between the average of all top characteristics angles minus the average of all bottom characteristic angles for a particular case for the z-wires in the NiCr weaves. Notice that the difference in characteristics angle is small, which validates the assumption that the z-wire is initially flat in the weave.

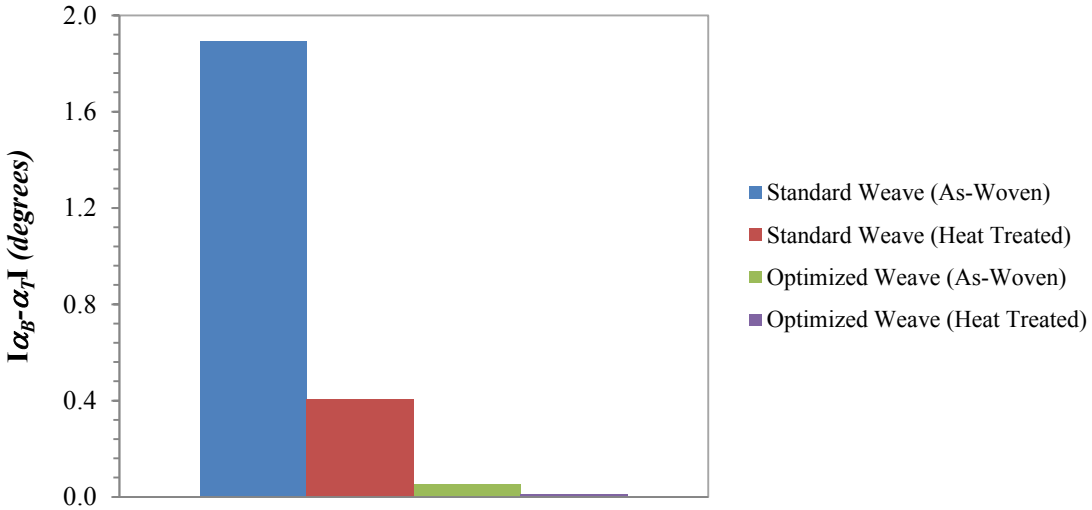

Figure 131: The absolute value of the difference in characteristic angle, α, between the average of all top characteristic angles minus the average of all bottom characteristic angles for a particular case for the z-wires in the NiCr weaves. Notice that the difference in characteristics angle is larger, which explains the change in curvature as the z-wire is removed from the weave.

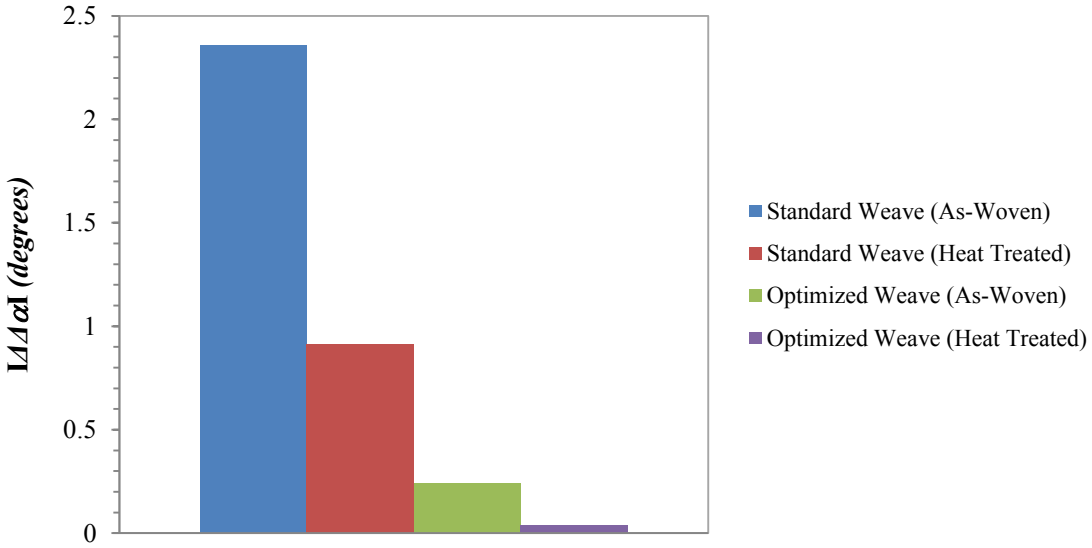

Figure 132: The relative curvature of the weave when the wire is remove reported in terms of the characteristic angle, α, normalized by the initial state of the z-wire in the weave. This is an indication of the relative amounts of residual stress in the z-wires in the different weaving patterns and states (as-woven and heat treated).

Overall, this series of measurements indicates that the changes in the weave as a result of heat treatment are small, but measureable. It has been shown that as a result of heat treatment, the weave spreads in the warp direction (as shown by the change in α_o and α) and shrinks in the thickness (as shown by the decrease in L with temperature exposure). Additionally, the z-wires also contain a residual stress that is a result of spring back of the z-wires during the weaving process. This is manifested as an overall global curvature of the z-wires along the warp direction in the warp/fill plane. This curvature was found to relax after heat treatment of the wires in the weaves. The relaxation is believed to decrease the modify the magnitude and direction of the forces between the fill and z-wires, although modeling of the average changes in contact forces is difficult since the number of contact points between the fill and z-wires is stochastic. This possible change in contact force could affect the normal force for frictional damping between the fill and z-wires, which would change the energy dissipation for frictional damping after heat treatment.

Although frictional damping may decrease with temperature since the normal forces for frictional damping are believed to change, inertial damping mechanisms remain present in the weave. As a result, the damping in the material decreases with temperature exposure, which is indicated to be the result of a decrease in the frictional energy dissipation, however, modeling indicates that inertial damping would remain unaffected. As a result, these 3D woven metallic microlattice materials exhibit a measurable decrease in damping with temperature, but they still exhibit high (inertial) damping at elevated temperatures. The effects of temperature on the inertial damping will be examined in the next section.

5.2.4: Effects of Temperature on Inertial Damping

Inertial damping in the weaves is a damping mechanism that is a result of vibrations of individual segments of the wires suspended between orthogonal wires that vibrate like a vibrating string. The individual wire segment lengths are determined by the spacing between columns of paired warp or fill wires. The length of a warp wire segment is therefore defined by the spacing between columns of fill wire pairs and the length of a fill wire segment is then the converse.

In order to understand how the changes in the weaves with temperature exposure affects the frequency bands in which the energy dissipation of the vibrating wire segments (through shifting the natural frequencies) we can examine the classical physics model of the simple vibrating string. In this model, the natural frequency of the wire is defined as [106],

$$f_n = \frac{1}{2\pi}\sqrt{\frac{k}{m}} \tag{40}$$

where, f_n is the natural frequency. k is the stiffness, and m is the mass. The mass, m, is not affected by temperature exposure, but the stiffness is affected by changes in the length of the wire segments.

For a wire segment supported on both ends the stiffness, k, is directly proportional to the inverse of the length, L, of the wire segment cubed [11,101],

$$k \propto \frac{1}{L^3} \tag{41}$$

Subsequently, the natural frequency of the wire segment is related to the length as,

$$f_n \propto L^{-3/2} \tag{42}$$

In the previous sections of this chapter, the changes in the z-wire geometry with temperature were examined. Measurements of the changes in the characteristic angle, $\Delta\alpha$, showed that the weave expanded in the warp direction when the weave was exposed to elevated temperatures. This indicates that the spacing of the z-loops (and subsequently the length of the vibrating warp wires) will increase with temperature. This will cause a decrease in the natural frequencies of the vibrating wires in the weave. The expansion, however, has a significant uncertainty that is nearly on the same order as the change itself. The uncertainty in the characteristic angle, α, and the change in the characteristic angle, $\Delta\alpha$, also indicates that the length of the vibrating wires that are responsible for the inertial damping will have a range of fundamental frequencies instead of a singular

frequency. This implies that the inertial damping occurs in bands of frequencies, and that defects and irregularities in the architecture may actually help increase damping abilities of the weaves.

5.2.5: Conclusions of High Temperature Damping Study

Overall, the high loss factor of the as-woven weaves has been shown to decrease with the exposure to elevated temperatures in both architectures and wire types. The loss factor decreased as the maximum temperature to which the material was exposed increased. Finite element modeling indicated that the damping in the weaves was a result of three damping mechanisms: internal damping of the individual wires, frictional sliding of wires against neighboring wires, and inertial damping of individual wire segments.

In order to develop a greater understanding of the changes in the weaves with temperature, standard and stiffness and permeability optimized architecture NiCr weaves were sectioned and the z-wires in the weave were analyzed both in the weave and after being carefully removed. NiCr weaves were also heated in air for 5 hours in order to evaluate the effect that temperature has on the geometry and spring back in the z-wires. The wires were likewise examined both in and out of these weaves as well.

From a culmination of literature and modeling, the changes in the internal damping of the wires that form the weave were determined to provide a small portion of the measured damping even after exposure to temperatures as high as 88% of the absolute melting temperature. Internal damping of the wires should not be affected by temperature exposure and the internal damping of the wires was orders of magnitude less than the measured damping. Any small changes that may occur in the internal damping of the wires could not be used to explain the large changes in the measured damping.

Frictional damping, specifically between the fill and z-wires, was examined and analytically modeled in this section. Measurements of the geometry changes in the z-wires, as a result of being removed from the weave before and after exposure to 300°C in air for 5 hours, allowed me to calculate the normal force between the fill and z-wires in the NiCr weaves. These values were then used to calculate the contribution of this frictional damping mechanism to the overall loss factor. The frictional (fill/z) and inertial damping were examined and found to make up 20-25% of the overall loss factor on average. Although the measurements do not directly indicate that the normal force for fill/z frictional damping decreases with temperature, these calculations indicate that this mechanism provides a significant contribution to the measured damping. Other observations indicate that the geometry and distribution of inter-wire forces in the weave may change with temperature and that the in-plane dimensions of the weaves increase with temperature, which is complemented by a decrease in the thickness (out-of plane dimension) of the weaves. The removal of the z-wires in the weaves revealed that there is also an overall curvature in the z-wires which is a result of an asymmetric distribution of residual stress (spring back) in the z-wires which is related to asymmetries in the

weaving process. This curvature is greater in the standard weave, but a clear decrease in both the standard and optimized weaves with thermal exposure are observed. This leads to a redistribution of the forces for frictional damping which could also help to explain some of the changes that occur with temperature exposure that affect the damping.

The inertial damping in the weaves was uncovered through FE modeling and experiments. The inertial damping dissipates energy individual wire segments, which are supported by orthogonal supporting wires, vibrating at their natural frequencies. This mechanism is affected by temperature by causing a shift in the natural frequencies. Uncertainties in the length of the vibrating segments and the changes in length with temperature exposure leads to broadening of the range of natural frequencies. The natural frequencies may shift and broaden with exposure to temperature which will shift the targeted frequencies of this mechanism, but not the overall magnitude of the response of the mechanism.

Chapter 6: Summary and Conclusions

Traditional material science techniques and understanding looks to develop and improve materials by controlling the processing and the resulting microstructure in order to obtain the desired properties. A new field is emerging, which looks to control the microscale architecture of materials in a manner analogous to controlling the architecture of civil engineering structures in order to develop materials with substantial improvements in properties. In this study, 3D weaving of metallic wires was used in combination with topology optimization in order to design and manufacture materials with well-defined microscale architecture. Selective bonding techniques (primarily brazing) were used to join tangentially contacting wires in order to turn the 3D woven materials into microlattice materials. The stiffness and permeability of these materials were characterized experiment and used to confirm the topology optimization predictions. Driven by potential applications, samples were made to explore the convective thermal transport and the high temperature damping properties of woven metallic lattices. The key research findings of this work in the areas where my research efforts were focused are described in the following section. Additionally, potential future activities that were inspired by these findings are described in Section 6.2.

6.1 Key Findings

This collaborative effort has shown that microlattice materials can be designed through the use of topology optimization that includes the constraints defined by the manufacturing process. Furthermore, metallic lattice materials with prescribed internal architecture were successfully manufactured through a combination of 3D weaving of metallic wires and selective bonding techniques. These metallic lattice materials possess high specific stiffness and permeability, and these properties were decoupled and permeability varied by more than an order of magnitude. My research in this work were primarily in the following areas: 1) the development of a brazing process in which these materials could be selectively bonded in order to improve their rigidity, while maintaining their permeability; 2) the characterization of the damping properties and developing an understanding of the changes that occur as a result of the exposure to elevated temperatures; 3) and the design and manufacturing of microlattice materials for use in heat transfer applications and their combination with headers that greatly improved their thermal performance and decreased lateral thermal gradients.

6.1.1: Key Finding Related to Brazing Include:

- The brazing process described in this thesis can be used to selectively bond the tangential junctions between wires in weaves that dramatically increases the stiffness of the material without negatively affecting the permeability. This

brazing process effectively turns the 3D woven materials into microarchitectured lattices.

- A modified version of the selective brazing technique can be used to successfully bond multiple layers of 3D woven material together in order to increase the maximum size of the lattices beyond what can be currently woven on the available loom.
- Weaving of 3D weaves containing a fraction of fugitive wires that have the same composition as the braze and can be melted and used to selectively bond the materials together while also simultaneously increasing the permeability and decreasing the density of the material beyond the limits of what is able to be directly woven.

6.1.2: Key Findings Related to Damping Include:

- The measured damping properties of the as-woven 3D weaves of both Cu and NiCr exhibit loss factors at room temperature that are comparable to many common polymers and elastomers, and orders of magnitude greater than bulk metals.
- Model predictions indicate that there are two main mechanisms that contribute to damping in these materials and the measurements and modeling in this work helped to confirm their presence and contribution. The first mechanism is frictional wire on wire sliding, and the second is inertial damping caused by the out of phase motions of individual wires during forced vibrations.

- Modeling was found to underestimate the as-woven damping of the weaves since it doesn't include stochastic gap spacings and twists that increase the number of wire to wire contact points in the weave. Additionally, the model doesn't account for residual stress in the weaves that increases the contact forces between the wires and the frictional damping.
- The damping capacity was measured to decrease with exposure to elevated temperatures. This is attributed to 1) the increase in the average wire spacing in the warp direction after temperature exposure; and 2) relaxation in the curvature in the z-wires along the warp/fill plane in the z-direction. These changes serve to decrease the number of contact points in the weave and lower the contact forces between wires, which lead to a decrease in the number and normal force of frictional contact points.
- Nevertheless, the measurements of these metallic weaves at 300°C and after exposure to their maximum services temperatures (1200°C for NiCr) indicate that these materials are still excellent dampers with service temperatures that are far superior to traditional polymers and elastomers that possess similar damping abilities.

6.1.3: Key Findings Related to Heat Transfer Include:

- The convective heat transfer properties of the Cu lattice materials that I manufactured for this project were shown to be superior to many common competing structures and materials, such as micro fins and metallic foams.

Moreover, the combination of the 3D woven microarchitecture lattice materials with header structures improves not only the heat transfer coefficient, but also the local temperature gradients on the material.

6.2 Potential Future Research Directions

As with any scientific work, discovery opens the door to more avenues and expanded opportunities to dig deeper and to uncover new understanding and knowledge. The work in this thesis has served to provide a greater understanding of the design, fabrication, and characterization of 3D woven metallic microlattice materials. Improvements in the brazing, damping and heat transfer of these materials are possible with further research. This section describes a few possible suggestions for work that might serve to further extend the capabilities of microarchitectured metallic lattices.

6.2.1: Possible Advances in the Area of Brazing

- A preliminary study of the brazing of NiCr weaves was addressed in this thesis Section 3.2.5, however the further development and optimization of a brazing methodology for the 3D woven NiCr weaves could be useful in regards to alloy selection, processing temperature, and amount of added braze.

- This work has shown that including fugitive wires in weaves allows for the design and manufacturing of architectures that have higher permeability and lower density than can be woven with only one wire type. This technique removes the restrictions of the necessary wire positions that are inherent in the weaving process. This increased design flexibility has not been topologically optimized and improved strategies for holding the wires in place during brazing are still needed. The development of this area could lead to novel lattice structures with unique properties.

6.2.2: Possible Advances in the Area of Damping

- The topology of these materials was optimized for the shear stiffness and the permeability. The loss factors that I measured for both standard and "optimized" architectures can be considered a very successful proof of concept, but the internal architecture of these 3D weaves were never really optimized for damping. Future work in these materials could use the understanding that was developed in this work in order to topological optimize and manufacture materials that would increase the damping and allow for tunable dampers.

6.2.3: Possible Advances in the Area of Heat Transfer

- The metallic lattices manufactured in this dissertation showed that the convective heat transfer coefficient and the temperature uniformity of these materials are both very high and can be further augmented by combining these lattices with specially designed and manufactured headers. Although four geometries of headers were manufactured, in both ABS plastic and copper, and modeled with computational fluid dynamics, the geometry of the headers was not rigorously optimized (thickness, inlet and outlet sizes, inlet and outlet design, materials, etc.). Future work in this area should include the optimization of header geometries and the design of lattices to obtain the highest heat transfer coefficient with the smallest pressure drop and temperature gradient.

References

1. Wise, C., Pawlyn, M., and Braungart, M. (2013) Eco-engineering: Living in a materials world. *Nature*, **494** (7436), 172–175.
2. Christian J. Yungwirth, Haydn N.G. Wadley, John H. O'Connor, et al. (2008) Impact response of sandwich plates with a pyramidal lattice core. *Int. J. Impact Eng.*, (35), 920–936.
3. Dharmasena, K.P., Wadley, H.N.G., Williams, K., et al. (2011) Response of metallic pyramidal lattice core sandwich panels to high intensity impulsive loading in air. *Int. J. Impact Eng.*, **38** (5), 275–289.
4. H.N.G. Wadley, K.P. Dharmasena, M.Y. He, et al. (2010) An active concept for limiting injuries caused by air blasts. *Int. J. Impact Eng.*, **37** (3), 317–323.
5. Wadley, H.N.G. (2006) Multifunctional periodic cellular metals. *Philos. Transact. A Math. Phys. Eng. Sci.*, **364** (1838), 31–68.
6. Craig A. Steeves, Sergio L. dos Santos e Lucato, Ming He, et al. (2007) Concepts for strucutrally robust materials that combine low thermal expansions with high stiffness. *J. Mech. Phys. Solids*, (55), 1803–1822.
7. James K. Guest, and Jean H. Prevost (2006) Optimizing multifunctional materials: Design of microstructures for maximized stiffness and fluid permeability. *Int. J. Solids Struct.*, **43** (22-23), 7028–7047.
8. Roper, C.S. (2011) Multiobjective optimization for design of multifunctional sandwich panel heat pipes with micro-architected truss cores. *Int. J. Heat Fluid Flow*, **32** (1), 239–248.
9. E.O. Hall (1951) The Deformation and Ageing of Mild Steel: III Discussion of Results. *Proc. Phys. Soc. Sect. B*, **64** (9), 747–753.
10. Petch, N.J. (1953) The cleavage strength of polycrystals. *J Iron Steel Inst Lond*, **173**, 25–28.
11. George E. Dieter (1986) *Mechanical Metallurgy*, McGraw Hill.
12. Y. Brechet, and J.D. Embury (2013) Architectured materials: Expanding materials space. *Scr. Mater.*, (68), 1–3.
13. Gibson, L.J., Ashby, M.F., and Ashby, M. (1999) *Cellular Solids: Structure and Properties*, Cambridge University Press.
14. Ashby, M.F. (2011) *Materials selection in mechanical design*, Butterworth-Heinemann, Burlington, MA.
15. V.S. Deshpande, M.F. Ashby, and N.A. Fleck (2001) Foam Topology Bending Versus Stretching Dominated Architectures. *Acta Mater.*, **49**, 1035–1040.
16. M.F. Ashby, and Y.J.M. Brechet (2003) Designing hybrid materials. *Acta Mater.*, **51** (19), 5801–5821.
17. Schaedler, T.A., Jacobsen, A.J., Torrents, A., et al. (2011) Ultralight Metallic Microlattices. *Science*, **334** (6058), 962–965.
18. Kang, K.-J. (2014) Wire-woven cellular metals: The present and future. *Prog. Mater. Sci.*
19. M.F. Ashby, Tony Evans, N.A. Fleck, et al. (2000) *Metal Foams: A Design Guide*, Butterworth-Heinemann.
20. Anthony G. Evans, John W. Hutchinson, and Michael F. Ashby (1998) Cellular metals. *Curr. Opin. Solid State Mater. Sci.*, **3** (3), 288–303.

21. A.G. Evans, J.W. Hutchinson, N.A. Fleck, et al. (2001) The topological design of multifunctional cellular metals. *Prog. Mater. Sci.*, **46** (3), 309–327.
22. E. Andrews, W. Sanders, and L.J. Gibson (1999) Compressive and tensile behavior of aluminum foams. *Mater. Sci. Eng. A*, (270), 113–124.
23. Heeman Choe, and David C. Dunand (2004) Synthesis, structure, and mechanical properties of Ni-Al and Ni-Cr-Al superalloy foams. *Acta Mater.*, (52), 1283–1295.
24. Kumar P. Dharmasena, Haydn N.G. Wadley, Zhenyu Xue, and John W. Hutchinson (2008) Mechanical response of metallic honeycomb sandwich panel strucutres to high-intensity dynamic loading. *Int. J. Impact Eng.*, **35** (9), 1063–1074.
25. Dharmasena, K.P., Queheillalt, D.T., Wadley, H.N.G., et al. (2010) Dynamic compression of metallic sandwich structures during planar impulsive loading in water. *Eur. J. Mech. - ASolids*, **29** (1), 56–67.
26. John Banhart (2001) Manufacture, characterisation and application of cellular metals and metal foams. *Prog. Mater. Sci.*, (46), 559–632.
27. Banhart, J., and Seeliger, H.-W. (2008) Aluminium Foam Sandwich Panels: Manufacture, Metallurgy and Applications. *Adv. Eng. Mater.*, **10** (9), 793–802.
28. Kathryn D. Fink, Joanna A. Kolodziejska, Alan J. Jacobsen, and Christopher S. Roper (2011) Fluid dynamics of flow through microscale lattice structures formed from self-propagating photopolymer waveguides. *AlChE*, **57** (10), 2636–2646.
29. S. Gu, T.J. Lu, and A.G. Evans (2001) On the design of two-dimensional cellular metals for combined heat dissipation and strucutral load capacity. *Int. J. Heat Mass Transf.*, **44** (11), 2163–2175.
30. Sypeck, D.J., and Wadley, H.N.G. (2001) Multifunctional microtruss laminates: Textile synthesis and properties. *J. Mater. Res.*, **16** (03), 890–897.
31. Sangil Hyun, J.-E.C. (2009) Effects of imperfections on the mechanical behavior of a wire-woven bulk Kagome cellular metal under compression. *Comput. Mater. Sci.*, (1), 73–82.
32. Min-Geun Lee, G.-D.K. (2010) Compressive characteristics of a wire-woven cellular metal. *Mater. Sci. Eng. A*, **539**, 185–193.
33. Lee, M.G., Yoon, J.W., Han, S.M., et al. (2014) Effects of Gaps between Discontinuous Wire Woven Kagome Cores upon Bending of Sandwich Panels. *Procedia Mater. Sci.*, **4**, 195–200.
34. Lee, M.-G., and Kang, K.-J. (2014) Mechanical Behaviors of Wire-woven Metals Composed of Two Different Thickness of Wires. *Procedia Mater. Sci.*, **4**, 25–29.
35. Lee, M.-G., and Kang, K.-J. (2014) Feasibility of a wire-woven metal for application as a sandwich core. *Int. J. Mech. Sci.*, **80**, 81–92.
36. A. Torrents, T.A. Schaedler, A.J. Jacobsen, et al. (2012) Characterization of nickel-based microlattice mateirals with structural hierarcy from the nanometer to the millimeter scale. *Acta Mater.*, **60** (8), 3511–3523.
37. Ladan Salari-Sharif, Tobias A. Schaedler, and Lorenzo Valdevit (2014) Energy dissipation mechanisms in hollow metallic microlattices. *J. Mater. Res.*, **29** (16), 1755–1770.
38. Kevin J. Maloney, Kathryn D. Fink, Tobias A. Schaedler, et al. (2012) Multifunctional heat exchangers derived from three-dimensional micro-lattice structures. *Int. J. Heat Mass Transf.*, **55** (9-10), 2486–2493.

39. Christopher S. Roper, Kathryn D. Fink, Samuel T. Lee, et al. (2013) Anisotropic convective heat transfer in microlattice materials. *Am. Inst. Chem. Eng.*, **59** (2), 622–629.
40. Jiwon Mun, Byoung-Gwan Yun, Jaehyung Ju, and Byung-Moon Chang (2015) Indirect additive manufacturing based casting of a periodic 3D cellular metal - Flow simulation of molten aluminum alloy. *J. Manuf. Process.*, **17**, 28–40.
41. Liz Nickels (2014) 3D printing the world's first metal bicycle frame. *Met. Powder Rep.*, **69** (2), 38–40.
42. Mohamed, M.H., and Salama, M.M. (2001) High speed three-dimensional weaving method and machine. US6315007 B1, filed Mar. 23, 2001 and issued Nov. 13, 2001.
43. Mohamed, M.H., and Bilisik, A.K. (1995) Multi-layer three-dimensional fabric and method for producing. US5465760 A, filed Oct. 25, 1993 and issued Nov. 14, 1995.
44. Keith Sharp, D. Mungalov, and J. Brown (2014) Metallic Cellular Materials Produced by 3D Weaving. *Procedia Mater. Sci. 4*, **4**, 15–20.
45. A. P. Mouritz, K.H.L. (1997) A review of the effect of stitching on the in-plane mechanical properties of fibre-reinforced polymer composites. *Compos. Part Appl. Sci. Manuf.*, **28** (12), 979–991.
46. A.P. Mouritz, and B.N. Cox (2000) A mechanistic approach to the properties of stitched laminates. *Compos. Part Appl. Sci. Manuf.*, **31** (1), 1–27.
47. A.P. Mouritz, and B.N. Cox (2010) A mechanistic interpretation of the comparative in-plane mechanical properties of 3D woven, stitched and pinned composites. *Compos. Part Appl. Sci. Manuf.*, **41** (6), 709–728.
48. Challis, V.J., Guest, J.K., Grotowski, J.F., and Roberts, A.P. (2012) Computationally generated cross-property bounds for stiffness and fluid permeability using topology optimization. *Int. J. Solids Struct.*, **49** (23-24), 3397–3408.
49. James K. Guest, and Jean H. Prevost (2007) Design of maximum permeability material structures. *Comput. Methods Appl. Mech. Eng.*, **196** (4-6), 1006–1017.
50. Zhao, L., Ha, S., Sharp, K.W., et al. (2014) Permeability measurements and modeling of topology-optimized metallic 3-D woven lattices. *Acta Mater.*, **81**, 326–336.
51. Yong Zhang, Seunghyun Ha, Keith Sharp, et al. Fabrication and mechanical characterization of 3D woven Cu lattice materials. *Mater. Des.*
52. Brazing vs Soldering | Lucas-Milhaupt.
53. Mechanical and Physical Properties.
54. R. Gabbay, S.F. Dirnfeld, J.J. Ramon, and H.Z. Wagner (1990) The Mechanism of Tough-Pitch Copper Embrittlement by Silver Brazing Alloys. *Weld. J. Suppl.*, 378–381.
55. S.F. Dirnfeld, R. Gabbay, J.J. Ramon, and H.J. Wagner (1991) Copper embrittlement by silver brazing alloys. *Mater. Charact.*, **26** (1), 17–22.
56. Chu, W.F., and Rahmel, A. (1979) The kinetics of the reduction of chromium oxide by hydrogen. *Metall. Trans. B*, **10** (3), 401–407.
57. Douglass, D.L. (1968) The oxidation mechanism of dilute Ni-Cr alloys. *Corros. Sci.*, **8** (9), 665–678.

58. David A. Porter, and Kenneth E. Easterling (1992) *Phase Transformations in Metals and Alloys*, CRC Press.
59. Daniel B. Butrymowicz, John R. Manning, and Michael E. Read (1974) Diffusion in Copper and Copper Alloys Part II. Copper-Silver and Copper-Gold Systems. *J. Phys. Chem. Ref. Data*, **3** (2).
60. G. Barreau, G. Brunel, G. Cizeron, and P. Lacombe (1970) Determination of Volume and Grain Boundary Heterodiffusion Coefficients of Silver in Pure Copper, and Effects of the Alloying Elements Chromium, Tellurium, Titanium, and Zirconium on these Coefficients. *C. R. Acad. Sci*, **270**, 516–519.
61. G. Barreau, G. Brunel, G. Cizeron, and P. Lacombe (1971) Diffusion in the Copper-Silver System: Heterodiffusion and Chemical Diffusion. Influence of Dilute Alloying Additions of Cr, Te, Ti, and Zr to the Copper. *Mem. Sci. Rev. Metall.*, **68**, 357–366.
62. D.A. Blackburn, and A.F. Brown (1962) Diffusion and Grain Boundary Slide in Copper Bicrystals. *91*, 106–113.
63. D.A. Blackburn, and A.F. Brown (1960) Diffusion in Moving Grain Boundaries.
64. Ag-Cu Phase Diagram & Computational Thermodynamics.
65. M. G. Nicholas (1998) *Joining processes: introduction to brazing and diffusion bonding*, Kluwer Academic Publishers, Boston.
66. Rudolf Strauss (1998) *SMT Soldering Handbook*, Newnes, Woburn, MA.
67. (2014) *Arcor Electronics*.
68. Amanda J. Levinson, and Richard W. Fonda (2015) Private Communications - Serial Sectioning and Microtomography Analysis.
69. Safa O. Kasap (2001) *Optoelectronics and Photonics: Principles and Practices*, Prentice-Hall, Upper Saddle River, NJ.
70. Coherent, Inc. Thermal Considerations in Design of Water-Cooled DPSS Laser Systems.
71. G. Frommeyer, and G. Wassermann (1975) Anomalous properties of in-situ-produced silver-copper composite wires I. Electrical conductivity. *Phys. Status Solidi A*, **27** (1), 99–105.
72. Devin E. Burns, Y.Z. (2012) Development of Ni-based superalloys for microelectromechanical systems. *Scr. Mater.*, **67** (5), 459–462.
73. Sara J. Perez-Bergquist, N.V. (2011) High-Temperature Performance of Actively Cooled Vapor Phase Strengthened Nickel-Based Thermostructural Panels. *Aiaa J. - AIAA J*, **49** (5), 1080–1086.
74. Dinc Erdeniz, Amanda J. Levinson, Keith W. Sharp, et al. (2014) Pack Aluminization Synthesis of Superalloy 3D Woven and 3D Braided Structures. *Metall. Mater. Trans. A*.
75. Dinc Erdeniz, and David C. Dunand (2014) Microstructure development during pack aluminization of nickel and nickel–chromium wires. *Intermetallics*, **50**, 43–53.
76. Ampika Bansiddhi, and David C. Dunand (2011) Processing of NiTi Foams by Transient Liquid Phase Sintering. *J. Mater. Eng. Perform.*, **20** (4), 511–516.
77. C. Bewerse, L.C. Brinson, and D.C. Dunand (2014) NiTi with 3D-interconnected microchannels produced by liquid phase sintering and electrochemical dissolution of steel tubes. *J. Mater. Process. Technol.*, **214** (9), 1895–1899.

78. Reza Sharghi-Moshtaghin, H.K. (2010) Low-Temperature Carburization of the Ni-base Superalloy IN718: Improvements in Surface Hardness and Crevice Corrosion Resistance. *Metall. Mater. Trans. A*, **41** (8), 2022–2032.
79. Frank P. Incropera, David P. DeWitt, Theodore L. Bergman, and Adrienne S. Lavine (2006) *Fundamentals of Heat and Mass Transfer*, John Wiley & Sons.
80. Lalanne, C., and Lalanne, C. (2002) *Fatigue Damage*, CRC Press.
81. Tedesco, J.W., McDougal, W.G., and Ross, C.A. (1999) *Structural dynamics: theory and applications*, Addison Wesley Longman, Menlo Park, Calif.
82. Szyniszewski, S., and Krauthammer, T. (2012) Energy flow in progressive collapse of steel framed buildings. *Eng. Struct.*, **42**, 142–153.
83. Szyniszewski, S. (2009) Dynamic energy based method for progressive collapse analysis. *2009 Struct. Congr. - Dont Mess Struct. Eng. Expand. Our Role April 30 2009 - May 2 2009*, 1259–1268.
84. Childs, D.W. (1978) The Space Shuttle Main Engine High-Pressure Fuel Turbopump Rotordynamic Instability Problem. *J. Eng. Gas Turbines Power*, **100** (1), 48–57.
85. Ertas, B.H., and Luo, H. (2008) Nonlinear Dynamic Characterization of Oil-Free Wire Mesh Dampers. *J. Eng. Gas Turbines Power*, **130** (3), 032503–032503.
86. Ertas, B., Luo, H., and Hallman, D. (2009) Dynamic Characteristics of Shape Memory Alloy Metal Mesh Dampers.
87. M. Carfagni, E. Lenzi, and M. Pierini The Loss Factor as a Measure of Mechanical Damping.
88. Lazan, B.J. (1968) *Damping of materials and members in structural mechanics*, Pergamon Press.
89. Liu, W. (2008) *Experimental and Analytical Estimation of Damping in Beams and Plates with Damping Treatments*, University of Kansas.
90. Granta Designs Ltd. (2014) *The CES EduPack '14*, Granta Design Ltd., Cambridge, UK.
91. Hallquist, J. (2006) *LS-DYNA theory manual*, Lawrence Software Technology Corporation, Livermore, California.
92. Ouyang, J.-H., Liang, X.-S., Liu, Z.-G., et al. (2013) Friction and wear properties of hot-pressed NiCr–BaCr2O4 high temperature self-lubricating composites. *Wear*, **301** (1–2), 820–827.
93. Hal Kahn (Private Communications) (2014) Private Communication - Dynamic Friction Measurements.
94. Avallone, E.A., Baumeister, T., and Marks, L.S. (1996) *Marks' Standard Handbook for Mechanical Engineers*, McGraw-Hill Publishing Co.
95. Dennis Coyne (2009) Allowable Bake Temperature for UHV Processing of Copper Alloys. 7.
96. Electrical Resistance Wire - RW80.
97. Nichrome Wire.
98. Nikrothal 80 — Kanthal.
99. Peter J. Blau (2009) *Friction Science and Technology: From Concepts to Applications*, CRC Press, Boca Raton.
100. E.J. Graesser, and C.R. Wong (1991) Analysis of Strain Dependent Damping in Materials via Modeling of Material Point Hysteresis.

101. Ugural, A.C. (2003) *Mechanical Design: An Integrated Approach*, McGraw-Hill Higher Education.
102. F.H. Stott, and G.C. Wood (1971) The mechanisms of oxidation of Ni-Cr-Al alloys at 1000°–1200°C. *Corros. Sci.*, **11** (11), 799–812.
103. Image Composite Editor - Microsoft Research.
104. A.C. Lewis, J.F. Bingert, D.J. Rowenhorst, et al. (2006) Two- and three-dimensional microstructural characterization of a super-austenitic stainless steel. *Mater. Sci. Eng. A*, 11–18.
105. A.C. Lewis, and A.B. Geltmacher (2006) Image-based modeling of the response of experimental 3D microstructures to mechanical loading. *Scr. Mater.*, (1), 81–85.
106. Ronald Lane Reese *University Physics*, Brook/Cole, Pacific Grove.

Vita

Stephen M. Ryan was born in Baltimore, Maryland in July 1986 to Robert and Jean Ryan. He has an older brother Robert. Stephen attended high school at the Boys' Latin School of Maryland in Baltimore, Maryland where he was the Valedictorian. He attended Loyola College of Maryland, where he was a Presidential Scholar. He graduated with a Bachelor of Science in engineering science with a concentration in mechanical engineering in 2008 and he was awarded the Engineering Science award. While at Loyola, Stephen was a Hauber Fellow for two summers, where he conducted research in computational fluid dynamics under the guidance of Dr. Robert Bailey. Upon graduation, he joined Dr. James Spicer's research group at Johns Hopkins University. He completed his Master of Science in Engineering Science with Thesis in December of 2011 on his work examining the optical properties and evolution of the NASA Solar Probe + thermal barrier coating system. Upon completion of his Master's, Stephen joined Dr. Kevin Hemker's group. In July of 2015 he completed his Doctor of Philosophy degree in Materials Science and Engineering for his work on the DARPA MCMA (Materials with Controlled Microscale Architecture) research project.